Università degli Studi di Camerino

School of Science and Technology
Physics Division

Reaction Mechanisms in Advanced Materials for Li and Na-ion Batteries Studied by X-ray Absorption Spectroscopy and Related Techniques

Doctoral Course in
Theoretical and Experimental Physics
Cycle XXXI

Candidate
Matteo Ciambezi

Supervisor
Prof. Andrea Di Cicco

Academic Year 2015/2018

Abstract

The research work presented in this thesis regarded the structural study of different materials employed as battery electrodes (for both Li and Na ion cells) by means of X-ray Absorption Spectroscopy (XAS), X-ray Photoelectron Spectroscopy (XPS) and Raman Spectroscopy. The main purpose of the thesis was to provide better insight, at a microscopic and atomic level, of all the mechanisms related to the insertion/de-insertion of lithium or sodium ions in the electrode structure at the electrolyte interface and the bulk. In particular we have tackled three main open problems concerning: i) the evolution of the local structure in zinc-ferrite conversion-alloying materials used in lithium-ion batteries, ii) the study of formation and evolution of the solid electrolyte interphase (SEI) in carbon-based anodes again used for lithium-ion cells, iii) the relationship between local structure distortion and electrochemical performances in a class of cathode materials for sodium-ion batteries.

By using X-ray absorption spectroscopy, we have shown that in the very early stages of Li^+ insertion (until 0.3 Li^+ per formula unit) carbon-coated zinc-ferrite nanoparticles anode retain the spinel structure while at higher level of Li uptake ($>$ 0.3 Li^+ per formula unit), Zn atoms migrate to vacant crystallographic sites. In this initial stage, Fe is found to be gradually reduced from Fe^{3+} to Fe^{2+} upon lithium insertion and remains in the original octahedral sites. Our EXAFS study indicates an increase in structural disorder upon lithiation. Lithiation proceeds with a continuous reduction of the Zn and Fe until those species are fully metallized in the form of nano-sized particles. Finally, we could provide direct proof of the reversible lithium-zinc alloying mechanism occurring in the very final stage of the lithiation.

The evolution and stability of the SEI were studied using an arsenic-containing compound as electrolyte. Arsenic acts as local probe for SEI formation for XAS and XPS, giving an insight into the oxidation state and structure of the SEI. Both XAS

and XPS revealed the presence of arsenic with oxidation state 3+ and 5+, possibly in the form of arsenic oxides (As_2O_5, As_2O_3) and arsenic-fluorine compounds (AsF_3, AsF_6^-, Li_xAsF_{3-x}). Moreover, XPS revealed the presence of As^0 (not detected by XAS) that could be present, in a small quantity, only on the outer layer of the SEI. The organic fraction of the SEI has been also studied with XPS, showing the presence of different lithium alkyls species and carbonates as a result of the degradation of the electrolyte organic solvents. Those species may contain lithium atoms contributing to the total capacity of the cell, in agreement with recent results. In-situ micro-Raman experiments, specifically developed during this thesis, were attempted showing the modifications of the graphitic host structure during lithium insertion in the material.

Finally, the structure of Mn-based layered oxides for sodium-ion cathodes, doped with Ti and Fe, was studied by X-ray Absorption Spectroscopy. We have verified that the oxidation states of Mn and Ti in P2-$Na_{2/3}Mn_{0.8}Fe_{0.2-x}Ti_xO_2$ are in agreement with the expected theoretical values. Our structural XAS refinement, compared with the results of DFT calculations and XRD data, confirmed experimentally the Jahn-Teller induced distortion of the structure for all the materials under consideration. A slight decrease of the local structural disorder is observed in the material where both Fe and Ti are present with equal proportions.

Most of the results presented in this thesis have been published in international journals, and the reader is referred to the published papers for further details.

Ringraziamenti

Desidero ringraziare il Prof. Andrea Di Cicco, supervisore della mia tesi di dottorato, per avermi concesso l'opportunità di affacciarmi al mondo della ricerca scientifica. Senza le sue indicazioni e supporto questo lavoro non sarebbe stato possibile.

Un grazie particolare ad Angela e Marco: indispensabili per me sia per i preziosissimi consigli e l'aiuto a svolgere il mio lavoro, sia per avermi sempre saputo incoraggiare ed ascoltare.

Ringrazio tutto il gruppo di Francesco Nobili, in particolar modo Marta, per la pazienza che hanno avuto nella costante collaborazione e per avermi insegnato e concesso l'utilizzo delle apparecchiature nel loro laboratorio.

Grazie ad i compagni di laboratorio, amici, colleghi dottorandi e non (Fabio, Matteo, Sara, Catia, Emin, Michele, Rahul, ...) per gli innumerevoli caffè, pranzi e "pause disperazione" passati insieme.

Un grazie immenso a Mamma, Babbo e Leonardo che mi hanno sempre dimostrato che posso contare su di loro, anche nei momenti di lontananza.

In fine un grazie speciale a Giulia che mi è stata vicina soprattutto nei periodi più frenetici e stressanti. Grazie per essere stata comprensiva nei momenti di mio maggiore impegno e per avermi dato incoraggiamento, conforto ed amore.

Matteo, Settembre 2019

Contents

Chapter 1

Introduction

1.1 The Climate Change Challenge

Climate change can be defined as the greatest health challenge of the 21samazfitt century [1]. The severity of the direct impact of climate change over human society and health is day by day more evident and clear. In fact, in the recent years, the public health community has rapidly agreed on the causal connection between climate change and health risks, with a better understanding of the factors that link these two issues, increasing the awareness on the significant health threats and offering possible solutions to avoid the worst impact [1].

Climate change impacts human health both directly and indirectly. The direct impact includes physiological effects from exposure to higher temperatures such as respiratory and cardiovascular diseases, and also injuries and death caused by the exposition of the population to extreme weather events such as heat-waves, severe flooding, wildfires and tropical storms; with a high impact on the global risk of populations. The indirect impact is related to the long-term modification of the local environment, with the possible degradation of air, water and soil quality that may cause climate-related displacement, immigration phenomena and conflicts [1, 2].

The drivers of climate change are for the big part derived from the combustion of fossil fuels and the subsequent emission of air-pollutant and greenhouse gases, which are emitted from several sectors: housing, transport, energy and agriculture [3].

1.1.1 Paris Agreement

In December 2015, the Paris Agreement [4] was adopted under the United Nations Framework Convention on Climate Change (UNFCCC) to combat the climate change [5]. It is the first climate agreement to obtain strong global support, and being now ratified by 183 countries [6]. Within this agreement, countries submitted national plans to address the climate change challenge after the year 2020; the main goal of Paris Agreement is to hold "the increase in the global average temperature to well below 2°C above pre-industrial levels and to pursue efforts to limit the temperature increase to 1.5°C above pre-industrial levels" [4]. This temperature goal represents the level of climate change that governments agree would prevent dangerous and irreversible interference with the climate system, while ensuring sustainable economic development and food production [5, 7, 8].

The Agreement allows each country to set their national targets and also supports low- and middle-income countries by a founding mechanism with a US$ 100 billion annual funding system [6]. This will allow all countries to find the most appropriate ways to overcome the issue of climate change while ensuring that all parties contribute to meet global goals [1].

Thus, Paris Agreement can be defined as the most important health agreement of this century [1], since it addresses not only the direct health risks, but also has the potential to bring strong positive changes and benefits in the industry, transport and energy sectors, since the proposed policies will widely and strongly influence social, cultural, economical, climate and environmental human activities [3].

1.2 Energy Policies against Climate Change and Renewable Energies

Currently, the big part of used energy source derives from fossil fuels. To fulfil the goals of Paris Agreement is necessary to perform a transition to affordable, reliable, sustainable and modern energy sources with zero greenhouse gases emission [1]. Nowadays the share of renewable energy sources is only 25% of the global electricity production [9], despite the fact that the cost of renewable energy production is falling quickly, and investments are growing fast. In order to successfully meet the goal of maintaining the global temperature 2°C above pre-industrial levels, the cut of renewable energy must be at least 65% [10].

Therefore, the policies on energy are based on scaling up renewable energy sources. In particular cutting down the share of energy derived from coal which represents more than 40% of CO_2 emission. Policy should, thus, ensure to phase out coal use as quickly as possible while ensuring a smooth transition to more eco-friendly sources.

The transport sector gives also another significant contribution to both greenhouse gas emissions and local air pollution. It is accountable for about 23% of the total energy-related greenhouse gas emissions globally [11]. More sustainable means of transport will include the employment of electric vehicles and encouraging the use of public transportation.

Nowadays private vehicles represent the main and more common means of transport worldwide and the most part of those employs heat engines running on petrol or diesel fuel; both emit greenhouse gases and also particulate which contribute to poor air quality. Even if there is a big increment in the number of electric vehicles (+50% between 2016 and 2017) they still represent a small number in the total of the global vehicle fleet. [11].

1.2.1 Role of Energy Storage Systems

The main issue with renewable energies is that the production is not constant nor always available. Most of renewable energy sources are, in fact, influenced or depend on external and natural phenomena, and cannot provide an immediate response to the demand since they are not easily adjustable to consumption needs. The unpredictable character of these sources requires that network provisioning and usage regulations be established for optimal system operation [12].

Delocalized electricity production and the use of time-fluctuating sources (wind turbines, solar, etc.) increase the difficulty of stabilizing the power network, due to an imbalance in supply/demand. Therefore may be convenient to produce the energy, transmit it, convert it and store it in case of surplus production in order to use the stored energy in times of higher demands [12].

Alongside to flexibility, Electrical Energy Storage (EES) will play a crucial role in the transition to low-carbon energy system. The International Energy Agency estimates that to fulfil the Paris Agreement it will be necessary to increase the energy storage capacity from the 140 GW of 2014 to 450 GW in 2050 [14]. This increase is furthermore necessary, as the European Commission underlined, to ensure the internal energy security and energy internal market. By using more EESs, the European Union can decrease its energy imports, improve the efficiency of the energy system and keep

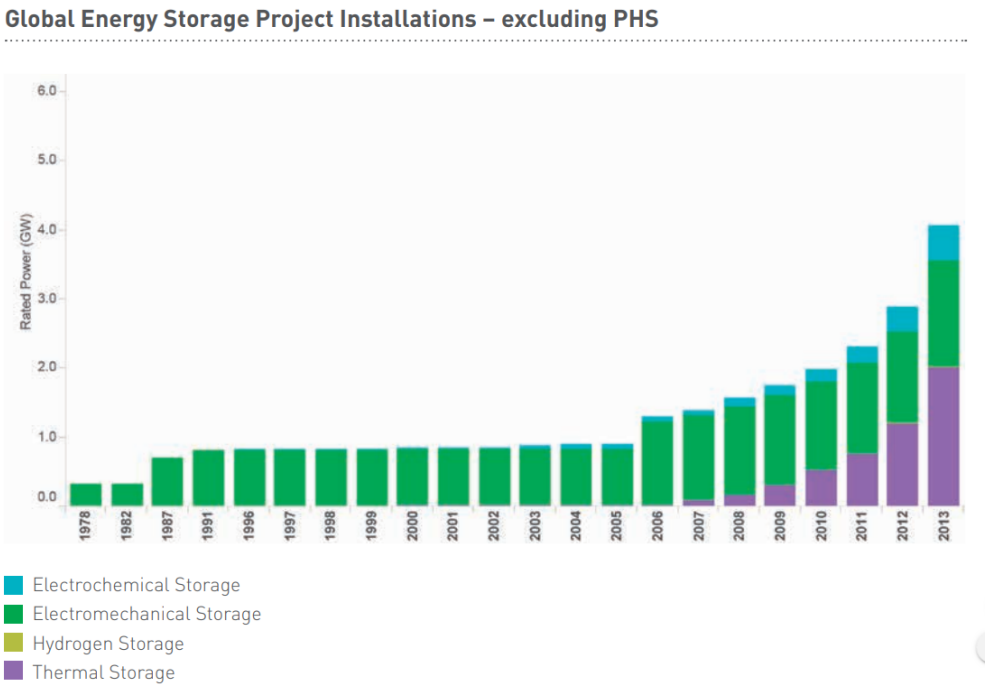

Figure 1.1: Globally installed energy storage capacity, 1978-2016, excluding pumped hydro storage [13]

the prices low [13].

At the present day, EES contribute to 10% of the installed generation capacity in Europe, where hydroelectric pumped storage is by far the most used storage technology. Many others EESs such as compressed air storage, flywheels, electrochemical (batteries) and thermal are available and can be competitive depending on the requirements of the application [15].

The largest representative of EESs for stationary applications (but also increasing in the automotive sector) is electrochemical storage or batteries that can store energy in a chemical form and convert it into electricity when needed. A more precise description of this class of EESs will be given in Chapter 2.

1.3 Purpose of this Thesis

As seen in the previous sections, electrochemical storage system is a crucial sector with a growing importance for a wide range of applications: from mobile electronic device energy storage, powering the future automotive fleet, and finally for micro-grid storage applications.

Modern battery technology (for example lithium/sodium ion cells) is relatively

recent (first commercial prototype were presented in the '90s) and presents a large margin of development. In particular, present research efforts, are focussed on increasing the capacity, energy density and durability; while at the same time improving safety, reliability, eco-friendliness and recyclability of the materials.

To pursue that, is fundamental to have a deeper and precise understanding of all the mechanisms that occur during the various chemical reactions and also at the structural level of the different active materials adopted. A description of electrochemical storage systems and relevant materials is presented in Chapter 2.

Within this scenario, I present my original doctoral thesis work. It collects the research activities carried out during the three years of my Ph.D. at the University of Camerino (Italy) under the supervision of Professor Andrea Di Cicco and during my six month visit period at the energy research center CIC EnergiGUNE in Vitoria (Basque Country - Spain) under the supervision of Doctor Miguel Àngel Muñoz-Màrquez. Moreover, part of the experimental work has been also carried out in Synchrotron Radiation facilities such as ESRF (Grenoble), Elettra (Trieste) and Soleil (Paris).

The thesis investigates structural properties and modifications occurring both on the surface of the electrodes and in the bulk of the electrochemical active materials, with a particular focus on the development of in-situ and in-operando experimental techniques, which allows to get a deeper understanding of the several and complex evolution processes occurring during the electrochemical-induced redox reactions. To achieve that, we employed several X-ray and optical spectroscopic techniques. In particular, X-ray Absorption Spectroscopy, X-ray Photo-emission Spectroscopy and Raman Spectroscopy; those techniques, when combined, result complementary one to each other, and are an optimal way to obtain both information regarding the surface of the material and the bulk. In particular X-ray Absorption Spectroscopy and X-ray Photo-emission spectroscopy are used in a large variety of research fields since they are element specific techniques and provide information about the local structure and the electronic structure around the single atomic sites also in complex systems. The description of the various experimental techniques adopted in this thesis is summarized in Chapter 3.

The first part of the original thesis work, presented in Chapter 4, concerns the study of the structural evolution in anodes for lithium-ion batteries composed of carbon-coated zinc-ferrite ($ZnFe_2O_4$) nanoparticles as active material. This is one member of a new

developing class of battery material with very promising performance, cost-effectiveness, ecological and safety characteristics: conversion/alloying materials. These materials employ a completely different reaction process if compared with standard and currently commercially available Li-ion cells; this mechanism involves major modification and re-organization of the material internal structure, leading to a full reduction and oxidation processes (of iron and zinc for $ZnFe_2O_4$ anodes) in order to store and de-insert lithium ions from the host electrode. These changes are not trivially investigable with commonly available laboratory techniques (X-ray Diffraction for example) due to the formation of amorphous phases and nano-crystallites. To overcome this issue, we performed different synchrotron-based X-ray Absorption Spectroscopy experiments, both on ex-situ samples (cycled electrodes, extracted from the Li-ion cell, sealed and measure) and in-situ/in-operando cells (experiments were performed in parallel with the operational cycles of the half-cell). For this material, it was important to have a better insight and a confirmation of the expected electrochemical reactions, in particular, to verify the final reversible alloying reactions between lithium and zinc which could provide an extra capacity storage for the material.

Chapter 5 is focused on the analysis of the interface which forms onto the electrode (referred as Solid Electrolyte Interphase - *cfr.* Chapter 2), mostly during the first lithiation/de-lithiation cycle. This interface is a crucial component of modern Li-ion and Na-ion battery cells since it acts as a protective layer, avoids further decomposition of the electrolyte and has a fundamental role on stability and cyclability of the battery. This aspect gained, in recent years, the attention of the scientific community. In particular, this research activity is a prosecution of the European project "Stable Interfaces for Rechargeable Batteries" (SIRBATT) in which my research group was involved. In this work we carried out X-ray Absorption Spectroscopy analysis of electrodes, obtaining information regarding the thickness, the oxidation state and structure of the interface. Moreover, my research activity included also the interfacial analysis of graphite anodes and the study of the formation processes and evolution of the SEI layer when using non-conventional electrolytes ($LiAsF_6$). Here I present a detailed X-ray Photo-spectroscopy analysis, performed on ex-situ samples, of such interface; providing supplementary and complementary details to the previous analysis.

The final part of the thesis, reported in Chapter 6, is devoted to sodium-ion battery materials. This work was done in close collaboration with CIC EnergiGUNE, and my original contribution was mainly the structural analysis of manganese-based P2-phase layered cathodes $Na_{2/3}Mn_{0.8}Fe_{0.2}O_2$, $Na_{2/3}Mn_{0.8}Fe_{0.1}Ti_{0.1}O_2$, and $Na_{2/3}Mn_{0.8}Ti_{0.2}O_2$

used in Na-ion cells. The analysis was focussed on understanding the role of non-electrochemical active species used as dopants (Fe and Ti) which can provide a huge improvement in the cell performances. The X-ray Absorption Spectroscopy was used to identify subtle structural modifications induced by the presence of such dopants which result in a deformation of the initial structure in the form of Jahn-Teller elongation.

The final chapter is devoted to the conclusion and outcomes of this thesis work.

Chapter 2

Electrochemical Storage Systems

2.1 Basic Concepts of Batteries

A battery is an electrochemical power source which converts chemical energy into electrical energy. At least two reaction partners undergo a chemical oxidation-reduction (redox) process during this operation. The energy of this reaction is available as electric current at a defined voltage and time [16]. The redox reaction involves the transfer of electrons from one material to another through an electric circuit and the restoring of charge neutrality through electrolyte migration [17]. The basic element of a battery is called *cell*. These can be connected in series, in parallel or both depending on the desired output voltage and capacity. The main constituents of a cell are:

- *The anode or negative electrode*: this is the reducing electrode which gives up electrons to the external circuit and is oxidized during the electrochemical reaction. It must have high efficiency as reducing agent, and high coulombic output (Ah/g), and be chemically stable.

- *The cathode or positive electrode*: this is the oxidizing electrode, it accepts electrons from the external circuit and is reduced during the electrochemical reaction. It must be an efficient oxidizing agent, stable when in contact with the electrolyte, and have a useful working voltage.

- *The electrolyte*: this is the ionic conductor, which provides the medium for transfer of charge, as ions, inside the cell between the anode and the cathode. Usually, the electrolyte is in a liquid form, made of solvents with dissolved salts, acids, or alkalies to impart ionic conductivity. There exist also solid electrolytes [16], that

are ionic conductors at the operating temperature of the cell. The electrolyte must have good ionic conductivity but not be electronically conductive, as this would cause internal short-circuiting; it must also be inert to the electrodes materials.

Physically the anode and cathode electrodes are electronically isolated in the cell to prevent internal short-circuiting but are surrounded by the electrolyte. In battery cells, a separator material is employed to divide the anode and cathode electrodes mechanically. The separator, however, is permeable to the electrolyte in order to maintain the desired ionic conductivity. In some cases, the electrolyte is immobilized for a non-spill design. Electrically conducting grid structures or materials may also be added to the electrodes to reduce internal resistance [17]. The electrochemical features of a battery are described by the following parameters:

- *Capacity (Q):* The theoretical capacity of a cell is determined by the quantity of active materials in the cell. It is expressed as the total quantity of electricity involved in the electrochemical reaction and is defined in terms of coulombs (C) or ampere-hours (Ah).

$$Q = I \cdot t = x \cdot n \cdot F \tag{2.1}$$

  where I is the current drawn from the battery, t is the amount of time (in hours) that a battery can sustain; x is the number of moles of active material, n is the number of electrons involved in the reaction and F is the Faraday constant. Usually the capacity is normalized to the electrode weight (Ahg^{-1}) or volume.

- *Energy (E)*: The capacity of a cell can also considered on an energy (watt hour) basis by taking both the voltage and the quantity of electricity into consideration,

$$E = Q \cdot V \tag{2.2}$$

  This is the theoretical maximum energy that can be delivered by the electrochemical system.

- *Power (P)*: is simply the energy per unit time, or the voltage times the current.

$$P = I \cdot V = Q \cdot V/t \tag{2.3}$$

Electrochemical cells are identified as *primary* (non-rechargeable) or *secondary* (rechargeable). A schematics of volumetric vs. gravimetric energy density is shown in Fig.(2.1) for various secondary battery technologies [18].

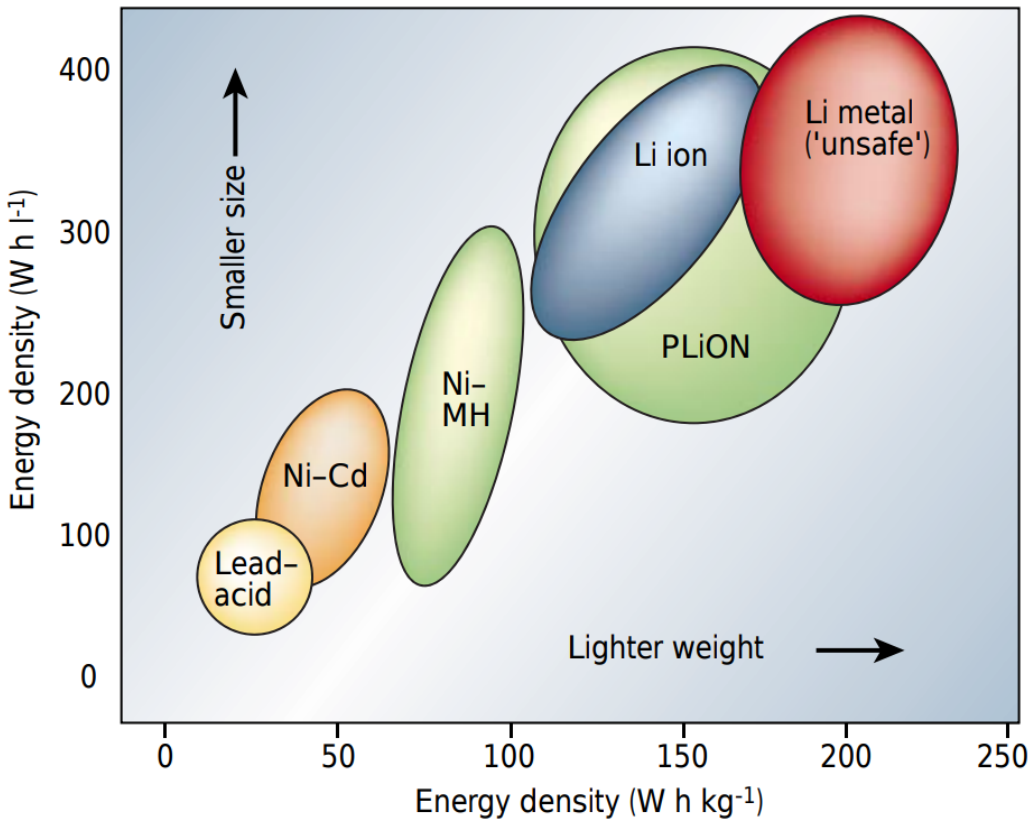

Figure 2.1: Volumetric and gravimetric energy density of different secondary battery technologies [18].

Primary batteries

These batteries are not capable of being easily and effectively recharged; hence, once discharged they are disposed. The reaction in these cells is irreversible. Primary batteries are usually inexpensive, have a good shelf life, high energy density and require no maintenance.

Secondary batteries

These batteries can be recharged several times. Only reversible electrochemical reactions offer such a possibility. After the cell is discharged, an externally applied electrical energy forces a reversal of the electrochemical process; as a consequence the reactants are restored to their original form, and the stored electrochemical energy can be used

Table 2.1: Voltage, capacity and specific energy of major primary battery systems [17].

Battery type	Anode, cathode	V	Ah/kg	Wh/kg
Alkaline	Zn, MnO_2	1.5	224	358
Mercury	Zn, HgO	1.34	190	255
Silver oxide	Zn, Ag_2O	1.6	180	288
Zinc / O_2	Zn, O_2	1.65	658	1085
Li−SO_2	Li, SO_2	3.1	379	1175
Li−MnO_2	Li, MnO_2	3.5	286	1001

once again by a consumer. The process can be reversed hundreds or even thousands of times, so that the lifetime of the cell can be extended. This is a fundamental advantage, especially as the cost of a secondary cell is normally much higher than that of a primary cell. Furthermore, the resulting environmental friendliness should be taken into account [16].

Table 2.2: Voltage, capacity, specific energy and cycle life of major secondary battery systems [17].

Battery type	Anode, cathode	V	Ah/kg	Wh/kg	Cycle life
Lead-acid	Pb, PbO_2	2.1	120	252	> 1000
Nikel-cadmium	Cd, Ni oxide	1.35	181	244	> 200
Nikel-metal hydrite	MH, Ni oxide	1.35	178	240	> 300
Lithium-ion	Li_xC_6, $Li_{i\text{-}x}CoO_2$	4.1	100	410	> 1200

2.2 Lithium-ion Batteries

Lithium is the lightest of all metals, has the greatest electrochemical potential (−3.04 V *vs* standard hydrogen electrode) and provides the highest specific energy per weight. For these reasons, starting from the 1970s, the first primary Li cells (based on metal lithium anodes) began to be developed and commercialized. First attempts to develop rechargeable lithium batteries followed when several inorganic compounds (later defined intercalation compounds) demonstrated to reversibly react with alkali metals [18, 19]. In 1972, Exxon [20, 21] started to prototype the first rechargeable Li using layered TiS_2 as positive electrode, Li metal as negative electrode and lithium perchlorate in dioxalane as electrolyte. Nevertheless, the commercialization of such prototype was not successful due to the shortcoming of Li-metal and liquid electrolyte combination causing the growth of Li dendrites [22] as metal was plated during the

discharge-recharge cycles. This phenomenon could lead to short-circuit between the electrodes and subsequently posing thermal runaway and explosion hazards.

In order to solve safety issues, it has been proposed to substitute Li-metal with a second insertion material in which Li-ions are stored in the layers of a suitable host [23]; the presence of Li in its ionic rather than its metallic state solved the problem of dendrites formation. The new cell concept was first demonstrated by Murphy *et al.* [24] and later by Scrosati *et al.* [25] between the end of the 1980s and the beginning of 1990s, and led to the so-called Li-ion or *rocking-chair* battery technology.

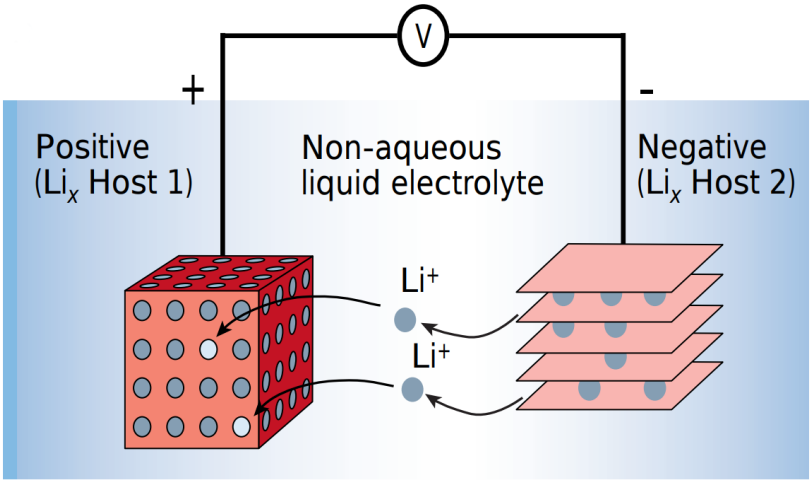

Figure 2.2: Schematic representation of rechargeable Li-ion battery [18].

Almost two decades to develop the concept of Li-ion cell and to obtain a reliable and safe commercializable prototype were due to the difficulties in finding suitable materials for negative electrode (insertion compounds or Li alloys) and in finding electrolytes which met, besides safety concerns, the cost and performance requirements for a successful battery technology. A schematic representation of a rechargeable Li-ion cell is shown in Figure 2.2.

In 1981, Goodenough first proposed layered $LiCoO_2$ as high energy and high voltage cathode material [26]. However, this did not attract much attention due to the lack of a safe anode material which limited the application of layered oxide cathodes of $LiMO_2$ (M = Ni, Co). In the same period Besenhard [27], Yazami [28] and Basu [29] discovered that graphite could be a good candidate to reversibly store Li ions by intercalation/deintercalation. Only at the end of the decade, in 1987, Yoshino *et al.* [30] filed a patent and build a prototype cell using carbonaceous anode and $LiCoO_2$ cathode; both materials are stable in air which simplifies the engineering and manufacturing

processes [31]. The large-scale manufacturing of similar Li-ion batteries (LIBs) started in 1991 by Sony Corporation [32]. Batteries with similar design are still present nowadays, almost after 30 years, becoming the standard for high-performance and portable electronic devices [18].

The major advantages and disadvantages of LIBs compared to other battery technologies are listed in Table 2.3. The high specific energy ($\sim$ 150 Wh/kg) and energy density ($\sim$ 400 Wh/L) of commercial LIBs make them perfectly suitable for applications where volume and weight must be minimized [17]. LIBs offer a low self-discharge ($2-8\%$ per month) long cyclability (more than 1000 cycles) and a broad temperature range of operation (charge $-20°/60°$C, discharge $-40°/65°$C) extending the usage in a variety of applications [17]. Single cells operate in the range of 2.5 to 4.2 V, almost three times that of NiCd or NiMH cells, allowing fewer cells for a given voltage. Also, the high rate capability has been demonstrated (discharge at 5C continuous or 25C pulse). These combined qualities, with the relative cost-effectiveness, are the key of LIBs success.

Main disadvantages of Li-ion batteries consist in over-charge and over-discharge effects which may degrade the cells, this can be avoided by the use of an electronic management circuitry that protects the system from extreme charge and temperature conditions; also LIBs permanently lose capacity at elevated temperatures ($< 65°$C).

Table 2.3: Advantages and disadvantages of LIBs [17].

Advantages	Disadvantages
High specific energy and energy density	Moderate initial cost
Long cycle and shelf life	Degradation at high temperatures
Low self-discharge	Capacity loss or thermal runway if overcharged
High rate and power capabilities	Ageing effect
High coulombic and energy efficiency	Need for protective circuitry
No memory effect	Venting and thermal runway when crushed

A commercial Li-ion battery is composed by graphite as anode and $LiCoO_2$ as cathode. The ionic conduction is achieved by the electrolyte, usually consisting of a lithium salt (for example $LiPF_6$ dissolved in a mixture of organic solvents (ethylene carbonate/dimethyl carbonate: EC/DMC). The two electrodes are physically separated by a micro-porous separator which allows the ionic flow and prevents internal short circuits. Other materials such as binders and fillers can be added to the cell in order to improve the conductivity, the stability or the cell chemistry.

The electrodes are usually wet-coated onto the current collectors: a foil of metal which has to be electrochemically stable in the potential operation window of the electrodes [33]. Usually, a copper foil is adopted as anode current collector, since it does not react with lithium ions at low potentials, aluminium foil can be used as cathode current collector because it is chemically stable at cathodic potentials, while it would form lithium alloys at the lower anodic potentials.

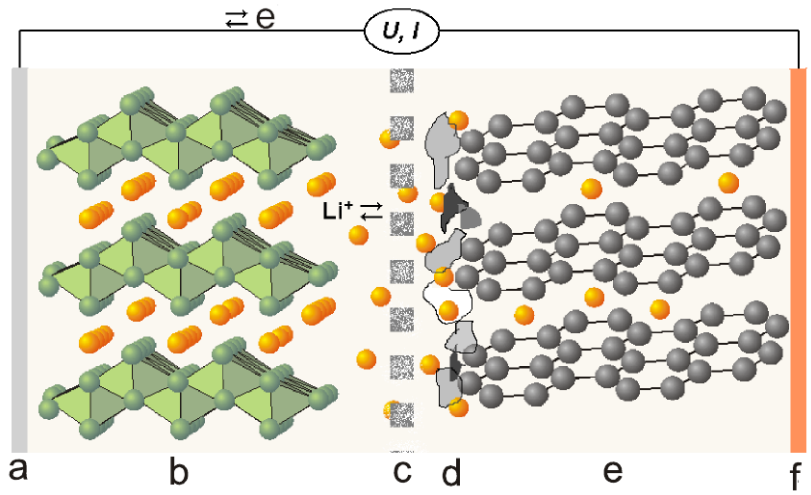

Figure 2.3: Schematic illustration of a typical Li-ion battery: a) aluminium current collector; b) oxide positive electrode material; c) porous separator soaked with liquid electrolyte; d) inhomogeneous SEI layer; e) graphite electrode material; f) copper current collector. Image by Verma *et al.* [34].

The working mechanism of a lithium-ion cell is schematized in Figure 2.3: during the discharge process, lithium atoms intercalated into graphite layers undergo an oxidation reaction. The positively charged lithium ions are dissolved in the electrolyte and flow into the the lattice of $LiCoO_2$ cathode. At the same time also electrons flow towards the positive electrode though an external circuit to power various systems. At the positive electrode, Li-ions recombine with the electrons and fill up the available sites into the cathode host matrix via a reduction reaction process. If the current is forced to flow in the opposite direction, by applying an external electromotive force, the redox reaction is reversed, and the battery is in a charging state. Following are listed the main reactions occurring on the positive electrode and negative electrode [17]:

Positive: $\mathrm{LiMO_2} \underset{discharge}{\overset{charge}{\rightleftharpoons}} \mathrm{Li_{1\text{-}x}MO_2} + \mathrm{xLi^+} + \mathrm{xe^-}$

Negative: $6\,C + xLi^+ + xe^- \underset{discharge}{\overset{charge}{\rightleftharpoons}} Li_xC_6$

Overall: $LiMO_2 + C \underset{discharge}{\overset{charge}{\rightleftharpoons}} Li_xC + Li_{1-x}MO_2$

2.2.1 Anode Materials

The negative electrode in LIBs must accept Li^+ ions during charge, and release them into the ionic flow during the discharge. The three basic requirements for anode materials are: low electrochemical potential versus Li/Li^+, high amount of lithium accommodable, long structural stability after several cycles of charge/discharge. It is possible to classify the various materials in three main categories, depending on the different lithiation mechanism (Fig. 2.4).

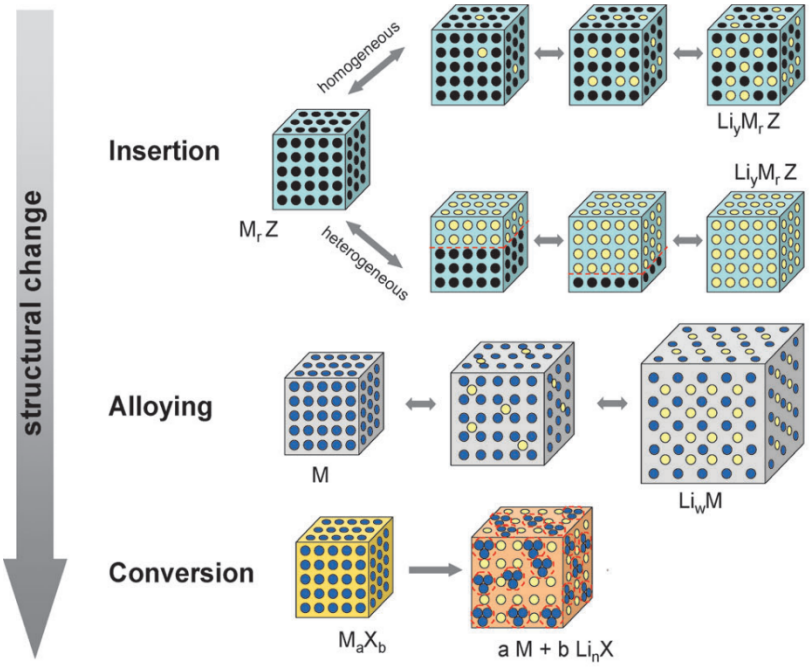

Figure 2.4: Different reaction mechanisms in anode materials for LIBs [35].

Insertion Anodes

- Carbonaceous materials

Carbon-based materials, with various morphologies, are largely used for commercial LIBs due their features: large availability; thermal. chemical and electrochemical stability, low cost and good reversibility for lithium intercalation and de-intercalation [36, 37]. The main distinction within carbonaceous materials can be made between *graphitic carbons* and *non-graphitic carbons* [38]. A schematic of the structures and discharge profiles is shown in Figure 2.5.

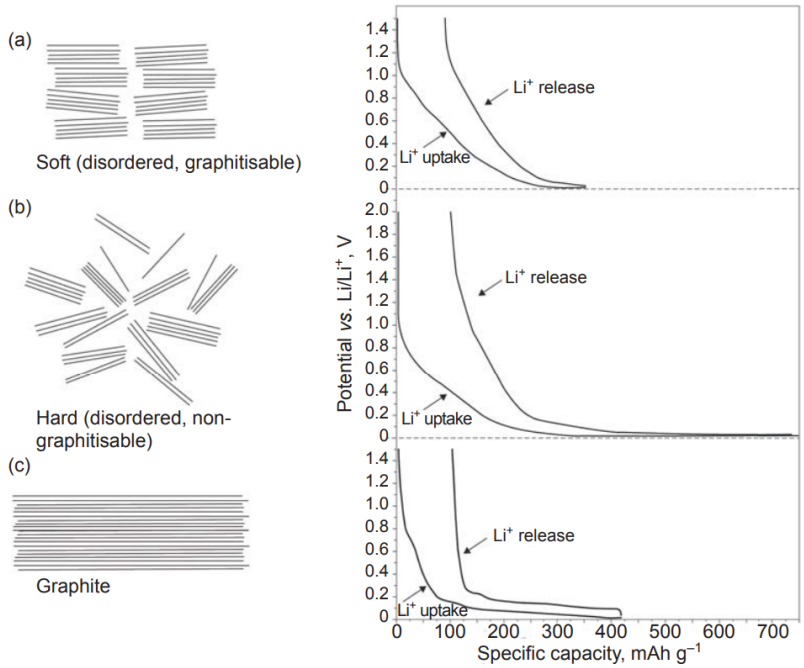

Figure 2.5: Scheme of: (a) soft carbons, (b) hard carbons, (c) graphitic carbons; and their typical potential profiles [39].

Graphite and graphitic carbons are composed by graphene layers (extended sheets of sp^2-hybridized carbon atoms arranged in hexagonal rings) stacked in AB or ABC layers held together by Van der Waals force [39]. During charge and discharge, lithium ions intercalate in between the layers by a so-called staging mechanism, ending with an AA stacking configuration once the material is fully litiathed [39–42]. The sp^2-hybridization, p-orbitals forming a delocalised electron network, also bring a big advantage in terms of electric conductivity of the material [38]. Intercalation of Li-ions into graphite layers consists in the insertion of one lithium-ion every six carbon atoms, thus graphite has a theoretical capacity of 372 $mAhg^{-1}$. This process occurs through the formation of different stages depending on the increasing ratio Li/C and corresponding to three well-defined potential plateaus in the potential window $0.05 - 0.25$ V shown in Figure 2.5 (c). The co-intercalation of solvents present in the electrolyte can, within several

cycles, cause the exfoliation of the layers in graphite and drive to battery failure [43]

Non-graphitic carbons consist of carbon atoms, arranged in the usual hexagonal network, but without a crystallographic order along the vertical axis, and they can be divided in *soft* and *hard* carbons, depending on their behaviour during heat treatment. Insertion of lithium into non-graphitic carbons cause negligible expansion of interlayer spacing, thus the volumetric deformation of the electrode is minimal. Both soft and hard carbons show a sloping potential-capacity curve with no significant plateaus. These carbons show a higher specific capacity with respect to graphite because the different structure and morphology allow alternative ways for lithium to be adsorbed by the material. For example, it can be stored on both sides of each layer of non-stacking graphene layers [40], in the micro-pores [38] and in other micro-structures of the material. Nevertheless, a certain fraction of lithium that has reacted with carbon during lithiation, cannot be recuperated in the charging process. Some of the Li atoms may, in fact, remain trapped in the micro-structures and internal porosity of non-graphitic carbons [43]. Part of the irreversible capacity is due to the formation of a surface film around the carbon particles (*cfr.* Section 2.4).

Alloying Anodes

Several elements are able to reversibly form alloys with lithium at a low potential, room temperature and in non-aqueous electrolytes. Sn, Pb, Al, Sb, Zn, Si are between the most studied due to their abundance, low cost and eco-friendliness, and, most important, for their appealing theoretical capacity. They can be used in the electrodes in their metallic state or as oxides. The generic reaction for element A can be written as:

$$\mathrm{xLi} + \mathrm{A} \underset{de-lithiation}{\overset{lithiation}{\rightleftharpoons}} \mathrm{xe^-} + \mathrm{xLi^+A}$$

The most important issue for these materials is the large volume expansion/contraction upon (de-)lithiation (even more than 200% volume increase), which will cause, after several cycles, the rupture of the active material and, consequently, a loss of electronic contact and finally the pulverization of the electrode [39, 44], causing an irreversible loss of capacity. To overcome this capacity loss, several strategies have been attempted: one is to use a host matrix which acts as a buffer to contain this large volume change in order to maintain the electrode integrity and electronic contact. This can be achieved in various ways, for example, using hollow carbon nano-spheres, core-shell nano-structure and micro-sized carbonaceous matrices (*cfr.* the review by Loeffer *et al.* [39]). Despite

the promising approaches and the appealing performances of alloying anodes, only tin-based materials have been successfully adopted for commercial LIBs, also silicon-based anodes (carbon-coated silicon nano-structure) have recently appeared into commercial LIBs [45].

Conversion Anodes

Conversion materials M_aO_b (M = Co, Fe, Ni, Mn, Cu, *etc.*) undergo a solid-state redox reaction during (de-)lithiation, in which there is a change in the crystalline structure, accompanied by a breaking and recombination of chemical bonds [46]. Initially, these kinds of displacement reactions were considered to be irreversible at room temperature due to the high energy needed for bond breakage, atomic reorganization and the formation of new bonds. But since 2000, when Poizot *et al.* [47] reported the first reversible lithium storage reaction in transition metal oxides, a growing interest on these material has started. In particular towards transition metals (TM) sulphides, nitrides, phosphides, fluorides and other phases, since they show high theoretical capacities (from two to six times higher than carbonaceous materials, depending on the molar mass, oxidation state of the TM and the density of the oxide) thanks to the ability to transfer multiple electron reactions per M. The conversion mechanism can be described as follows [36]:

$$TM_xA_y + ze^- + zLi^+ \underset{de-lithiation}{\overset{lithiation}{\rightleftharpoons}} xTM^0 + Li_zA_y$$

During lithiation the transition metal is reduced to its metallic state and embedded in a matrix of a (simultaneously formed) lithium compound Li_zA_y (where A can be O, N, P, F and others) [39]. A characteristic of this reaction is the *in-situ* formation of metallic nano-grains of the TM during the first lithiation process, ensuring the reversibility of the reaction and lithium reduction from Li_zA_y. These nano-particles, ensure a high electrochemical activity (due to a large amount of interfacial area) when a reverse polarization is applied [39, 47]. Nevertheless, we are still far from a practical application of these materials in commercial LIBs for the higher capacity fade and low cyclability when compared to the more common carbons. The capacity-potential curves show a large hysteresis which increases with the electro-negativity of the anion and with the increase of ionic conductivity of the lithiated matrix.

Conversion-Alloying Anodes

A good compromise between alloying and conversion reaction mechanisms can be achieved by a new developing class of active materials, of which a sketch of the involved reactions is shown in Figure 2.6. In order to further increase the lithium uptake per formula unit, it is possible to use mixed metal oxides, where an electrochemically inactive metal is replaced by an element which can reversibly form an alloy with lithium: those first undergo a conversion reaction, where they are fully reduced into their metallic phases, subsequentially one or more of those metals can further alloy with lithium resulting in an interesting extension of the capacity in the material [39, 48, 49]. In these materials, called conversion-alloying materials (CAMs), the Li_2O matrix formed during the initial stage of lithiation, coupled by the electron conductive transition metal network, add a buffering effect to the alloying reaction, resulting in an optimal combination of the two lithiation mechanisms [50]. Besides the increase in capacity, the alloying metals commonly react with lithium at lower potentials [50–53].

Major drawbacks of these materials are the significant volume changes and the structural rearrangement, the final properties and characteristics of lithiation reactions highly depend on the particle and electrode architecture.

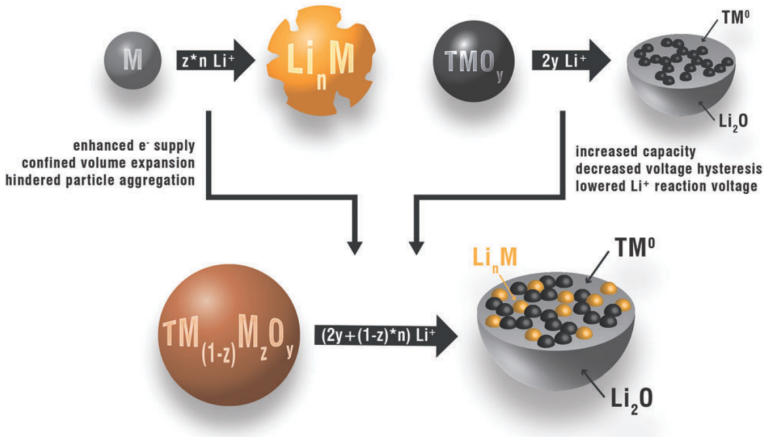

Figure 2.6: Combination of alloying and conversion mechanisms, schematics [50].

Zinc in conversion-alloying materials One of the most investigated CAMs are spinel-structured transition metal oxides, where one of the transition metal cations is replaced by divalent zinc, $ZnTM_2O_4$ (with TM = Fe, Co or Mn), since Zn can alloy with lithium reversibly and increasing the total number of hosted lithium by one.

$$ZnTM_2O_4 + 8\,Li^+ + 8\,e^- \longrightarrow 2\,TM^0 + 4\,Li_2O + Zn^0 \tag{2.4}$$

$$Zn^0 + Li^+ + e^- \longrightarrow LiZn \tag{2.5}$$

Three classic Zn-containing compounds with conversion alloying characteristics are $ZnFe_2O_4$ (ZFO), $ZnCo_2O_4$ (ZCO) and $ZnMn_2O_4$ (ZMO), all three with the theoretical capacity of intercalating up to 9 Li-ions per formula unit.

The general reversible (de-)lithiation reaction for spinel-structured $ZnTM_2O_4$ is:

$$2\,TM^0 + 4\,Li_2O + LiZn \longleftrightarrow ZnO + TM_xO_y + 9\,Li + 9\,e^- \tag{2.6}$$

A detailed analysis of one of these conversion-alloying materials (carbon-coated zinc ferrite) will be provided in Chapter 4.

2.2.2 Cathode Materials

The cathode is the positive electrode, where the electrochemical reduction takes place during cell discharge. In commercially available cells is utilized a lithiated metal oxide as active material (for example $LiCoO_2$ and $LiMn_2O_4$). Requirements for selecting and developing positive electrode materials are: the capability to incorporate high quantity of lithium (ensuring the high capacity of the cell); Li^+ exchange must be reversible with limited structural change (in order to ensure long cyclability and high energy efficiency); lithium exchange reaction must occur at high potential relative to Li, in order to achieve high cell voltage and high energy density; the material must have high electronic conductivity and high ionic mobility to increase the rate of redox reactions; also the material must be compatible with the other materials present in the cell, in particular, it must not be soluble in the electrolyte [17]. Finally, to minimize the production cost and the hazard for the environment, the material should be low-cost and non-toxic.

Cathode materials that fit these requirements are typically oxides of transition metals. At present time, the most common class of cathodes is represented by Li-insertion compounds, which can be further divided into three sub-classes (*cfr.* Figure 2.7) depending on ion diffusion pathways within the active material: two-dimensional layered oxides, three-dimensional spinel oxides, and uni-dimensional olivine compounds. Along these directions, the host structure is strongly bonded, and thus the intercalation reaction does not affect the host structure [43].

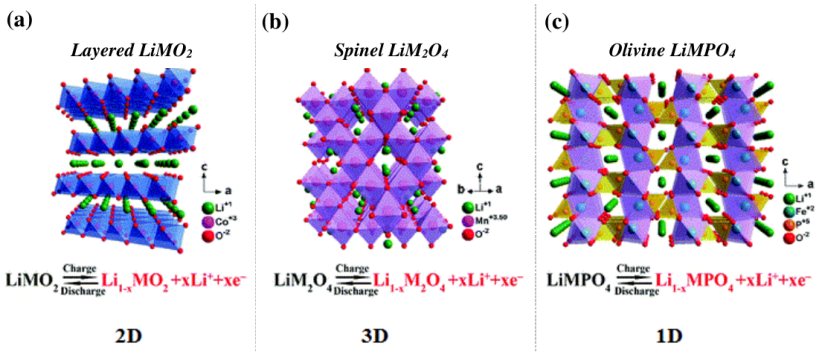

Figure 2.7: Crystal structure, electrochemical reactions, and ionic pathways of Li-ion transport mechanism of the principal cathode materials [54, 55].

Layered Oxides

Layered oxides have the generic formula $LiMO_2$ whit M = Co, Mn, Ni or a combination of those, and have been employed as commercial cathodes for LIBs. They belong to the space group R3m where lithium and transition metals are located in the octahedral sites of alternating layers in an ABCABC stacking sequence (O3-type) and separated by layers of cubic close-packed oxygen atoms Fig.2.7(a) [56, 57]. The most used layered materials in making LIBs cathodes are $LiCoO_2$ and $LiNiO_2$.

$LiCoO_2$ was first commercialized by *Sony Corporation* in 1990 for the first commercialised model of LIB used it's still commonly used for consumer devices nowadays [17]. The theoretical capacity of $LiCoO_2$ is 274 mAh g^{-1}, corresponding to the de-intercalation of 1 mol of Li per mol of $LiCoO_2$. Practically the empirical capacity of the material is reduced to $50\% - 55\%$ of the theoretical capacity ($130 - 150$mAh g^{-1}) due to the irreversible structural modification of the material after the extraction of 0.5 mol of lithium from a hexagonal phase to a monoclinic. The low practical capacity, in conjunction with the high cost and high toxicity of cobalt, pushed the need to replace $LiCoO_2$ with alternative cathode materials [56, 58].

$LiNiO_2$ is isostructural to $LiCoO_2$, first reported by Dahn as cathode material [59], and is considered to be an alternative to cobalt-based layered electrodes; it is relatively cheaper and has higher energy density (15% by volume and 20% by weight). This material, however, presents difficulties during the synthesis in obtaining a stable and ideal R3m layered structure because nickel tends to the 2+ oxidation state and to migrate into Li^+ sites [58].

To overcome these issues of $LiCoO_2$ and $LiNiO_2$, and to enhance the electrochemical performances and the structural stability of the materials, a layered cathode composed

by a combination of different metal oxides (Co, Ni and Mn oxides) has been proposed. These ternary oxides (reported by Ohzuku in 2001 [60]) are described by the general formula $LiNi_yMn_{1-x-y}Co_xO_2$, they are low-cost and present a low structural instability while the energy density is not much improved compared to $LiCoO_2$ [61, 62]. Another family of mixed layered oxides compounds are Li-rich cathode materials, with the general formula $xLi_2MnO_3(1-x)LiMO_2$ ($0 < x < 1$, M = Ni, Mn, Co, etc.). They show high capacity (over 300 mAh g^{-1}) in the optimal potential range $2 - 4.8$V, a low relative cost and no environmental issues; however, they suffer of a large initial irreversible capacity and a poor rate capability [62].

Spinel Oxides

Spinel oxide cathodes have been introduced in 1980 [63] as manganese spinel, as a cheaper and less-toxic alternative to cobalt layered materials. This manganese spinel ($LiMn_2O_4$) have a cubic close-packed structure (space group Fd3m), where manganese occupies the 16c sites and lithium the 8a sites, oxygen atoms are located at the 32e sites. Mn ions occupy 1/4 of the available octahedral sites, leaving the rest of the sites vacant and ready for a possible lithium insertion, the 8a and 16c sites form a 3D pathway for Li insertion and extraction [57, 58] Fig.2.7(b). This material can intercalate one Li per formula unit at room temperature [43]; the theoretical capacity, in this case, is 148mAh g^{-1}.

The main issue of these spinel cathodes is the capacity fade during charge and discharge cycles due to the dissolution of Mn^{3+} at the electrode surface according to the formula $2\,Mn^{+3} \longrightarrow Mn^{4+}_{solid} + Mn^{2+}_{solution}$ with the consequent dissolution of Mn^{2+} into the electrolyte. Another factor affecting the performances of manganese cathodes in LIBs is the Jahn-Teller induced distortion [64] and decomposition of the electrolyte at high-voltage regions [43, 64].

Olivine Phosphates

$LiFePO_4$ olivine was introduced by Radhi *et al.* [65] as cathode for rechargeable LIBs. Olivine structured transition metal phosphates $LiMPO_4$ (M = Co, Fe, Mn) have attracted the attention of research due to the low-cost, nontoxic and environmentally friendly nature of these materials [43]. $LiFePO_4$ operates at a very flat voltage of 3.4V versus Li^+/Li, carrying a theoretical capacity of 170mAh g^{-1}. The triphylite $LiFePO_4$ belongs to the olivine structured lithium ortho-phosphates in the space group *Pnma*; here the oxide ions form a hexagonal close packing arrangement; the iron ions form

zigzag chains of octahedra in alternate basal planes linked by the tetrahedral phosphate groups (PO_4) [43]. Each FeO_4 octahedron share corners with 6 PO_4 tetrahedra, and each of these tetrahedron shares, in turn, its corners with four FeO_4, forming a 3-D framework. The lithium atoms occupy octahedral sites in the remaining basal planes Fig.2.7(c).

Besides $LiFePO_4$, other olivine cathodes have been studied. In particular $LiMnPO_4$ whit a working potential of 4.1V and also mixed compounds as $Li(Mn_Fe)PO_4$, $Li(MnFeCo)PO_4$, and $Li_3V_2(PO_4)_3$. The latter one has a working potential of $3 - 4.8$V versus Li^+/Li and an high theoretical capacity of 197mAh g^{-1}, the highest among phosphates [66, 67].

The main weaknesses of olivine-based cathodes are the low average potential and low electronic and ionic conductivity. The strategy to overcome these problems is focused on carbon coating and the reduction of particles to nano-metric size [46].

2.2.3 Electrolytes for LIBs

Electrolytes are widely used and indispensable in all electrochemical devices since they serve as the medium for the transfer of charges, in the form of ions, between a pair of electrodes. For this reason, they are key determinants of battery performance. The rate capability, stability, coulombic efficiency, temperature range and safety of any lithium-ion battery are affected by the composition of the electrolyte.

A suitable electrolyte should the following properties [68, 69]:

- High ionic conductivity ($\sigma_{Li} > 10^{-4}$ S/cm) for minimizing the internal resistance and at the same time a very low electronic conductivity ($\sigma_{e^-} > 10^{-10}$ S/cm).
- Large and stable electrochemical window to ensure a wide operational voltage and avoid electrolyte degradation.
- Chemical compatibility with both the anode and cathode materials and all the other cell components.
- Low melting and high boiling point to enhance battery safety.
- Low cost, reliable safety characteristics, and environmental benignity.

Four types of electrolytes are used in Li-ion batteries: liquid electrolytes, gel electrolytes, polymer electrolytes and ceramic electrolytes. The most common are liquid electrolytes, solutions of a lithium salt in organic solvents, typically carbonates. The two main components of liquid electrolytes are the salt and the solvent. The

salt supplies the charge carriers needed to cycle Li-ions between anode and cathode. It must dissolve in the solvent and it should have high ion mobility to increase the conductivity [70]. Most commonly used salts and solvents are listed in Tables 2.4 and 2.5 respectively.

Table 2.4: Salts Used in Electrolytes for Li-ion Cells [17].

Common name	Formula	g/mol	Comments
Lithium hexafluorophosphate	$LiPF_6$	151.9	Most commonly used
Lithium etrafluoroborate	$LiBF_4$	93.74	Less hygroscopic than $LiPF_6$
Lithium perchlorate	$LiClO_4$	106.39	Less stable than $LiPF_6$
Lithium hexafluoroarsenate	$LiAsF_6$	195.85	Contains arsenic
Lithium triflate	$LiSO_3CF_3$	156.01	Al corrosion at low voltage
Lithium bisperfluoroethane-sulfonimide(BETI)	$LiN(SO_2C_2F_5)_2$	387	Stable to water

The solvent needs to dissolve the salt in high amounts (i.e. have a high dielectric constant) and be fluid over a wide range of temperatures to allow for rapid ion transfer. At the same time, it should remain inert towards the electrodes and all other cell components. Other requirements include safety, economy and toxicity [71]. A wide variety of solvents, including carbonates, ethers and acetates, has been evaluated for non-aqueous electrolytes. The industry has now focused on the carbonates as they offer excellent stability, good safety properties and compatibility with electrode materials. Neat carbonate solvents typically have intrinsic solution conductivity less than $10^{-7}\ S/cm$, dielectric constant > 3, and solvate lithium salts to high concentration [17].

From the first commercial Li-ion batteries, special attention was paid to ethylene carbonate (EC) [70], which has a dielectric constant (~ 89). The unique position of EC as a lithium-ion battery electrolyte was established in 1990 when Dahn and co-workers reported the fundamental difference between EC and PC (propylene carbonate) in their effects on the reversibility of lithium-ion intercalation/deintercalation with graphitic anodes [41]. Despite the little difference in molecular structure between the two, EC was found to form an effective protective film (SEI) on a graphitic anode that prevented

Table 2.5: Characteristics of main organic solvents [17].

Solvent	EC ethylene-carbonate	PC propylene-carbonate	DMC dimethyl-carbonate	DEC diethyl-carbonate	DME dimethyl-ether	EMC ethyl methyl-carbonate
BP ($°C$)	248	242	90	126	84	109
MP ($°C$)	39	−48	4	−43	−58	−55
Density (g/ml)	1.41	1.21	1.07	0.97	0.87	1.0
Viscosity (cP)	1.86	2.5	0.59	0.75	0.455	0.65
Dielectric constant	89.6	64.4	3.12	2.82	7.2	2.9
Mol. wt.	88.1	102.1	90.1	118.1	90.1	104.1

any sustained electrolyte decomposition on the anode, while this protection could not be realized with PC. Although ethylene carbonate as a single solvent is not suitable, because it is a solid at room temperature, it is used in mixtures containing linear alkyl carbonates such as dimethyl, diethyl, and ethyl-methyl carbonates (DMC, DEC, and EMC, respectively) [72]. Typical ready-to-use electrolytes contain 1 M $LiPF_6$ salt dissolved in mixtures of EC, DEC, DMC or EMC. Chemical structures of most commonly used electrolyte solvents are shown in Figure 2.8.

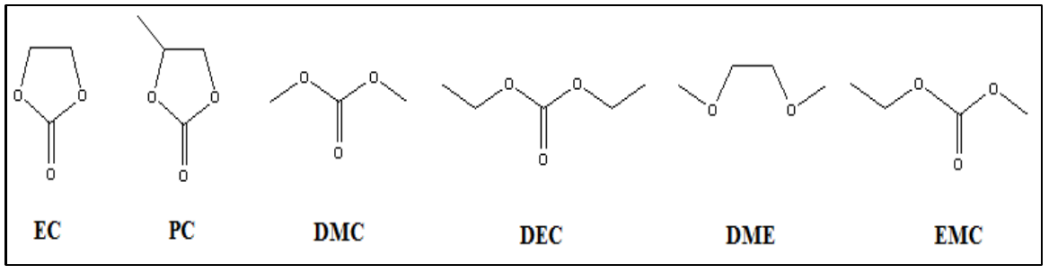

Figure 2.8: Structures of main organic solvents used in Lithium-ion batteries [70].

2.3 Sodium-ion Batteries

Sodium is the fourth most abundant element on earth with a uniform distribution [73,74] with a virtually unlimited source in salt deposit and seawater. The abundance of

the resources and the much lower cost of sodium-containing precursors with respect to lithium precursors ($135-165$ \$ per ton versus 5000 \$ per ton [73]), and similar chemical proprieties provide a compelling alternative to Li-ion batteries in the development of Na-ion batteries (NIBs) technology, which in the recent years yield the research and industrial attention as large-scale energy storage system [17, 73, 75]. Fig. 2.9 shows the limited and uneven distribution of lithium supplies around the world, it is estimated that 89% of total Li income is controlled by four companies: Albemarle Corporation (USA), American FMC Lithium (USA), Sociedad Química y Minera de Chile (SQM, Chile), and Talison Lithium (Australia), which is owned by Albemarle Corporation (49%) and Tianqi Lithium Industries (51%) from China [76].

The battery components and the electrical storage mechanisms of NIBs and LIBs are basically identical except for their ion-carriers. For cathode material, the intercalation process of sodium is very similar to the one of lithium, making it possible to use similar compounds for both systems [73]. However there are obvious differences between the two systems: Na^+ ions are larger than Li^+ ions (1.02Å, versus 0.76Å), this affects the phase stability, transport and also the interphase formation [73, 77]. Sodium is also heavier than lithium (23g/mol versus 6.9g/mol) and has a higher standard electrode potential ($\sim$ 2.71V vs. SHE-standard hydrogen electrode, compared to $\sim$ 3.02V vs. SHE for lithium), thus NIBs will not prevail in terms of energy density. However, the weight of the ionic carriers is only a small fraction of the total mass of the battery components, furthermore, the capacity is primarily affected by the structural characteristics of the host structures that are employed as electrodes. Hence, in principle, there should not be large consequences in terms of energy density in the transition from LINs to NIBs [73]. Moreover, aluminium current collector can be employed in NIBs (while this is not possible in LIBs since aluminium undergoes an alloy reaction with lithium at potentials below 0.1V vs. Li/Li^+) making it a cost-effective alternative to copper current collectors.

Also historically, the development of NIBs started parallel to that of LIBs. The first reversible electrochemical intercalation of sodium in TiS_2 at room temperature was reported in 1980 [78], with a cathode that was later proposed as cathode material for the first rechargeable Li-ion battery. In the same year were reported the electrochemical proprieties of Na-containing layered oxides, Na_xCoO_2 by Braconnier [79]. However, the limitations in resources, research condition and apparatuses including electrolyte solution, binders, separators, and glove box proved to be insufficient for handling sodium metal at that time (sodium is more reactive in air than lithium), which resulted

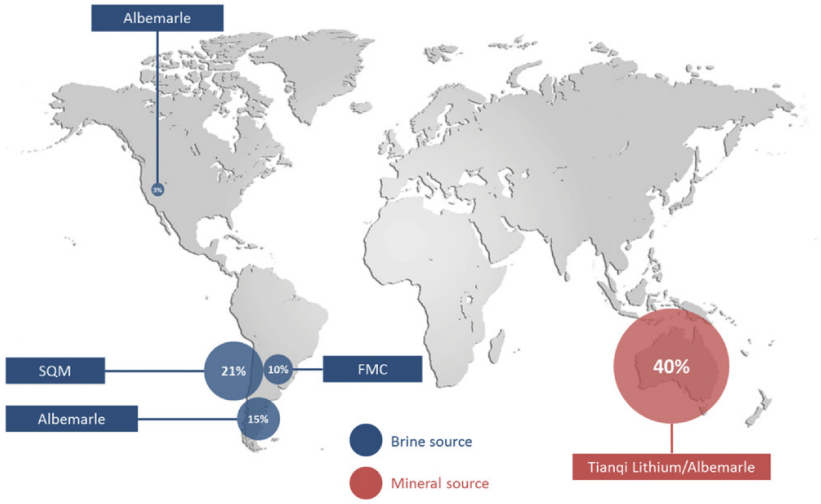

Figure 2.9: Global distribution of lithium supplies [76].

in difficulty in fairly observing potential of the electrode performance as batteries, led to a faster interest increasing into LIBs technology while NIBs research remained limited. Industrially, only a few Japanese and US companies developed, in the '80s, a commercial version of NIBs in full cell configurations where sodium-lead alloy composite and P2-type Na_xCoO_2 were used respectively as a negative and a positive electrode [80, 81]. Only in recent years, the interest towards sodium-ion technology has been renewed to find a more cost-effective replacement for LIBs with a minimum sacrifice on performance and risk avoidance from export restrictions for lithium resources [73, 82].

The main characteristics of Na compared to Li are summarized in Table 2.6

Table 2.6: Li and Na properties [55].

	Li	Na
Cationic radius (Å)	0.76	1.02
Atomic weight (g mol^{-1})	6.9	23
Potential vs SHE (V)	~ 3.04	~ 2.7
Melting point (°C)	180.5	97.7
Price, carbonates ($/ton)	5000	150
Capacity metal (mAh g^{-1})	3829	1165

A description of the most relevant classes of active materials and electrolytes under investigation for NIBs is given in the next sections, comparing them with LIBs relative counterparts, while a simplified schematics of a Na-ion cell with all the commonly used materials is presented in Figure 2.10.

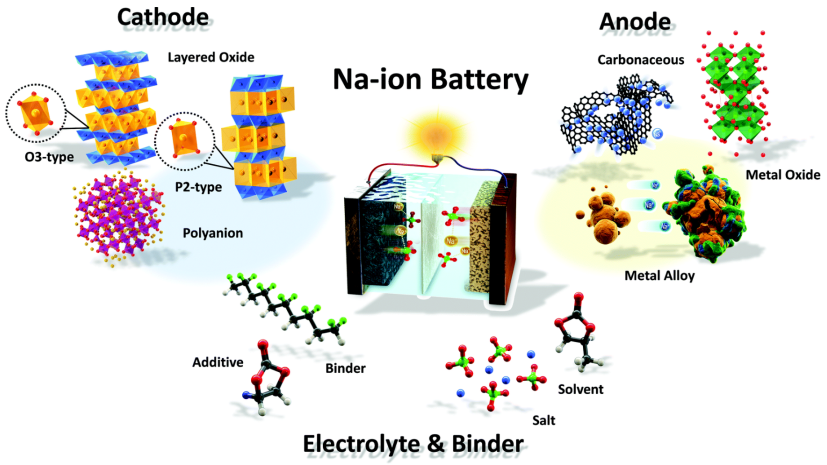

Figure 2.10: Schematics of a Na-ion battery and the principal classes of materials in the components [73].

2.3.1 Anode Materials

The main challenge in NIBs technology is mainly represented in finding a suitable replacement for the anode material for Na-ions storage. Similarly to LIBs, metallic Na cannot be used because of the dendritic growth upon cycling which leads to short circuits and safety hazards, also the low melting temperature of metallic sodium increases the safety risks and makes it not suitable in commercial uses [76, 83]. Similarly to LIBs, negative electrode materials for NIBs can be classified based on their reaction mechanism during the sodiation/de-sodiation process and divided in insertion, alloying and conversion anodes. An overview of these materials is shown in Figure 2.11 [55, 73].

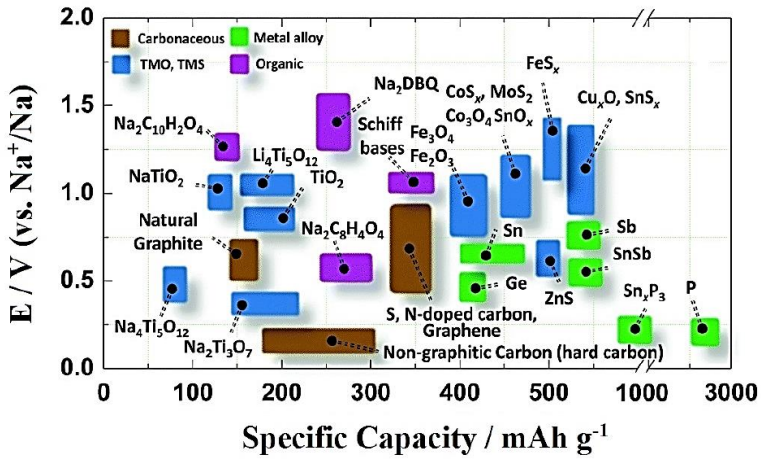

Figure 2.11: Overview of the materials used as anodes for NIBs [55, 73].

Insertion Anodes

- Carbonaceous materials

As seen in a previous section (2.2.1), carbon-based materials (graphite in particular) are the most common choice in LIBs manufacturing since Li rapidly forms intercalated compounds with it in which lithium ions are located at the graphene inter-layer until C:Li ratio reaches 6 : 1 (LiC_6). However, in NIBs, Na^+ insertion into graphite is significantly impeded since it is electrochemically less performing and furthermore causes the degradation of electrolyte and/or electrode materials, especially with common carbonate esters electrolyte solvents [84, 85]. Moreover the formation of NaC_6 and NaC_8 is unfavourable because of the thermodynamic instability of binary Na-Graphitic Intercalation Compounds (GICs) [73]. Early first-principles calculations indicated that it is hard for Na to form the intercalated graphite compounds compared to other alkali metals [86, 87]. Na-ion insertion into graphite can be facilitated by the use of solvated Na-ion co-intercalation reaction, by the use of diglyme (diethylene glycol dimethyl ether) electrolyte solvent [88].

On the other hand, disordered carbons showed better performances in intercalating Na^+, with a higher reversible specific capacity. First report of sodium-ions intercalating in soft carbons prepared by pyrolysis of petroleum cokes was in 1993 by Doeff *et al.* [84]; while in 2000, Steven and Dahn obtained a specific capacity of 300 mAh g^{-1} for sodium-ion intercalation in hard carbons prepared by carbonization of glucose [89].

- Titanium-based oxides

Similarly to LIBs, titanium-based active materials have been studied and extensively investigated as negative electrodes for NIBs, because of the relatively low redox potentials of $Ti^{3+/4+}$. Several Ti-based sodium compounds demonstrated to reversibly intercalate Na ions. For example layered $NaTiO_2$ and $Na_2Ti_3O_7$ [86]. Also intercalation into spinel-like structures is possible, reversible intercalation of Na^+ into spinel $Li_4Ti_5O_{12}$ has been reported [90], with a delivered reversible capacity of 145 mAh g^{-1} and a potential of 1 V. Ionic insertion mechanisms between LIBs and NIBs differ in spinel material. While Li^+ insertion occurs via a 2-phases mechanism, Na^+ insertion happens in a three-phases process; this mainly because of the larger ionic radius of sodium [73].

Another class of interest for NIBs anodes using an insertion mechanism is represented by sodium titanates, in particular $Na_2Ti_3O_7$ because it can reversibly uptake 2 Na^+

ions per formula unit through a two-phase reaction, giving a final theoretical capacity of 177 mAh g^{-1}, with a low operating potential plateau of 0.3 V vs Na/Na^+ [91].

Alloying Anodes

Similarly to lithium, also sodium can form binary compounds with pure metals and semi-metals of elements in group 14 and 15 in the periodic table ($M+nNa^+ + ne^- = Na_nM$). Those alloys are very attractive for the construction of NIBs due to their high theoretical capacities. For example, there are reports of alloying reactions of Pb to form $Na_{3.75}Pb$ [92]. The most encouraging candidates as alloying metals with sodium are Sn and Sb. Sn shows an high theoretical capacity of 847 mAh g^{-1} while Sb delivers a theoretical specific capacity of 660 mAh g^{-1}, based on full sodiation state of Na_3Sb.

The main withdraw of alloying sodium comes from the large ionic radius that inevitably causes more detrimental volume expansions upon (de)sodiations, causing irreversible structural modifications and finally the pulverization of the electrode active material, with the related capacity loss (a comparison of volumetric expansion between carbons anodes for LIBs and NIBs is provided in Figure 2.12). For this reason, the current research in this field is mainly focused on controlling the effect of volume changes with similar strategies used for lithium counterparts [93].

Whereas silicon has been considered the most promising anode in Li-ion batteries thanks to its electrochemical performances, it is not as promising in Na-ion batteries because it can only uptake one sodium ion per formula unit and exhibits poor Na diffusion kinetics [94]. An improvement of silicon electrochemical performances has been obtained with amorphous Si due to a more favourable binding reaction with Na [73].

The electrochemical alloying of Sb-Na was also reported [95] in Sb_2O_4 thin films which alloys sodium after conversion, showing a total theoretical capacity of 1227 mAh g^{-1} since it can store 14 Na ions per formula unit of Sb_2O_4.

Conversion Anodes

Conversion anodes for NIBs have been intensively tested, the main representatives of this class of materials are: transition metal oxides, transition metal sulphide and transition metal phosphide.

Conversion reactions have been studied also in spinel-like materials as $NiCo_2O_4$ [97] where a reversible reaction was described between the metal oxide and sodium, where Co and Ni metallized in a matrix of Na_2O after full sodiation. Also other types of

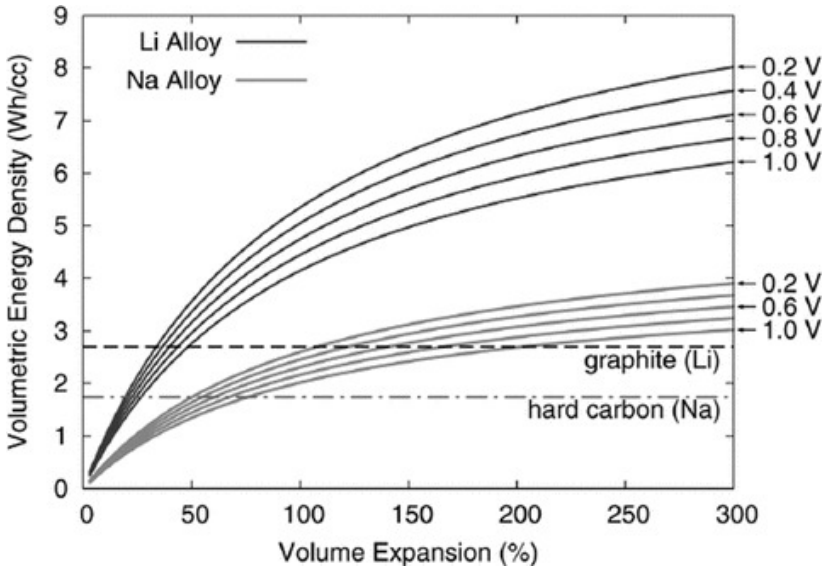

Figure 2.12: Universal expansion curves for Li and Na alloys [96]. Voltage of positive electrode was assumed to be 3.75 V to calculate the energy density.

transition metal oxides were proposed as electrodes in NIBs, such as iron oxides (Fe_3O_4 and Fe_2O_3), cobalt oxide Co_3O_4 and copper oxide CuO, molybdenum oxide (MoO_2), nickel oxide (NiO) and finally manganese oxide (Mn_3O_4).

These conversion materials gathered attention due to their high theoretical specific capacities but they suffer from poor cycling stability and large hysteresis. Therefore the main goal for improvement is focused on nanotechnology and carbon coating strategies [73].

2.3.2 Cathode Materials

Most of cathode materials used for NIBs are based on intercalation reactions, which involves sodium ion insertion into interstitial spaces of the material. Since intercalation chemistry of sodium is very similar to lithium, the same compounds used in LIBs have been tested also for NIBs. Therefore a large class of materials have been proposed as possible positive electrodes for NIBs, we can divide those into layered oxides, polyanionic compounds, Prussian blue and organic compounds. All those are characterized by minimal structural changes during intercalation, but due to the ionic dimension, these material are always subjected to continuous structural evolution during sodiation of the host structure [73]. Figure 2.13 gives an overview of the large class of NIBs positive electrode materials. Here we will focus only on layered oxides.

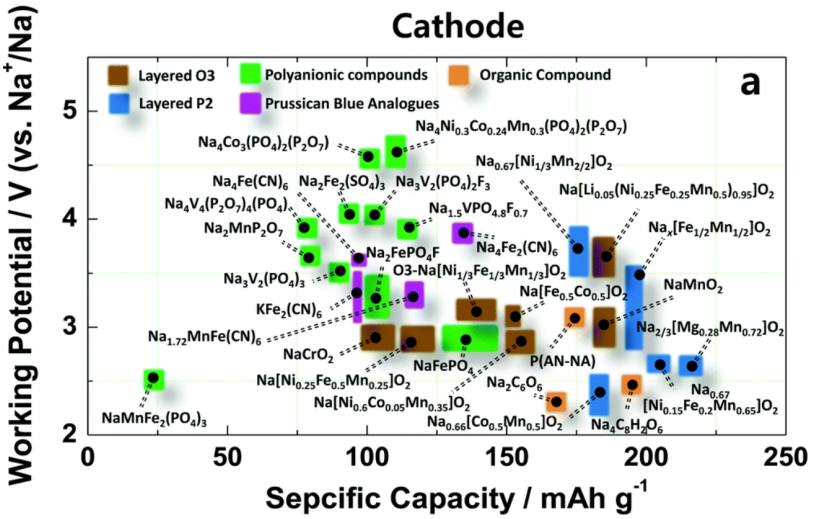

Figure 2.13: Overview of recent research on cathodes for Na-ion batteries [55, 73].

Layered Oxides

Layered oxides (NaT_MO_2, T_M=Ti,V,Cr,Mn,Fe,Co,Ni and any other mixture of 2 or 3 elements), among the other candidates for NIBs cathodes, offer many advantages due their simple structure, high specific capacity and simplicity in synthesis [98]. The first investigation regarding two-dimensional layered oxides was by Delmas, Hagenmuller and co-workers in 1982 [99], where they classified them into two main groups: O3 types and P2 types, depending on the stacking sequence of oxygen in the structure. Later on, feasible electrochemical insertion of sodium ions was demonstrated by other groups during the '80s although the initial approaches resulted in poor specific capacity and poor cycling performances due to poor conditions of electrolytes, equipment and so on. Over the years several improvements have been applied to layered oxides: incorporation of specific electrochemically active elements could activate targeted redox reactions at selected voltages in order to achieve smoother charge-discharge profiles; incorporating small fractions of electrochemical inactive elements into the oxide layers proved to be effective on the structural stabilization of the layers, resulting in better capacity retention and ciclability although the quantity of active material is reduced by substitution [98].

Layered oxides of general formula $Na_xT_MO_2$ are composed by repeating layers of T_MO_6 with Na ions sandwiched in between the layers of the oxide. Typical phases of Na layered oxides are O2, O3, P2 and P3 depending on the surrounding Na environment and the number of unique oxide layer packings. The letters indicate the environment where sodium is located: O is for octahedral, P is for prismatic; while the number

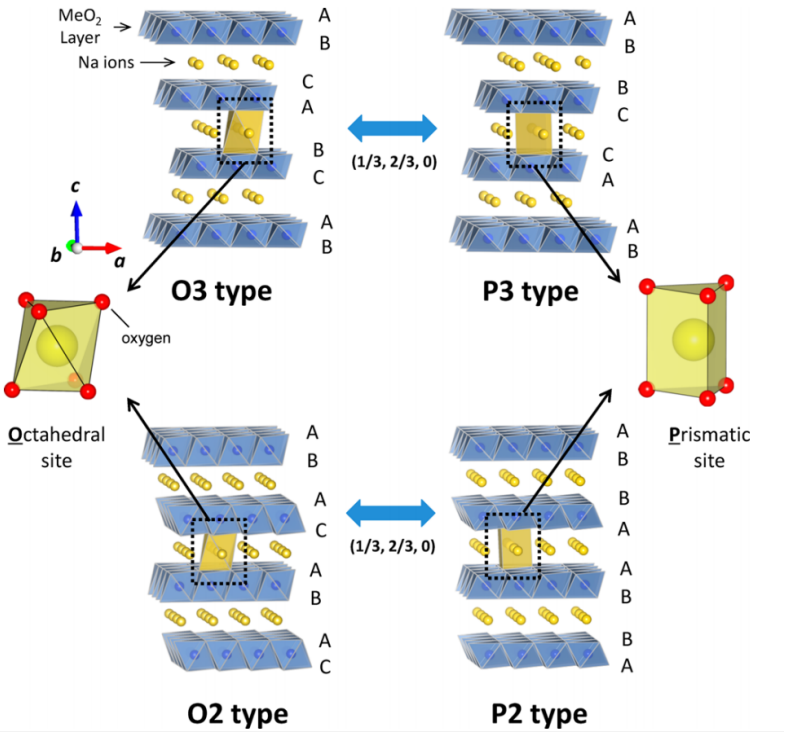

Figure 2.14: Classification of sodium - metal oxides layered materials, and phase transition induced by Na extraction [100, 101].

indicates the number of unique inter-layers within each unit cell. The symbol *prime* (') can be added to indicate a distorted phase. Sodium extraction from the material, as showed in Figure 2.14, leads to phase transition O3 $\longrightarrow$ P3 and P2 $\longrightarrow$ O2; while structural variation from O3/P3 to P2/O2 is not possible without breaking the T_M−O bond [93, 100, 102]. The O3-phase occurs when $0.7 \leq x \leq 1$ with a stacking sequence ABCABC and all Na share one edge and one face. In the P2-phase, occurring when $x \approx 0.7$, there is an oxide layer stacking sequence with ABBA pattern, all Na share either an entire edge or an entire face. The P3-phase, is known to occur when $x \approx 0.5$, the stacking sequence follows the pattern ABBCCA and all Na share one face with T_MO_6 octahedron and three edges with three T_MO_6 octahedra [98].

Electrochemical performances are heavily influenced by the type of phase, not only because of the quantity of Na in the initial state but also due to the different stability in the layers and due to the different kinetics in the surroundings of Na. At present day, better performances are achieved by the P2-phase cathodes, with better cycle life and higher energy density [103] because of the low diffusion barrier and high ionic conductivity.

Sodium cobaltate $NaCoO_2$ was the first compost to be examined for electrochemical

sodium intercalation [79]. It was shown that the various Na_xCoO_2 polymorphs could reversibly intercalate Na^+ within the P2-phase structure with a very limited capacity of 95 mAh g^{-1} [104]. Shacklette also examined a series of Na_xCoO_2 compounds and found that the P2 polymorph has the best capacity retention, probably due to the lack of gross structural changes during cycling [103, 105].

Layered sodium iron oxides ($NaFeO_2$) and sodium manganese oxides ($NaMnO_2$) are very attractive because of the cost-effectiveness of the materials and also for the non-toxicity. The implementation of $NaFeO_2$ in NIBs has been limited due to its limited electrochemical properties. While $\alpha-NaFeO_2$ is the structural prototype for layered materials in the R-3m space group, its performance in a Na cell is affected by the unstable Fe(IV) oxidation state [105]. Also, sodium manganese bronzes were studied as NIBs cathodes. The P2-$Na_{0.7}MnO_{2.25}$ structure showed to have a reversible capacity of 96 mAh g^{-1} after charging up to a potential of 3.5 V [106], later studies showed an increase in the reversible capacity when charging at higher potential (3.8 V) at expenses of cyclability.

One of these layered oxide cathode materials will be taken into consideration in Chapter 6.

2.3.3 Electrolytes for NIBs

Similarly to LIBs, the choice of the electrolyte will affect the whole cell electrochemical performances, cycle life, capacity and capacity retention, safety and other parameters of the battery [107]. A good electrolyte for NIBs should have the following properties:

- Lack of reactivity and form a stable passivation layer (*cfr.* Section 2.4).
- Electrochemical stability is a wide voltage range.
- Thermal stability at operational temperatures.
- High ionic conductivity for sodium ions.
- Absence of internal electronic conductivity.
- Low cost, reliable safety characteristics, and low toxicity (these aspects are more important for NIBs than LIBs).

As for electrode materials, also in the choice of electrolytes, the knowledge that was acquired for LIBs has been implemented in NIBs. In fact, most commonly used electrolytes for NIBs are the analogue of the ones used for LIBs: inorganic salts dissolved in organic solvents. The main difference is in the chemistry of the ions (Li^+ or Na^+): for example in the radius, Lewis acidity and cation-anion interactions that make the direct passage from LIBs to NIBs not so straight forward [108].

The choice of salt has a direct impact on the chemical and electrochemical stability. Indeed the anion limits the upper voltage (since it is the first to oxidize), while the lower voltage limit is limited by the solvent reduction. Furthermore, on the solvent depend also the thermal stability and ion mobility, which is inversely proportional to the electrolyte viscosity [107].

In general, sodium-salts present a higher melting point and thermal stability than the lithium counterparts, this presents an advantage in therm of cell safety. The most commonly used salts for NIBs are $NaClO_4$, $NaPF_6$, NaTFSI and NaFSI [108, 109].

Commonly used solvents are usually composed on a mixture of different compounds as seen for LIBs, such as EC:PC, EC:DMC, EC:DEC *etc.* [107] *cfr.* section 2.2.3.

2.4 Solid Electrolyte Interface (SEI)

The anode/electrolyte interphase, also referred to as the Solid-Electrolyte Interphase (SEI) [110], is a passivation layer-film of different chemical species formed on the negative electrode of Li-ion or Na-ion batteries, resulting from chemical reactions of the anode with the electrolyte solution [70]. The SEI layer acts as Li^+ or Na^+ conductor, but also as an insulator to electron flow and it limits itself the further electrolyte decomposition; on the other hand, consuming Li-ions or Na-ions in the formation of the SEI leads to an irreversible capacity loss [16, 110]. Thus, the SEI passivation layer plays a key role in battery performance, irreversible charge loss, rate capability, cyclability, exfoliation of graphite and safety, which are highly dependent on the quality of the SEI layer [111].

2.4.1 Formation and Features of SEI

Generally, the passivating layer of the SEI is almost completely formed during the first charge of the battery [16, 114]. Electrolyte salts, such as $LiPF_6$, $LiAsF_6$,

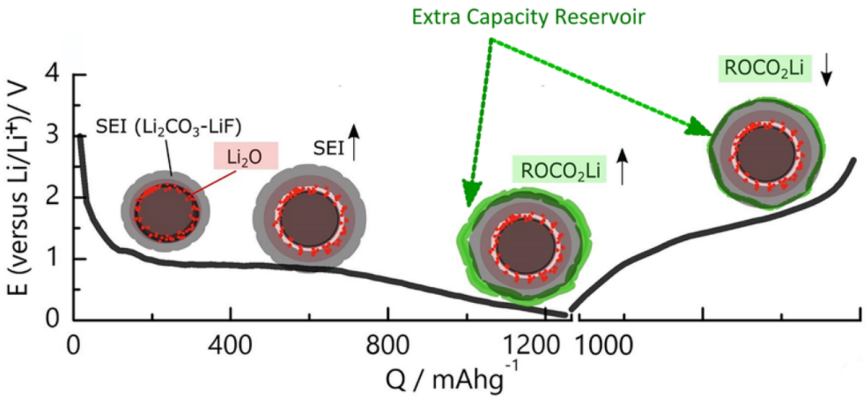

Figure 2.15: Sketch of the SEI evolution in zinc-ferrite anodes [112].

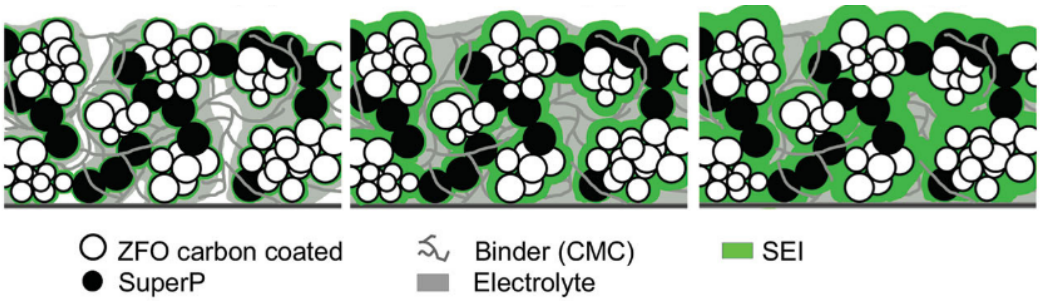

Figure 2.16: Sketch of the SEI formation and evolution in zinc-ferrite anodes and its composition [113].

LiBOB, $LiClO_4$ or $LiBF_4$ in a mixture of carbonate solvents (for example dimethyl carbonate, diethyl carbonate, ethylene carbonate, *etc...*) are widely used as electrolyte solutions [16, 115, 116]. This solution is thermodynamically unstable at low and very high potentials vs. Li/Li^+. Hence, during the first charge of the cell, the electrolyte solution begins to reduce/degrade; then, these products precipitate on the anode surface via nucleation and growth mechanisms [117] and form the SEI. The onset potential of SEI formation is not a fixed value since it varies depending on several factors like nature and composition of electrolyte, type of used electrode, nature of additives in the electrolyte, *etc...* [118]. The thickness of the SEI is largely variable depending on the initial conditions of its formation, it may vary from few Å up to hundreds of Å [119,120]. An example of SEI thickness evolution is shown in Figure 2.17. Besides the composition of electrode and electrolyte, also other factors contribute to the formation of SEI: temperature and current rate strongly influence the thickness and composition of the layer [121]. Schematics of SEI formation and evolution in zinc-ferrite LIBs anodes (studied by our group) are provided in Figures 2.15 and 2.16.

The reduction mechanism, at the electrode-electrolyte interface, builds up a protective film that will eventually cover the whole surface of the electrode. Moreover, in graphite-based electrodes, the SEI (called internal-SEI film) can penetrate the surface and form in the cracks and on the surface of the natural graphite spheres [122]. Ethylene carbonate (EC), due to its high dielectric constant, is preferentially coordinated to lithium ions and reduced. A wide range of EC reduction products have been listed by Aurbach *et al.* [123] after experimental studies of SEI layers, concluding that lithium alkyl carbonates dominate the SEI. Apart from EC reduction products, also a range of other SEI components have been proposed in a review by Verma *et al.* [111], including organic and inorganic products formed both by electrolyte salts and electrolyte solvents. A schematics of the chemical coponents present in the SEI is shown in Figure 2.18.

When considering NIBs, limited reported studies about SEI are available at present-day compared with the larger mole of SEI studied in LIBs. For commonly used electrolytes in NIBs, the electrochemical stability window is comprised in the range $1 - 4.5$ V, although this window is largely influenced by all the variables in the used electrochemical system as in LIBs [76, 126].

Comparative studies on noble metal negative electrodes, in conjunction with $LiClO_4$ and $NaClO_4$ in propylene carbonate (PC) based electrolytes, showed incomplete formation of the passivation layer onto the metal electrode, and partial dissolution of the surface film in the Na system, suggesting that the sodium-based organic compounds

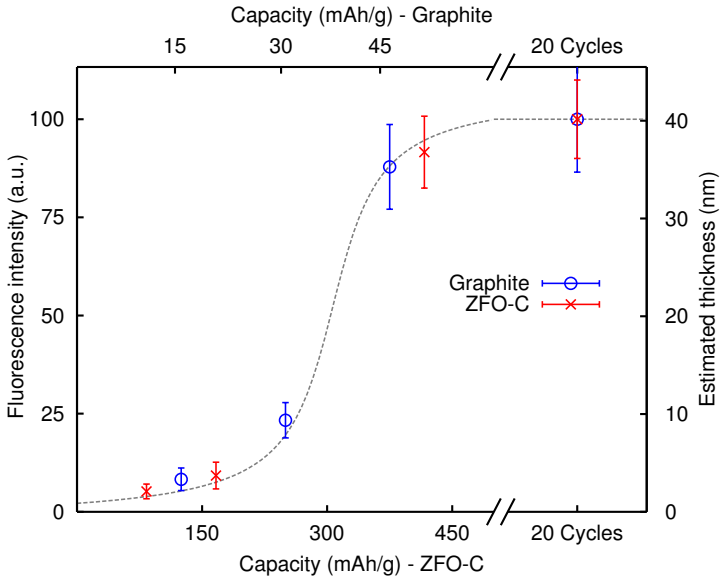

Figure 2.17: Schematics of the SEI thickness evolution for graphite and zinc-ferrite anodes, studied with As Kα X-ray Fluorescence [124].

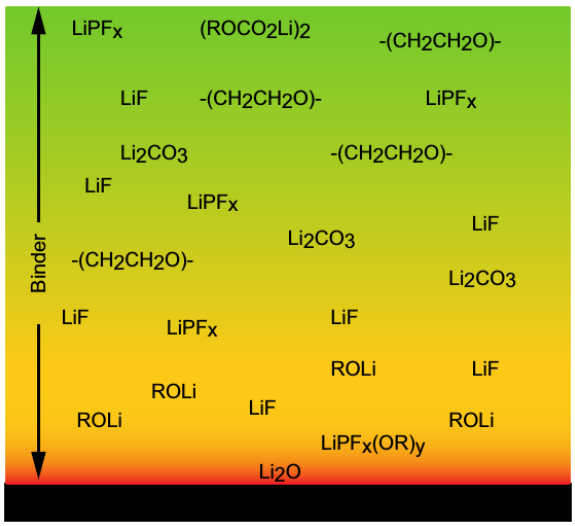

Figure 2.18: Schematic picture of SEI on a lithiated graphite anode with a list of chemical compounds at different depth found with XPS by Malmgrem *et al.* [125].

formed by electrolyte degradation are more soluble than the correspondents used in Li systems. This probably due to the lower Lewis acidity of Na^+ when compared to Li^+ ions, leading to different solubility of the electrolyte decomposition products [127].

SEI formation in NIBs was also studied using hard carbons as negative electrodes and as electrolyte 1 mol/dm^3 $NaClO_4$ and $LiClO_4$ in PC. The resulting SEI film in NIBs cells was formed for the big part by inorganic compounds, confirming the higher solubility of the decomposed products in sodium-ion cells [128] and showing the different thickness and morphology between lithium and sodium systems [101].

The different type of ionic carrier, even when using the same electrode materials and electrolyte, lead to different characteristics of the SEI layers. In particular, it is proven that the formation of a stable interface in sodium-ion based cells is more difficult than in LIBs.

The formation and evolution of the SEI in graphite electrodes, using an As-based electrolyte mixture, will be studied in Chapter 5.

2.5 The Solid Permeable Interphase (SPI)

Unlike the anode-electrolyte interface SEI, which forms mainly during the first cycle, significantly increasing amount of material is deposited at the cathode-electrolyte interface during the cycling life of the battery. The solid permeable interphase (SPI) [129] concept was introduced to distinguish the interface at the cathode from the significantly different SEI at the anode. The term "permeable" was chosen to highlight that the SPI, unlike the SEI, doesn't act as passivating layer [130]. Since the cathode operates at higher potentials than the cathode, there is no need of a passivating layer to avoid electrolyte reduction. However, other types of reactions at the surface may occur. For example electrolyte oxidation [131], dissolution of cations [132], transformation of metal oxides [133] and also deposition of electrolyte material formed elsewhere in the battery [70]. A schematic picture of SPI components is shown in Figure 2.19.

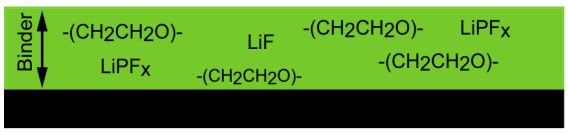

Figure 2.19: Schematic picture of SPI on a carbon coated delithiated lithium iron phosphate cathode with a list of chemical compounds at different depth found with XPS by Malmgrem *et al.* [125].

Only a limited number of studies have been dedicated to the interfacial electrode/electrolyte reactions onto the cathode. The SPI layer has been studied on $Li_{1-x}CoO_2$ [134], $LiMn_2O_4$, $LiNi_{0.8}Co_{0.2}O_2$ and $LiFePO_4$ [129], showing that similar organic and inorganic compounds are formed in all these kind of cathodes.

For Na-ion batteries, a study regarding the SPI layer was reported by Doubaji *et al.* [135] on layered P2-$Na_xCo_{2/3}Mn_{2/9}Ni_{1/9}O_2$ cathodes. Results showed an SPI layer much thinner than the usual SEI layer found on NIBs anodes, furthermore, it contains principally organic compounds (Na_2CO_3).

Chapter 3

Experimental Techniques

The physical and chemical characterization of the various materials has been performed using spectroscopic techniques, synchrotron-based or with laboratory equipment. In particular, the results reported in the following chapters are based on data collected with X-ray Absorption Spectroscopy, X-ray Photo-emission Spectroscopy and Raman Spectroscopy. All of these techniques, with different peculiarities, can provide information regarding the chemical composition and structure of the samples. They also provide crucial outcomes on the understanding of the deep processes occurring during ionic insertion in battery materials.

X-ray Absorption Spectroscopy and X-ray Photo-emission Spectroscopy involve the excitation of a core electron, thus both methodologies are element-specific, and are optimal for monitoring the evolution in the structure and electronic state of the various samples. Moreover, they are complementary one to each other since they can provide information regarding the surface or the bulk. Thus they are a well-suited technique for investigating the different features on battery electrodes as the structural evolution at the bulk, and the formation and modification of the superficial layers.

On the other hand, Raman Spectroscopy is a vibrational technique that can provide information on the structure at the atomic scale on both inorganic and organic compounds. When coupling the Raman spectrometer with an optical microscope, it is possible to use the technique as a microprobe and obtain a spatial resolution on the order of 1μm that can also allow detailed mapping of the electrodes and the study of particles of the active material with proper size. With this kind of set-up, if coupled with a specific electrochemical cell with an optical window, is also possible to perform in-situ studies directly on the electrode surface, when the cell is operating; thus providing a direct and detail monitoring on all the changes and an insight into

the mechanisms that govern the electrode performances.

The electrochemical characterization of the various electrodes is a fundamental step for validating their effectiveness as battery materials and for evaluating their electrochemical performances, such as the specific capacity, capacity retention, cyclability and operational voltage window. Moreover, constant electrochemical monitoring of cell performances is fundamental during its physical and chemical characterization. Especially when performing in-situ and in-operando characterization of the electrode, is crucial to have a direct corroboration on the electrochemical performances, in particular regarding the voltage, current, and capacity. Monitoring these parameters guarantees the proper functioning of the cell and provides a link between the physical parameters and the electrochemical ones.

The sections of this chapter are devoted to the description of the different experimental techniques employed and cited in the thesis.

3.1 X-ray Absorption Spectroscopy

X-ray absorption spectroscopy (XAS) is one of the most used techniques for the study of electronic and structural properties of condensed matter [136, 137]. In a typical XAS experiment the attenuation of a X-ray beam passing through a sample is studied as a function of photon energy E above the threshold of an absorption edge. In a transmission experiment the measured physical quantity is the *absorbance*, defined as:

$$\alpha = \mu(E)x = \ln \frac{I_0}{I_1} \tag{3.1}$$

where

- $\mu(E)$ is the absorption coefficient ($\mu(E) = \rho\sigma(E)$ whit ρ: photo-absorbers density and $\sigma(E)$: cross-section).
- x is the sample thickness.
- $I_0(E)$ is the intensity of radiation hitting the sample.
- $I_1(E)$ is the intensity of the radiation transmitted through the sample.

In the X-ray region ($0.1 - 100\ KeV$) the main contribution to the cross section comes from the photoelectric effect, which is dominant respect to the other scattering channels

as Compton effect and pair production (Fig. 3.1[1]). In correspondence of the binding

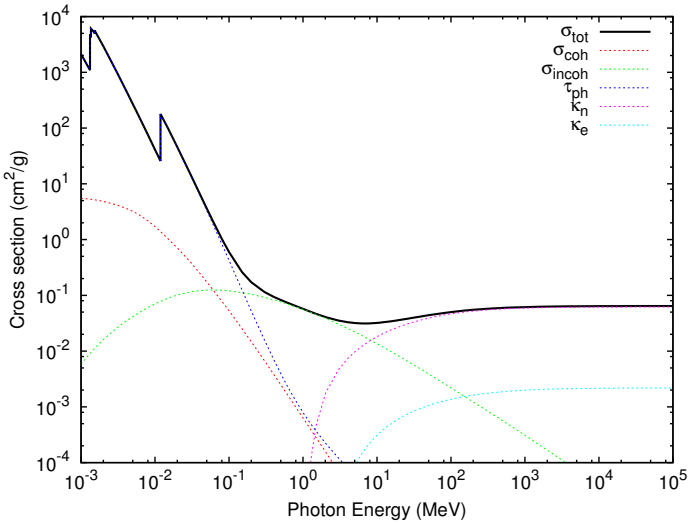

Figure 3.1: Total photon cross section σ_{tot} for arsenic, as a function of energy, showing the contributions of different processes: τ_{ph} , atomic photo-effect (electron ejection, photon absorption); σ_{coh} , coherent scattering (Rayleigh scattering-atom neither ionized nor excited); σ_{incoh} , incoherent scattering (Compton scattering off an electron); κ_n, pair production, nuclear field; κ_e , pair production, electron field.

energies of the core electrons ($1s$, $2s$, $2p$ ...) a sudden increase (*jump*) in the attenuation coefficient occurs; these are known as *edges* (K, L_1, L_2...). In an energy region beyond the edge of about 1000 eV, oscillations in the absorption coefficient are present, these are usually referred to as XAFS (*X-ray absorption fine structure*). These oscillations are caused by a quantic interference phenomenon: a photo-electron (the electron excited by the X-photon) can be consider as a spherical wave associated to a wave-length λ_e derived by the de Broglie formula:

$$\lambda_e = \frac{h}{\sqrt{2m_e(\hbar\omega - E_0)}} \tag{3.2}$$

where $\hbar\omega$ is incoming photon energy, E_0 is the edge energy. The waves, back-scattered from the nearby atomic sites, can interfere constructively or destructively with the outgoing wave from the photo-absorber, depending on λ_e, the photon energy and inter-atomic distances (a cartoon of the interference phenomenon leading to XAS is shown in Figure 3.2). The interference produces a modulation in the cross section and thus in the absorption spectrum. The photo-electron behaves like a probe strongly interacting with

[1]Data from `http://physics.nist.gov/PhysRefData/Xcom/html/xcom1.html`

the nearby atoms, having a mean free path of the order of $6 - 8$ Å, as a consequence we can obtain information only on the local structure near the photo-absorbing site, but very accurate. The term XAFS is broad and includes several different types

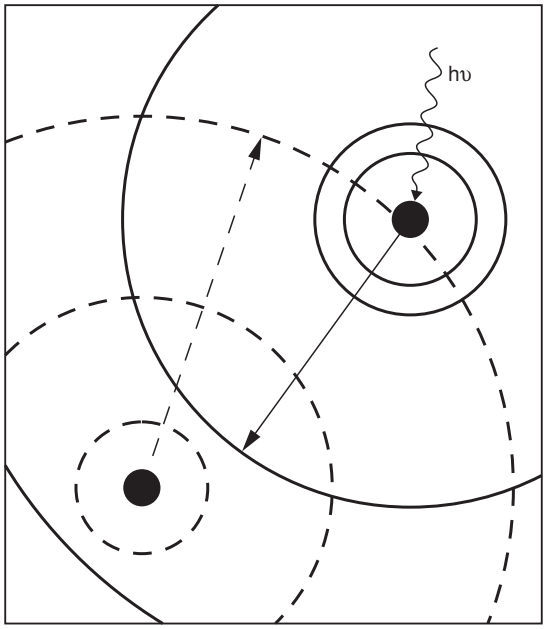

Figure 3.2: Schematic illustration of the interference leading to the EXAFS oscillations.

of analysis: EXAFS (*Extended X-ray Absorption Fine Structure*), XANES (*X-ray Absorption Near Edge Structure*), NEXAFS (*Near Edge XAFS*) and SEXAFS (*Surface EXAFS*), although those techniques are often referred in many papers as XAS (*X-ray Absorption Spectroscopy*) [137]. Let's now focus on the physics and analysis of the EXAFS range of the spectrum. The contribution to the absorption cross section from the interacting photo-electron with the nearby atoms is isolated from the atomic cross section $\sigma_0(k)$, defining the dimensionless EXAFS structural signal $\chi(k)$:

$$\chi(k) = \frac{\sigma(k) - \sigma_0(k)}{\sigma_0(k)} \tag{3.3}$$

where k is the magnitude of the wave vector of the emitted photo-electron, $k = \sqrt{2m(E - E_0)}/\hbar$. Even though the oscillations of the core level absorption cross-section are known since about 100 years, only in the '70s, with the spread and development of synchrotron facilities this technique has become widely used. First analysis methods where based on simple Fourier transform, only around 1970 Stern, Sayers, and Lytle [138–141] synthesized the essential aspects of a viable theory of XAFS, and further demonstrated that XAFS could be a practical tool for structure

determination; only in recent years, thanks also to computer developments, a more accurate analysis based on multiple scattering theory was possible for both near-edge and EXAFS spectra [142,143]. Further details on XAFS data analysis will be discussed in appendix A.

3.1.1 XANES and EXAFS in the Study of Atomic and Electronic Structure of Materials

The X-ray Absorption spectrum is usually divided into two energy regions: the X-ray Absorption Near-Edge Spectroscopy (XANES) typically within 30eV of the main absorption edge and the Extended X-ray Absorption Fine-structure Spectroscopy (EXAFS); (Fig. 3.3[2]). Even though the two have the same physical origin, this distinction is very useful and convenient in terms of analysis and interpretation of the experimental data.

XANES is strongly sensitive to the oxidation and coordination state (for example octahedral, tetrahedral coordination structures) of the absorbing atom, whereas EXAFS analysis can provide information regarding the distances, coordination number and chemical species of the neighbouring atoms of the photo-absorber [144].

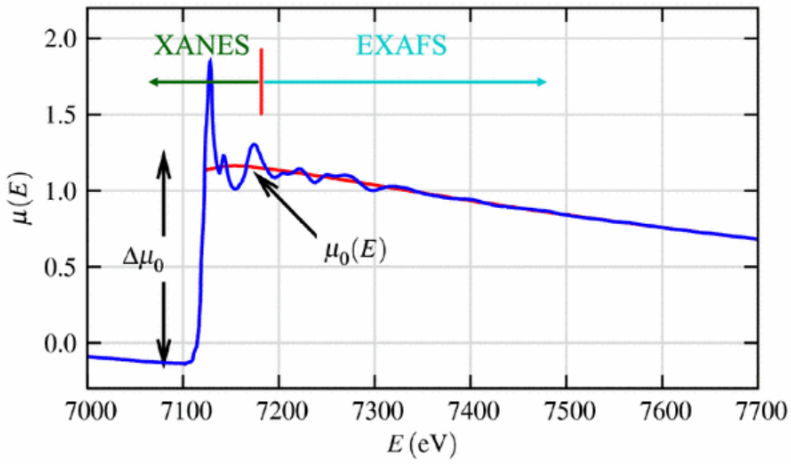

Figure 3.3: Example of XAS spectra of FeO, showing the XANES and EXAFS regions as well as the edge-step $\Delta\mu_0$(E0) and the smooth background function μ_0(E).

XANES The oscillations and signal of XANES are much larger than EXAFS, thus it is possible to acquire XANES more easily: in low concentration samples and with a

[2]Image from `http://www.ati.ac.at/index.php?id=247`

much-reduced acquisition time. However, the interpretation of XANES signal is not so straightforward since there is not a simple analytical description of the phenomenon. In fact, EXAFS equation (*cfr.* Eq. A.16) does not work at low-k for the presence of the term $1/k$ and for the increase in the mean-free-path at very low k values.

Still, a qualitative analysis of the XANES region can provide information in a more 'direct' way if compared to EXAFS. XANES shape and edge position are strictly connected to the formal valence state, type of ligand, and coordination environment; and give an insight on:

- Oxidation state
- Coordination Chemistry (regular, distorted, octahedral, tetrahedral, *etc.*)
- Molecular Orbitals (p-d orbitals hybridization)
- Band Structure (density of available electronic states)
- Multiple-Scattering

One of the common applications of XANES is for the determination of the valence state evaluating the position of the absorption edge. Comparing the obtained experimental value with the tabulated ones, it is possible to determine the average value of the absorber atoms valence state, as a fraction of different components. The heights and positions of pre-edge peaks can also be reliably used to empirically determine oxidation states and coordination chemistry [144].

For many systems, the XANES spectra can be also interpreted as a linear combination of known and tabulated spectra of reference compounds and used as a fingerprint for phases and oxidation state. Thus, trough a linear combination fitting procedure, it is possible to obtain the fraction of each compound present in the sample. More sophisticated linear algebra techniques such as Principle Component Analysis and Factor Analysis can also be applied to XANES spectra [144].

Information regarding the molecular orbitals can also be derived from XANES, for example for ions with partially filled d-electron bands, the p-d hybridization changes dramatically depending on the coordination environment, whit a very strong hybridization for tetrahedral configuration and a lower one for octahedral. This results in an evident pre-edge peak with a highly localized molecular orbital state and indicating a transition to a bound electronic state [144].

EXAFS After collecting and analysing the experimental signal (*cfr.* Section 3.1.2), it is possible to retrieve information about the chemical environment of the photo-absorber atom, in terms of number and type of its neighbours, inter-atomic distances, and structural disorder parameters [145]. All within a distance which is given by the mean-free-path of the photoelectron, which is in the range of $6 - 8$ Å- radius from the absorber. This makes of EXAFS a powerful and flexible structural probe.

In Appendix A we derive the EXAFS equation which links the experimental oscillations of the signal to the structural and non-structural parameters of the physical system. To have access to these parameters is necessary to process the raw experimental signal and perform data analysis.

EXAFS data analysis is normally done by using code programs which allow calculating the theoretical EXAFS spectrum based on *ab-initio* calculations, followed by a fitting refinement procedure which compares the experimental to the theoretical signal [146], providing the structural parameters.

XAS, and therefore the results obtained from EXAFS data analysis, is a bulk technique and this all the atoms irradiated by the X-ray beam contribute to the overall XAS spectrum. Furthermore, EXAFS data analysis of nanoparticles and nanostructures show a significant link with the size of the material, as a direct effect on the coordination number and the overall EXAFS signal intensity, due to the increase of the surface/bulk ratio [146–149].

Application of XAS to battery materials The simplest application of XAS to battery materials is by an ex-situ study. EXAFS spectra are collected at specific stages of charge or discharge of the chosen electrode. In this case the battery is stopped at the preferred state of charge, disassembled, and the electrodes collected, washed in organic solvents (usually the same used in the electrolyte solution) in order to remove all electrolyte residues, then the material is sealed and protected in order to avoid external contaminations from air and humidity, and finally transported to the synchrotron radiation facility where the XAS experiments take place. The experiments can be performed both in fluorescence or transmission geometries (*cfr.* Section 3.1.2).

More complex and delicate experiments can be performed in-situ and in-operando, which means that XAS measurements are taken directly during the charge or discharge process of the cell. Such methodology allows to avoid the phases of cell disassemble and transportation, which may cause the contamination of the material due to air, humidity exposure and inducing modifications on the unstable cell material. To do

so it is fundamental to design a specific in-situ electrochemical cell which can be used during the XAS experiment and to synthesize and build specific electrodes with optimal material load for optimal XAS absorption jump. The in-situ and in-operando experiments can be performed with transmission geometry, where the X-ray beam passes through the cell, and in this case, is important to choose separators and current collectors that have an optimal transmission for X-rays. Otherwise, in fluorescence geometry, it is possible to use a cell with ad-hoc optical window (beryllium or Kapton) which is placed directly on top of the electrode subject to the analysis.

3.1.2 Experimental modes

XAFS is typically measured in several modes: transmission, fluorescence and electron yield. The choice of the most appropriate method is crucial. Transmission mode is the most straightforward: it simply involves measuring the X-ray flux before and after the beam is passed through a uniform sample. Under these conditions, the transmitted flux I is related to the incident flux I_0 by $I/I_0 = \exp(-\mu(E)x)$, or $\mu(E)x = \ln(I_0/I)$. In fluorescence mode one measures the incident flux I_0 and the fluorescence X-rays I_f that are emitted following the X-ray absorption event. Usually, the fluorescence detector is placed at 90° to the incident beam in the horizontal plane, with the sample at an angle (usually 45°) with respect to the beam. Electron yield detection is similar to fluorescence yield, in that it indirectly measures absorption events by detecting the decay products when the core-hole is refilled. With this method, one measures the electrons that are emitted from the surface of the sample. The relatively short path length ($2 - 10\ nm$ for total electron yield, and $70 - 200\ nm$ for total fluorescence yield) makes the technique surface-sensitive, which can be beneficial if one is interested in near-surface phenomena. It also can be beneficial for avoiding "self-absorption" effects that can occur in fluorescence mode. These path lengths are valid for typical incoming photon energies in the soft X-ray range, thus with photon energies comprised between 50 and 1000 eV, hence for comparable kinetic energies (*cfr.* reference [113]). Other methods for detecting the energy released after the decay of the core hole are feasible: for example detection of visible light, but are seldom used [150].

3.2 X-ray Photoelectron Spectroscopy (XPS)

X-ray photoelectron spectroscopy (XPS) is a surface analysis technique that can provide information regarding the electronic state, atomic composition and chemical oxidation state of the sample under investigation.

XPS is based on a particular form of photoemission, i.e., the ejection of an electron from a core level by an X-ray photon of energy hν. The energy of the emitted photoelectrons is then analysed by the electron spectrometer and the data presented as a graph of intensity (counts) versus electron energy [151].

The kinetic energy (E_k) of the electron is the experimental quantity measured by the spectrometer, but this is dependent on the photon energy of the X-rays employed and is therefore not an intrinsic material property. The binding energy of the electron (E_B)is the parameter which identifies the electron specifically, both in terms of its parent element and atomic energy level. The relationship between the parameters involved in the XPS experiment is:

$$E_B = h\nu - E_k - \phi \tag{3.4}$$

where $h\nu$ is the photon energy, E_k is the kinetic energy of the electron, and ϕ is the spectrometer work function. All the quantities on the right side of the equation are experimentally measurable, thus deriving the value of the binding energy for the electron is a straight-forward process.

The process of photoemission is shown schematically in Fig. 3.4, where an electron from the K shell is ejected from the atom (a 1s photo-electron). The photoelectron spectrum will reproduce the electronic structure of an element quite accurately since all electrons with a binding less than the photon energy will be included in the spectrum.

All the electrons which are excited and ejected without energy loss contribute to the characteristic peaks in the spectrum; while the electrons which undergo inelastic scattering and lose energy contribute to the background of the spectrum [151]. After the emission of a photoelectron, it follows the relaxation of the ionized atom. This process may occur via the emission of an X-ray photon, known as X-ray fluorescence. Another possibility is the ejection of an Auger electron.

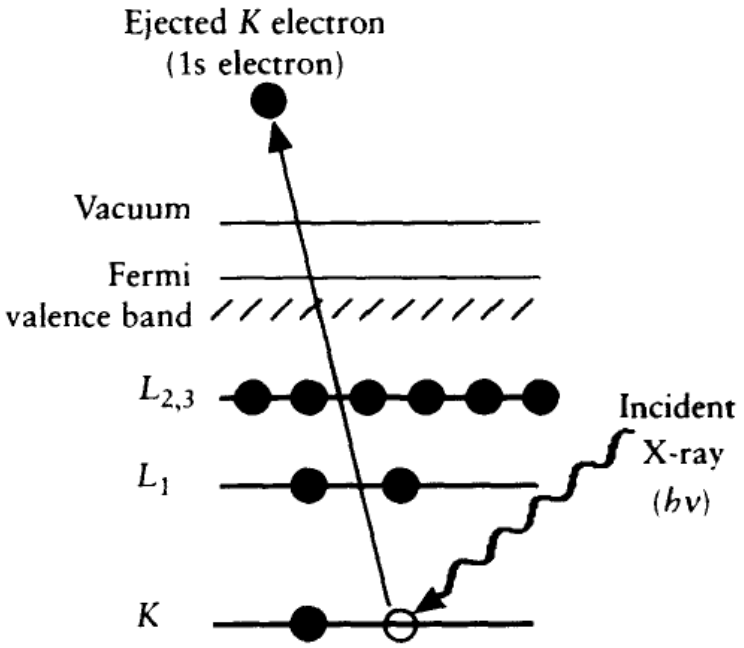

Figure 3.4: Schematic diagram of the XPS process, showing photo-ionization of an atom by the ejection of a 1s electron [151].

3.2.1 Qualitative and Quantitative Interpretation of the XPS Spectrum

The first step to take for characterizing an XPS spectrum is to identify the chemical elements present on the sample surface. For this purpose, it is possible to take a survey, or wide scan, spectrum (with a relatively large energy step size ~ 0.4 eV) over a region that can provide strong peaks for all the elements in the periodic table [151]; usually a range of $0 - 1000$ eV is sufficient. In this region, the individual peaks can be easily identified by comparison with the tabulated data. It is also important to know that the spectrum shows the superimposition of individual photoelectron peaks with the associated Auger lines resulting from the de-excitation process following photoemission and also an electron background curve. The shape of this background also provide useful information regarding the way in which near-surface layers are arranged [151]: in the case of a clean surface, the electronic background will be almost flat or with a slightly negative slope; on the other hand, a higher background curve with positive slope indicates the presence of a layer (oxides for example) covering the sample surface.

Chemical State Almost all the elements in the periodic table exhibit an XPS chemical shift of the order of a fraction of electron-volt up to several eV which is directly linked to the difference in the chemical environment of the emitting atom, ion or molecule. These shifts have origin either in the initial state or in the final state of the photo-electron.

Shifts linked to the initial state depend on the charge of the atom prior to the photoemission. The more the atom that experiences photoemission is bond with electronegative atoms, greater is the positive XPS electrochemical shift. For example C−O is shifted by 1.6 eV relative to the unfunctionalized carbon, while C=O and C≡O are both shifted by 2.9 eV. Considering the structure of the molecule it is possible to build up a synthesized spectrum where the relative intensities of the individual components reflect the stoichiometry of the sample [151]. An example of the XPS shift and peak labelling is provided in Figure 3.5.

Final state effects which occur after the emission of the photoelectron are: core-hole screening, relaxation of electron orbitals and the polarization of the surrounding ions. Those effects usually influence the magnitude of chemical shift. In metals, there is a positive shift between the elemental forms and the mono-, di- or trivalent ions [151].

There are available charts and tables of typical binding energies that can provide standard data to assign the individual components of the spectrum.

Auger Parameter In electron spectroscopy is crucial to determine the peak position with sufficient accuracy (at least ±0.1 eV). The possible sources of error in peak position derive from the spectrometer calibration and electrostatic charging of the sample. The first one may be overcome by an accurate calibration of the spectrometer using standard elements and tabulated values. The second one may be solved in several ways, one of which is using the chemical shift on both the Auger and the photoelectron peaks in the XPS spectrum and to record the separation distance between the two lines; this value is known as the Auger parameter (α) and it is defined as:

$$\alpha = E_B + E_K \tag{3.5}$$

where E_B is the binding energy of the most intense photoelectron peak and E_K is the kinetic energy of the Auger transition [151]. The measured value will, thus, be independent of any electrostatic charging of the sample.

Furthermore, the Auger parameter can provide information regarding the crystal structure and relaxation energy [151].

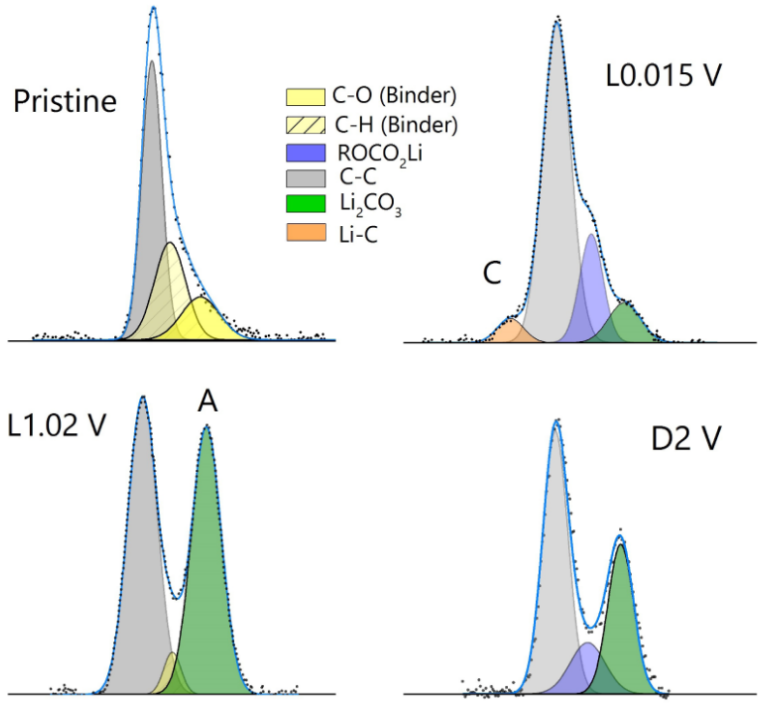

Figure 3.5: Example of quantitative analysis for XPS spectra. The image shows the C 1s XPS peaks for zinc-ferrite anodes. XPS spectra are compared with the results of a peak-fitting analysis including different carbon components [112].

Measuring the peak intensities or peak areas can provide quantitative information from XPS spectra. The intensity of the peaks can be affected by several factors that must be considered in the quantification of electron spectra, they can be sample.related or also spectrometer related factors [151]. Sample related factors include:

- The cross-section for emission (the probability of the emission of an electron due to the incoming radiation) that depends itself on the type of element investigated, the orbital from which the electron is ejected and the energy of the exciting radiation.
- The escape depth of the electron emitted, that depends on its kinetic energy and the nature of the sample.

Spectrometer related factors include:

- The transmission function of the spectrometer (usually is already taken into account before the data processing).
- The efficiency of the detector.
- Stray magnetic fields which affect the transmission of electrons.

3.2.2 Auger Electron Spectroscopy

Auger electrons, produced as a consequence of the XPS process often referred to as X-AES (X-ray induced Auger electron spectroscopy) or simply AES can give further (and complementary to XPS) information related to the chemical composition of the sample.

In the example reported in Fig.3.6 we can see a core hole (a K shell vacancy) in a ionized atom being filled by an electron of a higher level ($L_{2,3}$ in Fig.3.6). In order to respect the principle of conservation of energy, another electron must be ejected from the atom, for example (as reported in the schematic figure 3.6) another $L_{2,3}$ electron. This ejected electron, in this example, will be named the $KL_{2,3}L_{2.3}$ Auger electron. It is also common to omit the subscripts and just refer to it as KLL Auger electron [151].

The kinetic energy of a $KL_{2,3}L_{2.3}$ Auger electron is approximately equal to the difference between the energy of the core hole and the energy levels of the two outer electrons: $E_{L_{2,3}}$.

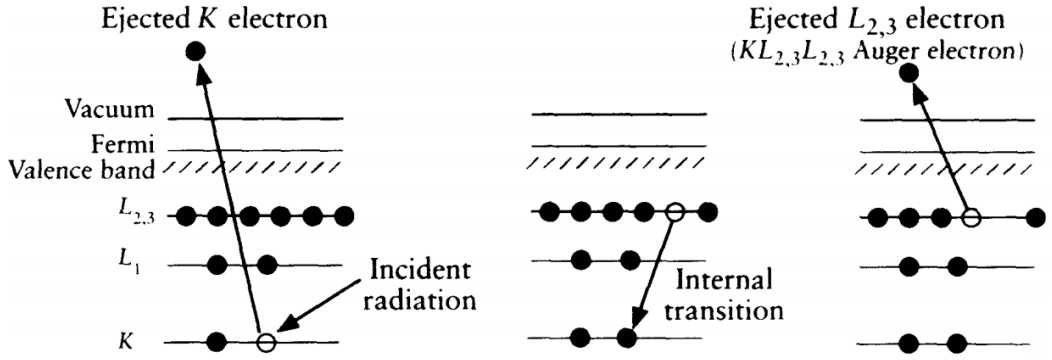

Figure 3.6: Schematics of the relaxation of a ionized atom by the emission of a $KL_{2,3}L_{2.3}$ Auger electron [151].

$$E_{KL_{2,3}L_{2,3}} \approx E_K - E_{L_{2,3}} - E_{L_{2,3}} \tag{3.6}$$

This simplified equation does not take into account the interaction energies between the core holes ($L_{2,3}$ and $L_{2,3}$) in the final atomic state neither the inter- and extra-relaxation energies which come about as a result of the additional core screening needed [151].

AES collects and measures the kinetic energies of the emitted Auger electrons, which are characteristic of elements present at the surface and "near-surface" of a sample, and do not depend on the type of energy of the X-ray source or electron gun. This makes possible elemental composition analysis. The typical sampling depth of AES is 2 to 5 nm (*cfr.* Figure 3.7), making it a surface-sensitive analytical technique.

AES spectroscopy is a technique that can be performed also with laboratory sources, often with the use of an electron gun or be induced after a photoelectron emission in XPS.

Depth of Analysis

The probability of electron-electron interaction is much larger when compared to the photon-electron interaction. That's why the detected electrons from XPS and AES derive from the surface or near-surface portion of the sample, making those surface-specific sensitive techniques [154].

The inelastic mean free path of electrons is reported in Figure 3.7 for different materials. However in the energy region of interest for XPS and AES ($100 - 2000$ eV) interaction probabilities follow an exponential function [154]. The path length of

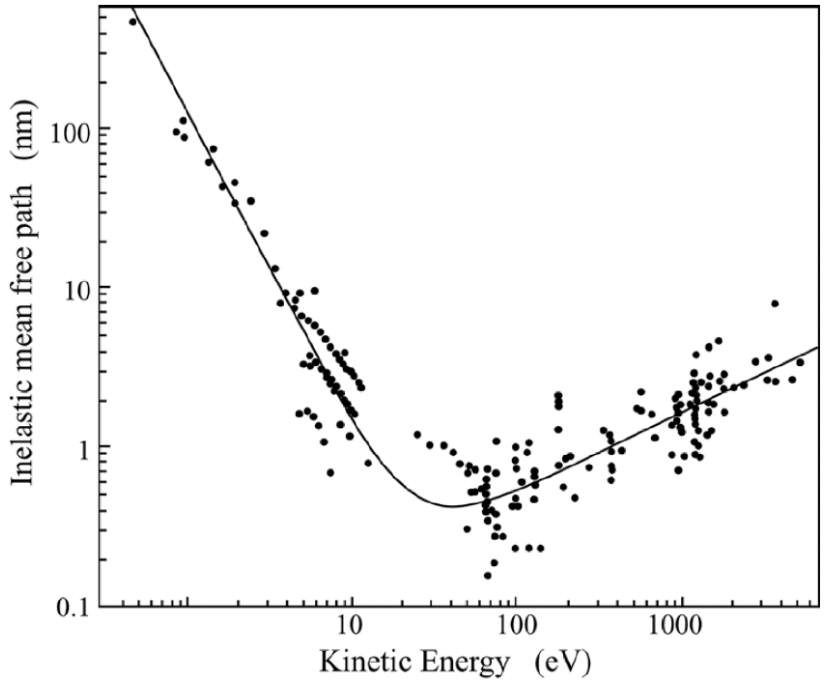

Figure 3.7: Electron mean-free-path universal curve in solids as a function of their kinetic energy (black dots) [152, 153].

electrons relative to the initial direction of travel can thus be approximated using the Beer-Lambert law. Hence we can define a quantity λ known as attenuation length which is directly related to the mean free path but also depends on the effects of elastic scattering. It can be shown that $\sim 65\%$ of the signal in electron spectroscopy derives from electrons emanated from a depth less than λ, $\sim 85\%$ from a depth $< 2\lambda$ and $\sim 95\%$ from a depth $< 3\lambda$, this latter value is defined as the sampling depth. The values of the inelastic mean free paths for elemental systems in XPS energy region are of the order of one nanometre.

Instrumentation for Electron Spectroscopy

An XPS instrument is composed of three principal components: the X-ray source, the energy analyser, and the detector [154].

The source produces the X-rays are and directed them onto the sample of interest. Usually, it is an X-ray tube with standard and/or monochromatic sources. The latter, with Al-Kα emissions used, are increasingly popular due to the energy and narrow energy spread produced. X-rays of narrower energy spread than this can only be produced in synchrotron radiation facilities. The energy resolution in XPS is primarily

dependent on the source [154].

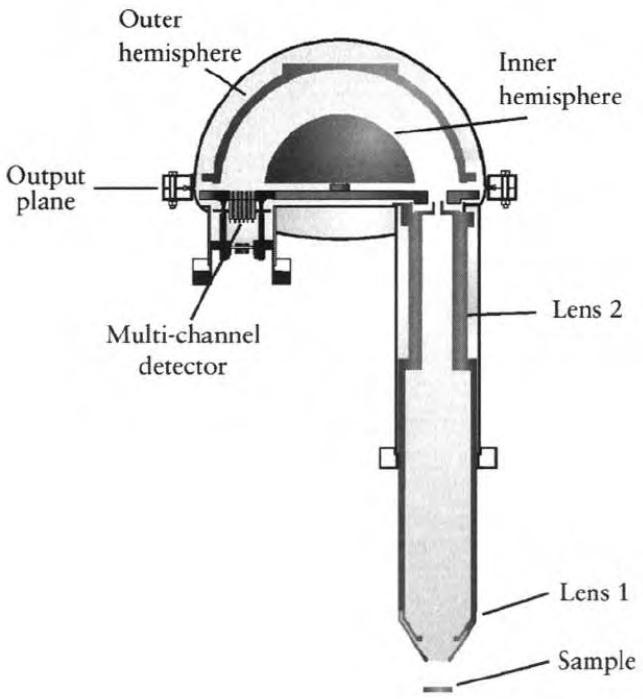

Figure 3.8: Schematic diagram of a modern HSA and transfer lens [151].

There are two types of electron energy analyser in general use for XPS and AES: the cylindrical mirror analyser (CMA) and the hemispherical sector analyser (HSA) [151]. The latter provides higher resolution improved more than a factor ten.

Finally, the electron detector is the necessary part to count the individual electrons arriving at the detector. These detectors are electron multipliers (channel electron multipliers and channel plates).

The most common detector, also the one used for the XPS experiments in this thesis is the hemispherical sector analyser (a schematic is provided in Figure 3.8). It consists of a pair of concentric hemispherical electrodes, in between which there is a gap for the electrons to pass. Between the sample and the analyser there is a series of lenses that can be used to slow down the ejected electrons since their kinetic energies may be too high for the analyser to handle properly [151].

The schematics in Figure 3.8 shows a typical HSA configuration for XPS. A potential difference is applied across the two hemispheres, with a higher potential applied to the inner one. Electrons that are injected at the input of the analyser with a tangential

velocity, will reach the detector only if their energy is:

$$E = e\Delta V \left(\frac{R_1 R_2}{R_2^2 - R_1^2} \right) \tag{3.7}$$

where E is the kinetic energy of the electron, e is the charge of the electron, ΔV is the potential difference between the hemispheres and R_1-R_2 are the curvature radii of the hemispheres. Since the radii are constant the equation can be written as:

$$E = ke\Delta V \tag{3.8}$$

where k is called the spectrometer constant and depends on the specific analyser [151].

Thus regulating the voltage difference across the two hemispheres it is possible to select one specific kinetic energy for the photoelectron that will be then counted by a detector at the end of the analyser.

This kind of instrument can provide a maximum energy resolution of ~ 1 eV.

3.3 Raman Spectroscopy

Raman scattering is a fundamental form of molecular spectroscopy [155, 156]. It is used to obtain information about the structure and properties of molecules derived from their vibrational transitions [155, 157–159].

Raman spectroscopy is both a similar and complementary technique of Infra-Red (IR) spectroscopy. For the latter one, IR absorption depends on direct resonance between the frequencies of the incident IR radiation and the vibrational frequency of a particular normal mode of vibration in the molecule. IR absorption is a one-photon event [155]. On the other hand, Raman spectroscopy is a two-photon event. In this case, the scattering event causes a change in the polarizability of the molecule with respect to its vibrational motion [155]. The interaction between the polarizability and the incoming radiation causes an induced dipole moment in the molecule, and the emitted radiation by this induce dipole moment contains the observed Raman scattering [155]. The scattered radiation by the induced dipole of the molecule is composed by Rayleigh scattering and Raman scattering. The first one is an elastic scattering event, the frequency of the Rayleigh radiation corresponds to the frequency of the incident radiation. On the other hand, Raman radiation is shifted in frequency (with respect to the incident radiation frequency) by a quantity depending on the

gained or lost vibrational energy of the molecule.

Raman Spectroscopy is a weak process that involves one in every $10^6 - 10^8$ photon. Figures 3.9 and 3.10 show the basic process that may occur for one vibration. At room temperature, most molecules, but not all, are present in the lowest energy vibrational level. Since the virtual states are not real states of the molecule but are created when the laser interacts with the electrons and causes polarization, the energy of these states is determined by the frequency of the light source used. The Rayleigh process will be the most intense since most photons scatter this way. It does not involve any energy change and consequently, the light returns to the same energy state [160].

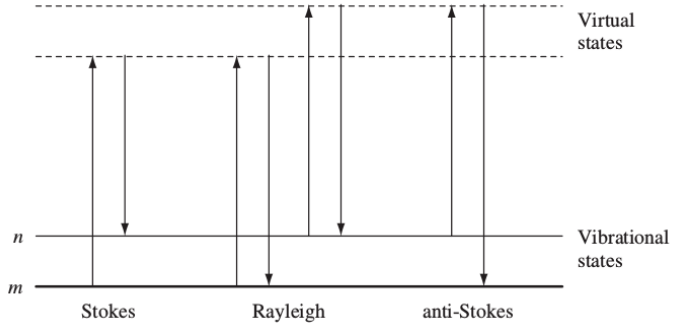

Figure 3.9: Diagram of the Rayleigh and Raman scattering processes. The lowest energy vibrational state m is shown on bottom with states of higher energies above. Both the low energy (upwards arrows) and the scattered energy (downwards arrows) have much larger energies than the energy of a vibration [160].

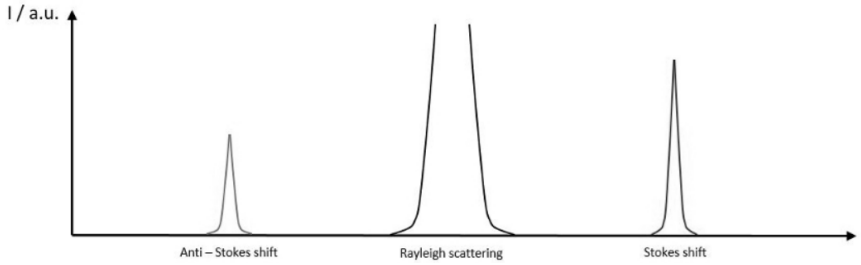

Figure 3.10: Rayleigh, Stokes and anti-Stokes peaks for a single state transition.

The Raman scattering process from the ground vibrational state m leads to the absorption of energy by the molecule and its promotion to a higher energy excited vibrational state (n), this is called Stokes scattering. On the other hand, if a molecule is at an excited state, due thermal energy, such (n), the scattering from these states to the ground state m is called anti-Stokes and involves the transfer of energy to the scattering photon [160]. Since at room temperature the number of molecules in

an excited state is low, anti-Stokes scattering will be weaker if compared to Stokes scattering. Usually, Raman spectroscopy measures only the low energy side, providing Stokes scattering.

The use of angular frequency $\omega = 2\pi\nu = 2\pi C_0/\lambda$ is convenient for theoretical treatment, but uncommon in the presentation of Raman spectra. Those are usually displayed with a wave-number scale (ν_m with unit cm^{-1}) which is related to ω_M by the relation $\nu_M = \omega_M/2\pi C_0$; expressing it as shift in energy from that of the exciting radiation.

3.3.1 Raman Set-up

Raman set-ups consist of several components: a source of monochromatic radiation (for example a laser), a sample device (for example a microscope for micro-Raman applications, or a series of lenses for focussing the incident radiation and collecting the scattered one), a dispersing system spectrometer and finally a detector. In Figure 3.11 is shown a schematic of a typical Raman apparatus.

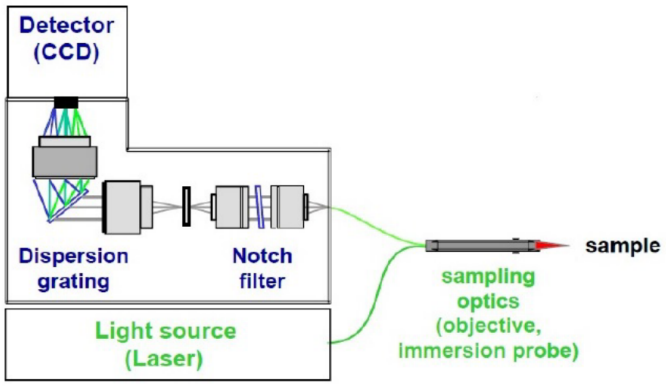

Figure 3.11: Diagram of a common Raman set-up.

Light Source In modern Raman set-ups, lasers are the ideal light sources for spectroscopy. They present the advantages to be intense, monochromatic, present a small divergence, they are polarised, and they are a coherent light source. Typical dispersive Raman instruments employ laser with a wavelength shorter than 750 nm [161].

Dispersive Spectrometer Dispersive spectrometers are used to analyse the frequency content of the scattered radiation. In modern systems diffraction gratings are used. Those can be described as a linear array of reflective (or transmitting) elements

(lines of the grating). Due to the periodic variation in the diffraction grating, the scattered light undergoes constructive or destructive interference, depending on the wavelength of the light and the angle under which the light is scattered; thus it is obtained a spatial resolution of the light as a function of the wavelength. The distance between these elements is similar to the wavelength of the dispersed radiation and also influences the spectral resolution and the spectral range.

Filters Different kind of filters are used in Raman Spectroscopy for signal attenuation or for filtering out unwanted radiation wavelengths. Filters can be classified in short as: gray filters (to absorb the light with constant value along the wavelength interval), long-pass filters (light with a wavelength shorter than the characteristic value of the filter is reflected, above this value the filter transmits the radiation), low-pass filters (the opposite of the long pass filters), band-pass filters (transmit radiation comprised in a certain interval, filtering the rest), band-block filters (also known as notch filters, filter out the light comprised in a certain interval of wavelengths, transmitting the radiation outside of such interval). The latter ones are commonly used before the spectrometer to filter out the Rayleigh scattered radiation.

Detector Most Raman spectrometers use Charge Coupled Device detectors (CCD) because they bring several advantages: they have a large dynamic range, low noise, high quantum efficiency and the ability to measure in two dimensions. Usually, the spectrum is projected along one of the dimensions of the CCD, and the pixels of the other direction are combined [161]. Generally, CCD detectors used in Raman Spectroscopy need to be cooled (with liquid nitrogen or with a Peltier plate)

Raman Microscopy

Raman spectrometer can be coupled to confocal microscopes to obtain a high spatial resolution for the sample analysis. In a confocal Raman microscope, the laser beam passes through a pinhole/aperture and is focused by the microscope objective lens in a small focal volume within the sample. The scattered light from the illuminated is then recollected by the same objective lens in a backscattering geometry. After passing in a second pinhole, and a notch filter to remove the laser radiation wavelength, the scattered radiation is finally analysed with the equipment described above. This provides a spatial resolution less than $1\mu m^3$ since the laser only hits a small portion of the sample, and the detector pinhole blocks the radiation that does not come from the

focal point.

3.3.2 Raman Spectroscopy for the Study of Electrode Materials

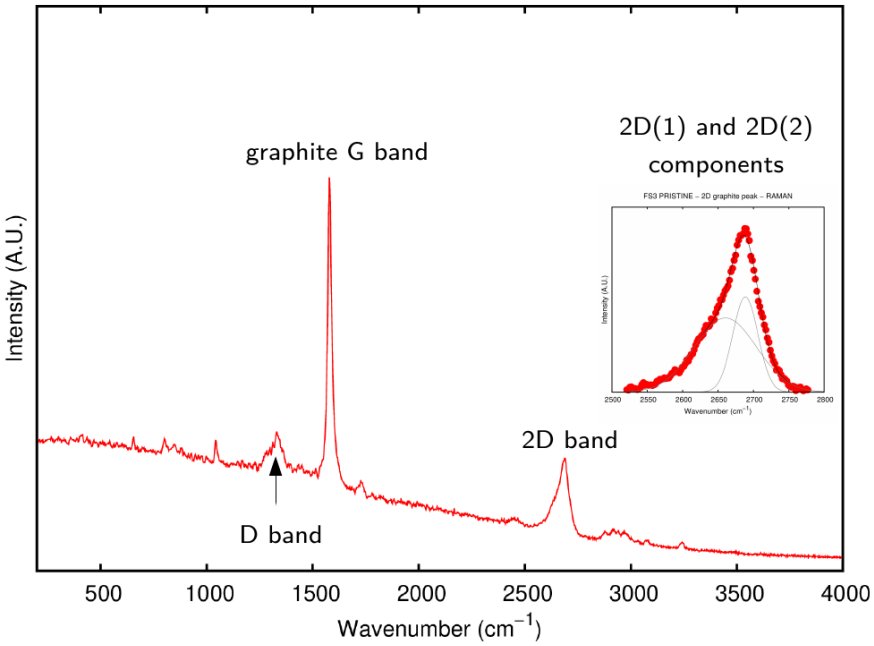

Figure 3.12: Raman spectrum of graphite electrode, used as anode for lithium-ion cell. In the inset a close-up to the 2D band components. This spectrum has been obtained with a laboratory set-up at UNICAM with an in-situ cell.

Raman Spectroscopy has optimal characteristics to be employed in the study of battery electrode materials. First of all, the analysis is non-destructive, thus it is possible to continue the experiment on the same sample and the same spot; it does not need a special preparation for the sample, no coating or controlled atmosphere are necessary to perform the measurement; the visible excitation can penetrate transparent containers, this Raman can be acquired even in samples sealed or covered with glass, plastic envelopes and other materials. This latter characteristic is optima for developing in-situ Raman investigations of electrodes under operation. Furthermore, Raman microspectroscopy, with its typical spatial resolution, allows to perform a detailed mapping of the sample surface permitting the investigation on heterogeneous mixtures; therefore, information about the structure and chemical composition can be provided for every single component in the sample [162]. An example of Raman spectrum and peak labelling for a graphite electrode is shown in Figure 3.12.

Raman is the technique of choice for the characterization of carbonaceous materials, transition metal oxides, used in Li and Na-ion batteries because it can provide information regarding the structure (for example differentiate the various carbon forms: graphitic, amorphous, *etc.*) and oxidation state.

The main drawbacks in Raman Spectrometry are the difficulties to make the technique quantitative, in measuring conductive samples (*i.e.* full lithiated or sodiated samples), possible background fluorescence coming from organic species in the electrolyte, and sample degradation due to laser-light sample heating.

3.4 Electrochemical Techniques

Galvanostatic Cycling with Potential Limitation

Galvanostatic cycling with potential limitation (also called chronopotentiometry [163]) is a technique where an instrument (potentiostat) has control of the voltage across the working electrode-counter electrode pair, and adjusts this voltage to maintain the potential difference between the working and reference electrodes (which it is measured through a high-impedance feedback loop) in accord with the program defined by a function generator [163].

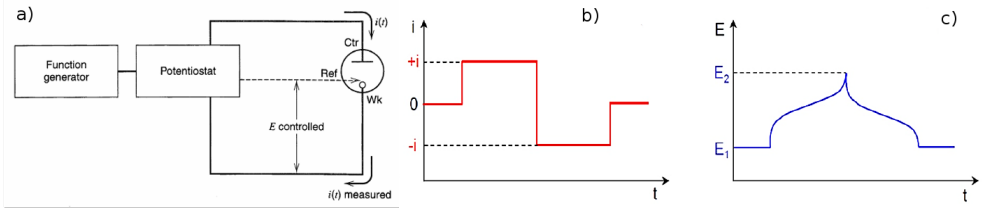

Figure 3.13: a) Schematics of an electrochemical cell connected to a potentiostat [163]; b)constant current excitation; c) corresponding voltage response [55].

The current, controlled by the potentiostat, will cause the reduction (oxidation) of the electroactive species at the working electrode, consequentially the potential will change to the characteristic working potential of the involved electroactive species involved in the redox process. The potential will change with time following the changes in the concentration of the reduced and oxidized species, as shown in Fig.(3.13).

As the voltage changes with the electrode redox state, the galvanostatic profile reflects the state of the phase diagram related to the system. Generally, a continuous variation (in time) of the electrode potential can be related to a single-phase reaction, while a presence of a potential plateau (vs. time) is ascribed to a two-phase system.

Therefore the information obtained from galvanostatic cycling is also strictly related to the thermodynamic of the electrochemical system.

Furthermore, integrating the measured current by the potentiostat with respect to time, it is possible to quantify the charge Q associated with the redox process. The ratio between the quantity of charge in the reduction reaction and the charge involved in the oxidation reaction is called *coulombic efficiency* and indicates the degree of reversibility of the redox process [55]. The amount of charge normalized by the mass of the active material in the electrode gives the *specific capacity* [mAh g^{-1}]. Measuring the evolution in the specific capacity during several cycles of charge and discharge it is possible to evaluate the cyclability (or cycle life) of the electrode.

The rate at which the cell is charged/discharged is often called *C-rate*. 1C rate correspond to a complete charge/discharge of the cell in one hour considering the theoretical specific capacity of the material: meaning that (theoretically) a cell should charge(/discharge) in one hour at 1C, in 30 minutes at 2C, in two hours at C/2 (or 0.5C), in five hours at C/5 (or 0.2C), and so on.

Constant Current/Constant Voltage Protocol (CC/CV)

Within this protocol a constant current is applied to the cell until a certain threshold voltage is reached; at this point, a constant voltage is applied to the cell until the current drops to a minimum set value. This charging method is safer and preferred over only constant voltage protocol: in fact, by applying a constant voltage the cell is vulnerable to sudden high current charge which could reduce the operational life of the battery and compromise safety. Whit the CC/CV protocol the current is kept constant and controlled, while a constant potential is applied only at the end of the charge/discharge phase as a *top-off* to ensure the maximum state of charge for the battery [163, 164].

A standard CC/CV charging plot for a cylindrical Li-ion battery is shown in Fig.3.14, is it possible to see the voltage rising (curve *(a)*) during the constant current interval ($I_S^{max} = 1C$) until the threshold voltage is reached (V_S^{max}). Subsequently the CV interval begins: the current is reduced and a constant potential (V_S^{max}) is applied. Charged is completed when the current reaches the lowest value I_S^{min} (current cut-off, an arbitrary value, typically 0.1C or 0.05C).

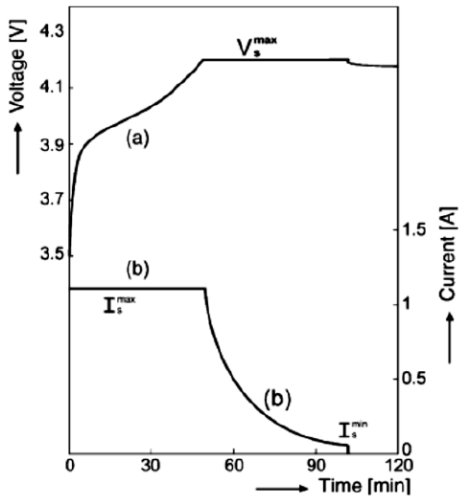

Figure 3.14: (a) Voltage and (b) current characteristics charge of a cylindrical Li-ion call when CC/CV protocol is applied [55].

Galvanostatic Intermittent Titration Technique (GITT)

In the galvanostatic intermittent titration technique [165], a constant current is applied for a given time to obtain a specific charge increment and then it is interrupted to achieve open circuit condition until the potential change is virtually zero. This process is repeated until the electrode potential reaches the cut-off voltage. The equilibrium electrode potential is obtained as a function of lithium content. In particular, during a negative current pulse, the cell potential quickly decreases to a value proportional to the iR drop. After this, due to the galvanostatic charge pulse, the potential slowly decreases in order to maintain a constant concentration gradient [165]. When the current pulse is interrupted (relaxation time interval) the potential first increases to a value proportional to the iR drop, and then slowly increases until the electrode is again in equilibrium and the open circuit potential for the cell is reached. Then the galvanostatic pulse is applied again, followed again by relaxation time. During a positive current pulse, the mechanism is the inverse.

Voltammetry

Voltammetry is a category of electroanalytical methods where the current flow is measured while controlling the potential of the working electrode.

Cyclic voltammetry is a series of linear potential scan over time, where anodic and cathodic scans are repeated alternately, the results are shown as a graphic potential vs. current. The voltammogram gives us information on the possible redox reactions of

the system, including the Faradaic insertion and extraction reaction [165].

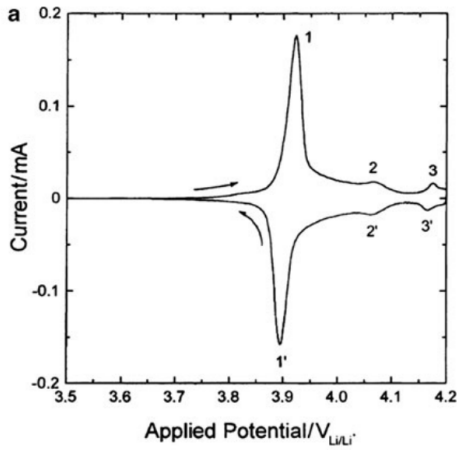

Figure 3.15: Cyclic voltammogram of $LiCoO_2$ electrode [165].

In Fig.3.15 it is presented the cyclic voltammogram of an $LiCoO_2$ film electrode as a cathode in rechargeable lithium battery. Three sets of anodic/cathodic current peaks can be observed. The first set of anodic/cathodic current peaks showing the largest value is caused by the insertion/extraction-induced phase transformation from/to Li-diluted hexagonal phase to/from Li-concentrated hexagonal phase. The second and third sets are due to the insertion (extraction)-induced order-disorder phase transition [165]. Furthermore, the presence of a surface reaction and its reversibility during the atom insertion-extraction process can be successfully examined using voltammetry.

Chapter 4

Lithiation Mechanisms in zinc-iron oxide Electrodes

The following Chapter will cover part of a research work started within the European project "Stable Interfaces for Rechargeable Batteries" (SIRBATT) and then followed, after its ending, by a collaboration with previous SIRBATT partners as Karlsruhe Institute of Technology (KIT) and Helmholtz Institute Ulm (HIU). Electrochemical characterization and preliminary morphological analysis have been carried out in collaboration with the research group of Dr. Nobili of the Chemistry Division of the School of Science and Technology at the University of Camerino. A more detailed discussion about the electro-chemistry analysis, performed by the research group, can be found in Dr. Pasqualini doctoral thesis [55].

4.1 Introduction

Transition metal-based oxides as anode materials are showing promising performances and characteristics compared to the currently largely used intercalation compounds as deeply discussed also in Chapter 2.

The charging mechanism of transition material is based on the conversion of the initial metal oxide into Li_2O and transitional metal particles embedded in the oxide. For example Fe_3O_4 has a theoretical capacity of 926 mAh per gram given by the possibility to store four lithium ions in form of Li_2O per formula unit. Furthermore this transition oxide is environmentally friendly, relatively abundant and cost-effective, resulting as an interesting candidate in recent research papers [47, 50, 166–170].

However the metallic iron nano-particles are not electrochemically active, the

theoretical capacity of the anode can be further improved by replacing iron with an element which can reversibly alloy with lithium, for instance zinc. In the case of $ZnFe_2O_4$ [171–173] the theoretical capacity increases up to 1000.5 mAh per gram, corresponding to nine lithium ions per formula unit (eight Li_2O and one LiZn); as shown in the following reaction:

$$ZnFe_2O_4 + 9Li^+ + 9e^- \rightleftharpoons LiZn + 2\,Fe^0 + 4Li_2O$$

The first report of the chemical reaction between lithium and zinc-ferrite spinel was reported by Chen *et al.* in 1986 [174]. In this first attempt, however, the maximum lithium uptake was limited to 0.5 Li^+ per formula unit and did not appear reversible. The first reversible reaction was reported in 2004 by NuLi *et al.* [175] in nano-crystalline thin films of $ZnFe_2O_4$, where they reported, due to limited reversible capacity (5 lithium ions per formula unit), the formation of FeO, LiZn and Li_2O as final reaction products. Guo *et al.* in 2010 [176] synthesized hollow $ZnFe_2O_4$ spheres, reaching almost the full theoretical capacity (900 $mAhg^{-1}$) when applying low currents.

Despite the high capacity reached in the years, the material suffers from poor cycling stability and rate capability due to the large volume expansion/contraction during cycling, particle aggregation and poor intrinsic electronic conductivity [177]. In order to solve these problems, new synthesis approaches have been tried. Deng *et al.* [178] obtained $ZnFe_2O_4$−C spheres, and showed good capacity only at low charge rates. Teh *et al.* [179] presented electro-spun $ZnFe_2O_4$ nanofibers as anode material

Bresser *et al.* in 2013 presented a new anode material consisting of carbon-coated $ZnFe_2O_4$ nanoparticles (ZFO-C) that partially overcame the problems regarding capacity fade due to loss of mechanical integrity caused by volume changes during cycling. An amorphous carbon coating on the surface of $ZnFe_2O_4$ nanoparticles (with an average diameter of 50 nm), and the utilization of fluorine-free, low-cost, and non-toxic carboxymethylcellulose (CMC) as aqueous binder material for the anode preparation, resulted in a an improvement of the electrochemical performances in terms of specific capacity, cycling stability, and power density [49].

In this Chapter, we will study the phase transition, electronic structure and structural modifications during lithiation and de-lithiation by means of several spectroscopic techniques.

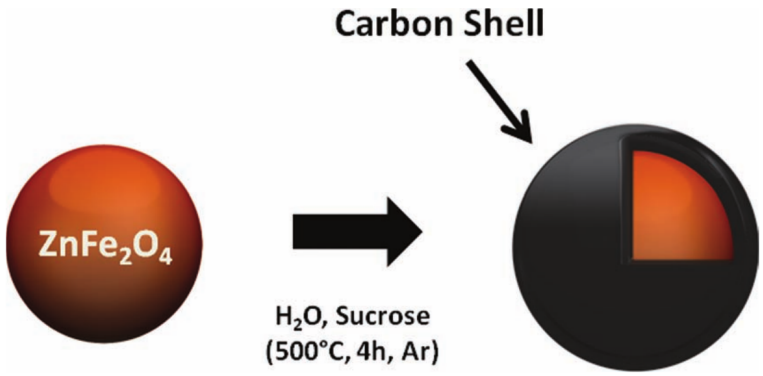

Figure 4.1: Schematic drawing of the carbon coating process of $ZnFe_2O_4$ nanoparticles, resulting in an amorphous carbon shell ($ZnFe_2O_4$−C) [49].

4.2 Experimental Characterizations and Synthesis Procedure for ZFO-C

ZFO-C Preparation

Carbon-Coated $ZnFe_2O_4$ Nano-particles synthesis procedure is reported in detail in Ref. [49].
ZFO-C has been prepared by dissolving 0.75g of sucrose (Sigma-Aldrich) in 3.5ml of deionized water (Millipore) and then adding 1.0g of $ZnFe_2O_4$ nanoparticles (< 100nm, purity > 99%, Sigma-Aldrich) under continuous stirring. The mixture obtained was homogenized in a planetary ball-mill set at 800rpm for 1.5 hours and later dried at 80°C overnight. The dried powder was then heated at 3°C/min up to 500°C for 4 hours in a tubular furnace (R50/250/12, Nabertherm) under argon atmosphere. Finally, the obtained composite was manually ground in an agave mortar.

Material Characterization

The prepared carbon-coated $ZnFe_2O_4$ powder was characterized by XRD and SEM analysis [55]. X-ray diffraction pattern was collected on a Philips diffractometer equipped with a Cu-Kα source ($\lambda = 1.54059$ Å) and Bragg-Brentano geometry in the $5° - 70°$ 2θ range while the morphological analysis was performed by using a Cambridge Stereoscan 360 electron microscope.

Electrode Preparation and Electrochemical Measurements

The electrodes were prepared by mixing and grinding in an agave mortar the active material with SuperC65 (Timcal) as conductive carbon, and then mixing it with Na-CMC (Sigma-Aldrich, MW $\sim$ 250000, D.S. 0.9) and deionized water (5 : 95 w/w), forming a slurry with a composition of 75 : 20 : 5 % of active material:SuperC65:Na-CMC. The slurry was then spread onto etched copper foil current collector via Doctor-Blade technique, with a wet-thickness of 200μm. The coated foil was then dried overnight at room temperature in order to remove the residual water and later roll-pressed. Circular electrodes with a diameter of 9mm were cut and finally dried at 120°C under vacuum for 12 hours. The final mass loading of the cut electrodes was comprised between $1 - 1.5$ mg/cm^2 (*cfr.* Ref. [55]).

Electrochemical measurements were carried out by using a T-shape polypropylene Swagelok-type 3-electrodes cells with stainless steel current collectors. Lithium metal was used as counter and reference electrode in the half-cell configuration. The cell separator consists in of glass fiber (Whatman GF/A); as electrolyte was employed a solution of 1 M $LiPF_6$ in EC:DMC 1 : 1 v/v (Solvionic). The tested cells were assembled in an argon-filled glove-box. Electrochemical characterization were performed on a multichannel galvanostat/potentiostat VMP2/Z (Bio-Logic).

4.3 Preliminary Morphological and Structural Characterization

The carbon coating procedure is schematized in Figure 4.1 and is obtained by a thermal treatment under argon atmosphere. In order to preserve the original zinc-ferrite spinel structure, is crucial to operate in a correct temperature range, in order to avoid precocious phase transitions, *i.e.* the conversion of $ZnFe_2O_4$ nano-particles into FeO and ZnO as reported by Ayyppan *et al.* [180].

The procedure developed by Bresser *et al.* [49] employs a carbonization temperature of 500 °C which preserves the morphology and structure of the pristine nano-powder, also confirmed by XRD and SEM analysis.

X-ray diffraction analysis (see Figure 4.2 (a)) has been performed also at university of Camerino with a Philips diffractometer equipped with a Cu-Kα source ($\lambda = 1.54059$ Å) and Bragg-Brentano geometry. The diffraction peaks of carbon-coated zinc ferrite correspond to a well-defined cubic structure with $Fd\bar{3}m$ space group matching very

well the standard reference (JCPDS card 00-022-1012), revealing the high crystallinity of the synthesized material and confirming the cubic spinel structure of the zinc ferrite before carbon coating. No additional reflections indicate the absence of crystalline impurities and confirm the amorphous nature of the carbon coating.

In Figure 4.2 (b) SEM image from reference [49] shows the carbon-coated nano-particles having a uniform dimension of ≈ 50 nm, with no significant morphological changes from the non-coated material.

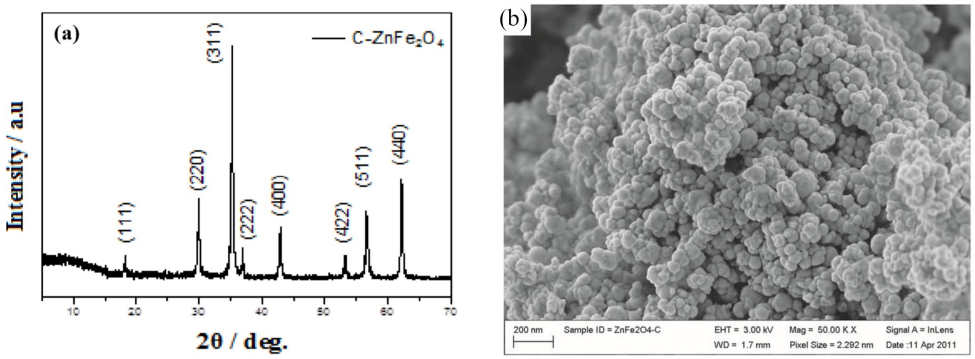

Figure 4.2: a) XRD pattern of ZFO-C [55] and (b) SEM image of carbon-coated zinc ferrite nano-particles [49].

4.3.1 Spinel Ferrite Structure

As shown by XRD, $ZnFe_2O_4$ is part of the family of spinel ferrites as well as its carbon-coated nanoparticles version. The cubic spinel $A[B_2]O_4$ belongs to the space group $Fd\bar{3}m$, is characterized by a cubic unit cell containing 8 formula units forming a cubic close packing of 32 anions which occupy the 32e position. The 8 A bivalent cations occupy one-eighth of tetrahedral sites (8a) while the 16 B trivalent cations half of the octahedral sites (16d). In the structure are also present empty interstitial spaces with octahedral symmetry (16c sites) and tetrahedral (8b and 48f sites).

Thus in normal zinc-ferrite spinel, we have zinc atoms in tetrahedral sites and iron atoms in octahedral sites $[Zn]^{tet}[Fe_2]^{oct}O_4$.

There is also the possibility of a partial rearrangement of the cations within the structure. Depending on the cations distribution the spinel can be *normal*, *inverted* or *partially inverted*. In the normal spinel structure, the 8 bivalent A cations all occupy tetrahedral sites, and all of the 16 B cations are placed in octahedral sites. On the other

hand in a completely inverted spinel structure, the A atoms all occupy vacant octahedral sites and B atoms are distributed half in octahedral and half in tetrahedral sites. For a partially inverted spinel the structure can be written as $[A_{x-1}B_x]^{tet}[A_xB_{2-x}]^{oct}O_4$ which for the zinc-ferrite structure corresponds to: $[Zn_{x-1}Fe_x]^{tet}[Zn_xFe_{2-x}]^{oct}O_4$ [181, 182] where the x index (with $0 \leq x \leq 1$) is called *inversion parameter*, which is 0 for a normal spinel and 1 for an inverse spinel.

4.4 Electrochemical Characterization

Electrochemical characterizations of electrodes based on ZFO-C active materials are reported in refs. [49, 183, 184]. Characterization of the same electrode materials was performed also at the University of Camerino within the SIRBATT project and detailed results can be found in ref [55].

4.4.1 Galvanostatic Tests and Cycling Performances

Preliminary cycling tests on ZFO-C were taken at T= 25°C alternating current rates of C/5 and 1C every 10^{th} cycle. On the first cycle the initial lithiation capacity was 1471 $mAhg^{-1}$ and the initial delithiation capacity of 1049 $mAhg^{-1}$, showing an high irreversible capacity loss of 422 $mAhg^{-1}$. This capacity loss on the first cycle can be attributed to the irreversible lithium storage into the SEI interfacial layer and partly to the formation of a polymeric "gel-type" layer on the surface of the active material nano-particles, which can be reversibly formed and dissolved upon cycling, as consequence of side reactions with cyclic electrolyte solvents [179, 185, 186].

First reversible capacities values are found to be 1085 $mAhg^{-1}$ and 998 $mAhg^{-1}$ at C/5 and 1C respectively. The coulombic efficiency tends to increase to values close to 100% as cyclation proceeds, while capacity values decrease with a capacity retention after 40 cycles of 78% and 73% at C/5 and 1C.

4.4.2 Cyclic Voltammetry

As seen from Figure 4.3, the first cycle shows a very different voltammetric curve if compared with the following ones. During the initial lithiation we can identify several reduction peaks: two small peaks at about 1.5 V (A) and 1.2 V (B), followed by a more pronounced one at about 0.9 V (C) and finally the main reduction feature (D) at a potential of 0.7 V. The latter main reduction peak (D) is associated with the main

conversion reaction of the material $Zn_xFe_yO + 6\,Li^+ + 6e^- \longrightarrow Zn^0 + 2\,Fe^0 + 3\,Li_2O$ and also with irreversible lithiation processes related with the electrolyte decomposition. Initial reduction peaks (A), (B) and (C) can be attributed to an initial insertion mechanism, where lithium is first stored into the vacant sites of the pristine spinel crystalline structure with the following proposed reactions: $Li_{0.2}ZnFe_2O_4$ [187] or $Li_{0.5}ZnFe_2O_4$ and $Li_2ZnFe_2O_4$ [176]; however the voltammetry of the first cycle suggests that the reduction reaction occurring before the main conversion phase are much more complicated, thus is necessary to investigate this phase with more appropriate tools. The last feature (E), at the end of the first lithium uptake, can be related with the final alloying reaction of Zn and Li forming ZnLi.

Subsequential cycles only show one main reduction (cathodic) peak at a potential around 1 V which shows a slight shift towards lower potential as the cycle number increases. During the anodic process, two oxidation peaks are present at around 1.7 V and 2.1 V related to the oxidation processes occurring to zinc and iron. From the second cycle and on we find comparable voltammetry curves, confirming the high reversibility of lithium uptake and release processes once the structural changes of the material are completed and stable.

initial 8*a* sites and occupy all the vacant 16*c*

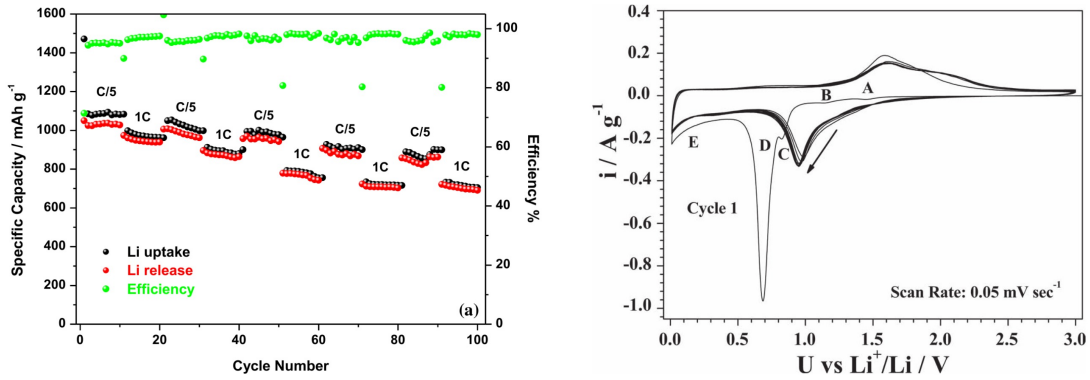

Figure 4.3: Cycling behaviour at C/5 and 1C rates [55]; b) Voltammogram of $ZnFe_2O_4$−C electrode; scan rate 0.05 mV sec^{-1}; Cycle 1 – 10 [49].

4.4.3 Voltage Profile of the First Galvanostatic Discharge and Expected Reactions and Structural Modifications

From the observed cathodic peaks in the voltammetry (Figure 4.3), we can divide the voltage profile of the first lithium uptake and release (Figure 4.4) into five different regions. In region (A) the potential decreases rapidly from 3 V to 1.6 V followed by a smoother decrease to 1.3 V. This first slope correspond to the first reduction peak (A) seen in the voltammetry (Figure 4.3 b) and occurs at a specific capacity of 0.4 Li^+ per formula unit of $ZnFe_2O_4$ resulting in $Li_{0.4}ZnFe_2O_4$. This amount of inserted lithium corresponds well with the value reported by Chen [174,188] where it was hypothesized a lithium insertion into the vacant octahedral 16*c* sites of the zinc-ferrite spinel structure. It was also suggested that Zn atoms are not displaced and remain in the original 8*a* sites due to its strong preference for tetrahedral configuration [189].

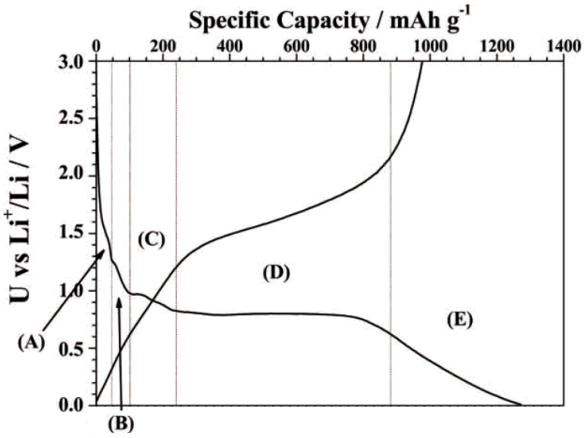

Figure 4.4: Voltage discharge and charge profile of the first galvanostatic cycle [49].

For lithium insertion above 0.4 atoms per formula unit, thus before the main lithiation phase corresponding to peak B in the voltammogram, Chen *et al.* predict that the coulombic repulsive force interaction between Li^+ and Zn^{2+} is strong enough to displace zinc atoms into the 16*c* sites. This behaviour has been reported also in other spinel structures up to a maximum of one lithium per formula unit [190].

When the lithium uptake overcomes the value of 1 Li^+ per formula unit the discharge profile shows a short plateau which corresponds to the reduction peak C in the voltammetry 4.3. In this phase Chen *et al.* [174,188] suggest a further modification of the initial spinel structure into a rock-salt type phase where lithium atoms are possibly occupying the vacant tetrahedral sites 8*a* or 48*f* and, at the same time, decomposing into Li_2O while iron reduces. The reduction reaction involves the formation of small

clusters of ZnO and FeO that could not be detected by XRD [49]

In the main plateau of the discharge profile (related to the main reduction peak D) the achieved capacity agrees with a full decomposition of both iron and zinc into their metallic forms: $ZnFe_2O_4 \longrightarrow Zn^0 + Fe^0 + Li_2O$.

Finally, in section E of the discharge curve, a last contribution to the reversible capacity of the material can be given by the alloying process between lithium and zinc forming LiZn which is known to occur within this potential region [171, 173, 191]. Once again, these new phases were not directly detected by XRD because of the amorphization of the material and the possible formation of nano-crystalline structures for which XRD is not sensitive.

The lithiation reaction proposed by Bresser *et al.* is the following:

(A) $ZnFe_2O_4 + 0.4Li^+ + 0.4e^- \longrightarrow [Li_{0.4}]_{16c}[Zn]_{8a}[Fe_2]_{16d}O_4$

(B) $[Li_{0.4}]_{16c}[Zn]_{8a}[Fe_2]_{16d}O_4 + 0.5Li^+ + 0.5e^- \longrightarrow [Li_{0.9}Zn]_{16c}[Fe_2]_{16d}O_4$

(C) $[Li_{0.9}Zn]_{16c}[Fe_2]_{16d}O_4 + 0.55Li^+ + 0.55e^- \longrightarrow [Li_{0.55}]_{8a,48f}[Li_{0.9}Zn]_{16c}[Fe_2]_{16d}O_4 \longrightarrow Zn_xFe_yO + Li_2O$ (x:y)=1:2

(D) $Zn_xFe_yO + 6Li^+ + 6e^- \longrightarrow Zn^0 + 2Fe^0 + 3Li_2O$

(E) $Zn^0 + Li^+ + e^- \longrightarrow LiZn$

Overall reaction:

$ZnFe_2O_4 + 9Li^+ + 9e^- \longrightarrow LiZn + 2Fe^0 + 4Li_2O$

4.5 Experimental Set-up for *in-situ* and *in-operando* XAS

Previous XRD studies [49,175,176] also performed in-situ, did not provide a complete insight of the structural modifications occurring during the various stages of lithium insertion/de-insertion; this because of the gradual loss of all diffraction reflections after the lithium content in the material is higher than a certain amount, and thus, probably due to a gradual amorphization of the material, or due to the formation of very small crystalline grains that are too small to give detectable diffraction peaks.

To overcome this problem, we performed a series of X-ray absorption spectroscopy experiments coupled with galvanostatic lithiation of the active material, in order to achieve XAS spectra directly from the cell during its operational state: thus an in-situ and in-operando experiment.

In-operando XAS experiments on electrochemical cells bear multiple advantages

instead of performing the same kind of experiments ex-situ: it is possible to collect a large number of spectra during the charge or discharge state of the cell, providing a very detailed monitoring of the electrochemical reactions and the related structural evolution; furthermore it makes possible to inspect the very same electrode in the same spot at different stages of the reaction, avoiding the possibility of having differences in composition and uniformity between the different samples; moreover a good electrochemical performance of the in-situ cell guarantees the absence of contamination from the ambient, in particular from oxygen and humidity, that could interfere and modify the oxidation state of the sample.

The main disadvantage related with this procedure regards the fact that it is not being used a standard cell during electrochemical characterization, this can be linked to slightly different electrochemical reaction (different voltage profile or difference in the specific capacity).

4.5.1 Pouch Cell for *in-situ* XAS in Transmission Mode

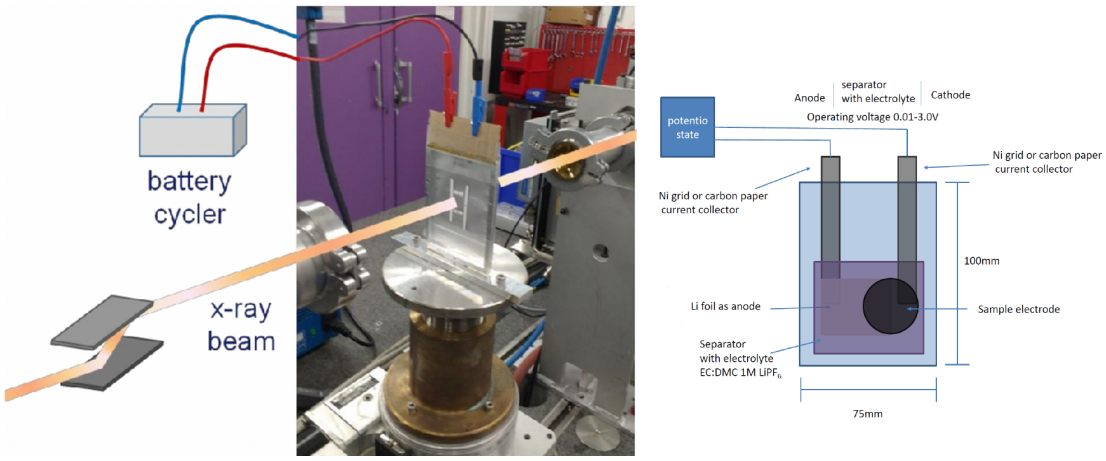

Figure 4.5: Experimental set-up for in-situ XAS in transmission mode: the pouch cell is connected to a potentiostat that controls the lithiation rate. On the right a schematics of the pouch cell.

A picture of the experimental set-up (in-situ XAS in transmission mode) is shown in Figure 4.5. The pouch cell (shown in 4.5, right side) is composed by several stacked layers, compressed and sealed in an aluminium laminated film as a pouch with protruding current contacts for the cell electrical connection. The two cell electrodes are divided by the separator soaked with the electrolyte inside the case.

ZFO-C electrodes were prepared by dissolving PVdF (polyvinylidene fluoride -

Kynar 761) in NMP (N-methyl-2-pyrrolidone). Conductive carbon (Super C65; Imerys) and ZFO-C active material were added to the binder solution in 20 : 70 : 10 wt% proportion (percentages are referred respectively to conductive carbon, ZFO-C active material and binder solution). The resulting slurry was cast on a carbon foil current collector (wet thickness of 300 μm) ensuring low X-ray absorbance, in fact, the usual procedure for assembling pouch cell would require to use a metallic current collector (aluminium or copper). The active material loading was $\sim 6\ mg/cm^2$ calculated to obtain a suitable absorption jump for XAS measurements in transmission mode. Finally, 12 mm diameter disk electrodes were punched. For the in-situ XAS measurements, pouch cells were assembled with metallic lithium as counter electrode, a ceramic separator (Separion, Evonic) and a solution of $LiPF_6$ (0.5 M) in EC:DMC 1 : 1 v/v as electrolyte (UBE).

4.5.2 X-ray Absorption Spectroscopy Experiment

XAS measurements were carried at beamline BM23 of the European Synchrotron Radiation Facility (ESRF) [192]. Fe and Zn K-edge spectra were collected in transmission mode using two ionization chambers filled with mixtures of Ar and He gases. The x-ray radiation was monochromatized by a double-crystal Si(111) monochromator and harmonics were rejected using a silicon mirror. Furthermore, XAS spectra of iron and zinc reference metal foils were measured simultaneously with each sample scan to monitor the energy scale and align successive scans.

The pouch cell was mounted on an aluminium frame and connected to a potentiostat (CH Instruments 660B) working with a two electrodes configuration to perform galvanostatic cycling of the electrode in parallel with the XAS measurements. The instrument during discharge applied a constant current of 0.9 mA.

Data collection in transmission mode allowed to get each extended spectrum (up to k=15 $Å^{-1}$) in a relatively short time ($\sim$ 20 min). Since the acquisition time is much smaller compared to the whole discharge time ($\sim$ 10 hours), we can assume the cell potential, the chemical state and the material structure to be unchanged during the whole time of one single scan.

In Figure 4.5 (left) a picture of the experimental set-up mounted on BM23 is shown. The frame holding the pouch cell is mounted on a motorized table in order to align the electrode to the X-ray beam. For each absorption edge energy was utilised a different pouch cell built with same procedures and similar material loadings. The cells (listed in Table 4.1) were discharged with a rate of C/10 (where 1C represent the rate to

discharge the theoretical capacity in one hour) down to a limit potential of 0.01 V.

Table 4.1: List and description of the in-situ cells.

Sample	El. mass [g]	Active mass [g]	Description
Cell A	0.0159	0.0079	Fe K-edge
Cell B	0.0159	0.0079	Zn K-edge

The discharge curves of the two pouch cells are shown in Figure 4.6. Both pouch cells present a final capacity higher than the theoretical expected one for the ZFO electrode (the pouch cell used during the XAS measurement at Fe K-edge has a final specific capacity of 1640 $\mathrm{mAh\,g^{-1}}$, while the one used for Zn K-edge has a final specific capacity of 1220 $\mathrm{mAh\,g^{-1}}$), this behaviour is normal since we were considering the very first galvanostatic discharge cycle for each cell, and in this phase there is an extra-capacity caused by lithium ions that are irreversibly stored and employed in the formation of the SEI passivation layer and involved in the degradation of the electrolyte products. Moreover, as recently shown in the paper by Rezvani et al. [112] an increase of the specific capacity can be also assigned to an extra-capacity related to the particular components of the SEI itself and by the carbon material used in the preparation of the electrodes.

The two cells show similar behaviours in the discharge potential curves: the initial OCV pot initial 8*a* sites and occupy all the vacant 16*c*ential is ~ 3 V and suddenly drops as the potentiostat circuit closes. The two initial plateau present in Figure 4.4 in sections (B) and (C) (which represent the related reduction peaks in the voltammogram Fig. 4.3) are present at similar potentials, but they present a significantly reduced extent (in standard conditions ~ 2 Li^+ per formula unit while in this case ~ 0.5 Li^+ per formula unit). Nevertheless, no significant differences are found in the spectra when compared to an ex-situ set. The main reduction plateau (region D in Figure 4.4) starts at 0.6 Li^+ per formula unit at a potential of ~ 0.75 V (consistently to the reference potential curve of Fig. 4.4).

Furthermore, a second set of electrodes (Table 4.2), at several lithiation rates, have been analysed for ex-situ comparison with the in-situ samples. The ex-situ electrodes have been prepared with the same procedures of the in-situ ones, then cycled in standard coin cells. After this, the electrodes have been disassembled from the cell in Ar atmosphere and washed in EC:DMC solvents to remove residues of electrolyte salts. The washed and dried electrodes have then been stored and sealed in plastic PE foils to prevent water and oxygen contamination of the samples.

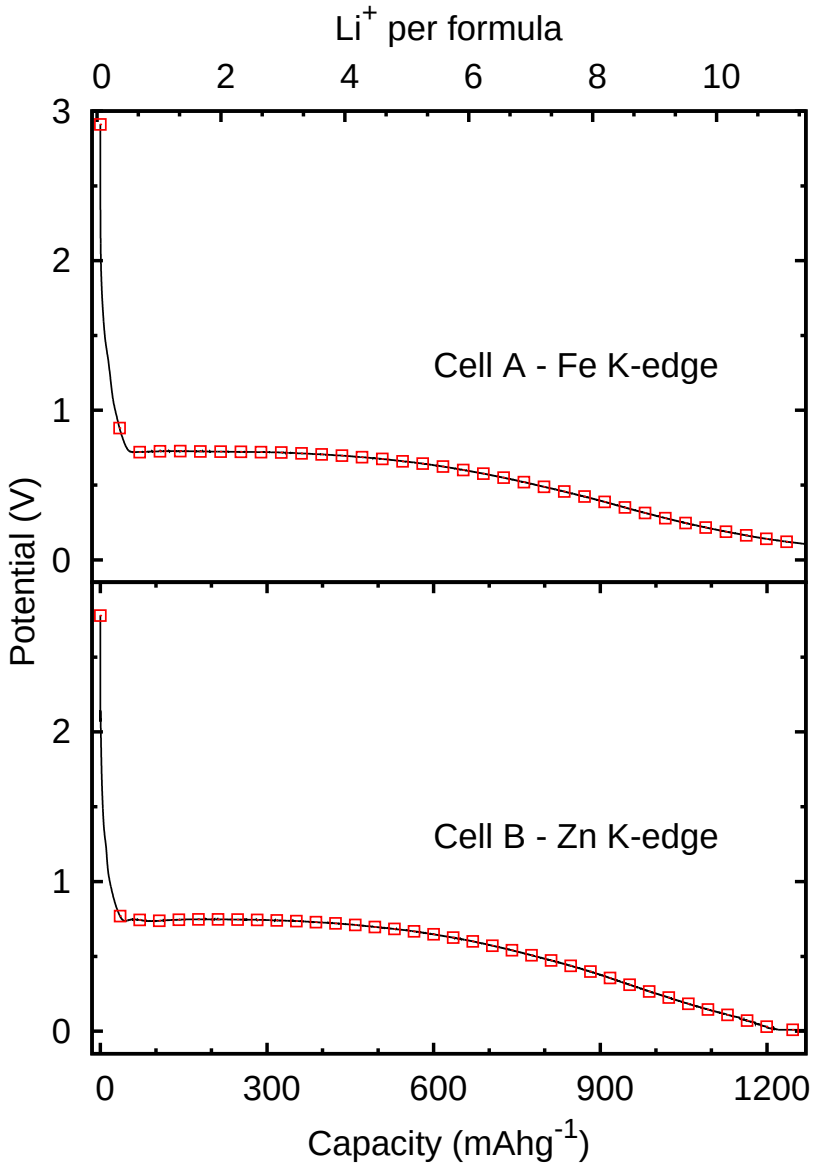

Figure 4.6: Voltage profile curves of the two pouch cells used in the in-situ XAS experiment.

Table 4.2: List of the ex-situ samples.

Sample	Electrode mass [g]	Active mass [g]	Procedure
CP1	0.0111	0.0046	3.0 V charge
CP2	0.0110	0.0045	1.7 V charge
CP3	0.0141	0.0066	0.7 V charge
CP4	0.0110	0.0061	0.01 V discharge (12 Li^+)
CP5	0.0133	0.0058	0.5 V discharge (7.8 Li^+)
CP6	0.0125	0.0056	5^{th} cycle (3.0V)
CP7	0.0129	0.0058	10^{th} cycle (3.0V)
CP8	0.0118	0.0051	20^{th} cycle (3.0V)
CP9	0.0144	0.0069	0.75 V discharge (5.5 Li^+)
CP10	0.0110	0.0045	1.5 V discharge (0.1 Li^+)
CP12	0.0144	0.0069	0.9 V discharge (0.7 Li^+)
CP-OCV	0.0125	0.0055	OCV

4.6 XAS Analysis and Results

4.6.1 XANES

The normalized near-edge spectra (XANES) of the in-situ pouch-cell with ZFO-C active material at various stages of lithiation are shown in Figures 4.7 and 4.8 for both Fe and Zn K-edges. In the latter one, they are spaced for better comparison (from initial state at open circuit voltage with no lithium inserted, on bottom, to the fully lithiated state, on top).

For both edges it is noticeable a shift of the white line towards lower energies as the lithiation proceeds; this is directly linked to the reduction processes of iron and zinc occurring during Li^+ insertion.

Specifically, Zn edge (calculated as the maximum of the derivative) for the pristine material is located at 9663 eV while for the full lithiated cell is located at 9658 eV. This latter value is slightly smaller if compared to the energy edge of metallic Zn standard foil (black dotted line) which is 9659 eV, this suggests that the various zinc oxides in the material completely convert to metallic Zn with a fraction of Zn^- in the form of a LiZn complex.

For Fe K-edge there is a more significant energy red-shift: starting from the pristine material at 7126 eV to the full lithiated electrode which has a white line at 7112 eV. This value perfectly matches the metallic Fe standard foil (black dotted line), suggesting that all the iron present in the electrode is converted into its metallic state in the form of nano-crystallites since the previous XRD studies did not detect the related

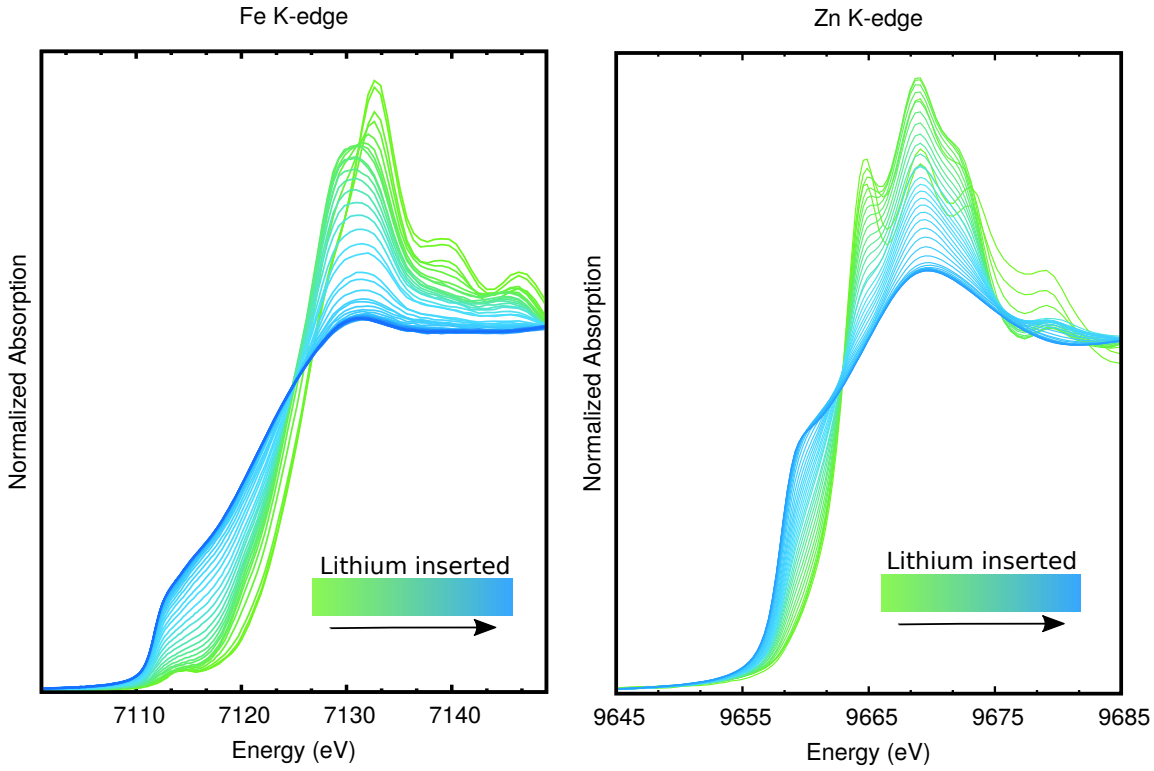

Figure 4.7: All the XAS spectra collected during the experiment (XANES section). On the left Fe K-edge, on the right Zn K-edge. The color gradient indicates the amount of lithium inserted into the material (green = no lithium inserted, blue = full lithiated state).

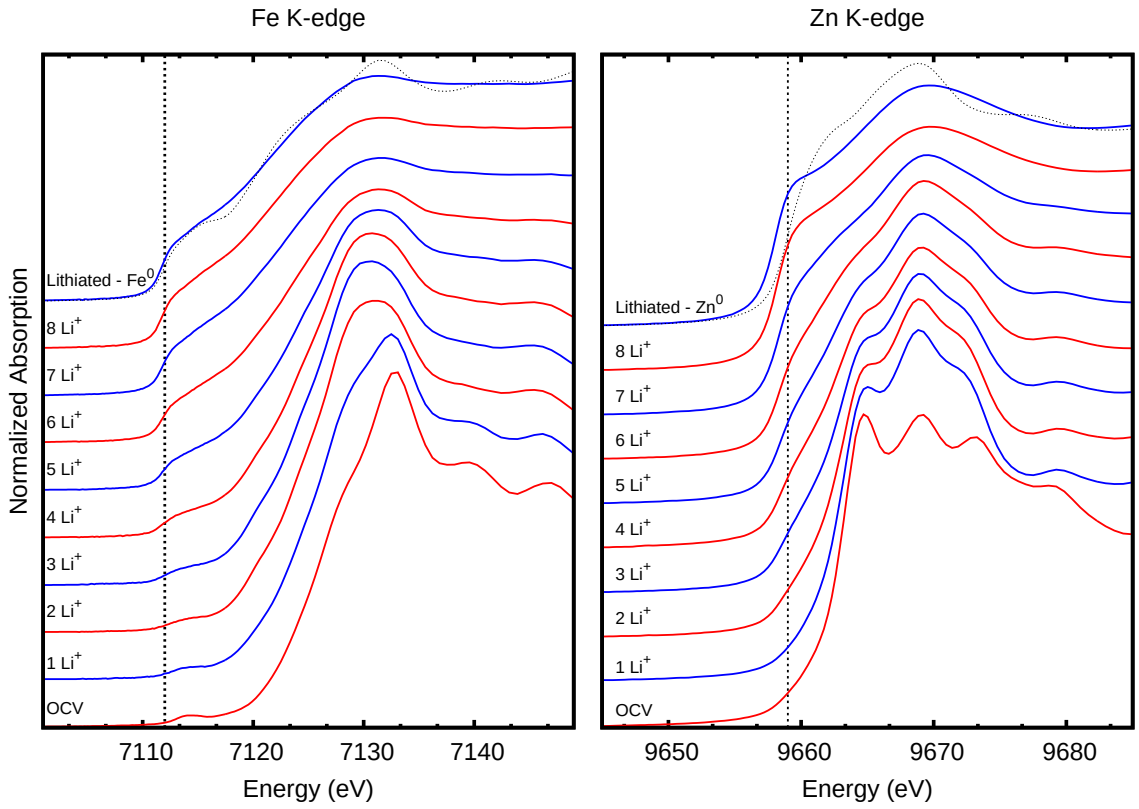

Figure 4.8: Normalized near edge XAS spectra for Fe (left) and Zn (right) K-edges during the first discharge (lithiation). The amount of lithium inserted increases from the bottom (no Li^+ inserted) to top (full lithiation, cell potential at 0.01 V). For comparison are inserted also the XANES of zinc and iron metal reference foils (top black dashed line).

reflections at this stage.

4.6.2 EXAFS

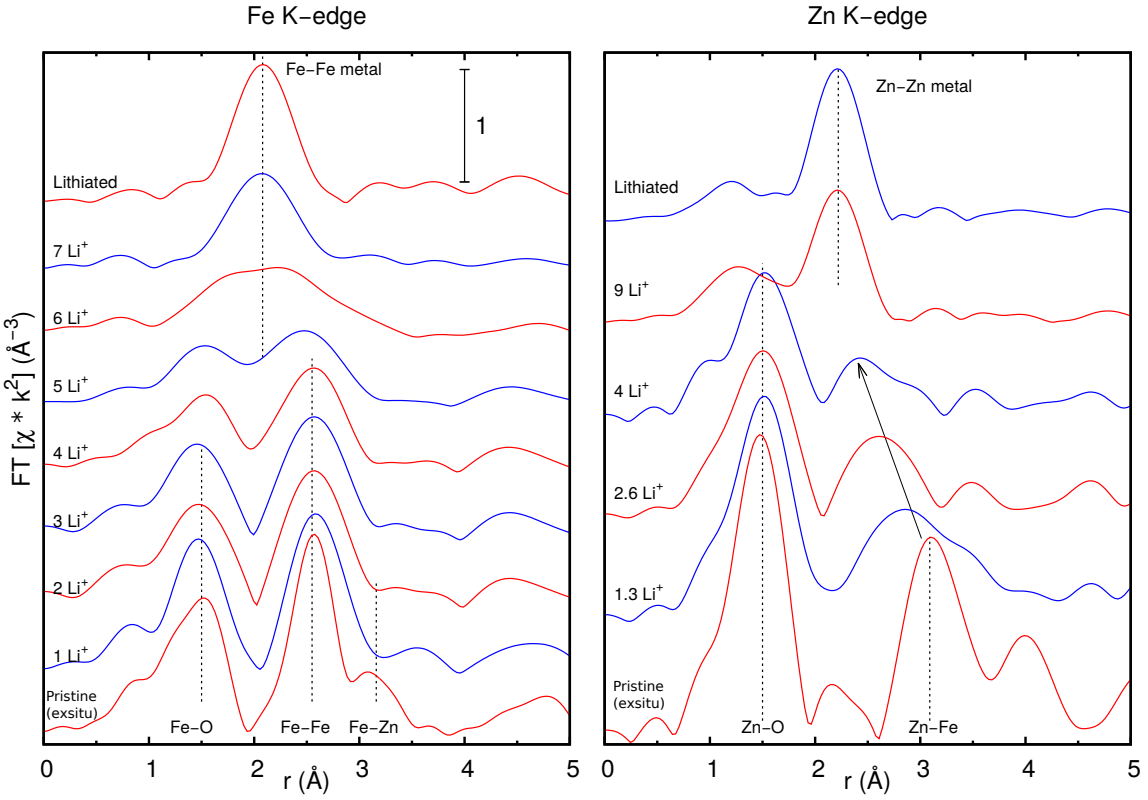

Figure 4.9: Fourier transform of EXAFS signal for Fe and Zn K-edges during the first discharge. Lithium uptake increases from bottom (OCV) to top (full lithiation).

In Figure 4.9 it is shown the Fourier transform of the experimental EXAFS signals collected during the cell discharge for both Fe and Zn K-edges. Starting from the bottom of the image we have the cell in OCV status. In the undischarged status, the Fourier transform of Fe K-edge clearly shows the presence of O_{32e}, Fe_{16d} and Zn_{8a} neighbouring atoms at distances 1.5 2.6 and 3.2 Å respectively, which are consistent with the expected structure for a spine zinc-ferrite (noticeably the distances of the Fourier transform are about 0.3 Å shorter than the actual inter-atomic distances due to phase shift). Also the pristine material Fourier transform of Zn-edge confirms the expected crystalline structure showing O_{32e} and Fe_{16d} first neighbours of zinc at distances 1.5 and 3.2 Å.

At the beginning of lithiation, when lithium reaches a concentration of 0.6 ions per

formula units, the shapes of the Fourier transform start to change, indicating atomic displacement of the initial structure due to the repulsion force of Li ions. In fact the shell of Zn_{8a} in Fe K-edge disappears as it is merged with the shell of Fe_{16d} (at 2.6 Å). This is even more evident in Zn K-edge where the shell of Zn is shifted toward lower distances (again around 2.6 Å). This atomic displacement affecting only zinc atoms is compatible with a migration of Zn_{8a} into Zn_{16c} octahedral sites [174].

Within the main reduction plateau in the discharge curve, corresponding to a potential of 0.75 V, a new component in the R-space appears, linked to the formation of metallic phases of both iron and zinc. Metallization of iron occurs first, already at 5 Li^+ per formula unit, appearing as a new shell in the Fourier transform of Fe K-edge at a distance of 2 Å typical of a metallic Fe-Fe bond. This reduction process is gradual and metallic iron is initial present alongside other iron oxides; finally, it is completed at about 9 Li^+ per formula unit when only the single shell of Fe-Fe is present. Metallization of zinc occurs consequentially to the beginning of iron reduction as expected from electrochemical tests [49]. Presence of metal zinc-zinc shell starts to appear after 6 Li^+ per formula unit, positioned at 2.2 Å. Also, the process of zinc metallization is finalized at the end of the lithiation, as the Fourier transform only shows one single main peak of the relative Zn-Zn metallic phase distance.

4.6.3 Initial Lithiation Phase

XANES of Initial Lithiation

The normalized near edge spectra (XANES) of ZFO-C at various stages of the initial lithiation (from 0 to 2 Li^+ per formula unit) are shown in Figure 4.10 for both the Fe and Zn K-edges. The red curves correspond to the XANES spectra of ZFO-C when the cell is at open circuit voltage (OCV), *i.e.* zero lithium inserted in the material structure. In the successive curves, the quantity of Li^+ in the material increases while the voltage of the cell decreases. The brown curves in the graph correspond to 2 Li^+ per formula unit: at this stage, the specific capacity is 222 mAh/g while the discharge potential is at 0.75 V. As lithium inserts in the structure, the Fe K-edge shows a red-shift. Also the white line is broadened and shifted towards lower energies (up to $\Delta E = -2$ eV). This behaviour indicates a gradual reduction of Fe^{3+} to Fe^{2+} as charge (from Li^+) is inserted into the active material.

A small pre-edge edge peak is present at $\sim$ 7114 eV. The small peak in the pre-edge region of Fe oxides is related with both 1s to 3d electric quadrupole transitions and

dipole transitions to 4p orbitals hybridized with the 3d band [193] and it is weak for metal sites having regular octahedral symmetry for which the p-d hybridization is forbidden [193, 194]. The intensity of this feature in ZFO-C is weak as expected for Fe in octahedral sites and remains almost constant upon lithiation up to 2 Li^+ per formula unit, revealing that Fe coordination symmetry does not change during the initial lithiation process, in agreement with previous reports [195, 196].

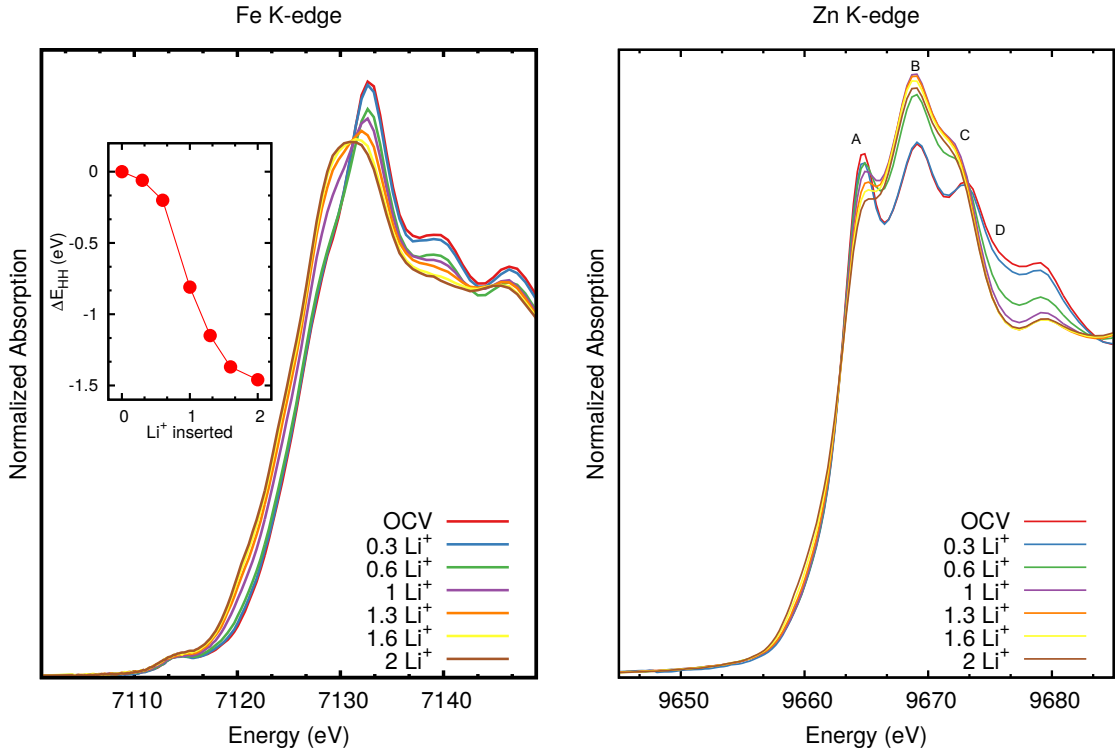

Figure 4.10: Normalized near edge XAS spectra for Fe (left) and Zn (right) K-edges during the first lithiation. The inset shows the edge shift $E_{HH} - E_{HH}^{OCV}$ as a function of the Li^+ inserted (the edge position has been chosen as the energy at half-height of the normalized edge step).

Zn K-edge spectra from 0 to 2 Li^+ per formula unit maintain the same energy edge (calculated as the maximum of the derivative) at 9663 eV, suggesting that at this stage zinc is not reduced. Nevertheless, a dramatic change in the XANES shape occurs. It is possible to identify three main peak features (labelled as A, B, and C) in the near edge spectra. feature A at 9665 eV, B at 9669 eV and feature C at 9673 eV, plus additional structure at higher energies.

As the lithium uptake increases feature A weakens, B becomes predominant over

all the others, and C slightly shifts to lower energies ($\Delta E \sim -1$ eV). Also the shoulder D at 9677 eV decreases as Li^+ increases. These changes in Zn K-edge XANES shape have been reported to be linked to a displacement of zinc towards sites with octahedral symmetry [181, 197]. According to the evolution of the XANES along the discharge (shown in Figure 4.10) such migration occurs already between 0.3 and 0.6 Li^+ in agreement with previous reports.

EXAFS Analysis of the Initial Lithiation Phase

The extended X-ray absorption fine structure (EXAFS) region of the spectra was analysed using the GNXAS [142, 143] package.

XAS two-body signals $\gamma^{(2)}$ associated with peaks of the two-body distribution function $g_2(r)$ describing the structure in the neighbourhood of the photoabsorbing atoms (Zn or Fe) were calculated ab-initio for a reference crystal structure of spinel zinc ferrite as suggested by XRD measurements [181] (Figure 4.11). The model included signals related with the photoabsorber first neighbours in the range $1.90 - 3.7$ Å: for the Zn K-edge, each Zn has 4 neighbouring oxygen at 1.996 Å, 12 iron at 3.5 Å, 12 oxygen neighbours at 3.534 Å, and 4 zinc atoms at 3.656 Å; while for the Fe K-edge, Fe has 6 oxygen neighbours at 2.018 Å, 6 iron at 2.985 Å, and 6 zinc neighbours at 3.5 Å(Table 4.3).

Table 4.3: The two model structures considered for ZFO-C.

Normal $ZnFe_2O_4$					
Fe neighbours			Zn neighbours		
Atom	R (Å)	N (Atoms)	Atom	R (Å)	N (Atoms)
Fe-O	2.018	6	Zn-O	1.996	4
Fe-Fe	2.985	6	Zn-Fe	3.5	12
Fe-Zn	3.5	6	Zn-O	3.533	12
			Zn-Zn	3.656	4
$ZnFe_2O_4$ with all Zn migrated in 16c sites					
Fe neighbours			Zn neighbours		
Atom	R (Å)	N (Atoms)	Atom	R (Å)	N (Atoms)
Fe-O	2.018	6	Zn-O	2.021	6
Fe-Fe	2.985	6	Zn-Fe	2.985	6
Fe-Zn	2.95	6	Zn-Zn	2.985	6

The structural refinement has been performed without prior EXAFS signal extraction by minimizing the difference between the raw experimental spectra and a model

curve including both the structural oscillations and a suitable background function. Variations of the structural parameters with respect to the initial model structure and disorder (both thermal and structural) have been accounted for by evaluating the configurational average of each structural signal over distance distribution functions (Gaussian), whose parameters (average distance and variance) were refined during the fitting procedure. The coordination numbers were kept fixed.

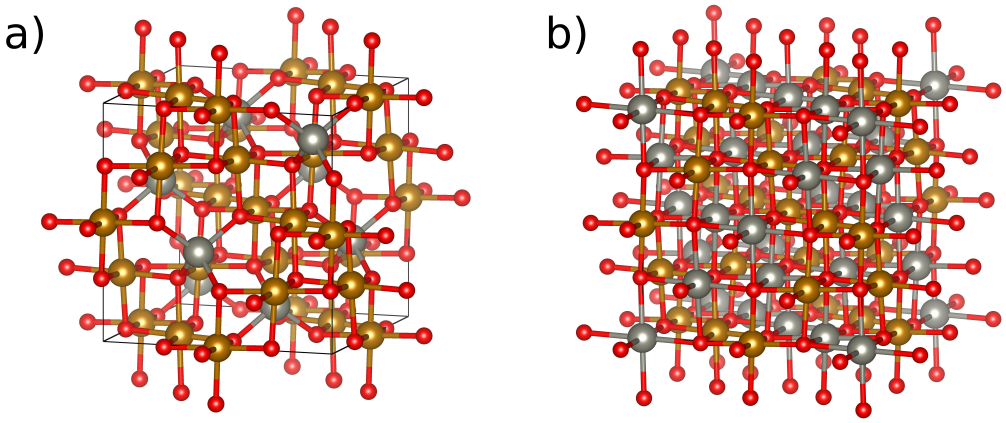

Figure 4.11: The two modelled structures. Red = oxygen atoms, gold = iron atoms, gray = zinc atoms. Model a) represents the normal spinel structure, with Fe in 16*d* octahedral sites, Zn in 8*a* tetrahedral sites. Model b) represents the same structure where all zinc atoms left the initial 8*a* sites and occupy all the vacant 16*c* octahedral sites. Both modelled structures share the same cell parameters and symmetry group. Drawings produced with Vesta [198].

The amplitude reduction factor S_0^2 was found to be 0.70 and 0.75 for the OCV at Fe and Zn edges respectively. The same values were used for fitting all spectra. The difference E0-EE between the zero of the energy scale of the theoretical model spectrum and the edge inflection point of the experimental spectrum was also found for the OCV and kept fixed for fitting all the other spectra. In Fig. 4.12 we show the Fourier transform of the $k^2\chi(k)$ EXAFS signals (open circles) and the best fit (solid curves) obtained.

The refined distances found for the material when the cell is at OCV (Table 4.4) are in good agreement with those reported in previous studies on spinel ferrite: Zn−O at 1.96(2) Å and 3.58(3) Å, Zn−Fe at 3.54(3) Å and Zn−Zn at 3.68(3) Å result from Zn K-edge signal best fit; and Fe−O at 2.00(2) Å Fe−Fe at 3.01(3) Å, and Fe−Zn at 3.53(3) Å from Fe K-edge signal.

It has been reported in the literature that nanosized spinel zinc ferrite exhibits some degree of inversion (e.g. Ref [181] and refs therein). A broader main Zn K-edge peak

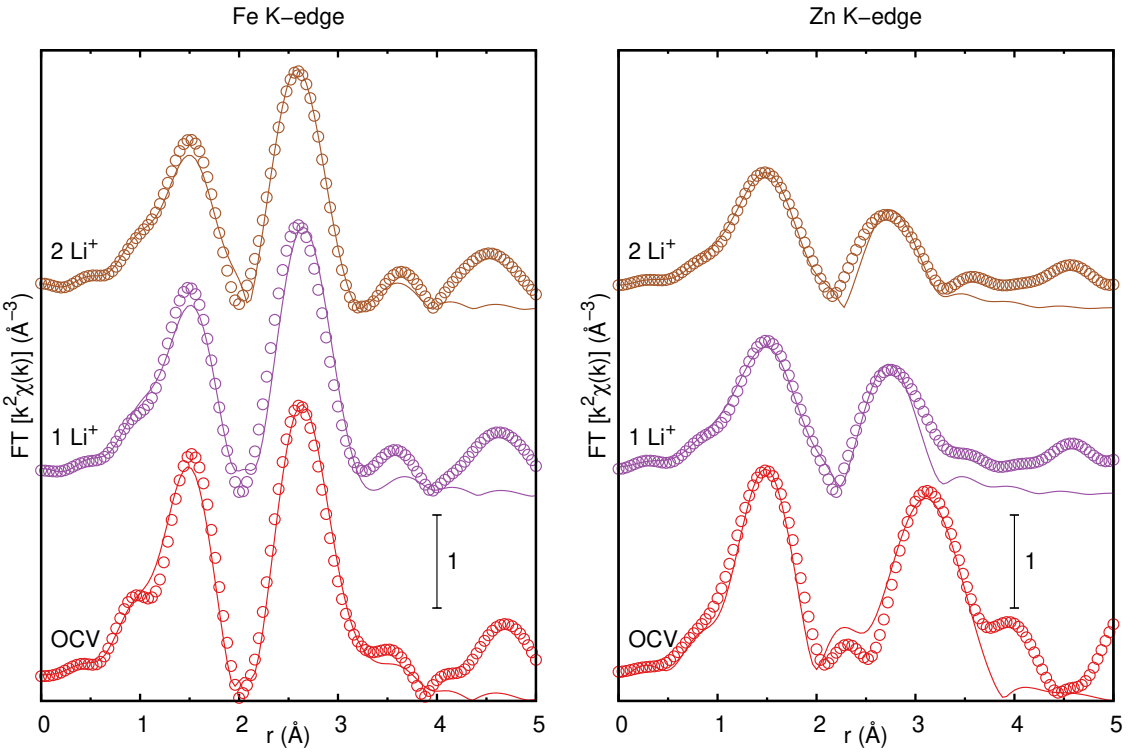

Figure 4.12: Fourier Transform of experimental EXAFS signal (open circles) and corresponding best-fit (solid line) for both the Fe and Zn K-edge (left and right respectively) at different lithiation stages from OCV (bottom) to 2 Li^+ per formula unit (top - 222 mAh/g and 0.75 V).

Table 4.4: EXAFS best fit result for the cell at its OCV state (normal spinel model).

ZFO-C OCV							
Fe K-edge				Zn K-edge			
Atom	R (Å)	N (Atoms)	σ^2 (Å^2)	Atom	R (Å)	N (Atoms)	σ^2 (Å^2)
Fe-O	1.99(2)	6	0.006	Zn-O	1.96(2)	4	0.003
Fe-Fe	3.01(3)	6	0.005	Zn-Fe	3.54(4)	12	0.01
Fe-Zn	3.53(4)	6	0.011	Zn-O	3.58(4)	12	0.03
				Zn-Zn	3.68(4)	4	0.008

has been reported [195] probably resulting from a high degree of cationic exchange in pristine spinel $ZnFe_2O_4$ due to different sample morphology. The present XANES and EXAFS results show that the experimental signal can be satisfactorily reproduced with a normal spinel structure. Nonetheless a minor spinel inversion (below 20%) cannot be completely ruled out by the EXAFS analysis and a more detailed investigation of the XANES features is being performed (submitted paper by Rezvani *et al.*) in order to estimate quantitatively the cation distribution within the tetrahedral and octahedral sites of the oxygen lattice.

Results of the best-fit indicate a slight elongation in the first Fe−O shell distance from 1.99(2)Å (OCV) to 2.03(2)Å ($1Li^+$) and finally to 2.06(2)Å ($2Li^+$), which is compatible with an initial reduction of Fe^{3+} to Fe^{2+}. Best fit of Fe−Zn shell at 2 Li^+ per formula unit shows a distance of 2.97(3) Å, which is in good agreement with the theoretical distance Fe_{16d}−Zn_{16c}= 2.985 Å, as expected when all Zn^{2+} has migrated into the 16c octahedral sites and the Fe-Zn distances merge into a single shell with the Fe/Fe ones.

Table 4.5: EXAFS Fe K-edge best fit result for the cell at ($1Li^+$) per formula unit inserted (normal spinel model).

ZFO-C $1Li^+$			
Fe K-edge			
Atom	R (Å)	N (Atoms)	σ^2 (Å^2)
Fe-O	2.03(2)	6	0.009
Fe-Fe	3.04(3)	6	0.006
Fe-Zn	3.53(4)	6	0.019

Table 4.6: EXAFS Fe K-edge best fit result for the cell at ($2Li^+$) per formula unit inserted (migrated zinc model).

ZFO-C $2Li^+$			
Fe K-edge			
Atom	R (Å)	N (Atoms)	σ^2 (Å^2)
Fe-O	2.06(2)	6	0.011
Fe-Fe	3.10(3)	6	0.013
Fe-Zn	2.97(4)	6	0.007

For the Zn K-edge, the Zn local environment is clearly modified upon Li insertion: the second peak of the Fourier transform related with the Zn-Fe/Zn coordination shell shows a clear shift from 3.14 Å to 2.7 Å (phase shift is not considered) already at 1 Li^+

per formula unit. From the best-fit, we obtained a Zn−Fe and Zn−Zn distance equal to 3.07(3) Å, at 1 Li^+ (Table 4.7), while at 2 Li^+ per formula unit the obtained distances are 3.08(3) Å and 3.13(3) Å for Zn−Fe and Zn−Zn respectively (Table 4.8). These values are in satisfactorily agreement with the expected distance Zn_{16c}−Fe_{16d}/Zn_{16c} = 2.99 Å and indicate the Zn migration into (16c) sites as previously reported [196].

The EXAFS signal at both edges gradually damps upon lithiation, possibly due to an increase of the structural disorder (variance of the first metal-oxygen shells increases from 0.006(1) $Å^2$ to 0.011(2) $Å^2$ upon lithiation).

Table 4.7: EXAFS Zn K-edge best fit result for the cell at ($1Li^+$) per formula unit inserted (migrated zinc model).

ZFO-C $1Li^+$			
Zn K-edge			
Atom	R (Å)	N (Atoms)	σ^2 ($Å^2$)
Zn-O	2.01(2)	6	0.015
Zn-Fe	3.07(3)	6	0.013
Zn-Zn	3.07(3)	6	0.013

Table 4.8: EXAFS Zn K-edge best fit result for the cell at ($2Li^+$) per formula unit inserted (migrated zinc model).

ZFO-C $2Li^+$			
Zn K-edge			
Atom	R (Å)	N (Atoms)	σ^2 ($Å^2$)
Zn-O	1.99(2)	6	0.012
Zn-Fe	3.08(3)	6	0.02
Zn-Zn	3.13(3)	6	0.02

4.6.4 Full Lithiated Phase

The EXAFS signal related to the full lithiated electrodes for both edges has been extracted and analysed. At this stage, both samples present the characteristic single peak of the metallic phase of both zinc and iron, even if the intensity of the EXAFS signal is strongly damped if compared to the EXAFS signal of the respective metallic standard references. This is compatible with the small size of the metallic particles formed in the active material, and of the possible crystalline defects present in the structure.

The two EXAFS signals and the related Fourier transform are shown in Figure 4.14. The best fit refinements on these two spectra have been performed starting from the known metallic structure model of the two, leaving the coordination number as a free parameter.

In order to perform the EXAFS structural refinement of the Fe K-edge, since from the XANES spectrum we expect to have a fully metallized iron, we started building a model with the typical BCC crystalline structure and the related inter-atomic distances. In fact, a qualitative analysis of the EXAFS signal shows similar inter-atomic distances to such structure (Figure 4.13). It also shows a dramatic lowering in the intensity of the EXAFS oscillations: this behaviour is directly correlated with the decrease of the particle size and to the presence of microstructural defects and vacancies in the formed iron nano-crystallites [199]. The best-fit of Fe K-edge of the fully lithiated spectrum involved the first two atomic shells (in the model: Fe-Fe_{shell1} at 2.485Å, with $CN = 8$ and Fe-Fe_{shell2} at 2.870Å, with $CN = 6$), setting the two coordination numbers as independent fit parameter. Fit result show compatible distances with the model: Fe-Fe_{shell1} at 2.43(2)Å, with $CN = 3.09$ and Fe-Fe_{shell2} at 2.87(3)Å, with $CN = 0.64$ (Table 4.9).

For the EXAFS fit of the fully lithiated cell at Zn K-edge, the initial reference structural model used was for metallic zinc structure, where we considered a theoretical first shell of $Zn{-}Zn_{model}$ with coordination number $N = 6$ and inter-atomic distance 2.60 Å. To this was successively added also a second 2-body signal related with the pair Li−Zn. We imposed R_{Zn-Zn} and R_{Zn-Li} to be the same inter-atomic distance, while the relative coordination numbers were kept free. The amplitude reduction factor S_0^2 was kept fixed at the value found after fitting the Zn metal standard. Results of the fit are listed in Table 4.10 and showed in Figure 4.14. They show slightly shorter inter-atomic distances with respect to the metallic zinc phase. Furthermore, it is evident the contribution of the EXAFS signal of the Li-Zn pair which is not negligible and confirms the reversible alloying process between lithium and zinc at the end of the reduction reaction of the ZFO-C anode.

Table 4.9: EXAFS Fe K-edge best fit result for the full lithiated cell.

ZFO-C Full lithiated cell			
Fe K-edge			
Atom	R (Å)	N (Atoms)	σ^2 (Å^2)
Fe-Fe (1st shell)	2.43(2)	3.09	0.0054
Fe-Fe (2nd shell)	2.87(3)	0.64	0.0054

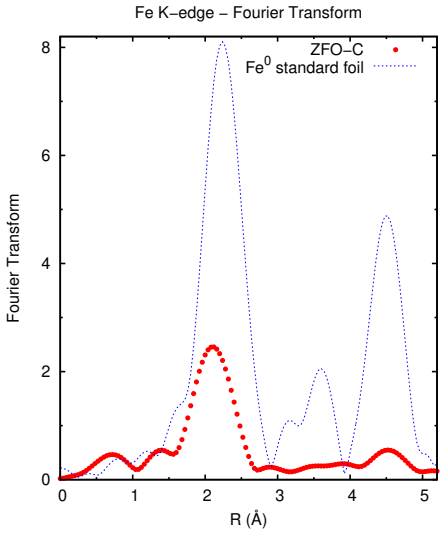

Figure 4.13: Comparison of the Fourier transforms of the fully lithiated cell Fe K-edge spectrum (red dots) and the spectrum of a reference BCC iron standard foil. The two samples present similar shell distances, while the intensity of the EXAFS signal is remarkably damped in the ZFO-C cell spectrum if compared with the standard iron foil.

Table 4.10: EXAFS Zn K-edge best fit result for the full lithiated cell.

ZFO-C Full lithiated cell			
Zn K-edge			
Atom	R (Å)	N (Atoms)	σ^2 (Å^2)
Zn-Zn	2.53(3)	6.07	0.016
Zn-Li	2.53(3)	2.78	0.009

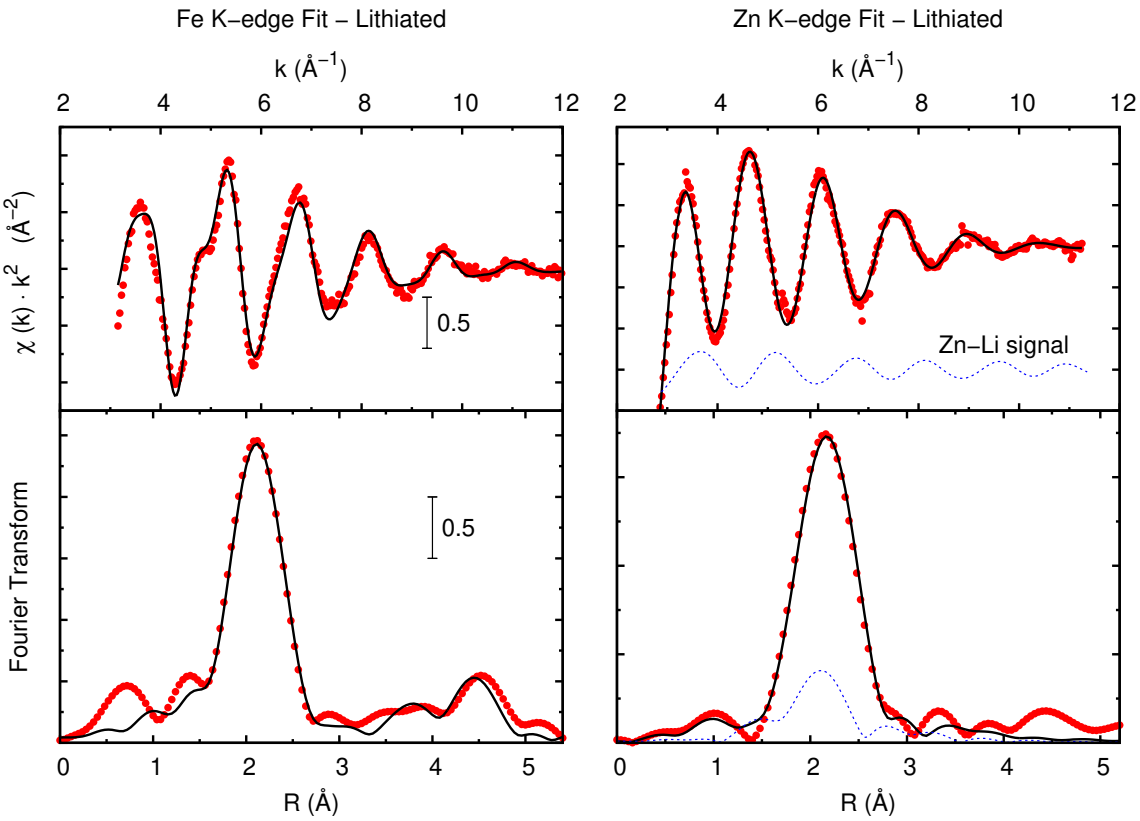

Figure 4.14: EXAFS fit for the full lithiated cell at Fe and Zn K-edges. In red dots are reported the experimental EXAFS signals and the relative Fourier transforms (top and bottom respectively). The corresponding best-fit of the EXAFS signals are reported with the black solid line. Blue dashed line represents the contribution of Zn-Li signal in the fit.

Chapter 5

Formation and Evolution of the Interface in Graphite Anodes

In this Chapter, we present a series of experiments aimed to investigate the superficial composition and evolution of graphite-based anodes used for lithium-ion batteries while employing a "non-conventional electrolyte" ($LiAsF_6$). This electrolyte was very popular at the early stages of LIBs diffusion, but nowadays is no more employed due to its intrinsic toxicity and safety hazardousness. Part of this research work has been performed in collaboration with CIC energigune in the Basque Country (Spain), in particular, there have been conducted all the XPS measurements.

We also present an attempt of investigating the evolution of the SEI using the in-situ Raman scattering technique, for which specific advances of the experimental set-up have been carried out at the University of Camerino. The experiment presented show the potential of this technique for understanding the evolution of graphite electrodes for different lithium content.

5.1 Aim of this Research

In previous works of our research group [70,124], we tried to investigate the formation and the evolution of the solid electrolyte interface (SEI) layer forming onto the surface by means of X-ray absorption spectroscopy. The strategy was to use arsenic atoms as a local probe of the SEI. In fact, by using a particular electrolyte containing arsenic, then washing the electrodes with proper solvents, and finally grinding them, it was possible to follow the evolution of the oxidation state of As during the various phases of the first galvanostatic cycle of lithiation and de-lithiation.

In this thesis, we present a follow-up of these experiments, where the same set of samples have been reproduced, aimed to probe the same kind of electrodes with surface-sensitive techniques, in particular, X-ray photoelectron spectroscopy and Raman spectroscopy.

5.2 Experimental

5.2.1 Samples Preparation

Electrolyte

A mixture of two types of electrolytes has been chosen: $LiPF_6$ 0.5 M + $LiAsF_6$ 0.5 M in EC:DMC 1 : 1 V/V, such that it is possible to investigate the physical and chemical characteristics of arsenic close neighbours measuring XAS at the As K-edge.

It is possible to assume that the two chemical species (phosphorus and arsenic) have similar electrochemical properties, such that the behaviour of batteries utilizing this mixture is very similar to commercial batteries where only $LiPF_6$ salts are used; this is also demonstrated by electrochemical tests performed on both types of cells [70].

Graphite Electrode vs. Li Half-Cells

Graphite electrodes were prepared using Sodium-Carboxymethylcellulose (Na-CMC, Walocel CRT 2000) dissolved in deionized water and left under magnetic stirring overnight. Graphite, Super C65 and the Na-CMC solution were mixed in an Electric Helical Blade Mixer at 2000 rpm for 3 hours under vacuum in a proportion of 92 : 3 : 5 (mass ratio). The resulting slurry was then cast using a battery-line on 10 μm thick copper foil applying the *"Doctor Blade"* technique, with a wet film thickness of 165 μm. The slurry was immediately dried blowing a 80°C air stream inside the battery line.

Circular electrodes with a diameter of 9 mm and a surface area of 0.636 cm^2 have been cut and dried overnight at 120°C under vacuum. The capacity of the electrodes has been calculated considering a specific theoretical capacity of 372 mAh/g.

Electrochemical measurements have been carried out using three-electrodes T cells (*Swagelok*), setting the graphite electrode as working electrode and metallic lithium as counter and reference electrodes. A glass fiber (*Whatman GF/A*) has been used as separator and a solution of $LiPF_6$ 0.5M / $LiAsF_6$ 0.5M in EC:DMC 1 : 1 V/V has been used as electrolyte. All cells have been assembled in a glove-box filled with Ar. The different electrochemical cells have been set to reach and maintain specific values

of charge and potential (*cfr.* Figure 5.1) in order to prepare ex-situ samples at different stages of lithiation.

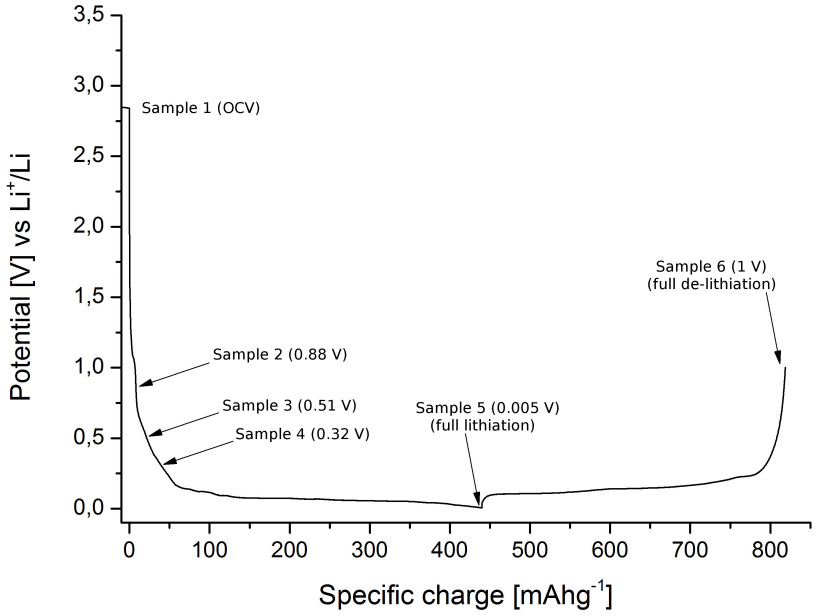

Figure 5.1: Potential curve for the first cycle and list of the graphite anode samples.

5.3 Results from Previous XAS Analysis

For XAS measurements of refs. [70, 124], graphite electrodes were cycled with a galvanostatic intermittent titration technique (GITT) ad different number of discharge steps (different final voltages) corresponding to significant phases of the SEI formation (showed in Figure 5.1). The cycled cells have been, then, disassembled in an Ar-filled glovebox, and the electrodes extracted and then soaked and washed in a solvent mixture (EC:DMC) and finally dried. The electrode material has been then scraped from the copper current collector, and the obtained powder pressed into pellets by adding CMC cellulose as filler. XAS measurements were taken at ESRF on beam-line LISA [200] in fluorescence mode.

5.3.1 XANES Analysis

XANES spectra of graphite electrodes (Figure 5.2 right) showed a significant evolution and modification of the shape and peak distribution across the different charge states of the electrodes. These changes have been associated with the mixed

presence of several valence states of As, in addition to the state As^{5+} which is dominant into the electrolyte salt. The other peaks can be identified to be As^{3+} and As^{2+}, as reported in Fig. 5.2, with a comparison with known XANES references of arsenic in different oxidation states [201–203].

This evolution of the XANES peaks can be explained considering the chemical reactions suggested for the reduction reaction of the electrolyte salt ($LiAsF_6$) in LIB as follow:

$$LiAsF_6 + 2\,Li^+ + 2\,e^- \longrightarrow {}_3LiF\downarrow + AsF_3 \tag{5.1}$$

$$AsF_3 + 2\,xLi^+ + 2\,xe^- \longrightarrow xLiF\downarrow + Li_xAsF_{3-x} \tag{5.2}$$

Equations above acknowledge the chemical reaction leading to two building blocks (LiF and $LiAsF_x$) of the inorganic SEI components, previously observed in Li-ion batteries [69, 204].

The XANES spectra show an evolution of the electrolyte salt ($LiAsF_6$) compatible with the reactions described in Eqs. 5.1 and 5.2 within the initial charging steps. This observation confirms the rapid onset in the formation of the SEI. By increasing the charging steps the reactions proceed to further reductions of As-F and formation of LiF and $LiAsF_x$ in the SEI structure. This is thus compatible with the formation of $LiAs_{3\text{-}x}$ phase (eq. 5.2) in which the higher the value of x, the higher the LiF concentration.

In the graphite electrodes, up to the lithiation state of sample 3 the conversion of electrolyte to form LiF (following eq. 5.2) is clearly visible by the appearance of a strong As^{2+} ($LiAsF_{3\text{-}x}$) peak. The reaction proceeds to reach a relative maximum of $LiAsF_{3\text{-}x}$ phase observed in sample 4 ($E = 0.32$ V, $Q = 20\ mAhg^{-1}$) in graphite electrode (see Fig. 5.2b) that corresponds to a high amount of reduced electrolyte, hence a relatively saturated SEI formation [70].

XRF measurements of the same samples show an increase in the intensity of As-related fluorescence signal as the electrode charge proceeds (Figure 5.2 left). This shows a clear trend linking the charge state to the As quantity present on the electrode surface (thus the increase in the number of compounds related to the SEI). Furthermore, the intensity of the As fluorescence signal can be used to estimate the amount of As atoms embedded in the SEI of the electrodes, considering that the total counting rate is proportional to the number of excited As atoms for a given photon flux, acquisition time and amount of active material for unit surface.

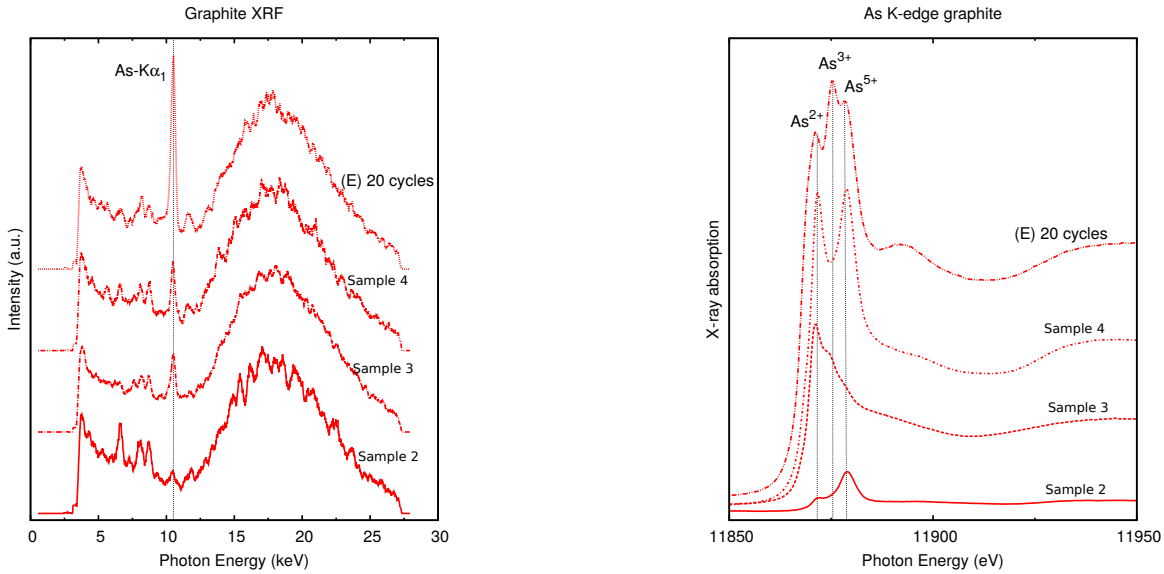

Figure 5.2: X-ray fluorescence spectra of graphite (left). XANES spectra of the graphite electrodes for different charging levels (right). The signal-intensity increase is associated with a corresponding increase of the SEI thickness. Three components in the XANES spectra, assigned to As^{5+}, As^{3+} and As^{2+}, are clearly observable [70].

Linear Combination Fit of As Species from XAS Results

A linear combination fitting (LCF) has been performed on the XANES spectra in order to evaluate the weight of each component. The LCF analysis was carried out using three reference spectra for As^{5+} ($LiAsF_6$), As^{2+} (As_2O_3) and As^{2+} (AsS), with typical peak energies of 11874.8 eV, 11871.6 eV and 11867.5 eV respectively [202, 205].

Results of LCF are reported in Tab.5.1, the trend of each component is in agreement with the type of redox reactions of equation 5.1, 5.2. In particular, the changes in As valence states indicate a possible re-oxidation process as an effect of electrode cycling.

Table 5.1: Distribution of As valence states following the SEI evolution, determined by LCF of the XANES.

Sample	Capacity ($mAhg^{-1}$)	As^{5+}	As^{3+}	As^{2+}
C Sample 2	16	0.70 ± 0.03	0.03 ± 0.04	0.27 ± 0.07
C Sample 3	31	0.01 ± 0.02	0.11 ± 0.05	0.88 ± 0.04
C Sample 4	46	0.17 ± 0.02	0.13 ± 0.05	0.70 ± 0.05
C 20cycles	–	0.10 ± 0.01	0.34 ± 0.02	0.56 ± 0.02

5.3.2 EXAFS Analysis

EXAFS analysis [124] has been performed on the electrodes to study the evolution of the local structure around As atoms of the SEI. The structural refinement was applied to EXAFS spectra of both graphite and ZFO-C electrodes at different charge states along with the $LiAsF_6$ electrolyte reference.

Results show that the main contribution to the EXAFS spectra is always given by the closest first neighbour distribution. The simulation was first carried on the $LiAsF_6$ electrolyte solution measured in transmission mode. For that case, excellent EXAFS data fitting has been obtained using a single first-shell As-F contribution within a simple Gaussian approximation. Fit results for the solutions are: distance of the first shell R= 1.727 Å and relative displacement $\sigma^2 = 0.002$ Å^2. The first neighbor As-F distance R is in excellent agreement with the molecular bond length range ($1.6 \div 1.7$ Å) reported in literature for AsF_6 [206].

The following analysis on the SEI local structure was carried out fixing S_0^2 to the one of the references (electrolyte) and finding the best fit refinement for R, σ^2 and N_{As-F} which is forced into the range $0 \leq N_{As-F} \leq 6$.

Table 5.2: Structural parameters obtained by EXAFS data analysis. Average coordination number N, distance R and mean-square relative displacement σ^2 of the As-F first neighbor shell are listed in the table.

Sample	Capacity ($mAhg^{-1}$)	N	R(Å)	σ^2(Å^2)
C Sample 2	16	4.0 ± 0.4	1.73 ± 0.03	0.002
C Sample 3	31	2.2 ± 0.2	1.74 ± 0.03	0.002
C Sample 4	46	2.7 ± 0.2	1.74 ± 0.03	0.002

For graphite electrodes, it has been observed a well-defined trend for the average coordination number N_{As-F} measured by EXAFS, as reported on Tab.5.2. The results can be assigned to a mixture of $LiAsF_6$ with other As-F phases produced by the reaction described in Eqs. 5.1, 5.2. Considering also the XANES result it is evident the presence of AsF_3 / $LiAsF_{3-x}$. In samples with higher capacities, the coordination number N_{As-F} reaches a minimum that corresponds to a maximum level of reduction (a majority of AsF_{3-x} phase). The small increase of bond length R is also in agreement with the change of oxidation state, which is also observed on As-O molecular bonds [205]. The bond length reported is associated with fragments AsF_N with different coordination N, embedded in the SEI, and represents an average As-F distance. Since several AsF_N complexes are present in each sample, it is reasonable that the average R is substantially

unchanged in all samples within the estimated uncertainty [70, 124].

After 20 cycles of charge/discharge, on the EXAFS spectra it shows a new structural signal corresponding to a second coordination shell. This second shell of neighbours can be reproduced in the simulation introducing a signal from As atoms. Excellent structural refinement has been obtained by adding As atoms at a distance R $\sim$ 2.48 Å, resulting in a best-fit coordination numbers of $N_{As-F} \sim 2$ and $N_{As-As} \sim 0.8$. The presence of *As* atoms as second neighbours is compatible with a re-oxidation process of the species forming the SEI. However, due to the similar backscattering properties and average bonding distances for *F* and *O* atoms, it is not possible to quantify the presence of oxygen [70, 124].

5.4 XPS Analysis

The SEI layer formation and evolution have been investigated by C1s, F1s, Li1s and As3d XPS and by As LMM Auger for different charging state of the graphite electrodes, during lithium insertion and de-insertion. A conventional XPS compositional analysis and an analysis of the Auger parameters has been carried out for all the samples that have been reproduced in the most identical way at CIC energigune laboratories. The graphite electrodes, prepared as described above (*cfr.* Section 5.2.1), were cycled at C/10 rate and stopped at the required potential (*cfr.* Figure 5.1). The cycled cells were, then, disassembled in an Ar-filled glovebox. The cycled electrodes were washed and rinsed in a solvent solution (EC:DMC) in order to remove residues from the electrolyte. The washed electrodes finally were inserted into the XPS vacuum chamber using an air-tight transfer system, never exposing them to the external atmosphere. Such electrodes were analysed by means of XPS with Mg Kα (1253.6 eV) and Al Kα (1487 eV) non-monochromatic sources.

Nevertheless it is important to keep in mind that the surface composition of the samples is not uniform: in fact there may be present inhomogeneities coming from non-conducting micro-domains and residual of the electrolyte salt, furthermore increasing the amount of lithium inserted in the graphite layers will result in a lower conductivity of the material: therefore charging effects will take place. Thus there may be a slight difference from literature data in the absolute binding energies. However a calibration procedure has been performed aligning selected peaks to known values, furthermore, the position of the As3d peaks has been identified after calculation the corresponding Auger parameter [207] which involves both photoelectron and Auger line energies. In

fact, the use of Auger parameter provides abundant information of the chemical state without the need of evaluating charge correction and work function measurements.

5.4.1 Calibration of XPS Spectra and Determination of the Auger Parameter

As mentioned above, conventional XPS analysis on charged electrodes may be affected by charge effects and peak overlap, thus it may be not sufficient to give a complete overlook onto the SEI layer formation. For this reason, the study of the Auger parameter and a precise energy calibration are crucial.

The energy calibration for all the samples has been made by taking into account the position of F1s XPS peak. In fact, the formation of the compound LiF onto the surface of the electrode is observed in all the samples as soon as the electrolyte is brought in contact with the graphite. This phenomenon is present even in the OCV sample, in this case, there is the passive formation of LiF compounds even without applying an external potential to the cell, resulting in a minimal, but not negligible, electrolyte degradation. On the other hand, the formation of this compound is well known in literature [208, 209], and is one of the main components of the SEI, forming a very resistive layer [210,211]. All the XPS spectra presented have been calibrated considering the position of the F1s peak attributed to LiF formation (confirmed also with the Auger parameter), setting the binding energy to 684.9 eV reported in literature [212]. Thus, including also the study of the Auger parameter ($\alpha + h\nu$) is fundamental to gain precise information related to the SEI composition and facilitating the identification of XPS components.

In this study, the Auger parameter (Eq. 5.3) will be determined for the As photoemission line. It will take into account the energy shift between the arsenic 3d photoemission line components and the As LMM Auger line.

$$\alpha' = \alpha + h\nu = E_K(\text{As LMM}) + E_B(\text{As 3d}) \tag{5.3}$$

In equation 5.3 $\alpha' = \alpha + h\nu$ is called the modified Auger parameter and depends on the X-ray source photon energy ($h\nu$), E_K(As LMM) is the kinetic energy of the As LMM Auger electrons, and E_B(As 3d) is the binding energy of the As 3d photoelectrons.

Thus to determine the value of the Auger parameter, one must first determine exactly the positions of the As 3d and As LMM peaks. To do so the experimental data were fitted using the *CasaXPS* software suite [213].

5.4.2 Analysis of Carbon 1s Lines

The XPS C 1s emission line (presented in Figure 5.3) provides information regarding the electrode material (since its active material is graphitic carbon), the electrolyte decomposition residuals (that were not washed away from electrode), and also about the stability and homogeneity of the composition of the SEI layer onto the surface. Furthermore, it is possible to determine a possible fracture/rupture of the SEI layer or inhomogeneities of its surface. The determination of C-based compounds in the different electrodes have been done considering the results found in previous XPS studies of carbon-based materials [214–217]. Results of C 1s XPS data analysis peak fit are reported in Table 5.3.

One of the components reported in Figure refFig:XPSC1s, which is dominant in samples 1, 2 and 3, and positioned at 284.4 eV is assigned to graphite compounds which is the main component of the electrode material. Graphite XPS peak, which is expected to be present only on the anode active material, is related to the fact that the surface of the electrode is yet not completely covered by the SEI layer. This peak completely disappears in sample 5, at fully lithiated state, meaning that this sample shows a uniform and compact layer of SEI thicker than the probing depth of XPS, in agreement with the expected SEI thickness reported in refs. [70, 113, 124] for the same electrolyte mixture. However, upon lithium de-insertion, the graphite XPS component is visible again in sample 6 (at one complete discharge and charge cycle). This may be explained by the fact that the completed SEI layer, in this sample, loses the outermost layer composed principally of organic components (as will be explained in Subsection 5.4.3). Another possible reason is that the SEI layer, in sample 6, might be less uniform or thinned (with respect to the previous fully lithiated state), indicating a possible rupture or cracking in the SEI layer and the consequent exposure of the anode surface.

A detectable asymmetry towards low binding energies (at $\sim$ 282 eV) is also detectable in sample 6. This can be assigned to the presence of molecules with Li-C bonds [218–221], probably deriving from the degradation of the organic solvents present in the electrolyte and that are embedded in the SEI.

Components at higher binding energies than the C−C graphitic peak are observed in all the samples. Those have been assigned to C−H, C−O, C−O_2 and C−O_3 bonds, respectively at binding energies 285.6, 286.7, 287.7, 289.6 eV. Small differences with the tabulated values may derive from the various surface charging effects. These carbon-containing species are not present in the electrode active material and have an organic origin coming from the degradation of the solvents (EC:DMC) in the

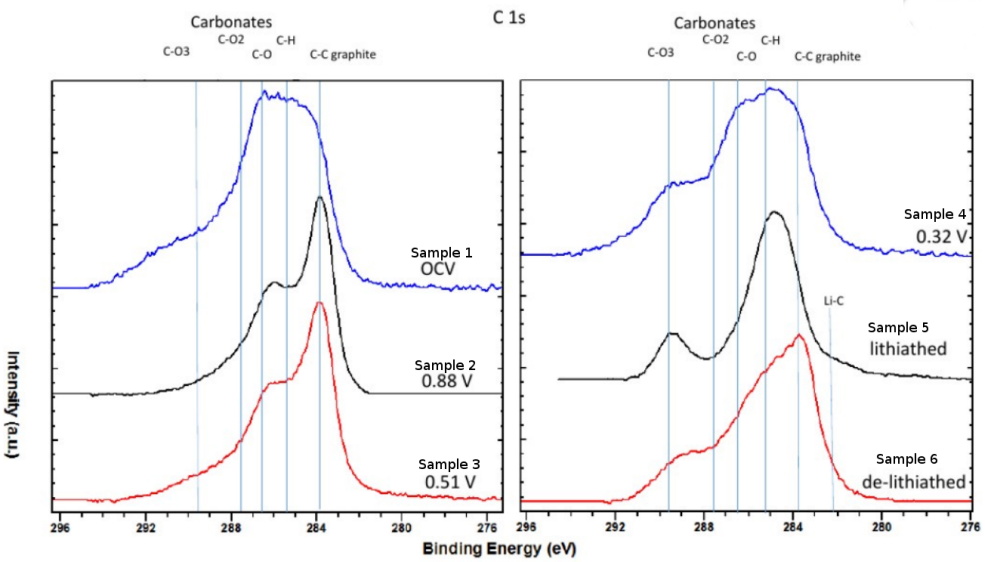

Figure 5.3: C 1s XPS photoelectron spectra of graphite electrodes at different stages of charge and voltage as in indicated in Figure 5.1.

electrolyte [214–217]. Those organic species become solid and precipitate onto the electrode surface forming the organic fraction of the SEI.

Those organic components belong to the family of lithium alkyl carbonates $ROCO_2Li$ and result from the reductive decomposition of dialkyl carbonates which are the organic solvents used in the electrolyte. They play a crucial role in the formation of the surface layers at the electrode/electrolyte interface. The most common reduction mechanisms of EC and DMC lead to the formation of Li methyl carbonate ($MeOCO_2Li$), Li ethyl carbonate ($EtOCO_2{-}Li$), Li propyl carbonate ($PrOCO_2Li$), Li ethylene dicarbonate ($-CH_2OCO_2Li)_2$, Li propylene dicarbonate ($LiO_2CO{-}CH{-}(CH_3)CH_2{-}OCO_2Li$), and ($Li_2CO_3$) as shown in Figure 5.4 [112, 222].

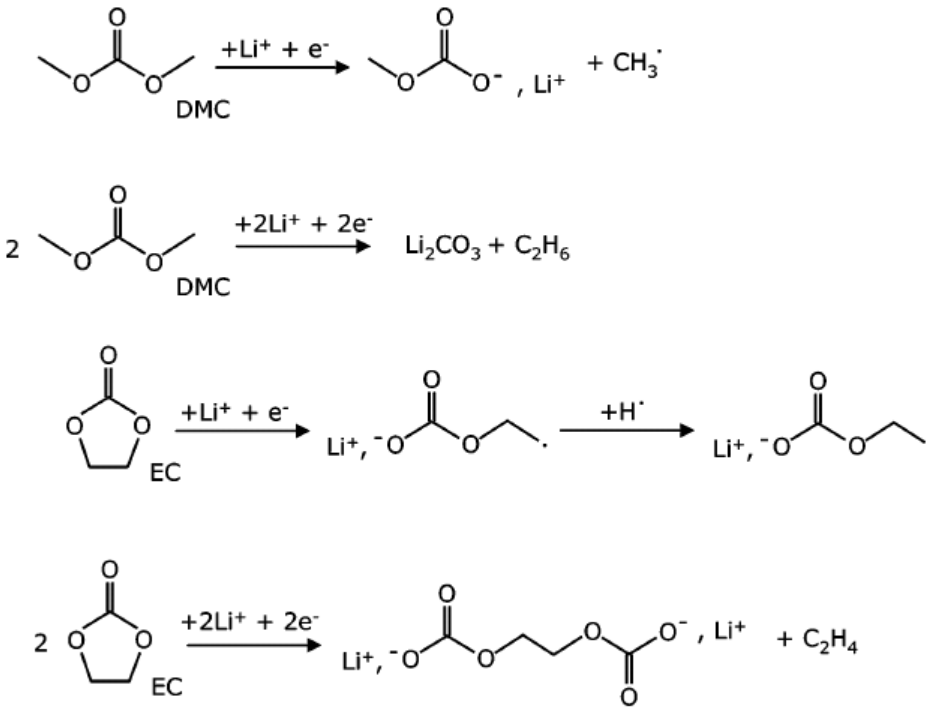

Figure 5.4: Proposed mechanisms of organic solvents reduction leading to the formation of Li alkyl carbonates [222].

Table 5.3: Best fit result of the areas, positions and atomic concentrations of the various component XPS peaks in C 1s and for the various samples 1-6.

Sample	Component	BE (eV)	Area/(RSF*T*MFP)	% Concentration
OCV (Sample 1)	Graphite C-C	284.4	2502.37	49.38
	C-O	286.67	560.822	11.07
	C-O3	290.82	725.108	14.31
	C-H	285.62	206.26	4.07
	C-O2	287.68	1073.31	21.18
0.88V (Sample 2)	Graphite C-C	283.78	3875.17	56.57
	C-O	286.23	1453.42	21.22
	C-O3	289.22	355.13	5.18
	C-H	285.38	348.747	5.09
	C-O2	287.52	818.322	11.94
0.51V (Sample 3)	Graphite C-C	283.86	3521.78	59.72
	C-O	286.35	905.842	15.36
	C-O3	289.68	511.413	8.67
	C-H	285.52	189.802	3.22
	C-O2	287.56	767.832	13.02
0.32V (Sample 4)	Graphite C-C	284.2	2624.48	51.71
	C-O	286.7	573.254	11.29
	C-O3	290.16	268.475	5.29
	C-H	285.71	596.981	11.76
	C-O2	289.11	1012.28	19.94
0.0V (Sample 5)	C-C (organic)	284.53	2521.74	47.33
	C-O	286.12	960.08	18.02
	C-O3	289.53	500.281	9.39
	C-H	285.4	330.549	6.2
	C-O2	288.64	329.362	6.18
	Li-C	282.5	686.382	12.88
1st-cycle (Sample 6)	C-C	283.65	2266.04	44.12
	C-O	285.84	1050.85	20.46
	C-O3	289.37	468.008	9.11
	C-H	284.98	187.372	3.65
	C-O2	287.56	819.038	15.95
	Li-C	282.5	345.226	6.72

5.4.3 Analysis of Lithium 1s Lines

Li 1s core spectra of all the samples show a similar (almost) symmetric peak centred at 55.5 eV with the exception of the fully lithiated Sample 5 (see Figure 5.5). These peaks can be reproduced using 3 components. The dominant one ($\sim$ 55.5 eV) for all

the samples, except Sample 5, is attributed to LiF inorganic phase, accordingly to tabulated values in literature [214, 215, 217, 223, 224]. The component at ~ 54.4 eV is related to the formation of organic precipitates from electrolytic solvents composed of various species of lithium carbonates as previously discussed. The other component at higher binding energies (56.5 eV) is assigned to electrolyte residuals of $LiPF_6$ and $LiAsF_6$ that have not been washed completely. The fully lithiated sample (Sample 5), on the other hand, shows a predominance of organic SEI species, in particular, Li alkyl carbonates, that covers the outer layer of the electrode/electrolyte interphase.

SEI evolution, from the study of C 1s and Li 1s XPS peaks show a similar trend regarding the organic fraction of the passivation layer: decomposition reactions between the electrode and the electrolyte begin as soon as the two components come in contact, without the need of applying an external potential. SEI formation proceeds with an irreversible stacking process of inorganic LiF phase, which is the principal component of the SEI [223, 224], deriving from the electrolyte salt decomposition reactions [224]

$$LiPF_6 \longrightarrow LiF{+}PF_5\,;\, LiAsF_6 \longrightarrow LiF{+}AsF_5 \tag{5.4}$$

but also as result of reactions of the salt with trace of water and byproducts such as Li_2CO_3 (as proposed by Leroy *et al.*, *cfr.* [225]):

$$PF_5{+}Li_2CO_3 \longrightarrow 2\,LiF{+}POF_3{+}CO_2 \tag{5.5}$$

$$LiPF_6{+}H_2O \longrightarrow LiF{+}POF_3{+}2\,HF \tag{5.6}$$

$$LiPF_6{+}Li_2CO_3 \longrightarrow 3\,LiF + POF_3 + CO_2 \tag{5.7}$$

$$LiCO_3 + 2HF \longrightarrow 2\,LiF + CO_2 + H_2O \tag{5.8}$$

A reaction mechanism similar to that occurring for phosphorus salts,should occur also for As-based electrolyte. As also demonstrated by the presence of LiF species in the OCV Sample 1, these reactions are not driven by lithium insertion processes. The formation of LiF is probably linked to the increase of acidity of the solution and the presence of HF or HF_2^- deriving from water contaminations of the electrodes [224].

At the final stage of the lithiation process, the outer layer of the SEI is finally covered by a thin film of Li-containing organic fraction, which is dominant in Sample 5; this layer is successively removed after the end of the de-lithiation phase (Sample 6), revealing again the predominance of inorganic LiF. This mechanism agrees well

with the one proposed by our group (*cfr.* Rezvani *et al.* [112] and Figure 2.15) where at the final stage of lithiation, a formation of a thin layer of organic carbonates is temporally formed acting as a reversible Li^+ storage buffer, giving to the material a modest extra-capacity.

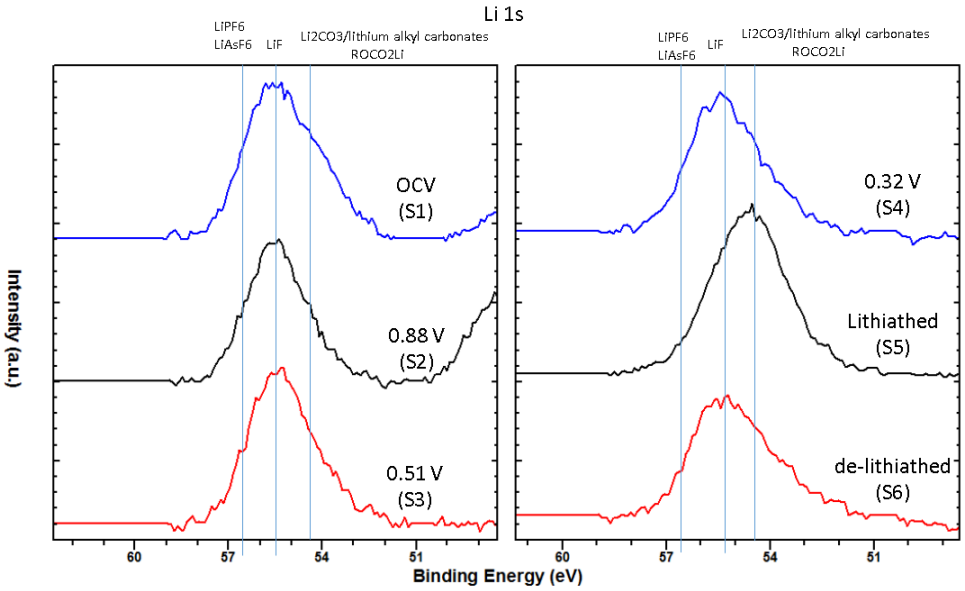

Figure 5.5: Li 1s XPS photoelectron spectra of graphite electrodes at different stages of charge and voltage as in indicated in Figure 5.1.

5.4.4 Analysis of Arsenic 3d Lines

XPS peaks related to As 3d have been analysed in order to monitor the evolution of the oxidation state of arsenic deposited onto the electrode during the SEI formation. As shown in Figure 5.6 arsenic compounds are also present in the surface films of the SEI, as confirmed by XAS measurements in Section 5.3.

As 3d electrons peak is composed of three main components which are related to the different oxidation states of arsenic in the SEI layer depending on the different As-based compounds formed. These three components are labelled as As-A (48.4 eV), As-B (45 eV) and As-C (41.3 eV); these As peaks may be an indicator of the formation of a variety of Li-As-F species, ranging from $LiAsF_2$ (As^+) via As^0 to Li_3As (As^{3-}) [208]. The only exception is represented by Sample 5 (at the fully lithiated state) that seems not to show any XPS signal from arsenic, probably due to the presence of a film (composed by several organic compounds, as showed in previous sections) that screens the As photoelectrons.

Sample 1 at OCV state presents almost a single peak component of As-B centred at 45.5 eV with a slight asymmetry towards lower binding energies. This component is attributed to As^{5+} probably in the state of arsenic oxide As_2O_5; while the shoulder component can be attributed to arsenic with valence 3+ in the form of a different arsenic oxide As_2O_3 as reported by tabulated values in literature (eg. [209, 217, 226]). The presence of arsenic oxide species is not related with the lithiation process, but only to oxidation processes due to the presence of oxygen contaminations, thus this agrees well with the fact that there is no lithium inserted into the sample.

Sample 2 shows all three peaks. The peak of As-A can be attributed to either AsF_3 or to AsF_6^- as reported by Aurbach in ref. [227] that are later reduced to LiF as the lithiation proceeds. Sample still shows the presence of arsenic oxides attributed to peak As-B. Peak As-C is finally attributed to the presence of As^0 species that have been reported in several publications (*cfr.* [208, 217, 226]) ; the presence of arsenic with this valence state has not been detected by the previous XAS analysis probably since it is present only in a small fraction and only on the upper layer of the SEI. Presence of As^0 is also corroborated by calculations of the Auger parameter (Table 5.5). Nevertheless samples 3 and 4 completely lose the peak of As-A, while sample 6 also loses the peak of As-B.

Calculation of the Auger parameter, performed as explained in the previous section, between the components of the As 3d peak and As LMM Auger peak, are reported in Table 5.5, and show compatible values between the various samples: Auger parameters for As-A range between 1261-1262 eV, for As-B between 1263-1264 eV and for As C between $1265 - 1266$ eV. Those values, confronted with the tabulated ones from the NIST X-ray photoelectron spectroscopy database [228], confirm the attribution to the different valences and species given before.

Table 5.4: Best fit result of the areas, positions and atomic concentrations of the various component XPS peaks in As 3d.

As 3d Mg Ka				
Sample	Component	B.E. (eV)	Area	% Concentration
OCV (Sample 1)	As A	48.43	428.229	2.89
	As B	45.08	1190.56	80.3
	As C	41.69	249.255	16.81
0.88V (Sample 2)	As A	48.37	272.96	16.98
	As B	44.65	613.039	38.15
	As C	41.21	721.121	44.87
0.51V (Sample 3)	As A	48.31	1,37E-17	0
	As B	44.61	625.324	38.88
	As C	41.23	983.021	61.12
0.32V (Sample 4)	As A	48.2	1,37E-17	0
	As B	44.53	897.054	64.61
	As C	41.29	491.413	35.39
1st-cycle (Sample 6)	As A	48.23	1,37E-16	0
	As B	44	869.933	7.52
	As C	40.91	1070.12	92.48

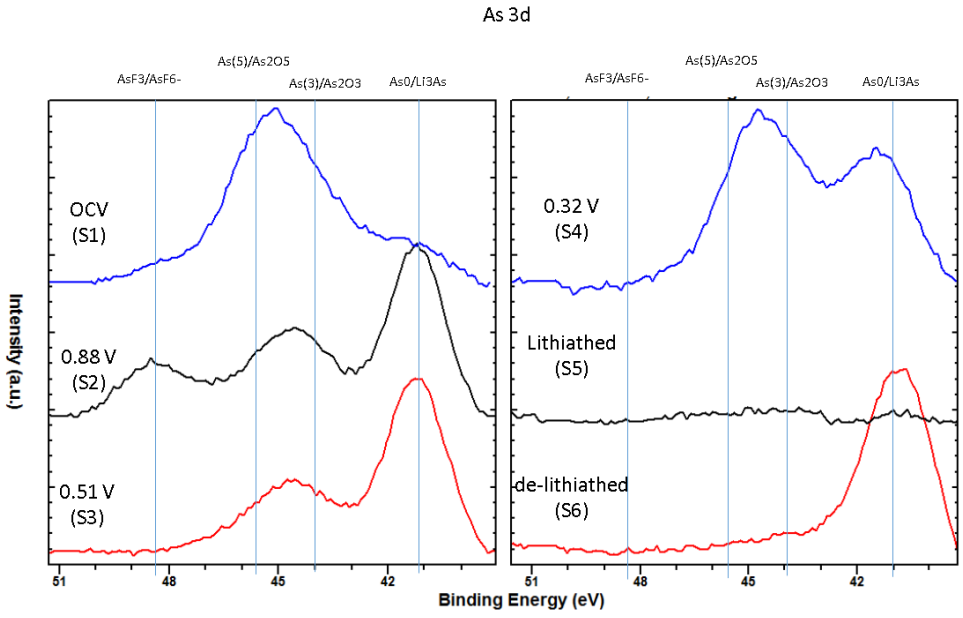

Figure 5.6: As 3d XPS photoelectron spectra of graphite electrodes at different stages of charge and voltage as in indicated in Figure 5.1.

Table 5.5: Peak center and Auger parameter for the three arsenic 3d components

	As LMM (KE)			As 3d (BE) Al Ka			As 3d (BE) Mg Ka			Auger parameter (eV) [Al Ka]			Auger parameter (eV) [Mg Ka]		
Sample/comp	As-a	As-b	As-c	As-a	As-b	As-c	As-a	As-b	As-c	As-a	As-b	As-c	As-a	As-b	As-c
OCV (Sample 1)	1213.62	1218.62	1222.64	48.2	44.53	41.29	48.43	45.08	41.69	1261.82	1263.15	1263.93	1262.05	1263.7	1264.33
0.88V (Sample 2)	1212.68	1218.28	1225.15	48.38	44.61	41.22	48.37	44.65	41.21	1261.06	1262.89	1266.37	1261.05	1262.93	1266.36
0.51V (Sample 3)	1212.04	1218.4	1225.18	48.2	44.71	41.2	-	44.61	41.23	1260.24	1263.11	1266.38	-	1263.01	1266.41
0.32V (Sample 4)	1212.02	1218.24	1223.95	-	44.53	41.29	-	44.53	41.29	-	1262.77	1265.24	-	1262.77	1265.24
1st c. (Sample 6)	-	1221	1225.32	-	44.53	41.16	-	44	40.91	-	1265.53	1266.48	-	1265	1266.23

5.5 Raman Spectroscopy Analysis

5.5.1 MicroRaman Set-up for *in-situ* Analysis

Micro-Raman analysis was performed at the University of Camerino. The set-up consisted in a modular micro-Raman composed by two different light sources (a 532 nm laser diode and an helium-neon 633 nm laser tube), an Olympus optical microscope with several objectives with a magnification up to 100x (typical laser spot size of 2-5 microns), an Horiba iHR320 spectrometer with two selectable gratings (1800/600 lines per mm) and an Horiba-Sincerity (model J810050) CCD detector. The optical transport consists of optical fiber and standard filter techniques have been used for detecting the Stokes components of the Raman signal (*cfr.* 3.3)

5.5.2 In-situ Electrochemical Cell

In-situ micro-Raman spectroscopy was performed using a specifically designed electrochemical cell that has an optical window that exposes one of the electrodes and allows Raman radiation to be collected and analysed. The cell used for these experiments is produced by EL-CELL[1] (type ECC-Opto-Std), and allows the performance of optical spectroscopy techniques by looking through an optical transparent window (made of silica-glass or sapphire-glass or calcium-fluoride or other transparent media) directly to the backside of the working electrode. For this purpose, the working electrode has to be self-standing (a plastic polymer is added to the slurry and the electrode does not need to be cast onto the current collector foil) and coupled to a perforated current collector. The cell is assembled in Ar atmosphere, the electrolyte is injected through specific ports, and finally, the cell is sealed and ready to be taken out for measurements. The cell presents electrical contacts to connect it to a potentiostat and control/monitor the electrochemical reaction.

The cell is assembled stacking a 9 mm diameter Li metal foil, glass fiber separator, the graphite working electrode and, finally, placing on top a copper current collector with a 1 mm hole in correspondence with the optical window. The electrolyte solution is finally injected with a syringe applying negative pressure and allowing the cell to absorb the largest possible quantity of liquid in order to completely soak the separator and the electrodes.

[1] `https://el-cell.com/`

A schematics of the in-situ electrochemical cell is provided in Figure 5.7[2]. The specific cell holder designed for in-situ micro-Raman is shown in Figure 5.8 (left), while the position of the in-situ cell in the micro-Raman set-up is shown in Figure 5.8 (right).

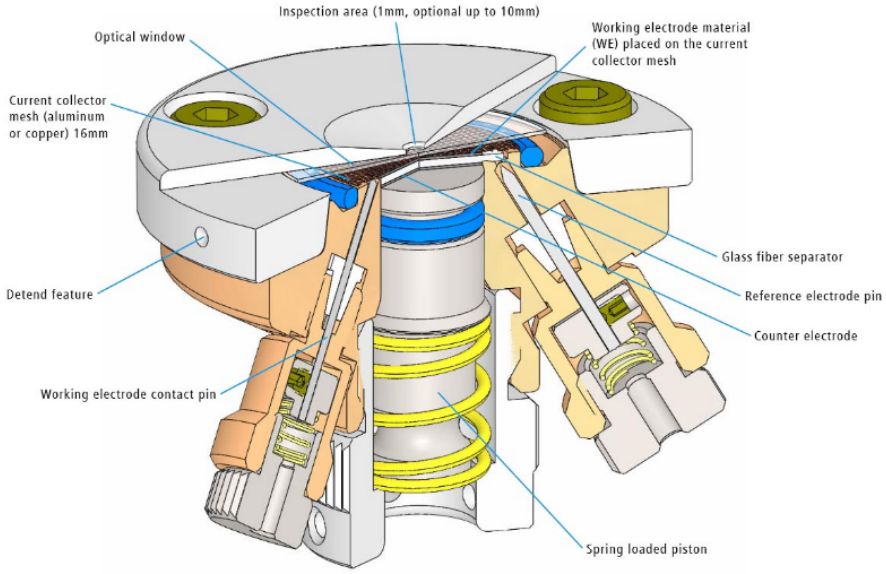

Figure 5.7: Schematic view of the ECC-Opto-Std showing a possible assembly mode for a typical sandwich geometry.

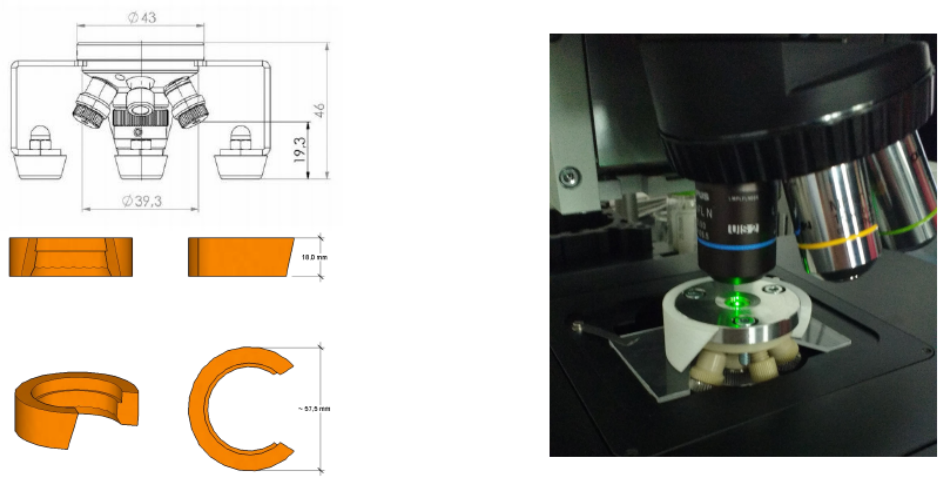

Figure 5.8: Micro-Raman set-up: on the left the in-situ electrochemical cell (EL-CELL ECC-Opto-Std), on the right a picture of the cell placed under the microscope during a micro-Raman experiment.

[2]Image from `https://el-cell.com/products/test-cells/optical-test-cells/ecc-opto-std`

5.5.3 Preparation of the Self-Standing Electrodes

The self-standing electrodes were prepared by dissolving in acetone the graphite active material, the binder (Na-CMC) and a plasticiser polymer (Dibutyl Phthalate) in 70:20:10 % weight proportion. Similar procedures have been successfully used in previous in-situ Raman experiments [177]. The mixture was then spread on a glass surface (using *Doctor Blade* technique) with a wet thickness of 200 μm; dried and washed in diethyl ether in order to remove the residues of Dibutyl Phthalate. The obtained dried material was then cut into circular electrodes with diameter of 9 mm and pressed in order to obtain a uniform dry thickness of $\sim$ 60 μm. The resulting electrodes had an average mass of $\sim$ 3.5 mg with a loading of $\sim$ 5.5 mg/cm^2 and an active material loading of $\sim$ 2.76 mg/cm^2. The in-situ electrochemical cell was finally assembled, in a two electrodes configuration, following the procedure described in Subsection 5.5.2.

5.5.4 Raman Experiment and Results

The assembled cell was finally mounted onto the microscope motorized stage (see Figure 5.8 right) and connected to a single channel galvanostat/potentiostat (BIO-Logic) programmed to cycle the cell with a rate of C/10. Raman experiments were performed using the 633 nm laser light source, since the 532 nm had demonstrated to cause heating and consequent degradation of the electrolyte. Raman spectra were obtained by integrating 5 consecutive scans of one minute each, starting the acquisition at specific points in the potential discharge curve of the electrode. We can assume that the potential and the chemical state of the cell is unchanged during the interval of one single scan, being the discharge time much larger than the Raman acquisition time.

The laser spot (dimension $\sim$ 5 μm) was focussed using a long-range focusing objective with 50x magnification (Olympus) onto a single graphite particle of the dimension of $\sim$ 26 μm, and the selected measurement spot has been maintained during the entire discharge process. In this way, we avoided changes in the Raman pattern due to slight inhomogeneities of the electrode surface and variation of the local lithium content.

Voltage Profile Curve

Figure 5.9 shows the discharge (lithiation) profile of the graphite anode in the in-situ electrochemical cell during the first cycle. The cell had an open-circuit-voltage (OCV)

potential of ~ 3 V (all quoted potentials are vs. Li/Li^+). The potential interval was set to be between 3 and 0.1 V with a current rate of C/10. The discharge profile is compatible with the cycling behaviour of graphite anodes reported in literature [229,230] and shows the typical plateaus in the voltage range $1-0.4$ V attributed to the SEI layer formation during the first lithiation. While the main process of lithium intercalation in graphite is related to the long plateau portion at a potential of 0.1 V. The final specific capacity of the cell is 360 $mAh \cdot g^{-1}$ in good agreement with the expected theoretical capacity of graphite.

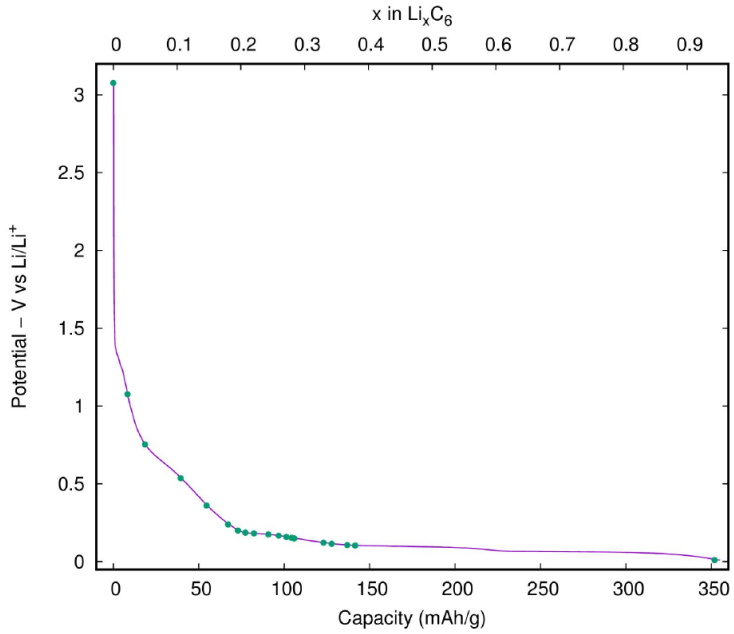

Figure 5.9: Voltage profile of the first discharge (lithiation phase) of graphite anode in the in-situ electrochemical cell (purple). In green are highlighted the points at which Raman spectra have been acquired.

Raman Spectrum at OCV

Figure 5.10 shows the Raman spectrum for the graphite anode at OCV state. The main observed peaks are assigned to the electrolyte and to the graphite active material of the electrode. The main Raman components of the electrolyte, which is mainly composed of large organic molecules, are located in the low wave-number region ($\sim 150-250$ cm^{-1}). Three main bands,in the region between $1000-3000$ cm^{-1}, are associated with graphite: a strong and sharp G band at 1580 cm^{-1}, a weak D band at 1330 cm^{-1} and the 2D band at 2670 cm^{-1}. The 1580 cm^{-1} peak (E_{2G2}) is called G band after crystalline graphite, and is due to the relative motion of sp^2 carbon atoms in rings

and in chains indeed (*cfr.* [231–233] and references therein). The peak at 1330 cm^{-1} is called D band after disordered graphite, and can be assigned to the breathing motion of sp^2 atoms in the ring, being also effected by defects within the layers [232]; the 2D band (also referred in literature as the G' band) is placed at about double frequency of the D band (2670 cm^{-1}) and is due to a second-order (two phonon) Raman scattering and seems not to be related to disorder [233]. The 2D band is asymmetric and is reproduced by a superposition of two components [232]: 2D(1) and 2D(2), at 2649 cm^{-1} and 2686 cm^{-1} respectively.

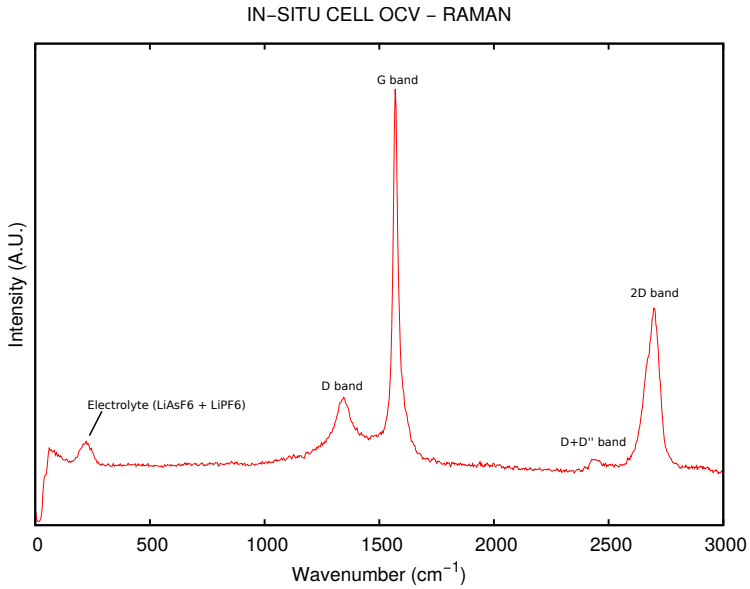

Figure 5.10: Raman spectrum of graphite anode in the in-situ cell with electrolyte at OCV state.

Raman Evolution During the Discharge

During the discharge process, important changes in the Raman pattern occur. In particular, we observed a gradual increase in the count-rate in the entire wave-number interval measured by our micro-Raman equipment. This important increase of the background represented a severe limitation for a direct measurement of the components related to the SEI formation and evolution in different electrodes that we have been using in this thesis work. This effect has been already observed in other works. On the other hand, we have been able to study the evolution of the Raman components related to the active materials of the electrodes, namely graphite in the experiment under

consideration. This allowed us to test our procedure for in-situ Raman experiment.

Raman Evolution During Lithium Intercalation in Graphite

During lithium intercalation into graphite, Raman spectra evolve following the structural changes of the host material after lithium insertion (see Figure 5.11). The main events are related to the blue-shifting and weakening of the G band from 1580 cm^{-1} to 1590 cm^{-1}, accompanied by the gradual weakening of the peak intensity in the final stage of lithiation ($0.6 - 0.01$ V) due to the formation of an highly conductive layer on the surface which limits the penetration depth of the laser. Furthermore the G band shows a splitting into two components: E_{2g2}(i) (1573 cm^{-1}) and E_{2g2}(b) (1595 cm^{-1}) in the potential interval $0.2 - 0.01$ V. The 2D(2) component of the 2D band, on the other hand, undergoes a red-shift process and finally completely disappears at the end of the discharge cycle at ~ 0.1 V.

The blue-shift of the G band can be explained with an increase of the constraint forces of the in-plane C−C bonds following the lattice expansion due to lithium intercalation in the graphene planes: in fact, as shown in Figure 5.12 the peak shift begins at around 0.6 V, effect compatible with the beginning of the main lithiation plateau. At lower potential ($\sim$ 0.15 V) the G band starts to broaden and finally splits (process shown in the left part of Figure 5.11) into two distinct bands (assigned to E_{2g2}(i) at 1573 cm^{-1} and E_{2g2}(b) at 1595 cm^{-1}). This can be related to a phase transition depending on the change of the lithium distribution from a random to a more compact one in the graphite-lithium compound and to a further increase of the C−C bond force constant [232].

The 2D band remains visible until the discharge potential reaches ~ 0.2 V before being masked by the effects of the highly conductive graphitic carbon, intercalated with lithium, as previously mentioned. The 2D band remains constant until ~ 0.5 V during the formation of the solid electrolyte interphase. Between 0.5 and 0.2 V there is a gradual red shift of the 2D(2) component (Figure 5.11, right side). The trend of the 2D peak position is shown in Figure 5.12. This shift may be related to the increased in-plane lattice strain that follows lithium-ion insertion. In this final stage of the discharge, the graphene layers in graphite are becoming increasingly distorted to the heavy lithium intercalation between the graphite planes.

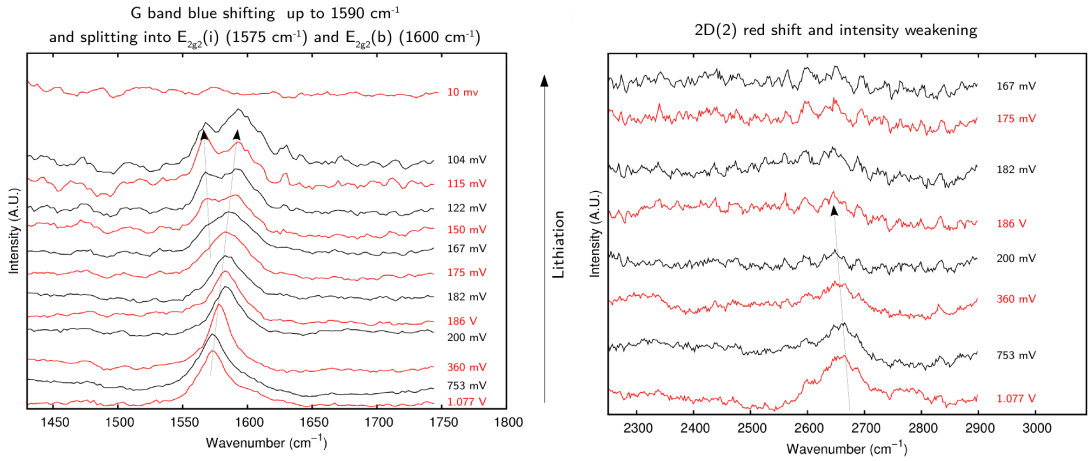

Figure 5.11: Raman spectra of graphite anode in the in-situ cell during the lithiation phase. On the left side of the figure is shown the shift and splitting of the peak related to the G band. On the right side of the picture is shown the red-shift of the 2D band peak.

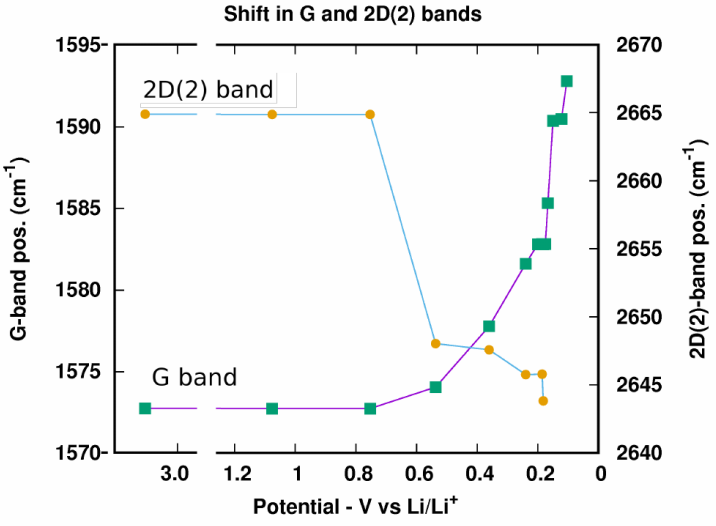

Figure 5.12: Result of the peak fit of Raman G and 2D(2) bands, showing the blue and red shift respectively as lithium insertion proceeds.

Chapter 6

Local Structure of Advanced Cathodes for Na-ion batteries

This Chapter will cover part of a research work done in collaboration with CIC-energigune in the Basque Country (Spain). The goal was to prove the effects onto Mn-rich layered oxides structure caused by the presence of electrochemical inactive species (such as Ti or Fe) as dopant, which is related to an improvement in the electrochemical performances and the stability of the material.

The possibility of controlling structural and electrochemical properties by transition metal substitution is the starting point towards the design of electrode materials that will ultimately lead toward competitive Na-ion batteries.

This work is mainly focussed on XAS experiments of a specific class of Mn-rich layered oxides aimed to study the local structural distortions around the Mn sites induced by the presence of dopant materials.

6.1 Background on Material Properties

Sodium layered electrodes are showing interesting electrochemical performances when used in NIBs and are currently extensively investigated as cathode materials, since they have a simple structure, high capacity and high rate capability thanks to the fast structural diffusion of sodium ions in the layers. Among the many kinds of layered electrodes, a growing interest is building around sodium manganese layered oxides since they present the advantages to be low-cost, environmentally friendly and easy to manufacture [98, 234, 235].

The main drawbacks related to this material and that affect the electrochemical

performances are the dissolution of Mn in the electrolyte [236] and the Jahn–Teller (JT) distortion associated with high spin Mn^{3+} which possesses a d^4 high-spin electronic configuration with a single electron on the e_g orbital [235,237]. A sketch of the electronic configuration is shown in Figure 6.1.

Since the Jahn-Teller distortion leads to structural degradation during cycling and a rapid loss of the cell performances, two strategies to overcome this issue are: protecting the active material surface [238] and the partial substitution of Mn with electrochemical inactive species [98]. It has been demonstrated that these approaches, and in particular the latter, improves the cycle stability of the material. In particular, the Na-Fe-Mn system has been widely studied [239, 240] because the combination of Mn and Fe in the electrode active material leads to higher specific capacities and better capacity retention, as well as higher stability and an increased operational voltage if compared to pure $NaMnO_2$ [235].

In this chapter we will take into account three Mn-rich P2 phase layered oxides as cathodes for Na-ion batteries: $Na_{2/3}Mn_{0.8}Fe_{0.2}O_2$, $Na_{2/3}Mn_{0.8}Fe_{0.1}Ti_{0.1}O_2$ and $Na_{2/3}Mn_{0.8}Ti_{0.2}O_2$ (from this point they will be referred as MnFe, MnFeTi and MnTi respectively). P2 structures materials are generally the most chosen cathodes since they have a lower diffusion barrier, higher ionic conductivity and higher structural stability with respect to other phases (O3) [100, 135, 241].

Han *et al.* [234, 242] showed that the introduction of Ti^{4+} into $Na_xMn_yFe_{1-y}O_2$ ($x \leq 1$; $0 \leq y \leq 1$) improves the electrochemical performances in terms of coulombic efficiency and capacity retention and also stabilizes the structure [55].

As mentioned above, here we will investigate the presence of induced Jahn-Teller distortion and the structural properties of these materials by a series of X-ray absorption spectroscopy experiments. This analysis is part of a wider paper regarding this material class published in collaboration with the CICenergigune research group [243]. In particular, the preparation and electrochemical tests were performed by Elena Gonzalo and Maider Zarrabeitia and co-workers, the synthesis procedures and the electrochemical performances of such materials are described in details in refs [234, 242–245]

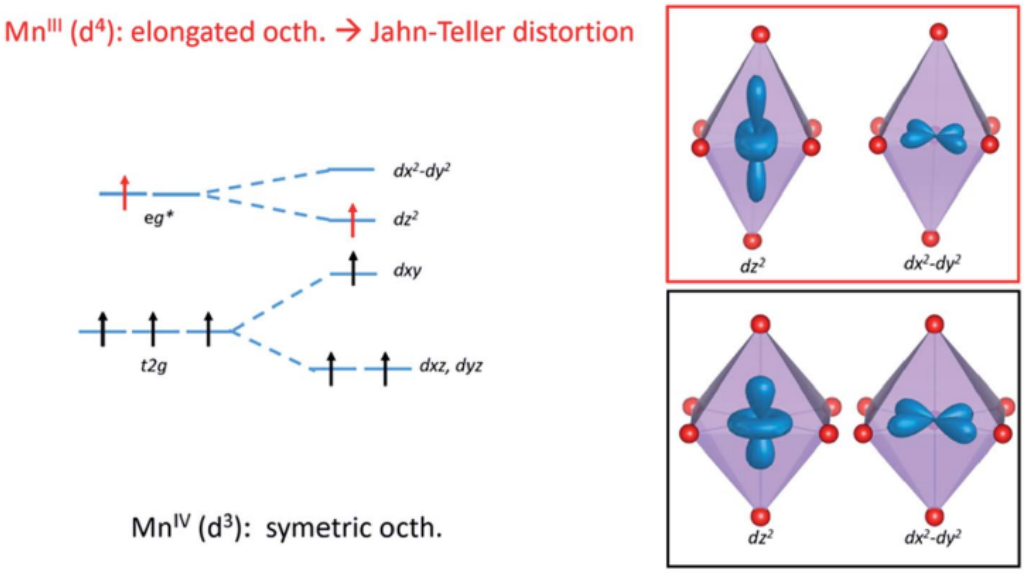

Figure 6.1: Schematics of Mn^{3+} and Mn^{4+} electronic configuration and visualization of Jahn-Teller distortion [243].

6.2 Preliminary Characterization

6.2.1 X-ray Diffraction

Powder X-ray diffraction (PXRD) patterns were collected using a Bruker Discover D8 instrument with Cu radiation (Cu K$\alpha_{1,2}$, λ 1.540530 Å) in the 2θ range of $10 - 80°$. Samples were covered with Kapton tape in order to preserve the inert atmosphere. X-ray diffraction patterns were refined using FullProf Suite software [246] while drawings of the structures were made with Vesta software [198]. A sketch of the structure and typical diffraction patterns are showed in Figure 6.2.

Diffraction peaks of both samples containing iron (MnFe, MnFeTi) were indexed using hexagonal symmetry (Space Group $P6_3/mmc$). Also the sample without iron doping (MnTi) has been fitted using the same space group, even if some of the reflection peaks could not be indexed (for example $2\theta = 38.2°, 42.40°, 47.70°$ and $61.06°$ see Figure 6.2 right panel). One must notice that layered oxides can form a range of different polymorphs which depend on the conditions of the synthesis, Na content and presence of T_M vacancies [106, 247].

Furthermore, in the case of Mn-compounds, Kumakura *et al.* [248] have reported that the Jahn-Teller-active high spin Mn^{3+} in the MnTi sample can induce a lattice distortion from hexagonal to orthorhombic symmetry due to cooperative Jahn-Teller

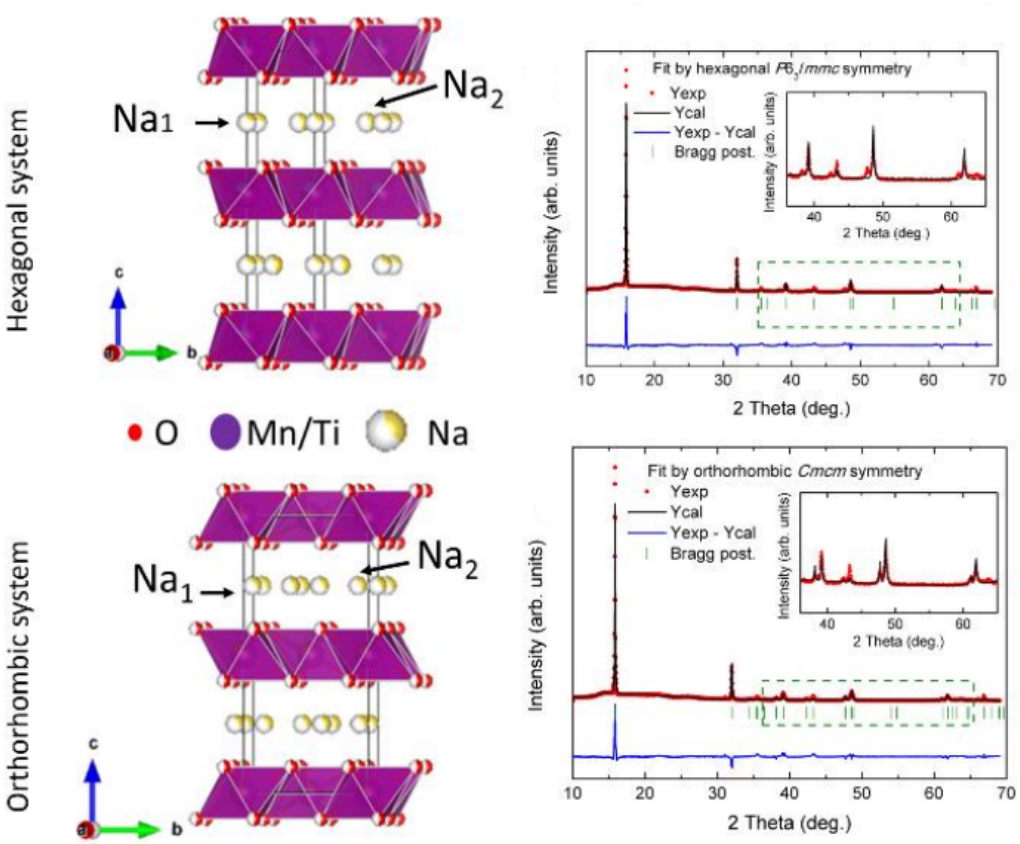

Figure 6.2: Structure and Rietveld refinement of the P2-$Na_{2/3}Mn_{0.8}Ti_{0.2}O_2$ (MnTi) powder by Rietveld method using hexagonal (S.G.: $P6_3/mmc$) and orthorhombic (S.G.: Cmcmc) symmetry, with relative X-ray powder diffraction patterns between $2\theta = 35 - 65°$ [243].

distortion (CJTD). Since in the MnTi sample the amount of Mn^{3+} is higher if compared to the other samples (MnFe and MnFeTi), it can be said that the observed lattice distortion of MnTi derives from CJTD effects. In fact, refining PXRD pattern with this different symmetry structure provides better indexing of the PXRD peaks. Hence, from PXRD results, we can conclude that doping the structure with higher amounts of Ti than 0.1, and consequently a higher amount on JT-active Mn^{3+}, results in increased distortion of the structure and a modification of the symmetry.

The cell parameters (reported in details in ref. [243]) for MnFe and MnFeTi samples are in agreement with the values reported in literature ([234, 242]), while MnTi sample shows values which are close to orthorhombic P′2-$Na_{2/3}Mn_{0.8}T_{M0.1}O_2$ [248]. The averaged T_M-O distance obtained by PXRD refinement could provide indirect information regarding the T_MO_6 octahedral distortion relating the amount of Mn^{3+} CJTD-inducing to the distortion of the relative octahedron. The PXRD refinement of our samples show an increase of the JT-distortion and the T_M-O distance when increasing the amount of Mn^{3+} in the sample (MnTi>MnFeTi>MnFe) [243].

6.2.2 Electrochemical Performances

The electrochemical properties of the three samples under consideration (MnFe, MnFeTi, MnTi) are reported in Figure 6.3. MnFe shows higher charge/discharge capacities (200/190 $mAh \cdot g^{-1}$) than MnFeTi (146/144 $mAh \cdot g^{-1}$) at the second cycle at C/10, since both Fe and Ti are electrochemically inactive species in the considered potential interval ($4.0 - 2.0V$ vs. Na^+/Na). Fe inactivity was also confirmed by Mössbauer spectroscopy [234]. Nevertheless, after 50 cycles, the charge/discharge capacities of the two samples (MnFe and MnFeTi) reach compatible values of ~ 140 $mAh \cdot g^{-1}$. For this reason the capacity retention, after 50 cycles, is better for MnFeTi than MnFe (95.1% vs. 71.7%). On the other hand, the capacity at the second galvanostatic charge/discharge cycle for the sample MnTi is considerably inferior with a value of 55 $mAh \cdot g^{-1}$, resulting with only 0.2 Na^+ ions inserted/de-inserted per formula unit (theoretical specific capacity of 265.89 $mAh \cdot g^{-1}$). This modest specific capacity might be related to the higher presence of JT-active Mn^{3+} since the octahedral distortion in this type of layered oxides is considered to be a drawback for the electrochemical performances [237, 245, 249]. Even though the specific capacity is low, MnTi shows good capacity retention of 92% after 50 cycles, but is lower than the capacity retention of MnFeTi. This confirms that the structural stabilization effects of Ti^{4+} doping must be controlled since it can also influence negatively the electrochemical

performances.

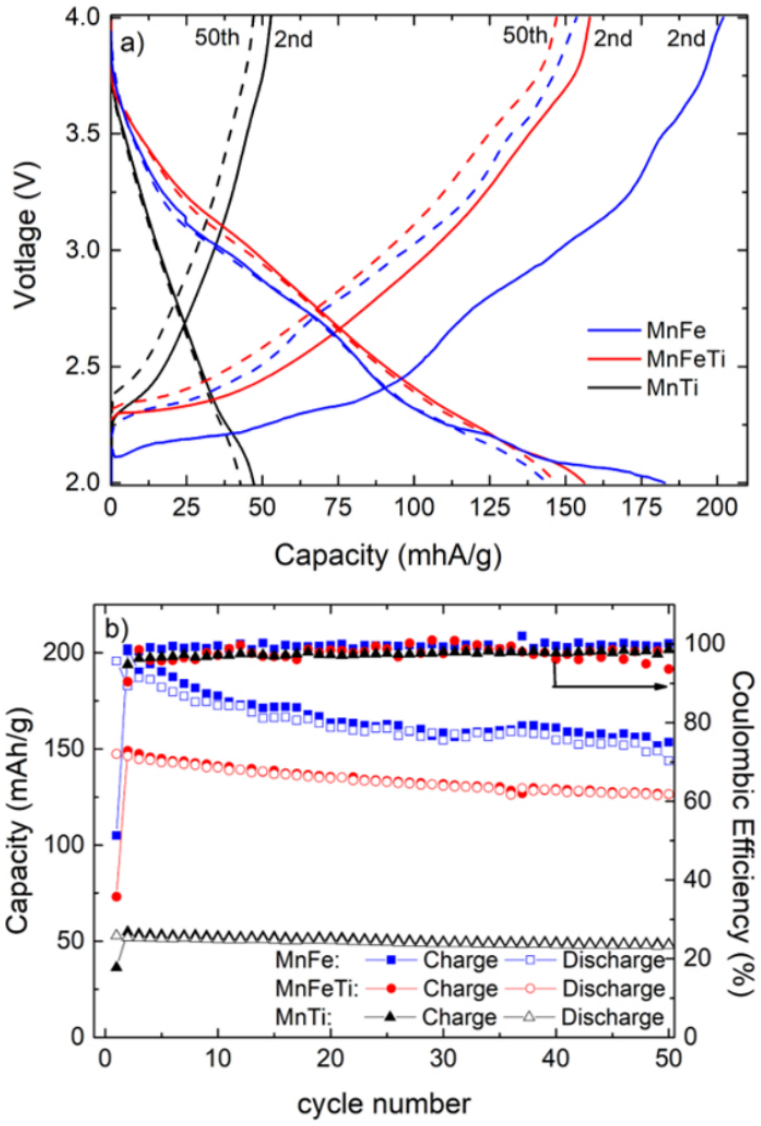

Figure 6.3: Voltage profile and cycle retention for MnFe, MnFeTi and MnTi:on top galvanostatic charge/discharge profile of the 2^{nd} (line) and 50^{th} (dash) cycles; on the bottom evolution of the capacity upon 50 cycles in the voltage range $4.0 - 2.0$V vs. Na^+/Na at C/10 [243].

6.2.3 Structural Determination from ab-initio Calculations

Density functional theory (DFT) calculations have been performed to analyse the enhanced structural stability of MnFeTi at the molecular level, and better understand the role of T_M doping on the JT-effect. Results (reported in Table 6.1 and in ref. [243])

shows that the Mn^{4+}−O distance distribution, relative to the undistorted sites, are characterized by a single main peak with an averaged distance of 1.95 Å, independently of the Ti content. However, Mn^{3+}−O distances distribution split into two distinct peaks. One below 2.0 Å, and one above 2.2 Å. This splitting is caused by the Jahn-Teller distortion typical of ions with electronic configuration ($(t^2g)^3(eg)^1$), as Mn^{3+} [243].

Table 6.1: Calculated DFT mean values of T_M−O distances (Å) in P2-$Na_{2/3}Mn_{0.8}Fe_{0.2-x}Ti_xO_2$. The two values in the Mn^{3+} column correspond to the short (planar) and long (apical) distances [243].

x	Mn^{4+}−O	Mn^{3+}−O	Fe^{3+}−O	Ti^{4+}−O
0	1.961	1.977 / 2.213	2.049	-
0.1	1.953	1.97 / 2.246	2.051	1.999
0.2	1.953	1.964 / 2.27	-	1.997

The first peak corresponds to the four planar bonds in the equatorial plane, the second peak is related to the two apical (on the axial line orthogonal to the equatorial plane) Mn^{3+}−O distances; both distances are compatible with a distorted [Mn^{3+}−O_6] octahedron and it is significantly affected by the Ti content, showing a shift towards larger distances as Ti^{4+} doping is increased in the system (as observable in Figure 6.4 and in ref. [243]). From these theoretical calculations it seems that the presence of Ti in the structure mainly affects the distortion of [Mn^{3+}−O_6] octahedra, by increasing the Mn^{3+}−O apical distance. In addition the Distortion Index (D.I.) has been calculated with the expression proposed by W. H. Baur [250]; in Figure 6.4 are showed the averaged value and dispersion range of D.I. for each T_M−O_6 octahedra. As expected, the largest distortion is given by [Mn^{3+}−O_6] octahedra due to the increased JT effect, furthermore, this distortion increases with Ti content. This can be explained by CJTD, since the substitution of Fe^{3+} by Ti^{4+} necessarily involves an increment of [Mn^{3+} ions in the structure. Furthermore, it can be noticed that amongst the non-active JT ions, the distortion index of the Ti^{4+}−O_6 octahedra is 2-3 times higher than the one of Fe^{3+}−O_6 and Mn^{4+}−O_6 octahedra, revealing that titanium acts as a structural buffer that can actively help to relieve structural stresses and better accommodate the induced JT distortions. The other ions present a much lower DI values, indicating that they are rigid and less able to adapt their geometries to account for distortions [243].

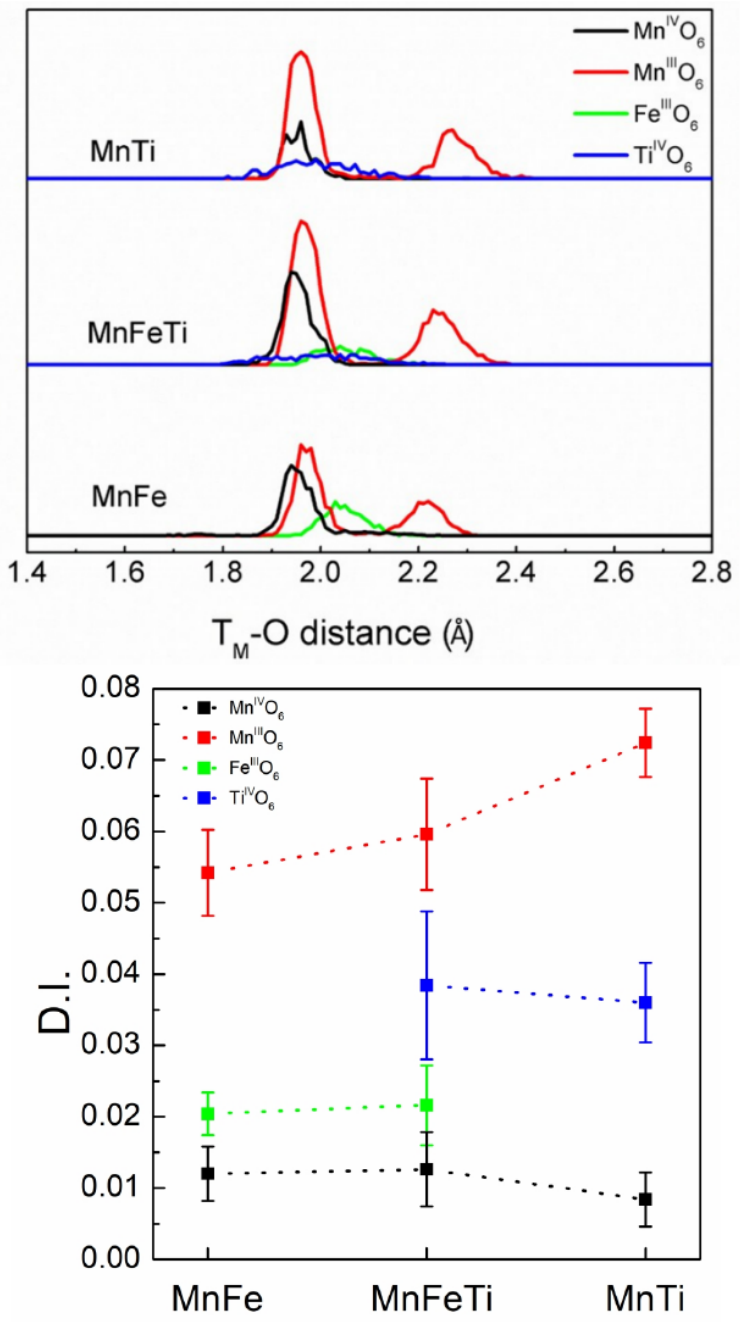

Figure 6.4: Top: T_M−O distance distribution within the $[T_MO_6]$ octahedra in MnFe, MnFeTi and MnTi (intensities for Fe and Ti distances are doubled for better visualization). Bottom: distortion index of $[T_MO_6]$ octahedra as function of Ti content for MnFe, MnFeTi and MnTi; points and bars represent mean values and standard deviations respectively [243].

6.3 Experimental - XAS

Mn and Ti K-edge XAS spectra were collected at the XAFS beamline of the Elettra synchrotron radiation facility (Trieste, Italy) [251]. The X-ray beam delivered by a bending magnet source was monochromatized by using a Si(111) double-crystal monochromator.

The cathode active materials were finely grounded into powders, then mixed with carboxymethyl cellulose (CMC) in an optimal amount in order to collect measurements in transmission mode, the mixture has been pressed into pellets and sealed into Kapton tape to avoid air contamination. Spectra were collected at room temperature using two ionization chambers to measure the incident and transmitted flux.

Metal reference foils of Mn and Ti were used for energy calibration: the first inflection point of the absorption spectrum of Mn and Ti metal was set to 6539 eV and 4966 eV respectively.

Spectra of reference metal foils were measured simultaneously with any sample spectrum by a third ion chamber to monitor the energy scale between different scans. The EXAFS analysis was done by using the GNXAS package [142, 143] using standard procedures.

6.4 XANES

X-ray absorption spectroscopy (XANES and EXAFS) measurements have been taken in order to evaluate and confirm the oxidation state of manganese and titanium present in each sample and also to gain further information relative to the internal structure of the MnFe, MnFeTi and MnTi samples.

Figure 6.5 shows the Mn K-edge XANES spectra of the three samples. The absorption edge position, taken as the first maximum of the derivative spectrum (shown in the inset) shifts to lower energies with increasing Ti concentration. In Figure 6.5 (right) is shown a comparison of the Mn absorption edge energy vs the oxidation state of reference Mn oxides [252], the position of the measured energy edges indicates that all the samples contain Mn ions in oxidation state intermediate between 3+ and 4+.

Exploiting the linear relationship between the edge energy and the Mn oxidation state of the reference compounds, a mean oxidation state of 3.48, 3.34 and 3.26 was found for MnFe, MnFeTi and MnTi, respectively. These values agree well with the expected oxidation states (assuming oxidation state 3+ and 4+ for Fe and Ti

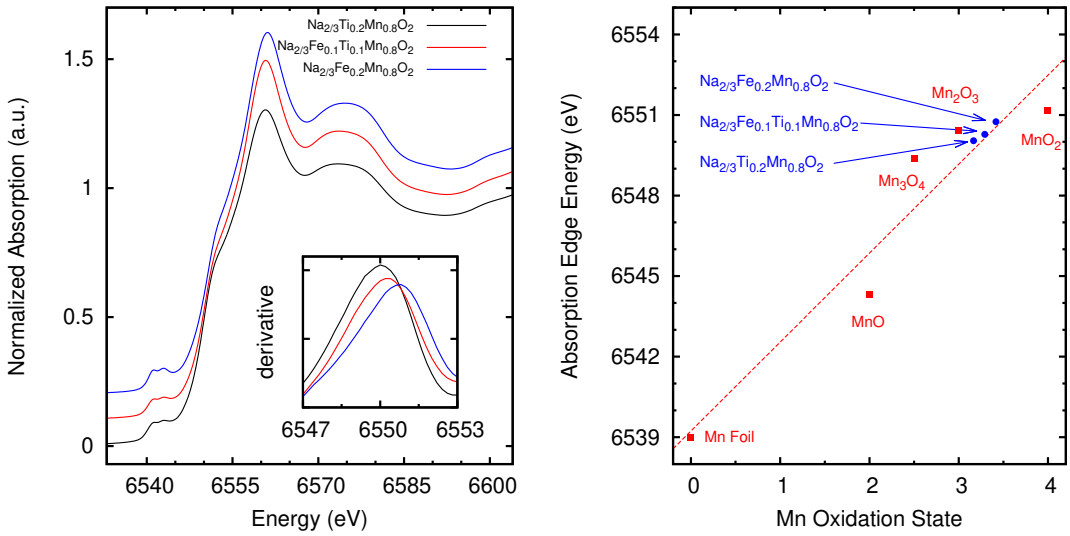

Figure 6.5: (Left) Mn K-edge XANES spectra for MnFe (blue), MnFeTi (red) and MnTi (black). The inset shows the first derivatives of the spectra. (Right) XAS Mn K-edge energy vs calculated Mn oxidation state for the studied samples (blue circles) and reference compounds (red squares). The dashed line is a linear fit for the reference compounds.

respectively) calculated from electronic balance, shown in Figure 6.5 (right) with blue circles.

The Ti K-edge position, shown in Figure 6.6 (derivative spectra in the inset), does not change with the Fe concentration. Comparison with reference Ti oxides [253] indicates that the mean oxidation state is 4+ in both the MnFeTi and MnTi samples.

6.5 Modelling the Structure

Pair Distribution Function (PDF) theoretical calculations were performed at CIC-Energigune (see Subsection 6.2.3) and proposed a model that considered two different manganese-oxygen shells with $(4 + 2)$ coordination number at different distances: 4 planar and 2 elongated apical.

In order to compare the model PDFs with present experiments, we have calculated the EXAFS signals of the first shell Mn-O distribution (related to the structural parameters listed in Table 6.2) and compared it with the experimental first shell back Fourier Transform.

Data reported in Figure 6.7 show that the distribution of apical oxygen atoms affects the total EXAFS signal. It is shown, also, that there is a qualitative agreement

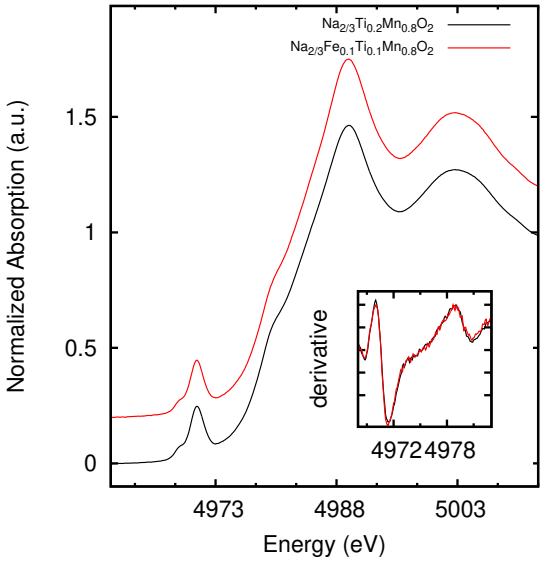

Figure 6.6: Ti K-edge XANES spectra for the MnFeTi (red) and MnTi (black) and derivatives in the inset.

Table 6.2: Structural parameters for the planar and apical Mn-O distributions derived from PDF theoretical calculations.

Model	MnFe	MnFeTi	MnTi
R_{Mn-O} (Å) planar	1.961(2)	1.960(1)	1.958(2)
R_{Mn-O} (Å) apical	2.215(2)	2.243(3)	2.273(2)
σ^2_{Mn-O} (10^{-3}Å^2) planar	0.88(2)	0.89(2)	0.76(2)
σ^2_{Mn-O} (10^{-3}Å^2) apical	1.30(2)	1.44(2)	1.33(2)

between calculations and experimental data. Moreover, the effect of thermal vibrations and of possible extra-contributions of structural disorder are present as a reduction of the amplitude of the EXAFS signal for increasing wave-vector values. The amplitude decrease observed in the experimental data reduces the EXAFS sensitivity to the details of the oxygen distribution.

6.6 EXAFS Analysis

To obtain more information about the local Mn-O coordination of the MnFe, MnFeTi and MnTi samples, Mn K-edge spectra were collected in the extended energy range (EXAFS) and analysed. The k^2 weighted EXAFS signals and the corresponding Fourier transforms in the $3.7 - 11.9$ Å^{-1} window are shown in Figure 6.8 for all the three samples. The first peak of the FT at around 1.6Å is assigned to the first Mn-O

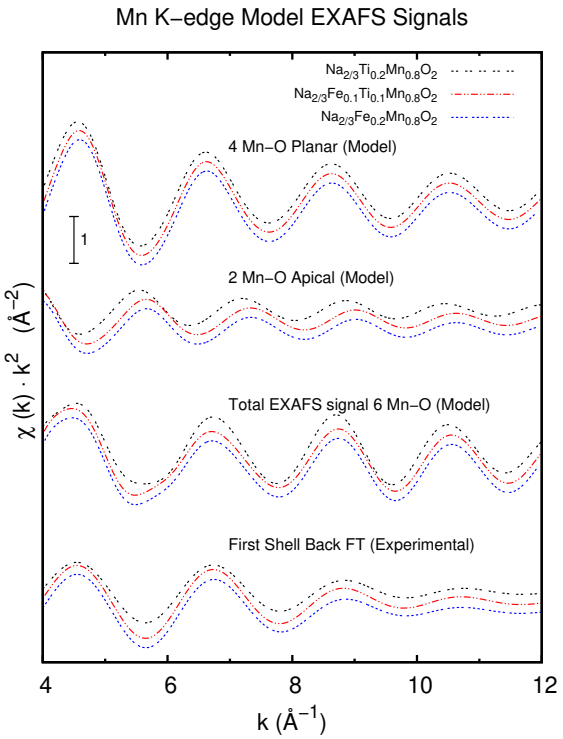

Figure 6.7: EXAFS signals calculated from the PDF model and the first shell ($1 - 2$ Å) backward Fourier transform of the experimental data.

coordination shell while the second peak at around 2.5 Å represents the Mn-Mn(Fe, Ti) second coordination shell with some contribution from Mn-Na distances.

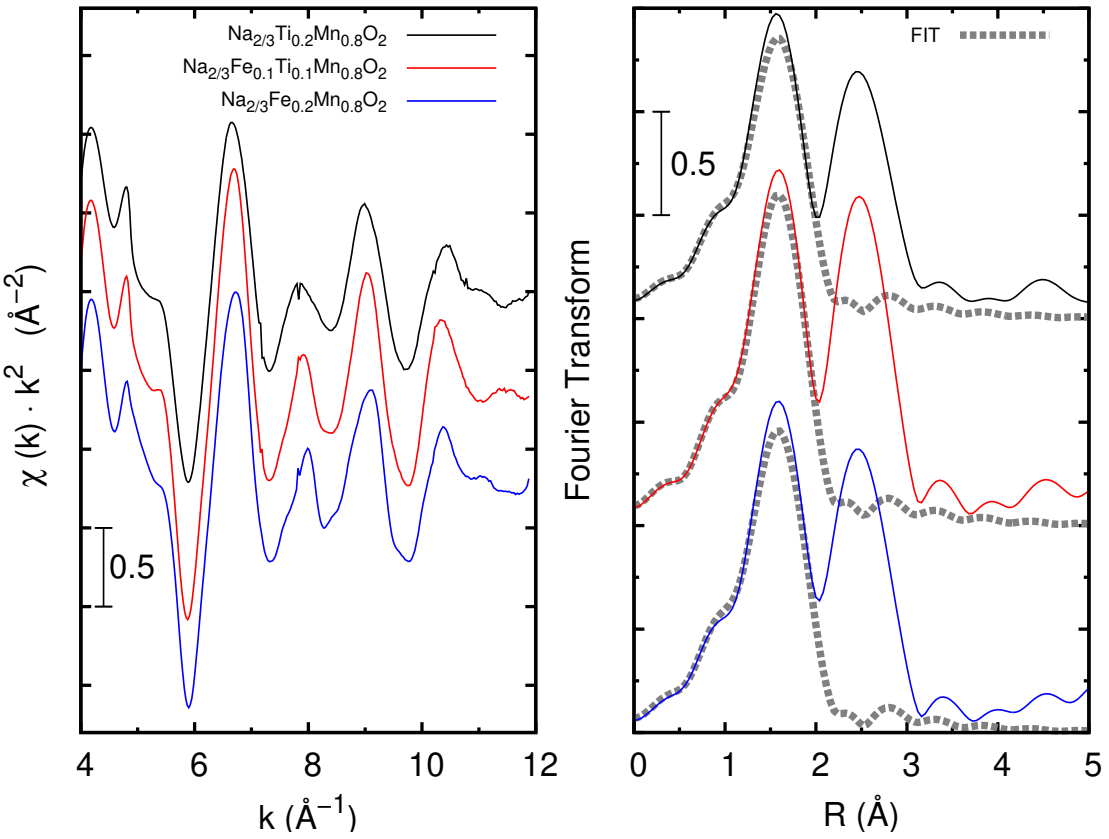

Figure 6.8: Mn K-edge k^2-weigthed EXAFS signals (left) for the three samples (MnFe, MnFeTi and MnTi) and the corresponding Fourier transforms in the $3.7 - 11.9$ Å^{-1} window (right). The gray dots are the best fit with the distorted $(4 + 2)$ coordination model.

The similarity of the EXAFS features shows that the presence of Ti does not affect sensibly the local environment of Mn, nevertheless a small reduction of the signal amplitude between the three is observed and it is possibly related to an increase in the structural disorder in both the first and second shell. The EXAFS signals were analysed using different models for the Mn-O oxygen coordination shell.

As expected from the theoretical calculations, the first peak of the Fourier Transform could not be modelled considering an undistorted octahedral structure with a single shell of Mn-O with coordination number 6. However, a distorted structure $(4 + 2)$ coordination model, having 4 oxygen atoms around 1.95 Å and 2 oxygen around 2.30 Å reproduces the first peak of the FT in substantial agreement with the results of the previous simulations.

The best-fits curves are reported in Figure 6.8 (gray dots)and the resulting structural parameters are listed in Table 6.3. Results of inter-atomic distances appear to be compatible with those of the theoretical calculations (Tab.6.2), however, the effects of thermal vibration and structural disorder contributions cause a reduction of EXAFS signal at high wave-vector values. By present data is not possible to confirm the increasing Jahn-Teller distortion with increasing Ti content.

Table 6.3: Average inter-atomic distances and corresponding variances for the three samples as obtained from EXAFS analysis. The two values correspond to the short (planar) and long (axial) coordination shells having coordination numbers 4 and 2 respectively.

Best-Fit	MnFe	MnFeTi	MnTi
R_{Mn-O} (Å) planar	1.940(2)	1.944(2)	1.947(2)
R_{Mn-O} (Å) apical	2.298(5)	2.303(5)	2.297(5)
σ^2_{Mn-O} (10^{-3}Å^2) planar	8.3(8)	7.0(7)	8.5(9)
σ^2_{Mn-O} (10^{-3}Å^2) apical	6.8(7)	7.0(7)	7.6(8)

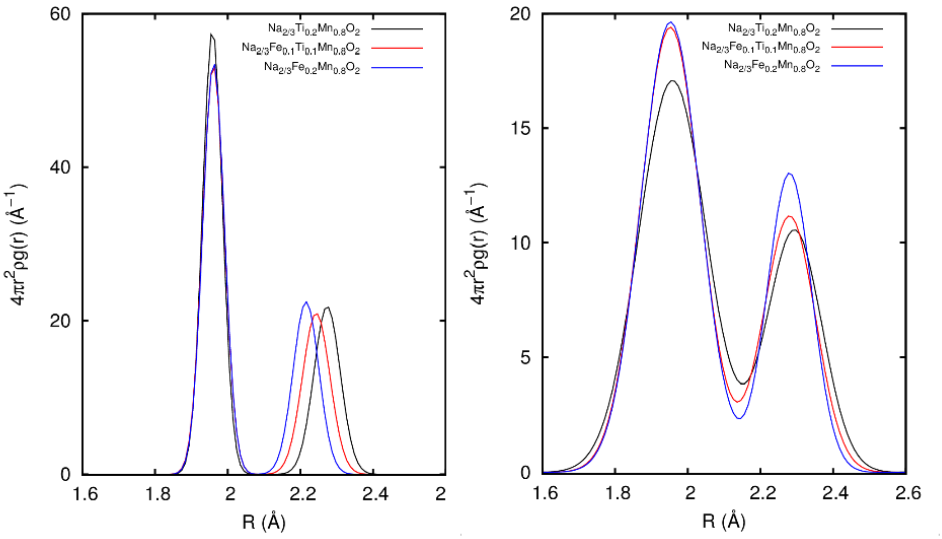

Figure 6.9: Radial distribution functions. On the left the $g(r)$ derived from PDFs calculations. On the right the $g(r)$ derived from the experimental XAS best fits.

Chapter 7

General Conclusions

The research work presented in this thesis regarded the structural study of different materials employed as battery electrodes (for both Li and Na ion cells) by means of X-ray Absorption Spectroscopy, X-ray Photoelectron Spectroscopy and Raman Spectroscopy. The main purpose of the thesis was to provide better insight, at a microscopic and atomic level, of all the mechanisms related to the insertion/de-insertion of lithium or sodium ions in the electrode structure at the electrolyte interface and in the bulk.

The process of Li^+ insertion into carbon-coated zinc-ferrite nanoparticles was studied by X-ray Absorption Spectroscopy performing an in-situ and in-operando experiment which provided a detailed description of the modifications occurring in the electrochemical cell employed in function of the quantity of lithium inserted into the active material. We have shown that in the very early stages of Li^+ insertion (until 0.3 Li^+ per formula unit) ZFO-C retains the spinel structure while at higher level of Li uptake (> 0.3 Li^+ per formula unit), Zn atoms migrate to vacant 16c sites due to electrostatic repulsion from Li^+ inserted into octahedral (16c) sites. In this initial stage, Fe is found to be gradually reduced from Fe^{3+} to Fe^{2+} upon lithium insertion and remains in the octahedral sites; furthermore, gradual damping of the EXAFS signals indicates an increasing structural disorder within the active material accompanying these structural changes. The lithiation phase proceeds with a gradual and continuous reduction of the Zn and Fe until those species are fully metallized in the form of nano-sized particles. During this phase, lithium ions are stored in the cell material as lithium oxide (Li_2O), until lithium concentration reaches 8 Li^+ per formula unit. Finally, we could provide direct proof of the alloying mechanism occurring in the very final stage of the lithiation which allows the material to achieve one more lithium per formula unit stored by a

reversible alloying mechanism of lithium with zinc.

The evolution and stability of the SEI layer were also studied in graphite electrodes with X-ray Absorption Spectroscopy and X-ray Photoelectron Spectroscopy during the first charge/discharge cycle. An arsenic-containing compound was used as electrolyte and employed as local probe for XAS As K-edge analysis, giving an insight into the oxidation state and structure of the various As-species formed in the inorganic components. XPS provided complementary information, with a study of the outermost layer of the SEI, on both the organic and inorganic fraction of the SEI. Both XAS and XPS revealed the presence of arsenic with oxidation state 3+ and 5+, possibly in the form of arsenic oxides (As_2O_5, As_2O_3) and arsenic-fluorine compounds (AsF_3, AsF_6^-, Li_xAsF_{3-x}) both deriving from the degradation and precipitation of the electrolyte salts. Moreover, XPS revealed the presence of As^0 (not detected by XAS) that could be present, in a small quantity, only on the outer layer of the SEI. The organic fraction of the SEI has been studied with XPS, showing the presence of different lithium alkyls species and carbonates as result of the degradation of the electrolyte organic solvents. At full lithiation stage, the outer part of the SEI is covered by a film of lithium-carbonates species, this film gets thinner after de-lithiation. Therefore, the SEI may also act as a lithium-ions buffer providing an extra reversible capacity to the anode as recently suggested by our group. We also developed a new set-up for in-situ micro-Raman experiments of battery materials, attempting to measure the evolution and structure of the SEI upon lithiation. While the SEI signal was shown to be very difficult to detect and analyse, we have been able to study the modifications of the graphitic host structure in-operando, in substantial agreement with previous results. Several experiments are still in the data analysis and preparation stage and will be completed soon.

Finally, the structure of Mn-based layered oxides for sodium-ion cathodes cells has been studied with X-ray Absorption Spectroscopy, with the aim of measuring the local structural distortion induced by doping. In fact, doping the material (P2-$Na_{2/3}Mn_{0.8}Fe_{0.2-x}Ti_xO_2$) with electrochemical inactive species (Ti^{4+}, Fe^{3+}) induce a Jahn-Teller distortion of the Mn-O octahedra, and may provide improvements on the electrochemical performances. DFT calculations and XRD experiments substantially confirm this scenario. In our XANES experiments at Mn and Ti K-edges, we proved that the oxidation states of manganese and titanium are in good agreement with the expected ones. Our structural Mn K-edge EXAFS refinement, compared with the

results of DFT calculations and XRD data, confirmed experimentally the Jahn-Teller induced distortion of the structure, with no substantial changes for all the materials under consideration. A slight decrease of the local structural disorder is observed in the material where both Fe and Ti are present with equal proportions.

All of the results listed above have an impact on obtaining better batteries. The study of electrode materials based on conversion-alloying reactions will result in batteries with enhanced capacity (conversion-alloying reactions can deliver 2-3 times more specific capacity than intercalation reactions). Identifying the SEI components and understanding its evolution is key to obtain more stable batteries. Finally, understanding the role of environmentally friendly dopants (such as Ti) in the layered oxides has resulted in electrodes with increased stability: one step more towards commercialization of Na-ion batteries.

Most of the results presented in this thesis have been published in international journals, or are under preparation, and the list of publications follows in the next pages.

List of Publications

1. S. Javad Rezvani, Matteo Ciambezi, Roberto Gunnella, Marco Minicucci, Miguel Àngel Muñoz-Màrquez, Francesco Nobili, Marta Pasqualini, Stefano Passerini, Christian Schreiner, Angela Trapananti, Agnieszka Witkowska, Andrea Di Cicco
   Local Structure and Stability of SEI in Graphite and ZFO Electrodes Probed by As K-Edge Absorption Spectroscopy
   The Journal of Physical Chemistry C 120 (8) (2016)

2. Maider Zarrabeitia, Elena Gonzalo, Matteo Ciambezi, Oier Lakuntza, Francesco Nobili, Angela Trapananti, Andrea Di Cicco, Giuliana Aquilanti, Nebil A Katcho, Juan-Miguel Lopez del Amo, Javier Carrasco, Miguel Àngel Muñoz-Màrquez, Teofilo Rojo
   Unraveling the role of Ti in the stability of positive layered oxide electrodes for rechargeable Na-ion batteries
   Journal of Materials Chemistry A 9 (2019)

3. Matteo Ciambezi, Angela Trapananti, S. Javad Rezvani, Fabio Maroni, Dominic Bresser, Marco Minicucci, Francesco Nobili, Roberto Gunnella, Stefano Passerini, Andrea Di Cicco
   Initial lithiation of carbon-coated zinc ferrite anodes studied by in-situ X-ray absorption spectroscopy
   Radiation Physics and Chemistry (in press)
   doi:10.1016/j.radphyschem.2019.108468

4. S. Javad Rezvani, Yimin Mijiti, Roberto Gunnella, Francesco Nobili, Angela Trapananti, Marco Minicucci, Matteo Ciambezi, Dominic Bresser, Stefano Nannarone, Stefano Passerini, Andrea Di Cicco
   Structure Rearrangements Induced by Lithium Insertion in Metal Alloying Oxide Mixed Spinel Structure Studied by X-ray Absorption Near-edge Spectroscopy
   Journal of Physics and Chemistry of Solids (just accepted)

5. Matteo Ciambezi, Angela Trapananti, S. Javad Rezvani, Fabio Maroni, Dominic Bresser, Marco Minicucci, Francesco Nobili, Roberto Gunnella, Stefano Passerini, Andrea Di Cicco
   In Situ XAS Study of Lithiation Mechanism in Carbon Coated $ZnFe_2O_4$

Nanoparticles Anodes for Li-ion Batteries
(In preparation)

Author's Contributions to the Experiments and Analysis

- Chapter 4: The author participated in the experimental part, beginning from the proposal at ESRF (Ref. No 52300), then he was present during the beam-time at beamline BM23 (experiment MA-3176). Furthermore, he took care of the data analysis (under the supervision of Prof. A. Di Cicco and Dr. A. Trapananti), performing the initial calibrations, a qualitative analysis of the XANES and the systematic analysis and simulations of the EXAFS spectra. He presented his contributions at several international conferences and schools, producing posters and conference proceedings. He was first author and corresponding author of the manuscript *'Initial lithiation of carbon-coated zinc ferrite anodes studied by in-situ X-ray absorption spectroscopy'* and co-author of the manuscript *'Structure Rearrangements Induced by Lithium Insertion in Metal Alloying Oxide Mixed Spinel Structure Studied by X-ray Absorption Near-edge Spectroscopy'*, both published in international journals.

- Chapter 5: The author participated in the experiment at ESRF BM08 (experiment MA-2716) and took care of the EXAFS data analysis presented in Section *5.3*. He participated in the writing and was co-author of the manuscript *'Local Structure and Stability of SEI in Graphite and ZFO Electrodes Probed by As K-Edge Absorption Spectroscopy'* which was published in an international journal. Moreover, during his visiting period in Spain at CICenergigune, he took care of the data analysis (under the supervision of Dr. Muñoz) of the XPS data of graphite electrodes shown in the chapter. Furthermore, at University of Camerino, the author designed a novel experimental set-up for in-situ and ex-situ Raman spectroscopy on electrochemical cells: he designed and produced various 3D-printed appliances for adapting the galvanostat-potentiostat to the in-situ electrochemical cell and to the micro-Raman spectrometer. He also designed and tested several 3D-printed sealed cells for ex-situ micro-Raman spectroscopy. He synthesised (with the collaboration of Dr. Marta Pasqualini) the specific self-standing electrodes required for the in-situ cell. The author personally took care of all the phases in the experimental and data analysis of the Raman experiments,

also of several other compounds not presented in this thesis.

- Chapter 6: The author participated in the sample preparation during his visiting period at CICenergigune. He took care of preparing the samples with the optimal composition required for the XAS experiments. At University of Camerino, he performed (under the supervision of Prof. A. Di Cicco and Dr. A. Trapananti) the XANES and EXAFS analysis presented in the Chapter. He participated in the writing of the manuscript *'Unraveling the role of Ti in the stability of positive layered oxide electrodes for rechargeable Na-ion batteries'* (in particular of the EXAFS section) which has been published in an international journal.

Conferences and Schools

- **EUSpec training school - Multiple scattering codes**
  University of Rennes 1, France, *June 2016*
- **4th MSNano conference on recent advances in the multiple scattering spectroscopies**
  University of Rennes 1, France, *June 2016*
- **SILS 24th conference**
  University of Bari, Italy, *September 2016*
- **Power our Future 2017 - 3rd International forum on progress of battery and capacitor**
  Vitoria-Gasteiz, Spain, *July 2017*
- **XIV SILS School on synchrotron radiation: fundamentals, methods and applications**
  Muggia - Elettra Sincrotrone Trieste, Italy, *September 2017*
- **3rd joint AIC-SILS conference**
  CNR Rome, Italy, *June 2018*
- **XAFS18 - 17th international conference on X-ray Absorption Fine Structure**
  Krakow, Poland, *July 2018*

Appendix A

XAS Data-Analysis

A.1 Absorption cross section

In this section, we will give a brief theoretical derivation of the X-ray absorption cross section σ, to better interpret the physical meaning of the EXAFS structural signal $\chi(k)$. The mechanism of absorbing an electromagnetic wave by matter can be interpreted by an elementary process involving a photon and an atom (also called photoelectric effect). At certain energies, a photon can be absorbed by the atom which becomes excited, this corresponds to the promotion of an electron to a higher energy level. The Hamiltonian of an atomic system in an electromagnetic field can be approximated as:

$$H = H_0 + H_{int}(t) \tag{A.1}$$

where H_0 is the time independent - non interactive atomic Hamiltonian, and $H_{int}(t)$ is the Hamiltonian which gives the interaction with the electromagnetic field depending on the vector potential $\mathbf{A}$; in particular we have:

$$H_{int}(t) = \frac{e}{m}\mathbf{A} \cdot \mathbf{p} \tag{A.2}$$

Fermi's golden rule gives the transition rate (probability of transition per unit time) from the initial quantum state $|i\rangle$ to the final $|f\rangle$, in presence of a perturbation $V(t)$:

$$W_{fi} = \frac{2\pi}{\hbar}|\langle f|V(t)|i\rangle|^2 \delta(E_f - E_i) \tag{A.3}$$

Which in our case becomes:

$$W_{fi} = \frac{2\pi}{\hbar} \sum_f |\langle f|H_{int}(t)|i\rangle|^2 \delta(E_f - E_i - \hbar\omega) \tag{A.4}$$

where we sum over all the final accessible states permitted by energy conservation, E_f is the total energy of the final configuration, E_i is the unperturbed system energy and $\hbar\omega$ is the energy of the absorbed photon. Let's introduce few useful approximations to derive an efficacious form for the cross-section σ.

1. *One electron* approximation for the states $|f\rangle$ and $|i\rangle$. Many electrons states can be described as N contributions of single electron states:

$$|i\rangle = \sqrt{N!} \sum_n c_n A\{\Phi_c(\mathbf{r})\Phi_{i,n}^{N-1}(\mathbf{r}_1, \ldots, \mathbf{r}_N)\} \tag{A.5}$$

$$|f\rangle = \sqrt{N!} A \sum_m \{\Phi_f^m(\mathbf{r})\Phi_{f,m}^{N-1}(\mathbf{r}_1, \ldots, \mathbf{r}_N)\} \tag{A.6}$$

   where Φ_c and Φ_f are the single electron wave functions for the initial state (single *core* electron) and final, the Φ^{N-1} are the Slater determinants of the remaining $N-1$ electrons, A is the anti-symmetrizing operator [254].

2. *Sudden* approximation. This further simplification comes from the assumption that the interaction involves only the bound core electron, such that Eq. A.4 becomes:

$$W_{fi} = \frac{2\pi e}{\hbar m} \sum_f |\langle \Phi_f|H_{int}(t)|\Phi_c\rangle\langle \Phi_f^{N-1}|\Phi_i^{N-1}\rangle|^2 \delta(E_f - E_i - \hbar\omega) \tag{A.7}$$

   The overlap between the initial and final states for all the passive electrons that are not directly excited by the incident photon is indicated by: $|S_0|^2 = |\langle \Phi_f^{N-1}|\Phi_i^{N-1}\rangle|^2$. $|S_0|^2$ represents the cross-section reduction due to the atomic relaxation and it is typically introduced as an empiric parameter, with values in the range $0.7 - 1$, when calculating the cross-section.

3. *Dipole* approximation. In our system the photon wavelength is larger than the dimensions of the core (1 Å is the typical wave length of an X-photon, while the core state Φ_c extends for less than 0.1 Å), so the electromagnetic field (thus $\mathbf{A}$)

can be considered constant.

$$e^{i\mathbf{k}\cdot\mathbf{r}} \approx 1 + i\mathbf{k}\cdot\mathbf{r} + \ldots \overset{\text{dipole}}{\simeq} 1 \quad \Rightarrow \quad \mathbf{A} = \hat{\epsilon}A = C\hat{\epsilon}e^{i\mathbf{k}\cdot\mathbf{r}} \overset{\text{dipole}}{\simeq} C\hat{\epsilon} \tag{A.8}$$

Considering these approximation we can write Eq. A.7 as:

$$W_{fi} = \frac{2\pi eC}{\hbar m} \sum_f |\langle \Phi_f | \hat{\epsilon}\cdot\mathbf{p} | \Phi_c \rangle|^2 \, S_0^2 \, \delta(E_f - E_i - \hbar\omega) \tag{A.9}$$

In few steps and remembering that $\sigma = W/\Psi$, where Ψ is the flux of incoming photons, we have:

$$\sigma_0 = 4\pi^2 \alpha\hbar\omega \sum_f |\langle \Phi_f | \hat{\epsilon}\cdot\mathbf{r} | \Phi_c \rangle|^2 \, S_0^2 \, \delta(E_f - E_i - \hbar\omega) \tag{A.10}$$

where $\alpha = 1/137$ is the fine-structure constant and σ_0 is the cross section for a single atom system.

A.2 Analytical expression for EXAFS signal

In this section we will briefly present the fundamentals of the scattering theory of a wave packet by a perturbative potential [255, 256], then extend these results to the calculations of the cross section. The Hamiltonian of the system is:

$$H = H_0 + V \tag{A.11}$$

where V is a potential that we can consider different from zero in a spherical region of radius a. Asymptotically the function Ψ^+ (solution of $H\Psi^+ = E\Psi^+$) can be written as a superposition of a plane wave and a spherical wave[1]:

$$\Psi^+(\mathbf{r}) \overset{\text{r} \geq \text{a}}{=} \frac{1}{(2\pi)^{2/3}} \left(e^{i\mathbf{k}\cdot\mathbf{r}} + f_k(\hat{r}) \frac{e^{ikr}}{r} \right) \tag{A.12}$$

The factor $f_k(\hat{r})$ is the scattering amplitude, from which can be derived the differential cross section ($d\sigma/d\Omega = |f_k(\hat{r})|^2$). Easier calculations can be obtained with the use of the *Muffin-Tin* approximation (MT) for the atomic potential. This is represented

[1] This result can be showed using the Green's function formalism, which will be discussed in the following section.

as a collection of spherically symmetric potentials centered on each atomic site (with radii chosen according to Norman criterion [257]) embedded in a constant potential interstitial region; this approximation has been shown to be sufficiently accurate in the EXAFS region, because photoelectrons with kinetic energies greater than $E_k \sim 30\,eV$ are only weakly sensitive to the details of the effective potential. Let's write the solutions of Eq. A.11 as separated functions for the radial and angular part.

$$\Psi^{+}(r,\theta,\phi) = R_{l,k}(r)Y_{l,m}(\theta,\phi) \tag{A.13}$$

The radial part, outside the MT sphere ($r > a$) can be simplified as:

$$R_{l,k}(K) = \frac{\sin(kr - \frac{\pi}{2}l + \delta_l)}{kr} \tag{A.14}$$

where δ_l is the phase-shift of the outgoing wave coming from one MT sphere. Once all the phase-shifts are well known it's possible to derive the scattering amplitude as following:

$$f_k(\theta) = \frac{1}{k}\sum_{l=0}^{\infty}(sl+1)e^{i\delta_l(k)}\sin\delta_l(k)P_l(\cos\theta) \tag{A.15}$$

where P_l are Legendre polynomials. In the MT approximation the partial wave expansion of Eq. A.15 will converge quickly. The phase-shift coefficients can be derived applying the boundary conditions for the MT spheres to the solutions of Eq. A.11; from this it's possible to derive the scattered wave function Ψ_k^{+} with equations A.12 and A.15. Now we can express Eq. 3.3 in an analytical form. The cross section σ is measured in the experiment; it's different from σ_0 since we consider a final state Φ_f as a composition of interfering scattered and back-scattered waves, while σ_0 only takes in account the analytical final state Φ_f derived by the scattering theory. The final state is critical for solving scattering problems, and can be derived using equations A.12 and A.15. Using the plane wave and single scattering approximations, the signal $\chi(k)$ can be considered as a sum of sinusoidal contributions:

$$\chi(k) = \sum_j A(r_j,k)\sin(2kr_j + \Phi_j(k))e^{-2\sigma_j^2k^2}e^{-2r_j/\lambda_j(k)} \tag{A.16}$$

where $e^{-2\sigma_j^2k^2}$ express the thermal disorder and $e^{-2r_j/\lambda_j(k)}$ describes the EXAFS signal reduction due to the mean free path λ of the electron in the condensed matter. The

amplitude factor $A(r_j, k)$ is proportional to the number of atoms (N_j); inversely proportional to kR_j^2 (where R_j is the distance between the photo absorber and the others atoms in the shell); The frequency of the signal is dominated by the term $2kR_j$ and it's slightly shifted by the phase factor $\Phi_j(k)$, this means that EXAFS signals from further shells have higher frequencies and go to zero more rapidly than closer shells. At the beginning of EXAFS analysis, Fourier transform of $\chi(k)$ was the preferred method to interpret the signal [138]. These results rely on very strong approximations (for example the single scattering approximation) which leads to only qualitative results. In the last two decades have been developed more powerful and refined analysis methods of the EXAFS signal based on *multiple scattering theory* [142, 143].

A.3 Multiple-scattering expansion

In this section will be shown the fundamentals steps for calculation of the cross-section and it will be given a basic description of the multiple scattering theory, focusing more on the physical meaning of the newly introduced hypothesis than on the complex formalism of the theory. For the evaluation of the cross section from Eq. A.10 we will introduce the Green's function formalism [258, 259]. The sum over the final states can be expressed in terms of the Green's function representing the propagation of an electronic wave of energy E between the two sites $\mathbf{r}$ and $\mathbf{r}'$ in the potential generated by all atoms. Using the relation:

$$G(E) = \lim_{\eta \to 0^+} \frac{1}{\hbar\omega + E_i - E_f - i\eta} = \mathcal{P}\left[\frac{1}{\hbar\omega + E_i - E_f}\right] + i\pi\delta(\hbar\omega + E_i - E_f) \quad \text{(A.17)}$$

we get the following relation for the cross section,

$$\sigma = 4\pi^2 \alpha \hbar\omega \, \Im\langle i|(\hat{\epsilon}^* \cdot \mathbf{r}')\frac{1}{\pi}G(\mathbf{r}, \mathbf{r}', E_i + \hbar\omega)(\hat{\epsilon} \cdot \mathbf{r})|i\rangle \quad \text{(A.18)}$$

Since the initial core state $\langle i|$ is a well localized function, the integral in A.18 is different from zero only when $\mathbf{r}$ and $\mathbf{r}'$ fall into the MT sphere centered on the photo-absorber. In this particular case, the equation A.18 has an exact solution:

$$\frac{1}{\pi}G(\mathbf{r}_n, \mathbf{r'}_n, E) = \sum_{LL'} R_L^n(\mathbf{r}_n, E)\tau_{nn}^{LL'} R_n^{L'}(\mathbf{r'}_n, E) + \sum_L R_L^n(\mathbf{r}_n, E) S_L^n(\mathbf{r'}_n, E) \quad \text{(A.19)}$$

where R_L^n, S_L^n are the solutions, respectively regular and irregular in the origin $\mathbf{r}_n = 0$, of the Schroedinger equation in the MT sphere. These functions are normalized to be continuous and derivable with the spherical waves solutions for $r > R_{MT}$. The term $\tau_{nn}^{LL'}$, generally called *scattering path operator*, is a matrix which represents the multiple scattering of the photoelectron:

$$\tau_{ij}^{LL'} = (T^{-1} - G)^{-1}|_{ij}^{LL'} = (I - TG)^{-1}\,|_{ij}^{LL'} \tag{A.20}$$

where I is the unitary operator, T and G are the *atomic scattering* and *spherical wave propagator* matrices respectively. An element of one of these matrices is indicated by the indices i, j running over the different atomic centers in the structure, and by a further set of angular momenta L, L' . Each couple of atomic indices identifies an atomic block of the matrices. T is a block diagonal matrix ($T_{ij} = t_i\delta_{ij}$) and, in the MT approximation for the potential, the scattering matrix for the atomic center i is diagonal in the L indices ($t_i^{LL'} = t_i^l\delta_{LL'}$), since the angular momentum is conserved in the scattering from a single site. In terms of the l-th potential phase shift δ_i^l at site i, we have: $t_i^l = e^{i\delta_i^l}\sin\delta_i^l$. The elements of the wave propagator matrix G are expressed in terms of *Gaunt coefficients* $C_{L,L''}^{L'}$ and Hankel spherical functions $h_l^+(kr_{ij})$. The propagators $G_{ij}^{LL'}$ describe the partial wave expansion of the spherical wave centered in the site i with respect to a second site j. Thus diagonal elements of G matrix are all null. To derive the absorption cross section from a core level, we can determine the Green function in the sphere centered on the photo-absorber atom ($n = 0$); we can, then, use Eq. A.19 considering only the case $n = 0$. If the MT potential is real, the cross section can be written as:

$$\sigma = (l_0 + 1)\sigma_0^{l_0+1}\chi^{l_0+1} + l_0\sigma_0^{l_0-1}\chi^{l_0-1} \tag{A.21}$$

where we have the single atom cross section:

$$\begin{aligned}\sigma_0^{l_0\pm1} &= \frac{8}{3}\pi^2\alpha\hbar\omega\left(M_{l_0,l_0\pm1}\right)^2\Im\left(T|_{l_0\pm1,m\,l_0\pm1,m}^{00}\right)\\ &= \frac{8}{3}\pi^2\alpha\hbar\omega\left(M_{l_0,l_0\pm1}\right)^2\sin^2\delta_{l_0\pm1}^0\end{aligned} \tag{A.22}$$

and a structural signal:

$$\chi^{l_0\pm1} = \Im\left[\frac{1}{2(l_0\pm1)+1}\cdot\frac{1}{\sin^2\delta_{l_0\pm1}^0}\left(\sum_m\left(I - TG\right)^{-1}T|_{l_0\pm1,m\,l_0\pm1,m}^{00}\right)\right] \tag{A.23}$$

Information on the local structure around the photo-absorbing site is stored in the structural term $\chi(k)$. From equation A.23 it is clear that the relationship between geometry and signal is strongly non-linear (the G matrix appears in an inverse expression $(I + GT)^{-1}$) and for this reason the effects of different structural arrangements on the cross section can hardly be decoupled. The non-linearity is the mathematical consequence of the strong coupling of the photo-electron with the surrounding atoms and it is the major reason responsible for the difficulty in analyzing XAS data. The traditional method for treating the inverse expression $(I + GT)^{-1}$ is the multiple-scattering expansion [260]. We assume that the norm of the TG matrix, defined as the maximum modulus of its eigenvalues, is less than one, $||TG|| < 1$; in this case the formal matrix expansion $(I - TG)^{-1} = (I + TG + TGTG + TGTGTG + \cdots)$ is convergent and gives rise to the multiple scattering series. The condition above is verified in the EXAFS region (around 50 eV above the edge). We can write equation A.23 in the following form:

$$\chi^{l_0\pm1} = \Im\left[\frac{1}{2(l_0 \pm 1) + 1} \cdot \frac{1}{\sin^2 \delta^0_{l_0\pm1}} \left(\sum_m (T + TGT + TGTGT + \cdots)\,|^{00}_{l_0\pm1,m\,l_0\pm1,m}\right)\right] \tag{A.24}$$

then the structural signal can be expanded in a multiple scattering series:

$$\chi^{l_0\pm1} = \sum_n \chi_n^{l_0\pm1} \tag{A.25}$$

Thus, in generic terms we obtain:

$$\chi^{l_0\pm1} = \Im\left[\frac{1}{2(l_0 \pm 1) + 1} \cdot \frac{1}{\sin^2 \delta^0_{l_0\pm1}} \left(\sum_m (TG)^n T|^{00}_{l_0\pm1,m\,l_0\pm1,m}\right)\right] \tag{A.26}$$

Indicate in a more compact form

$$\left[\sum_m (TG)^n T|^{00}_{L_0,L_0}\right] = \left[\sum_m \Xi_n^{\{0i,\cdots,j0\}}|^{00}_{L_0,L_0}\right] \tag{A.27}$$

and specifically: $\Xi^{0i0} = G_{0,i}t_iG_{i,0}t_0$ for χ_2^{0i0}, $\Xi^{0ij0} = G_{0,j}t_jG_{j,i}t_iG_{i,0}t_0$ for χ_3^{0ijk0}, and $\Xi^{0ijk0} = G_{0,k}t_kG_{k,j}t_jG_{j,i}t_iG_{i,0}t_0$ for χ_4^{0ijk0}. In the above expression, each term χ_n of the multiple scattering series can be related to a scattering path starting and ending at the origin with the constraint that successive sites must be distinct. Therefore the sums in the above expressions extend to all of the distinct sequences of sites of the

type $0ijk\cdots pqr0$, with the constraint that i and r cannot be 0 and in general that any two successive indexes must be different. Note that the internal sites $j, k, \cdots, p, q$ can be the origin again. The χ_n signals are oscillating functions of the type:

$$\chi_n(k) = A(k, R)\sin\left[kR_p + \phi(k, R)\right] \tag{A.28}$$

where A and ϕ are smooth functions of k and of the geometrical parameters R. The relevant frequency of the signal is determined by the path length R_p. The χ_2 terms probe the relative position of atoms 0 and i, whereas χ_3 terms probe the positions of the atoms 0, i and j and therefore they are sensitive to the two-particle and three-particle distribution respectively. Starting with the χ_4 term the situation becomes more complicated, in fact, while the general $0ijk0$ probes four-particle correlations, special paths like $0i0k0$ or $0iji0$ and $0i0i0$ probe lower-order correlations. In general at order n, in χ_n there are paths involving all particle distributions from 2 to n if n is even or from 3 to n if n is odd.

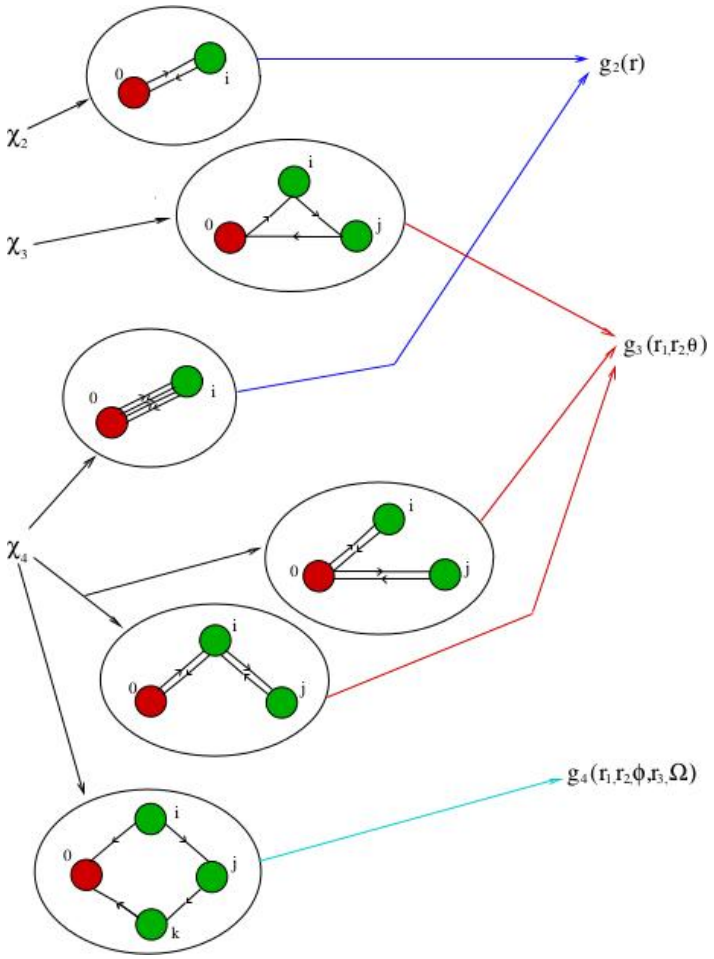

Figure A.1: Graphical representation of the different contributions coming from the multiple-scattering expansion.

A.4 n-body decomposition

A different approach to the solution of the XAS structural problem is based on a n-body decomposition of the cross-section, which partially avoids the drawbacks related to the multiple scattering expansion. Let's indicate, as usual, the photo-absorber with 0 and the surrounding atoms with $i, j, k, \cdots$. Define now the n-atom cross section:

- $\sigma(0) = \sigma_0$, atomic cross section;
- $\sigma(0, i)$, cross section of the structure including atoms 0 and i only;
- $\sigma(0, i, j)$, cross section of the structure including atoms 0, i and j;

- $\sigma(0,i,j,k)$, cross section of the structure including atoms 0, i, j and k;

and so on. In the MT approximation these cross sections can be easily calculated using the appropriate number of blocks in the G and T matrices. The irreducible n-body cross sections $\sigma^{(n)}(0,i_1,\cdots,i_{n-1})$ can be defined inductively starting from these quantities. For $n=2$ it is the contribution due to the presence of a second atom i that is given by:

$$\sigma^{(2)}(0,i) = \sigma(0,i) - \sigma_0 \tag{A.29}$$

For $n=3$ the cross section for atoms 0, i and j can be decomposed into the photo-absorber contribution, the two $0-i$ and $0-j$ two-body contributions, and an irreducible three-body contribution, that is given, by this definition as:

$$\sigma^{(3)}(0,i,j) = \sigma(0,i,j) - \sigma^{(2)}(0,i) - \sigma^{(2)}(0,j) - \sigma_0 \tag{A.30}$$

By induction, we can define the irreducible n-body contributions as:

$$\begin{aligned}\sigma^{(n)}(0,i,j,\cdots,r) = \sigma(0,i,j,\cdots,r) - \sum \sigma^{(n-1)}[0,S(n-2)] - \\ - \sum \sigma^{(n-2)}[0,S(n-3)] - \cdots - \sum_i \sigma^{(2)}(0,i) - \sigma_0\end{aligned} \tag{A.31}$$

where $S(m)$ indicates a choice of m elements among $i,j,\cdots,r$ and the sums are extended to all possible choices. Solving equation A.31 for the total cross section $\sigma(0,i,j,\cdots,r)$ a useful expansion for this quantity in the n-body cross sections is obtained:

$$\begin{aligned}\sigma(0,i,j,\cdots,r) = \sigma_0 + \sum_i \sigma^{(2)}(0,i) + \sum_{i,j} \sigma^{(3)}(0,i,j) + \\ + \sum_{i,j,k} \sigma^{(4)}(0,i,j,k) + \cdots + \sigma^{(n)}(0,i,j,\cdots,r)\end{aligned} \tag{A.32}$$

By introducing the dimensionless quantities $\gamma^{(n)} = \sigma^{(n)}/\sigma_0$, representing the irreducible n-body contributions to the EXAFS, we arrive to an equivalent expansion for the dimensionless experimental structural signal χ that differs substantially from the multiple scattering series:

$$\begin{aligned}\chi(0,i,j,\cdots,r) = \sum_i \gamma^{(2)}(0,i) + \sum_{i,j} \gamma^{(3)}(0,i,j) + \\ + \sum_{i,j,k} \gamma^{(4)}(0,i,j,k) + \cdots + \gamma^{(n)}(0,i,j,\cdots,r)\end{aligned} \tag{A.33}$$

In this equation a linear relationship between structure and signal is obtained. The equation contains a finite number of terms if the system is finite (cluster) and becomes a series only in the case of a system with an infinite number of atoms. In this case it is expected anyway, due to mean free path effects, that the higher order n-body terms are smaller than the lower order ones and that the series has very good convergence properties. The $\gamma^{(n)}$ signals are associated with well precise n-body arrangements of the atoms and two different methods for their calculation are available: the first makes use of total cross section calculations and continued fraction expansions, the second consists in expanding the $\gamma^{(n)}$ signals in an appropriate multiple scattering series (see Fig. A.2 for example). Generally speaking the $\gamma^{(n)}$ signals are, like the χ_n , oscillating functions of the photo-electron wave-vector modulus k. The dominant frequency is that associated with the shortest path (lower order contribution) of the corresponding multiple scattering series. The oscillation shape has not necessarily a regular sinusoidal behavior because of the presence of higher harmonics.

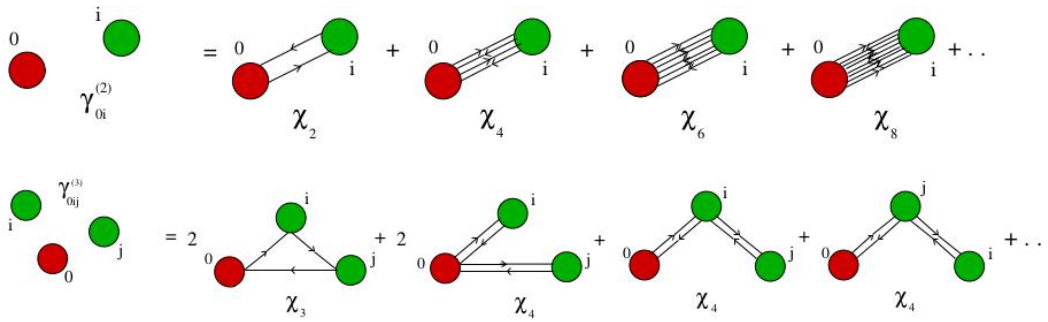

Figure A.2: Graphical representation of the MS expansion for the $\gamma^{(2)}$ and $\gamma^{(3)}$ signals.

Bibliography

[1] W. H. Organization, et al., COP24 special report: health and climate change.

[2] R. Reuveny, Climate change-induced migration and violent conflict, Political geography 26 (6) (2007) 656–673. doi:10.1016/j.polgeo.2007.05.001.

[3] S. Z. Attari, D. H. Krantz, E. U. Weber, Climate change communicators' carbon footprints affect their audience's policy support, Climatic Change (2019) 1–17doi:10.1007/s10584-019-02463-0.

[4] UNFCCC. Adoption of the Paris Agreement. Report No. FCC-C/CP/2015/L.9/Rev.1, (UNFCCC, 2015).

[5] J. Rogelj, M. Den Elzen, N. Höhne, T. Fransen, H. Fekete, H. Winkler, R. Schaeffer, F. Sha, K. Riahi, M. Meinshausen, Paris Agreement climate proposals need a boost to keep warming well below 2 C, Nature 534 (7609) (2016) 631. doi:10.1038/nature18307.

[6] United Nations Framework Convention on Climate Change, 2015).

[7] R. Knutti, J. Rogelj, J. Sedláček, E. M. Fischer, A scientific critique of the two-degree climate change target, Nature Geoscience 9 (1) (2016) 13.

[8] UNFCCC. United Nations Framework Convention on Climate Change. Report No. FCCC/INFORMAL/84, (UNFCCC, 1992).

[9] Global energy & CO2 status report. Vienna : International Energy Agency (2017).

[10] I. R. E. Agency, Renewable energy: a key climate solution. Abu Dhabi, 2017.

[11] I. C. Change, et al., Mitigation of climate change, Contribution of Working Group III to the Fifth Assessment Report of the Intergovernmental Panel on Climate Change 1454.

[12] H. Ibrahim, A. Ilinca, J. Perron, Energy storage systems. Characteristics and comparisons, Renewable and sustainable energy reviews 12 (5) (2008) 1221–1250. doi:10.1016/j.rser.2007.01.023.

[13] J. EASE/EERA, European Energy Storage Technology Development Roadmap, 2017.

[14] I. E. Agency, Technology Roadmap Energy Storage,, 2014.

[15] Z. Yang, J. Zhang, M. C. Kintner-Meyer, X. Lu, D. Choi, J. P. Lemmon, J. Liu, Electrochemical energy storage for green grid, Chemical reviews 111 (5) (2011) 3577–3613. doi:10.1021/cr100290v.

[16] C. Daniel, J. O. Besenhard, Handbook of battery materials, John Wiley & Sons, 2013.

[17] D. Linden, T. B. Reddy (Eds.), Handbook of batteries, 3rd Edition, McGraw-Hill handbooks, McGraw-Hill, New York, 2002.

[18] M. Armand, J. Tarascon, Issues and challenges facing rechargeable batteries, Nature 414 (2001) 359–367.

[19] W. Van Gool, Fast ion transport in solids, solid state batteries and devices.(Proceedings of the NATO-sponsored advanced study institute of fast ion transport in solids, solid state batteries and devices, Belgirate, Italy 5-15 September 1972).

[20] M. S. Whittingham, Electrical energy storage and intercalation chemistry, Science 192 (4244) (1976) 1126–1127. doi:10.1126/science.192.4244.1126.

[21] M. S. Whittingham, Chalcogenide battery, uS Patent 4,009,052 (Feb. 1977).

[22] B. Scrosati, K. Abraham, W. A. van Schalkwijk, J. Hassoun, Lithium batteries: advanced technologies and applications, Vol. 58, John Wiley & Sons, 2013.

[23] M. Armand, Intercalation electrodes, in: Materials for advanced batteries, Springer, 1980, pp. 145–161. doi:10.1007/978-1-4684-3851-2_7.

[24] D. Murphy, F. Di Salvo, J. Carides, J. Waszczak, Topochemical reactions of rutile related structures with lithium, Materials Research Bulletin 13 (12) (1978) 1395–1402. doi:10.1016/0025-5408(78)90131-9.

[25] M. Lazzari, B. Scrosati, A cyclable lithium organic electrolyte cell based on two intercalation electrodes, Journal of the Electrochemical Society 127 (3) (1980) 773–774. doi:10.1149/1.2129753.

[26] K. Mizushima, P. Jones, P. Wiseman, J. Goodenough, Li_xCoO_2: A new cathode material for batteries of high energy density, Solid State Ionics 3 (1981) 171–174.

[27] J. Besenhard, G. Eichinger, High energy density lithium cells: Part I. Electrolytes and anodes, Journal of Electroanalytical Chemistry and Interfacial Electrochemistry 68 (1) (1976) 1–18. doi:10.1016/0368-1874(76)80027-5.

[28] R. Yazami, P. Touzain, A reversible graphite-lithium negative electrode for electrochemical generators, Journal of Power Sources 9 (3) (1983) 365–371. doi:10.1016/0378-7753(83)87040-2.

[29] S. Basu, C. Zeller, P. Flanders, C. Fuerst, W. Johnson, J. Fischer, Synthesis and properties of lithium-graphite intercalation compounds, Materials Science and Engineering 38 (3) (1979) 275–283. doi:10.1016/0025-5416(79)90132-0.

[30] A. Yoshino, K. Sanechika, T. Nakajima, USP4, 668,595, 1985; A, Yoshino, K. Sanechika, T. Nakajima, JP1989293.

[31] D. Deng, Li-ion batteries: basics, progress, and challenges, Energy Science & Engineering 3 (5) (2015) 385–418. doi:10.1002/ese3.95.

[32] T. Nagaura, Lithium ion rechargeable battery, Progress in Batteries & Solar Cells 9 (1990) 209.

[33] S.-T. Myung, Y. Hitoshi, Y.-K. Sun, Electrochemical behavior and passivation of current collectors in lithium-ion batteries, Journal of Materials Chemistry 21 (27) (2011) 9891–9911. doi:10.1039/c0jm04353b.

[34] P. Verma, P. Maire, P. Novák, A review of the features and analyses of the solid electrolyte interphase in Li-ion batteries, Electrochimica Acta 55 (22) (2010) 6332–6341. doi:10.1016/j.electacta.2010.05.072.

[35] M. R. Palacin, Recent advances in rechargeable battery materials: a chemist's perspective, Chemical Society Reviews 38 (9) (2009) 2565–2575. doi:10.1039/b820555h.

[36] S. Goriparti, E. Miele, F. De Angelis, E. Di Fabrizio, R. P. Zaccaria, C. Capiglia, Review on recent progress of nanostructured anode materials for Li-ion batteries, Journal of Power Sources 257 (2014) 421–443. doi:10.1016/j.jpowsour.2013.11.103.

[37] R. Marom, S. F. Amalraj, N. Leifer, D. Jacob, D. Aurbach, A review of advanced and practical lithium battery materials, Journal of Materials Chemistry 21 (27) (2011) 9938–9954. doi:10.1039/c0jm04225k.

[38] M. Winter, J. O. Besenhard, M. E. Spahr, P. Novak, Insertion electrode materials for rechargeable lithium batteries, Advanced Materials 10 (10) (1998) 725–763. doi:10.1002/(sici)1521-4095(199807)10:10<725::aid-adma725>3.0.co;2-z.

[39] B. N. Loeffler, D. Bresser, S. Passerini, M. Copley, Secondary lithium-ion battery anodes: from first commercial batteries to recent research activities, Johnson Matthey Technology Review 59 (1) (2015) 34–44. doi:10.1595/205651314x685824.

[40] J. R. Dahn, T. Zheng, Y. Liu, J. Xue, Mechanisms for lithium insertion in carbonaceous materials, Science 270 (5236) (1995) 590–593. doi:10.1126/science.270.5236.590.

[41] R. Fong, U. Von Sacken, J. R. Dahn, Studies of lithium intercalation into carbons using nonaqueous electrochemical cells, Journal of the Electrochemical Society 137 (7) (1990) 2009–2013. doi:10.1149/1.2086855.

[42] D. Aurbach, Y. Ein-Eli, O. Chusid, Y. Carmeli, M. Babai, H. Yamin, The Correlation Between the Surface Chemistry and the Performance of Li-Carbon Intercalation Anodes for Rechargeable 'Rocking-Chair'Type Batteries, Journal of the Electrochemical Society 141 (3) (1994) 603–611.

[43] X. Yuan, H. Liu, J. Zhang, Lithium-ion batteries: advanced materials and technologies, CRC press, 2011. doi:10.1201/b11292.

[44] J. Besenhard, M. Hess, P. Komenda, Dimensionally stable Li-alloy electrodes for secondary batteries, Solid State Ionics 40 (1990) 525–529. doi:10.1016/0167-2738(90)90062-v.

[45] C.-H. Yim, F. M. Courtel, Y. Abu-Lebdeh, A high capacity silicon–graphite composite as anode for lithium-ion batteries using low content amorphous silicon and compatible binders, Journal of Materials Chemistry A 1 (28) (2013) 8234–8243. doi:10.1039/c3ta10883j.

[46] N. Nitta, F. Wu, J. T. Lee, G. Yushin, Li-ion battery materials: present and future, Materials Today 18 (5) (2015) 252–264. doi:10.1016/j.mattod.2014.10.040.

[47] P. Poizot, S. Laruelle, S. Grugeon, L. Dupont, J.-M. Tarascon, Nano-sized transition-metal oxides as negative-electrode materials for lithium-ion batteries, Nature 407 (6803) (2000) 496–499. doi:10.1038/35035045.

[48] D. Bresser, F. Mueller, M. Fiedler, S. Krueger, R. Kloepsch, D. Baither, M. Winter, E. Paillard, S. Passerini, Transition-Metal-Doped Zinc Oxide Nanoparticles as a New Lithium-Ion Anode Material, Chemistry of Materials 25 (24) (2013) 4977–4985. doi:10.1021/cm403443t.

[49] D. Bresser, E. Paillard, R. Kloepsch, S. Krueger, M. Fiedler, R. Schmitz, D. Baither, M. Winter, S. Passerini, Carbon Coated $ZnFe_2O_4$ Nanoparticles for Advanced Lithium-Ion Anodes, Advanced Energy Materials 3 (4) (2013) 513–523. doi:10.1002/aenm.201200735.

[50] D. Bresser, S. Passerini, B. Scrosati, Leveraging valuable synergies by combining alloying and conversion for lithium-ion anodes, Energy & Environmental Science 9 (11) (2016) 3348–3367. doi:10.1039/c6ee02346k.

[51] M. Obrovac, V. Chevrier, Alloy negative electrodes for Li-ion batteries, Chemical Reviews 114 (23) (2014) 11444–11502. doi:10.1021/cr500207g.

[52] D. Larcher, S. Beattie, M. Morcrette, K. Edstroem, J.-C. Jumas, J.-M. Tarascon, Recent findings and prospects in the field of pure metals as negative electrodes for Li-ion batteries, Journal of Materials Chemistry 17 (36) (2007) 3759–3772. doi:10.1039/b705421c.

[53] N. Nitta, G. Yushin, High-capacity anode materials for lithium-ion batteries: choice of elements and structures for active particles, Particle & Particle Systems Characterization 31 (3) (2014) 317–336.

[54] R. Chen, T. Zhao, X. Zhang, L. Li, F. Wu, Advanced cathode materials for lithium-ion batteries using nanoarchitectonics, Nanoscale Horizons 1 (6) (2016) 423–444. doi:10.1039/c6nh00016a.

[55] M. Pasqualini, Investigation of interfacial and transport properties of electrodes for Li-ion and Na-ion batteries, Ph.D. thesis, University of Camerino (2017).

[56] N. Bensalah, H. Dawood, Review on synthesis, characterizations, and electrochemical properties of cathode materials for lithium ion batteriesdoi:10.4172/2169-0022.1000258.

[57] C. Julien, A. Mauger, K. Zaghib, H. Groult, Comparative issues of cathode materials for Li-ion batteries, Inorganics 2 (1) (2014) 132–154. doi:10.3390/inorganics2010132.

[58] C. Daniel, D. Mohanty, J. Li, D. L. Wood, Cathode materials review, in: AIP Conference Proceedings, Vol. 1597, AIP, 2014, pp. 26–43. doi:10.1063/1.4878478.

[59] J. Dahn, U. Von Sacken, M. Juzkow, H. Al-Janaby, Rechargeable $LiNiO_2$/carbon cells, Journal of the Electrochemical Society 138 (8) (1991) 2207–2211.

[60] T. Ohzuku, Y. Makimura, Layered lithium insertion material of $LiCo_{1/3}Ni_{1/3}Mn_{1/3}O_2$ for lithium-ion batteries, Chemistry Letters 30 (7) (2001) 642–643. doi:10.1246/cl.2001.642.

[61] Y.-K. Sun, S.-T. Myung, B.-C. Park, J. Prakash, I. Belharouak, K. Amine, High-energy cathode material for long-life and safe lithium batteries, Nature Materials 8 (4) (2009) 320. doi:10.1038/nmat2418.

[62] M. Hu, X. Pang, Z. Zhou, Recent progress in high-voltage lithium ion batteries, Journal of Power Sources 237 (2013) 229–242. doi:10.1016/j.jpowsour.2013.03.024.

[63] M. Thackeray, W. David, P. Bruce, J. B. Goodenough, Lithium insertion into manganese spinels, Materials Research Bulletin 18 (4) (1983) 461–472. doi:10.1016/0025-5408(83)90138-1.

[64] Y.-H. Rho, L. F. Nazar, L. Perry, D. Ryan, Surface chemistry of $LiFePO_4$ studied by Mössbauer and X-ray photoelectron spectroscopy and its effect on

electrochemical properties, Journal of the Electrochemical Society 154 (4) (2007) A283–A289.

[65] A. K. Padhi, K. S. Nanjundaswamy, J. B. Goodenough, Phospho-olivines as positive-electrode materials for rechargeable lithium batteries, Journal of the Electrochemical Society 144 (4) (1997) 1188–1194. doi:10.1149/1.1837571.

[66] J. W. Fergus, Recent developments in cathode materials for lithium ion batteries, Journal of Power Sources 195 (4) (2010) 939–954. doi:10.1016/j.jpowsour.2009.08.089.

[67] M. Saıdi, J. Barker, H. Huang, J. Swoyer, G. Adamson, Electrochemical properties of lithium vanadium phosphate as a cathode material for lithium-ion batteries, Electrochemical and Solid-State Letters 5 (7) (2002) A149–A151. doi:10.1149/1.1479295.

[68] J. B. Goodenough, Y. Kim, Challenges for rechargeable batteries, Journal of Power Sources 196 (16) (2011) 6688–6694. doi:10.1016/j.jpowsour.2010.11.074.

[69] K. Xu, Nonaqueous liquid electrolytes for lithium-based rechargeable batteries, Chemical Reviews 104 (10) (2004) 4303–4418. doi:10.1002/chin.200450271.

[70] M. Ciambezi, Probing the evolution of SEI in Li-ion cells by As K-edge X-ray absorption spectroscopy, Master's thesis, Università di Camerino, Camerino, ITALY (2015).

[71] M. Park, X. Zhang, M. Chung, G. B. Less, A. M. Sastry, A review of conduction phenomena in Li-ion batteries, Journal of Power Sources 195 (24) (2010) 7904–7929. doi:10.1016/j.jpowsour.2010.06.060.

[72] O. Y. Chusid, E. E. Ely, D. Aurbach, M. Babai, Y. Carmeli, Electrochemical and spectroscopic studies of carbon electrodes in lithium battery electrolyte systems, Journal of Power Sources 43 (1) (1993) 47–64. doi:10.1016/0378-7753(93)80101-t.

[73] J.-Y. Hwang, S.-T. Myung, Y.-K. Sun, Sodium-ion batteries: present and future, Chemical Society Reviews 46 (12) (2017) 3529–3614. doi:10.1039/c6cs00776g.

[74] E. de la Llave, V. Borgel, K.-J. Park, J.-Y. Hwang, Y.-K. Sun, P. Hartmann, F.-F. Chesneau, D. Aurbach, Comparison between Na-Ion and Li-Ion cells: understanding the critical role of the cathodes stability and the anodes pretreatment

on the cells behavior, ACS applied materials & interfaces 8 (3) (2016) 1867–1875. doi:10.1021/acsami.5b09835.

[75] M. D. Slater, D. Kim, E. Lee, C. S. Johnson, Sodium-ion batteries, Advanced Functional Materials 23 (8) (2013) 947–958.

[76] M. Á. Muñoz-Márquez, D. Saurel, J. L. Gómez-Cámer, M. Casas-Cabanas, E. Castillo-Martínez, T. Rojo, Na-Ion Batteries for Large Scale Applications: A Review on Anode Materials and Solid Electrolyte Interphase Formation, Advanced Energy Materials 7 (20) (2017) 1700463. doi:10.1002/aenm.201700463.

[77] P. Adelhelm, P. Hartmann, C. L. Bender, M. Busche, C. Eufinger, J. Janek, From lithium to sodium: cell chemistry of room temperature sodium–air and sodium–sulfur batteries, Beilstein Journal of Nanotechnology 6 (1) (2015) 1016–1055. doi:10.3762/bjnano.6.105.

[78] G. H. Newman, L. P. Klemann, Ambient Temperature Cycling of an Na-TiS_2 Cell, Journal of the Electrochemical Society 127 (10) (1980) 2097–2099.

[79] J.-J. Braconnier, C. Delmas, C. Fouassier, P. Hagenmuller, Comportement electrochimique des phases Na_xCoO_2, Materials Research Bulletin 15 (12) (1980) 1797–1804. doi:10.1016/0025-5408(80)90199-3.

[80] L. Shacklette, J. Toth, N. Murthy, R. Baughman, Polyacetylene and polyphenylene as anode materials for nonaqueous secondary batteries, Journal of the Electrochemical Society 132 (7) (1985) 1529–1535. doi:10.1149/1.2114159.

[81] T. Shishikura, M. Takeuchi, Secondary batteries, Showa Denko KK Hitachi, Ltd., Japan.

[82] K. Kubota, S. Komaba, Practical issues and future perspective for Na-ion batteries, Journal of the Electrochemical Society 162 (14) (2015) A2538–A2550.

[83] V. Palomares, M. Casas-Cabanas, E. Castillo-Martínez, M. H. Han, T. Rojo, Update on Na-based battery materials. A growing research path, Energy & Environmental Science 6 (8) (2013) 2312–2337. doi:10.1039/c3ee41031e.

[84] M. M. Doeff, Y. Ma, S. J. Visco, L. C. De Jonghe, Electrochemical insertion of sodium into carbon, Journal of the Electrochemical Society 140 (12) (1993) L169–L170. doi:10.1149/1.2221153.

[85] A. Varzi, R. Raccichini, S. Passerini, B. Scrosati, Challenges and prospects of the role of solid electrolytes in the revitalization of lithium metal batteries, Journal of Materials Chemistry A 4 (44) (2016) 17251–17259. doi:10.1039/c6ta07384k.

[86] S.-W. Kim, D.-H. Seo, X. Ma, G. Ceder, K. Kang, Electrode materials for rechargeable sodium-ion batteries: potential alternatives to current lithium-ion batteries, Advanced Energy Materials 2 (7) (2012) 710–721. doi:10.1002/aenm.201200026.

[87] D. DiVincenzo, E. Mele, Cohesion and structure in stage-1 graphite intercalation compounds, Physical Review B 32 (4) (1985) 2538. doi:10.1103/physrevb.32.2538.

[88] B. Jache, P. Adelhelm, Use of graphite as a highly reversible electrode with superior cycle life for sodium-ion batteries by making use of co-intercalation phenomena, Angewandte Chemie International Edition 53 (38) (2014) 10169–10173. doi:10.1002/anie.201403734.

[89] D. Stevens, J. Dahn, High capacity anode materials for rechargeable sodium-ion batteries, Journal of the Electrochemical Society 147 (4) (2000) 1271–1273. doi:10.1149/1.1393348.

[90] Z. Liang, P. Hui-Lin, H. Yong-Sheng, L. Hong, C. Li-Quan, Spinel lithium titanate ($Li_4Ti_5O_{12}$) as novel anode material for room-temperature sodium-ion battery, Chinese Physics B 21 (2) (2012) 028201. doi:10.1088/1674-1056/21/2/028201.

[91] P. Senguttuvan, G. Rousse, V. Seznec, J.-M. Tarascon, M. R. Palacin, $Na_2Ti_3O_7$: lowest voltage ever reported oxide insertion electrode for sodium ion batteries, Chemistry of Materials 23 (18) (2011) 4109–4111. doi:10.1021/cm202076g.

[92] T. Jow, L. Shacklette, M. Maxfield, D. Vernick, The role of conductive polymers in alkali-metal secondary electrodes, Journal of the Electrochemical Society 134 (7) (1987) 1730–1733. doi:10.1149/1.2100746.

[93] M. Sawicki, L. L. Shaw, Advances and challenges of sodium ion batteries as post lithium ion batteries, RSC Advances 5 (65) (2015) 53129–53154. doi:10.1039/c5ra08321d.

[94] H. Morito, T. Yamada, T. Ikeda, H. Yamane, Na–Si binary phase diagram and solution growth of silicon crystals, Journal of Alloys and Compounds 480 (2) (2009) 723–726. doi:10.1016/j.jallcom.2009.02.036.

[95] Q. Sun, Q.-Q. Ren, H. Li, Z.-W. Fu, High capacity Sb_2O_4 thin film electrodes for rechargeable sodium battery, Electrochemistry Communications 13 (12) (2011) 1462–1464. doi:10.1016/j.elecom.2011.09.020.

[96] V. Chevrier, G. Ceder, Challenges for Na-ion negative electrodes, Journal of the Electrochemical Society 158 (9) (2011) A1011–A1014. doi:10.1149/1.3607983.

[97] R. Alcántara, M. Jaraba, P. Lavela, J. Tirado, NiCo2O4 spinel: First report on a transition metal oxide for the negative electrode of sodium-ion batteries, Chemistry of Materials 14 (7) (2002) 2847–2848. doi:10.1021/cm025556v.

[98] M. H. Han, E. Gonzalo, G. Singh, T. Rojo, A comprehensive review of sodium layered oxides: powerful cathodes for Na-ion batteries, Energy & Environmental Science 8 (1) (2015) 81–102. doi:10.1039/c4ee03192j.

[99] C. Delmas, J.-J. Braconnier, P. Hagenmuller, A new variety of $LiCoO_2$ with an unusual oxygen packing obtained by exchange reaction, Materials Research Bulletin 17 (1) (1982) 117–123. doi:10.1016/0025-5408(82)90192-1.

[100] N. Yabuuchi, K. Kubota, M. Dahbi, S. Komaba, Research development on sodium-ion batteries, Chemical Reviews 114 (23) (2014) 11636–11682. doi:10.1021/cr500192f.

[101] M. Dahbi, N. Yabuuchi, K. Kubota, K. Tokiwa, S. Komaba, Negative electrodes for Na-ion batteries, Physical Chemistry Chemical Physics 16 (29) (2014) 15007–15028. doi:10.1039/c4cp00826j.

[102] H. Hwang, M. G. Kim, Y. Kim, S. W. Martin, J. Cho, The electrochemical lithium reactions of monoclinic ZnP_2 material, Journal of Materials Chemistry 17 (30) (2007) 3161. doi:10.1039/b702648j.

[103] L. Shacklette, J. Wolf, S. Gould, R. Baughman, Structure and properties of polyaniline as modeled by single-crystal oligomers, The Journal of chemical physics 88 (6) (1988) 3955–3961. doi:10.1063/1.453844.

[104] C. Delmas, J.-J. Braconnier, C. Fouassier, P. Hagenmuller, Electrochemical intercalation of sodium in Na_xCoO_2 bronzes, Solid State Ionics 3 (1981) 165–169. doi:10.1016/0167-2738(81)90076-x.

[105] M. D. Slater, D. Kim, E. Lee, C. S. Johnson, Sodium-Ion Batteries, Advanced Functional Materials 23 (8) (2013) 947–958. doi:10.1002/adfm.201200691.

[106] A. Mendiboure, C. Delmas, P. Hagenmuller, Electrochemical intercalation and deintercalation of $NaxMnO_2$ bronzes, Journal of Solid State Chemistry 57 (3) (1985) 323–331. doi:10.1016/0022-4596(85)90194-x.

[107] A. Ponrouch, D. Monti, A. Boschin, B. Steen, P. Johansson, M. Palacin, Non-aqueous electrolytes for sodium-ion batteries, Journal of Materials Chemistry A 3 (1) (2015) 22–42. doi:10.1039/c4ta04428b.

[108] M. Zarrabeitia Ipiña, Low and high voltage stability of Na-ion battery materials: study of structural, transport and interfacial properties, Ph.D. thesis, UNIVERSIDAD DEL PAÌS VASCO EUSKAL HERRIKO UNIBERSITATEA (2016).

[109] D. Kundu, E. Talaie, V. Duffort, L. F. Nazar, The emerging chemistry of sodium ion batteries for electrochemical energy storage, Angewandte Chemie International Edition 54 (11) (2015) 3431–3448. doi:10.1002/anie.201410376.

[110] E. Peled, The electrochemical behavior of alkali and alkaline earth metals in nonaqueous battery systems—the solid electrolyte interphase model, Journal of the Electrochemical Society 126 (12) (1979) 2047–2051. doi:10.1149/1.2128859.

[111] P. Verma, P. Maire, P. Novák, A review of the features and analyses of the solid electrolyte interphase in Li-ion batteries, Electrochimica Acta 55 (22) (2010) 6332–6341. doi:10.1016/j.electacta.2010.05.072.

[112] S. J. Rezvani, R. Gunnella, A. Witkowska, F. Mueller, M. Pasqualini, F. Nobili, S. Passerini, A. D. Cicco, Is the solid electrolyte interphase an extra-charge reservoir in li-ion batteries?, ACS applied materials & interfaces 9 (5) (2017) 4570–4576. doi:10.1021/acsami.6b12408.

[113] A. Di Cicco, A. Giglia, R. Gunnella, S. L. Koch, F. Mueller, F. Nobili, M. Pasqualini, S. Passerini, R. Tossici, A. Witkowska, SEI Growth and Depth

Profiling on ZFO Electrodes by Soft X-Ray Absorption Spectroscopy, Advanced Energy Materials 5 (18). doi:10.1002/aenm.201500642.

[114] S. Zhang, K. Xu, T. Jow, Formation of solid electrolyte interface in lithium nickel mixed oxide electrodes during the first cycling, Electrochemical and Solid-State Letters 5 (5) (2002) A92–A94. doi:10.1149/1.1464506.

[115] V. A. Agubra, J. W. Fergus, The formation and stability of the solid electrolyte interface on the graphite anode, Journal of Power Sources 268 (2014) 153–162. doi:10.1016/j.jpowsour.2014.06.024.

[116] P. B. Balbuena, Y. Wang, Lithium-ion batteries: Solid-Electrolyte Interphase, World Scientific, 2004. doi:10.1142/p291.

[117] P. Novák, F. Joho, M. Lanz, B. Rykart, J.-C. Panitz, D. Alliata, R. Kötz, O. Haas, The complex electrochemistry of graphite electrodes in lithium-ion batteries, Journal of Power Sources 97 (2001) 39–46. doi:10.1016/s0378-7753(01)00586-9.

[118] Y. Ein-Eli, B. Markovsky, D. Aurbach, Y. Carmeli, H. Yamin, S. Luski, The dependence of the performance of Li-C intercalation anodes for Li-ion secondary batteries on the electrolyte solution composition, Electrochimica Acta 39 (17) (1994) 2559–2569. doi:10.1016/0013-4686(94)00221-5.

[119] C. Liebenow, M. Wagner, K. Lühder, P. Lobitz, J. Besenhard, Electrochemical behaviour of coated lithium-carbon electrodes, Journal of Power Sources 54 (2) (1995) 369–372. doi:10.1016/0378-7753(94)02104-b.

[120] T. Yoshida, M. Takahashi, S. Morikawa, C. Ihara, H. Katsukawa, T. Shiratsuchi, J.-i. Yamaki, Degradation mechanism and life prediction of lithium-ion batteries, Journal of the Electrochemical Society 153 (3) (2006) A576–A582. doi:10.1149/1.2162467.

[121] S. Bhattacharya, A. R. Riahi, A. T. Alpas, Electrochemical cycling behaviour of lithium carbonate (Li_2CO_3) pre-treated graphite anodes–SEI formation and graphite damage mechanisms, Carbon 77 (2014) 99–112. doi:10.1016/j.carbon.2014.05.011.

[122] H.-L. Zhang, F. Li, C. Liu, J. Tan, H.-M. Cheng, New insight into the solid electrolyte interphase with use of a focused ion beam, The Journal of Physical Chemistry B 109 (47) (2005) 22205–22211. doi:10.1021/jp053311a.

[123] D. Aurbach, Y. Ein-Ely, A. Zaban, The surface chemistry of lithium electrodes in alkyl carbonate solutions, Journal of the Electrochemical Society 141 (1) (1994) L1–L3. doi:10.1149/1.2054718.

[124] S. J. Rezvani, M. Ciambezi, R. Gunnella, M. Minicucci, M. A. Muñoz, F. Nobili, M. Pasqualini, S. Passerini, C. Schreiner, A. Trapananti, A. Witkowska, A. Di Cicco, Local Structure and Stability of SEI in Graphite and ZFO Electrodes Probed by As K-Edge Absorption Spectroscopy, The Journal of Physical Chemistry C doi:10.1021/acs.jpcc.5b11798.

[125] S. Malmgren, K. Ciosek, M. Hahlin, T. Gustafsson, M. Gorgoi, H. Rensmo, K. Edström, Comparing anode and cathode electrode/electrolyte interface composition and morphology using soft and hard X-ray photoelectron spectroscopy, Electrochimica Acta 97 (2013) 23–32. doi:10.1016/j.electacta.2013.03.010.

[126] A. Bhide, J. Hofmann, A. K. Dürr, J. Janek, P. Adelhelm, Electrochemical stability of non-aqueous electrolytes for sodium-ion batteries and their compatibility with $Na_{0.7}CoO_2$, Physical Chemistry Chemical Physics 16 (5) (2014) 1987–1998. doi:10.1039/c3cp53077a.

[127] M. Moshkovich, Y. Gofer, D. Aurbach, Investigation of the electrochemical windows of aprotic alkali metal (Li, Na, K) salt solutions, Journal of the Electrochemical Society 148 (4) (2001) E155–E167. doi:10.1149/1.1357316.

[128] S. Komaba, W. Murata, T. Ishikawa, N. Yabuuchi, T. Ozeki, T. Nakayama, A. Ogata, K. Gotoh, K. Fujiwara, Electrochemical Na insertion and solid electrolyte interphase for hard-carbon electrodes and application to Na-Ion batteries, Advanced Functional Materials 21 (20) (2011) 3859–3867. doi:10.1002/adfm.201100854.

[129] K. Edström, T. Gustafsson, J. O. Thomas, The cathode–electrolyte interface in the Li-ion battery, Electrochimica Acta 50 (2) (2004) 397–403. doi:10.1142/9781860946448_0008.

[130] S. Malmgren, Insights into Li-ion battery and Stainless steel interfaces using refined photoelectron spectroscopy methodology, Ph.D. thesis, Uppsala Universitet (2013).

[131] M. Moshkovich, M. Cojocaru, H. Gottlieb, D. Aurbach, The study of the anodic stability of alkyl carbonate solutions by in situ FTIR spectroscopy, EQCM, NMR and MS, Journal of Electroanalytical Chemistry 497 (1) (2001) 84–96. doi:10.1016/s0022-0728(00)00457-5.

[132] S. Martha, E. Markevich, V. Burgel, G. Salitra, E. Zinigrad, B. Markovsky, H. Sclar, Z. Pramovich, O. Heik, D. Aurbach, et al., A short review on surface chemical aspects of Li batteries: A key for a good performance, Journal of Power Sources 189 (1) (2009) 288–296. doi:10.1016/j.jpowsour.2008.09.084.

[133] E. Markevich, G. Salitra, D. Aurbach, Influence of the PVdF binder on the stability of $LiCoO_2$ electrodes, Electrochemistry Communications 7 (12) (2005) 1298–1304. doi:10.1016/j.elecom.2005.09.010.

[134] M. Thomas, P. Bruce, J. B. Goodenough, AC impedance analysis of polycrystalline insertion electrodes: application to $Li_{1-x}CoO_2$, Journal of the Electrochemical Society 132 (7) (1985) 1521–1528.

[135] S. Doubaji, B. Philippe, I. Saadoune, M. Gorgoi, T. Gustafsson, A. Solhy, M. Valvo, H. Rensmo, K. Edström, Passivation layer and cathodic redox reactions in sodium-ion batteries probed by HAXPES, ChemSusChem 9 (1) (2016) 97–108.

[136] B. Teo, D. Joy, EXAFS spectroscopy, Techniques and Applications, Springer, 1981.

[137] D. Koningsberger, R. Prins, X-ray absorption: principles, applications, techniques of EXAFS, SEXAFS, and XANES, John Wiley and Sons, New York, NY, 1988.

[138] D. E. Sayers, E. A. Stern, F. W. Lytle, New technique for investigating noncrystalline structures: Fourier analysis of the extended X-ray—absorption fine structure, Physical Review Letters 27 (18) (1971) 1204. doi:10.1103/physrevlett.27.1204.

[139] E. A. Stern, Theory of the extended x-ray-absorption fine structure, Physical Review B10 (8) (1974) 30273037. doi:10.1103/physrevb.10.3027.

[140] F. W. Lytle, D. E. Sayers, E. A. Stern, Extended x-ray-absorption fine-structure technique. II. Experimental practice and selected results, Physical Review B 11 (1975) 4825–4835. doi:10.1103/PhysRevB.11.4825.

[141] E. Stern, D. Sayers, F. Lytle, Extended x-ray-absorption fine-structure technique. III. Determination of physical parameters, Physical Review B 11 (12) (1975) 4836. doi:10.1103/physrevb.11.4836.

[142] A. Filipponi, A. Di Cicco, C. R. Natoli, X-ray-absorption spectroscopy and n-body distribution functions in condensed matter. I. Theory, Physical Review B 52 (21) (1995) 15122. doi:10.1103/PhysRevB.52.15122.

[143] A. Filipponi, A. Di Cicco, X-ray-absorption spectroscopy and n-body distribution functions in condensed matter. II. Data analysis and applications, Physical Review B 52 (21) (1995) 15135. doi:10.1103/physrevb.52.15135.

[144] M. Newville, Fundamentals of XAFS. Consortium for Advanced Radiation Sources, University of Chicago, Chicago, IL.

[145] G. Vlaica, L. Olivi, EXAFS spectroscopy: a brief introduction, Croatica chemica acta 77 (3) (2004) 427–433.

[146] M. Giorgetti, L. Stievano, X-Ray Absorption Spectroscopy Study of Battery Materials, X-ray Characterization of Nanostructured Energy Materials by Synchrotron Radiation (2017) 51–75doi:10.5772/66868.

[147] F. Boscherini, Applications of XAFS to nanostructures and materials science, in: Synchrotron Radiation, Springer, 2015, pp. 485–498.

[148] S. A. Guda, A. A. Guda, M. A. Soldatov, K. A. Lomachenko, A. L. Bugaev, C. Lamberti, W. Gawelda, C. Bressler, G. Smolentsev, A. V. Soldatov, et al., Optimized finite difference method for the full-potential XANES simulations: application to molecular adsorption geometries in MOFs and metal–ligand intersystem crossing transients, Journal of chemical theory and computation 11 (9) (2015) 4512–4521. doi:10.1021/acs.jctc.5b00327.

[149] A. I. Frenkel, C. W. Hills, R. G. Nuzzo, A view from the inside: complexity in the atomic scale ordering of supported metal nanoparticles (2001). doi:10.1021/jp012769j.

[150] G. Bunker, Introduction to XAFS a practical guide to X-ray absorption fine structure spectroscopy, Cambridge University Press, Cambridge; New York, 2010. doi:10.1017/CBO9780511809194.

[151] J. F. Watts, J. Wolstenholme, An introduction to surface analysis by XPS and AES, An Introduction to Surface Analysis by XPS and AES, by John F. Watts, John Wolstenholme, pp. 224. ISBN 0-470-84713-1. Wiley-VCH, May 2003. (2003) 224doi:10.1002/9781119417651.

[152] A. Damascelli, Z. Hussain, Z.-X. Shen, Angle-resolved photoemission studies of the cuprate superconductors, Reviews of modern physics 75 (2) (2003) 473. doi:10.1103/revmodphys.75.473.

[153] M. P. Seah, W. Dench, Quantitative electron spectroscopy of surfaces: A standard data base for electron inelastic mean free paths in solids, Surface and interface analysis 1 (1) (1979) 2–11. doi:10.1002/sia.740010103.

[154] P. Van der Heide, X-Ray photoelectron spectroscopy, An Introduction to Principles and Practices, Wiley Online Library, 2011. doi:10.1002/9781118162897.

[155] I. R. Lewis, H. Edwards, Handbook of Raman spectroscopy: from the research laboratory to the process line, CRC Press, 2001. doi:10.1201/9781420029253.

[156] G. Herzberg, B. L. Crawford Jr, Infrared and Raman spectra of polyatomic molecules., The Journal of Physical Chemistry 50 (3) (1946) 288–288. doi:10.1021/j150447a021.

[157] J. G. Grasselli, B. J. Bulkin, Analytical Raman Spectroscopy, New York : Wiley, 1991.

[158] J. R. Ferraro, Introductory Raman spectroscopy, Elsevier, 2003.

[159] B. Schrader, Infrared and Raman spectroscopy: methods and applications, John Wiley & Sons, 2008.

[160] E. Smith, G. Dent, Modern Raman spectroscopy: a practical approach, Wiley, 2019. doi:10.1002/9781119440598.

[161] P. Vandenabeele, Practical Raman Spectroscopy, an Introduction, Wiley, 2013.

[162] R. Baddour-Hadjean, J.-P. Pereira-Ramos, Raman Microspectrometry Applied to the Study of Electrode Materials for Lithium Batteries, Chemical Reviews 110 (3) (2010) 1278–1319. doi:10.1021/cr800344k.

[163] A. J. Bard, L. R. Faulkner, J. Leddy, C. G. Zoski, Electrochemical methods: fundamentals and applications, Vol. 2, wiley New York, 1980.

[164] W. He, N. Williard, M. Osterman, M. Pecht, Prognostics of lithium-ion batteries based on Dempster–Shafer theory and the Bayesian Monte Carlo method, Journal of Power Sources 196 (23) (2011) 10314–10321. doi:10.1016/j.jpowsour.2011.08.040.

[165] S.-I. Pyun, H.-C. Shin, J.-W. Lee, J.-Y. Go, Electrochemistry of insertion materials for hydrogen and lithium, Springer Science & Business Media, 2012. doi:10.1007/978-3-642-29464-8.

[166] H. Wang, L.-F. Cui, Y. Yang, H. Sanchez Casalongue, J. T. Robinson, Y. Liang, Y. Cui, H. Dai, Mn_3O_4- graphene hybrid as a high-capacity anode material for lithium ion batteries, Journal of the American Chemical Society 132 (40) (2010) 13978–13980. doi:10.1021/ja105296a.

[167] S. Grugeon, S. Laruelle, L. Dupont, F. Chevallier, P. Taberna, P. Simon, L. Gireaud, S. Lascaud, E. Vidal, B. Yrieix, et al., Combining electrochemistry and metallurgy for new electrode designs in Li-ion batteries, Chemistry of Materials 17 (20) (2005) 5041–5047. doi:10.1021/cm0511825.

[168] P. Meduri, E. Clark, J. H. Kim, E. Dayalan, G. U. Sumanasekera, M. K. Sunkara, MoO_{3-x} nanowire arrays as stable and high-capacity anodes for lithium ion batteries, Nano Letters 12 (4) (2012) 1784–1788. doi:10.1021/nl203649p.

[169] P. Balaya, H. Li, L. Kienle, J. Maier, Fully reversible homogeneous and heterogeneous Li storage in RuO_2 with high capacity, Advanced Functional Materials 13 (8) (2003) 621–625. doi:10.1002/adfm.200304406.

[170] J. Cabana, L. Monconduit, D. Larcher, M. R. Palacin, Beyond intercalation-based Li-ion batteries: the state of the art and challenges of electrode materials reacting through conversion reactions, Advanced Materials 22 (35) (2010) E170–E192. doi:10.1002/adma.201000717.

[171] J. Wang, P. King, R. Huggins, Investigations of binary lithium-zinc, lithium-cadmium and lithium-lead alloys as negative electrodes in organic solvent-based electrolyte, Solid State Ionics 20 (3) (1986) 185–189. doi:10.1016/0167-2738(86)90212-2.

[172] F. Belliard, P. Connor, J. Irvine, Novel tin oxide-based anodes for Li-ion batteries, Solid State Ionics 135 (1-4) (2000) 163–167. doi:10.1016/s0167-2738(00)00296-4.

[173] F. Belliard, J. Irvine, Electrochemical performance of ball-milled ZnO–SnO_2 systems as anodes in lithium-ion battery, Journal of Power Sources 97 (2001) 219–222. doi:10.1016/s0378-7753(01)00544-4.

[174] C. Chen, M. Greenblatt, J. Waszczak, Lithium insertion reactions of spinels: Effect of the distribution and reducibility of cations in selected manganite and zinc spinels, Materials Research Bulletin 21 (5) (1986) 609–619. doi:10.1016/0025-5408(86)90116-9.

[175] Y.-N. NuLi, Y.-Q. Chu, Q.-Z. Qin, Nanocrystalline $ZnFe_2O_4$ and Ag-Doped $ZnFe_2O_4$ Films Used as New Anode Materials for Li-Ion Batteries, Journal of the Electrochemical Society 151 (7) (2004) A1077. doi:10.1149/1.1760576.

[176] X. Guo, X. Lu, X. Fang, Y. Mao, Z. Wang, L. Chen, X. Xu, H. Yang, Y. Liu, Lithium storage in hollow spherical $ZnFe_2O_4$ as anode materials for lithium ion batteries, Electrochemistry Communications 12 (6) (2010) 847–850. doi:10.1016/j.elecom.2010.04.003.

[177] L. Cabo-Fernandez, F. Mueller, S. Passerini, L. J. Hardwick, In situ Raman spectroscopy of carbon-coated $ZnFe_2O_4$ anode material in Li-ion batteries, an investigation of SEI growth, Chemical Communications 52 (20) (2016) 3970–3973. doi:10.1039/C5CC09350C.

[178] Y. Deng, Q. Zhang, S. Tang, L. Zhang, S. Deng, Z. Shi, G. Chen, One-pot synthesis of $ZnFe_2O_{4/}$C hollow spheres as superior anode materials for lithium ion batteries, Chemical Communications 47 (24) (2011) 6828–6830. doi:10.1039/c0cc05001f.

[179] P. F. Teh, Y. Sharma, S. S. Pramana, M. Srinivasan, Nanoweb anodes composed of one-dimensional, high aspect ratio, size tunable electrospun ZnFe 2 O 4 nanofibers for lithium ion batteries, Journal of Materials Chemistry 21 (38) (2011) 14999–15008. doi:10.1039/c1jm12088c.

[180] S. Ayyappan, G. Paneerselvam, M. Antony, J. Philip, Structural stability of $ZnFe_2O_4$ nanoparticles under different annealing conditions, Materials Chemistry

and Physics 128 (3) (2011) 400–404. doi:10.1016/j.matchemphys.2011.03.012.

[181] D. Carta, C. Marras, D. Loche, G. Mountjoy, S. I. Ahmed, A. Corrias, An X-ray absorption spectroscopy study of the inversion degree in zinc ferrite nanocrystals dispersed on a highly porous silica aerogel matrix, The Journal of Chemical Physics 138 (5) (2013) 054702. doi:10.1063/1.4789479.

[182] V. G. Harris, N. C. Koon, C. M. Williams, Q. Zhang, M. Abe, J. P. Kirkland, Cation distribution in NiZn-ferrite films via extended x-ray absorption fine structure, Applied Physics Letters 68 (15) (1996) 2082. doi:10.1063/1.115591.

[183] F. Martinez-Julian, A. Guerrero, M. Haro, J. Bisquert, D. Bresser, E. Paillard, S. Passerini, G. Garcia-Belmonte, Probing Lithiation Kinetics of Carbon-Coated $ZnFe_2O_4$ Nanoparticle Battery Anodes, The Journal of Physical Chemistry C 118 (12) (2014) 6069–6076. doi:10.1021/jp412641v.

[184] F. Mueller, D. Bresser, E. Paillard, M. Winter, S. Passerini, Influence of the carbonaceous conductive network on the electrochemical performance of $ZnFe_2O_4$ nanoparticles, Journal of Power Sources 236 (2013) 87–94. doi:10.1016/j.jpowsour.2013.02.051.

[185] Y. Sharma, N. Sharma, G. Subba Rao, B. Chowdari, Nanophase $ZnCo_2O_4$ as a High Performance Anode Material for Li-Ion Batteries, Advanced Functional Materials 17 (15) (2007) 2855–2861. doi:10.1002/adfm.200600997.

[186] F. Maroni, S. Gabrielli, A. Palmieri, E. Marcantoni, F. Croce, F. Nobili, High cycling stability of anodes for lithium-ion batteries based on Fe_3O_4 nanoparticles and poly (acrylic acid) binder, Journal of Power Sources 332 (2016) 79–87. doi:10.1016/j.jpowsour.2016.09.106.

[187] Y. Sharma, N. Sharma, G. S. Rao, B. Chowdari, Li-storage and cyclability of urea combustion derived $ZnFe_2O_4$ as anode for Li-ion batteries, Electrochimica Acta 53 (5) (2008) 2380–2385. doi:10.1016/j.electacta.2007.09.059.

[188] C. J. Chen, M. Greenblatt, J. V. Waszczak, Lithium insertion into spinel ferrites, Solid State Ionics 18–19, Part 2 (1986) 838–846. doi:10.1016/0167-2738(86)90273-0.

[189] V. S. Urusov, Interaction of cations on octahedral and tetrahedral sites in simple spinels: A reply, Physics and Chemistry of Minerals 10 (4) (1984) 194–195. doi:10.1007/bf00311478.

[190] M. M. Thackeray, W. I. F. David, J. B. Goodenough, Structural characterization of the lithiated iron oxides $Li_xFe_3O_4$ and $Li_xFe_2O_3$ (0< x< 2), Materials Research Bulletin 17 (6) (1982) 785–793. doi:10.1016/0025-5408(82)90029-0.

[191] T. Fujieda, S. Takahashi, S. Higuchi, Cycling behaviour of electrodeposited zinc alloy electrode for secondary lithium batteries, Journal of Power Sources 40 (3) (1992) 283–289. doi:10.1016/0378-7753(92)80016-5.

[192] O. Mathon, A. Beteva, J. Borrel, D. Bugnazet, S. Gatla, R. Hino, I. Kantor, T. Mairs, M. Munoz, S. Pasternak, et al., The time-resolved and extreme conditions XAS (TEXAS) facility at the European Synchrotron Radiation Facility: the general-purpose EXAFS bending-magnet beamline BM23, Journal of synchrotron radiation 22 (6) (2015) 1548–1554. doi:10.1107/s1600577515017786.

[193] F. de Groot, High-Resolution X-ray Emission and X-ray Absorption Spectroscopy, Chemical Reviews 101 (6) (2001) 1779–1808, pMID: 11709999. doi:10.1021/cr9900681.

[194] T. Yamamoto, Assignment of pre-edge peaks in K-edge x-ray absorption spectra of 3d transition metal compounds: electric dipole or quadrupole?, X-Ray Spectrometry 37 (6) 572–584. doi:10.1002/xrs.1103.

[195] D. Zhou, H. Jia, J. Rana, T. Placke, T. Scherb, R. Kloepsch, G. Schumacher, M. Winter, J. Banhart, Local structural changes of nano-crystalline $ZnFe_2O_4$ during lithiation and de-lithiation studied by X-ray absorption spectroscopy, Electrochimica Acta 246 (2017) 699–706. doi:10.1016/j.electacta.2017.06.098.

[196] Y. Zhang, C. J. Pelliccione, A. B. Brady, H. Guo, P. F. Smith, P. Liu, A. C. Marschilok, K. J. Takeuchi, E. S. Takeuchi, Probing the Li Insertion Mechanism of $ZnFe_2O_4$ in Li-Ion Batteries: A Combined X-Ray Diffraction, Extended X-Ray Absorption Fine Structure, and Density Functional Theory Study, Chemistry of Materials 29 (10) (2017) 4282–4292. doi:10.1021/acs.chemmater.7b00467.

[197] V. Blanco-Gutiérrez, F. Jiménez-Villacorta, P. Bonville, M. J. Torralvo-Fernández, R. Sáez-Puche, X-ray Absorption Spectroscopy and Mössbauer Spectroscopy Studies of Superparamagnetic $ZnFe_2O_4$ Nanoparticles, The Journal of Physical Chemistry C 115 (5) (2011) 1627–1634. doi:10.1021/jp109368z.

[198] K. Momma, F. Izumi, VESTA 3 for three-dimensional visualization of crystal, volumetric and morphology data, Journal of applied crystallography 44 (6) (2011) 1272–1276. doi:10.1107/s0021889811038970.

[199] A. Di Cicco, M. Berrettoni, S. Stizza, E. Bonetti, G. Cocco, Microstructural defects in nanocrystalline iron probed by x-ray-absorption spectroscopy, Physical Review B 50 (17) (1994) 12386. doi:10.1103/PhysRevB.50.12386.

[200] F. d'Acapito, Introduction to ab-initio methods for EXAFS data analysis.

[201] B. Manning, Arsenic speciation in As (III)-and As (V)-treated soil using XANES spectroscopy, Microchimica Acta 151 (3-4) (2005) 181–188. doi:10.1007/s00604-005-0398-4.

[202] P. Kappen, J. Webb, An EXAFS study of arsenic bonding on amorphous aluminium hydroxide, Applied geochemistry 31 (2013) 79–83. doi:10.1016/j.apgeochem.2012.12.007.

[203] Y. Arai, E. J. Elzinga, D. L. Sparks, X-ray absorption spectroscopic investigation of arsenite and arsenate adsorption at the aluminum oxide–water interface, Journal of Colloid and Interface Science 235 (1) (2001) 80–88. doi:10.1006/jcis.2000.7249.

[204] K. Tasaki, A. Goldberg, J.-J. Lian, M. Walker, A. Timmons, S. J. Harris, Solubility of lithium salts formed on the lithium-ion battery negative electrode surface in organic solvents, Journal of The Electrochemical Society 156 (12) (2009) A1019–A1027. doi:10.1149/1.3239850.

[205] J. Parsons, M. Lopez, J. Peralta-Videa, J. Gardea-Torresdey, Determination of arsenic (III) and arsenic (V) binding to microwave assisted hydrothermal synthetically prepared Fe_3O_4, Mn_3O_4, and $MnFe_2O_4$ nanoadsorbents, Microchemical Journal 91 (1) (2009) 100–106. doi:10.1016/j.microc.2008.08.012.

[206] C. Davies, R. Gillespie, J. Park, J. Passmore, Polyatomic cations of sulfur. II. Crystal structure of octasulfur bis (hexafluoroarsenate), $S_8(AsF_6)_2$, Inorganic Chemistry 10 (12) (1971) 2781–2784. doi:10.1021/ic50106a031.

[207] C. Wagner, A. Joshi, The auger parameter, its utility and advantages: a review, Journal of Electron Spectroscopy and Related Phenomena 47 (1988) 283–313. doi:10.1016/0368-2048(88)85018-7.

[208] D. Aurbach, I. Weissman, A. Schechter, H. Cohen, X-ray photoelectron spectroscopy studies of lithium surfaces prepared in several important electrolyte solutions. A comparison with previous studies by Fourier transform infrared spectroscopy, Langmuir 12 (16) (1996) 3991–4007. doi:10.1021/la9600762.

[209] D. Aurbach, B. Markovsky, A. Shechter, Y. Ein-Eli, H. Cohen, A Comparative Study of Synthetic Graphite and Li Electrodes in Electrolyte Solutions Based on Ethylene Carbonate-Dimethyl Carbonate Mixtures, Journal of the Electrochemical Society 143 (12) (1996) 3809–3820. doi:10.1149/1.1837300.

[210] D. Aurbach, A. Zaban, Impedance spectroscopy of nonactive metal electrodes at low potentials in propylene carbonate solutions a comparison to studies of Li electrodes, Journal of The Electrochemical Society 141 (7) (1994) 1808–1819.

[211] D. Aurbach, A. Zaban, Impedance spectroscope of lithium electrodes: Part 2. The behaviour in propylene carbonate solutions: the significance of the data obtained, Journal of Electroanalytical Chemistry 367 (1-2) (1994) 15–25.

[212] J. F. Moulder, C. Wagner, W. Riggs, L. Davis, G. Mullenberg, Handbook of X-ray photoelectron spectroscopy, Perkin-Elmer Corporation, Physical Electronics Division, Eden Prairie, Minnesota, 1979.

[213] J. Walton, P. Wincott, N. Fairley, A. Carrick, Peak Fitting with CasaXPS: A Casa Pocket Book.

[214] A. M. Andersson, K. Edström, Chemical Composition and Morphology of the Elevated Temperature SEI on Graphite, Journal of the Electrochemical Society 148 (10) (2001) A1100. doi:10.1149/1.1397771.

[215] A. Andersson, A. Henningson, H. Siegbahn, U. Jansson, K. Edström, Electrochemically lithiated graphite characterised by photoelectron spectroscopy, Journal of Power Sources 119-121 (2003) 522–527. doi:10.1016/S0378-7753(03)00277-5.

[216] E. Peled, D. Golodnitsky, C. Menachem, D. Bar-Tow, An advanced tool for the selection of electrolyte components for rechargeable lithium batteries, Journal of the Electrochemical Society 145 (10) (1998) 3482–3486. doi:10.1149/1.1838831.

[217] D. Bar-Tow, E. Peled, L. Burstein, A Study of Highly Oriented Pyrolytic Graphite as a Model for the Graphite Anode in Li-Ion Batteries, Journal of the Electrochemical Society 146 (3) (1999) 824–832. doi:10.1149/1.1391688.

[218] K. Kanamura, S. Shiraishi, H. Takezawa, Z.-i. Takehara, XPS Analysis of the surface of a carbon electrode intercalated by lithium Ions, Chemistry of Materials 9 (8) (1997) 1797–1804. doi:10.1021/cm970042v.

[219] K. Kanamura, H. Tamura, Z.-i. Takehara, XPS analysis of a lithium surface immersed in propylene carbonate solution containing various salts, Journal of Electroanalytical Chemistry 333 (1-2) (1992) 127–142. doi:10.1016/0022-0728(92)80386-i.

[220] K. Kanamura, H. Tamura, S. Shiraishi, Z.-i. Takehara, Morphology and chemical compositions of surface films of lithium deposited on a Ni substrate in nonaqueous electrolytes, Journal of Electroanalytical Chemistry 394 (1-2) (1995) 49–62. doi:10.1016/0022-0728(95)03972-j.

[221] K. Kanamura, H. Takezawa, S. Shiraishi, Z.-i. Takehara, Chemical reaction of lithium surface during immersion in LiClO4 or LiPF6/DEC electrolyte, Journal of the Electrochemical Society 144 (6) (1997) 1900–1906.

[222] R. Dedryvère, L. Gireaud, S. Grugeon, S. Laruelle, J.-M. Tarascon, D. Gonbeau, Characterization of Lithium Alkyl Carbonates by X-ray Photoelectron Spectroscopy: Experimental and Theoretical Study, The Journal of Physical Chemistry B 109 (33) (2005) 15868–15875. doi:10.1021/jp051626k.

[223] S. Leroy, H. Martinez, R. Dedryvère, D. Lemordant, D. Gonbeau, Influence of the lithium salt nature over the surface film formation on a graphite electrode in Li-ion batteries: An XPS study, Applied Surface Science 253 (11) (2007) 4895–4905. doi:10.1016/j.apsusc.2006.10.071.

[224] S. Leroy, F. Blanchard, R. Dedryvère, H. Martinez, B. Carré, D. Lemordant, D. Gonbeau, Surface film formation on a graphite electrode in Li-ion batteries:

AFM and XPS study, Surface and Interface Analysis 37 (10) (2005) 773–781. doi:10.1002/sia.2072.

[225] R. Naejus, D. Lemordant, R. Coudert, P. Willmann, Nouveau procede de synthese de l'hexafluorophosphate de lithium, Journal of fluorine chemistry 90 (1) (1998) 81–85. doi:10.1016/s0022-1139(98)00161-4.

[226] V. Eshkenazi, E. Peled, L. Burstein, D. Golodnitsky, XPS analysis of the SEI formed on carbonaceous materials, Solid State Ionics 170 (1-2) (2004) 83–91. doi:10.1016/S0167-2738(03)00107-3.

[227] D. Aurbach, E. Zinigrad, Y. Cohen, H. Teller, A short review of failure mechanisms of lithium metal and lithiated graphite anodes in liquid electrolyte solutions, Solid state ionics 148 (3-4) (2002) 405–416. doi:10.1016/s0167-2738(02)00080-2.

[228] J. Rumble Jr, D. Bickham, C. Powell, The NIST x-ray photoelectron spectroscopy database, Surface and interface analysis 19 (1-12) (1992) 241–246. doi:10.1002/sia.740190147.

[229] J. Tarascon, D. Guyomard, The $Li_{1+x}Mn_2O_4$/C rocking-chair system: a review, Electrochimica Acta 38 (9) (1993) 1221–1231. doi:10.1016/0013-4686(93)80053-3.

[230] R. Bittihn, R. Herr, D. Hoge, The SWING system, a nonaqueous rechargeable carbon/metal oxide cell, Journal of power sources 43 (1-3) (1993) 223–231. doi:10.1016/0378-7753(93)80118-9.

[231] F. Tuinstra, J. L. Koenig, Raman spectrum of graphite, The Journal of Chemical Physics 53 (3) (1970) 1126–1130. doi:10.1063/1.1674108.

[232] C. Sole, N. E. Drewett, L. J. Hardwick, Insitu Raman study of lithium-ion intercalation into microcrystalline graphite, Faraday Discussionsdoi:10.1039/C4FD00079J.

[233] L. Malard, M. Pimenta, G. Dresselhaus, M. Dresselhaus, Raman spectroscopy in graphene, Physics reports 473 (5-6) (2009) 51–87. doi:10.1016/j.physrep.2009.02.003.

[234] M. H. Han, E. Gonzalo, N. Sharma, J. M. López del Amo, M. Armand, M. Avdeev, J. J. Saiz Garitaonandia, T. Rojo, High-Performance P2-Phase $Na_{2/3}$ $Mn_{0.8}$ Fe

$_{0.1}$ Ti $_{0.1}$ O $_{2}$ Cathode Material for Ambient-Temperature Sodium-Ion Batteries, Chemistry of Materials 28 (1) (2016) 106–116. doi:10.1021/acs.chemmater.5b03276.

[235] N. Ortiz-Vitoriano, N. E. Drewett, E. Gonzalo, T. Rojo, High performance manganese-based layered oxide cathodes: overcoming the challenges of sodium ion batteries, Energy & Environmental Science 10 (5) (2017) 1051–1074. doi:10.1039/C7EE00566K.

[236] J. Cho, Y. J. Kim, T.-J. Kim, B. Park, Zero-strain intercalation cathode for rechargeable Li-Ion cell, Angewandte Chemie International Edition 40 (18) (2001) 3367–3369. doi:10.1002/1521-3773(20010917)40:18<3367::aid-anie3367>3.0.co;2-a.

[237] K. Kubota, S. Kumakura, Y. Yoda, K. Kuroki, S. Komaba, Electrochemistry and Solid-State Chemistry of $NaMeO_2$ (Me= 3d Transition Metals), Advanced Energy Materials 8 (17) (2018) 1703415.

[238] S. Guo, Q. Li, P. Liu, M. Chen, H. Zhou, Environmentally stable interface of layered oxide cathodes for sodium-ion batteries, Nature communications 8 (1) (2017) 135. doi:10.1038/s41467-017-00157-8.

[239] J. Thorne, R. Dunlap, M. Obrovac, Structure and electrochemistry of $Na_xFe_xMn_{1-x}O_2$ (1.0< x< 0.5) for Na-ion battery positive electrodes, Journal of The Electrochemical Society 160 (2) (2013) A361–A367.

[240] B. M. De Boisse, D. Carlier, M. Guignard, C. Delmas, Structural and electrochemical characterizations of P2 and New O_3−$Na_xMn_{1-y}Fe_yO_2$ Phases prepared by auto-combustion synthesis for Na-ion batteries, Journal of The Electrochemical Society 160 (4) (2013) A569–A574. doi:10.1149/2.032304jes.

[241] K. Kubota, N. Yabuuchi, H. Yoshida, M. Dahbi, S. Komaba, Layered oxides as positive electrode materials for Na-ion batteries, Mrs Bulletin 39 (5) (2014) 416–422. doi:10.1557/mrs.2014.85.

[242] W. M. Dose, N. Sharma, J. C. Pramudita, H. E. Brand, E. Gonzalo, T. Rojo, Structure–Electrochemical Evolution of a Mn-Rich P2 $Na_{2/3}Fe_{0.2}Mn_{0.8}O_2$ Na-Ion Battery Cathode, Chemistry of Materials 29 (17) (2017) 7416–7423. doi:10.1021/acs.chemmater.7b02397.

[243] M. Zarrabeitia, E. Gonzalo, M. Ciambezi, O. Lakuntza, F. Nobili, A. Trapananti, A. Di Cicco, G. Aquilanti, N. A. Katcho, J.-M. L. del Amo, et al., Unraveling the role of Ti in the stability of positive layered oxide electrodes for rechargeable Na-ion batteries., Journal of Materials Chemistry Adoi:10.1039/c9ta02710f.

[244] N. Sharma, E. Gonzalo, J. C. Pramudita, M. H. Han, H. E. Brand, J. N. Hart, W. K. Pang, Z. Guo, T. Rojo, The Unique Structural Evolution of the O3-Phase $Na_{2/3}Fe_{2/3}Mn_{1/3}O_2$ during High Rate Charge/Discharge: A Sodium-Centred Perspective, Advanced Functional Materials 25 (31) (2015) 4994–5005. doi:10.1002/adfm.201501655.

[245] M. Han, N. Sharma, E. Gonzalo, J. Pramudita, H. Brand, J. L. del Amo, T. Rojo, Moisture exposed layered oxide electrodes as Na-ion battery cathodes, Journal of Materials Chemistry A 4 (48) (2016) 18963–18975. doi:10.1039/c6ta07950d.

[246] J. Rodríguez-Carvajal, Recent advances in magnetic structure determination by neutron powder diffraction, Physica B: Condensed Matter 192 (1-2) (1993) 55–69. doi:10.1016/0921-4526(93)90108-i.

[247] J.-P. Parant, R. Olazcuaga, M. Devalette, C. Fouassier, P. Hagenmuller, Sur quelques nouvelles phases de formule NaxMnO2 (x< 1), Journal of Solid State Chemistry 3 (1) (1971) 1–11. doi:10.1016/0022-4596(71)90001-6.

[248] S. Kumakura, Y. Tahara, S. Sato, K. Kubota, S. Komaba, P'2-$Na_{2/3}Mn_{0.9}Me_{0.1}O_2$ (Me= Mg, Ti, Co, Ni, Cu, and Zn): correlation between orthorhombic distortion and electrochemical property, Chemistry of Materials 29 (21) (2017) 8958–8962.

[249] J. Billaud, G. Singh, A. R. Armstrong, E. Gonzalo, V. Roddatis, M. Armand, T. Rojo, P. G. Bruce, $Na_{0.67}Mn_{1-x}Mg_xO_2$ (0< x< 0.2): a high capacity cathode for sodium-ion batteries, Energy & Environmental Science 7 (4) (2014) 1387–1391.

[250] W. Baur, The geometry of polyhedral distortions. Predictive relationships for the phosphate group, Acta Crystallographica Section B: Structural Crystallography and Crystal Chemistry 30 (5) (1974) 1195–1215. doi:10.1107/s0567740874004560.

[251] A. Di Cicco, G. Aquilanti, M. Minicucci, E. Principi, N. Novello, A. Cognigni, L. Olivi, Novel XAFS capabilities at ELETTRA synchrotron light source, in:

Journal of Physics: Conference Series, Vol. 190, IOP Publishing, 2009, p. 012043. doi:10.1088/1742-6596/190/1/012043.

[252] M. Abuín, A. Serrano, J. Chaboy, M. García, N. Carmona, XAS study of Mn, Fe and Cu as indicators of historical glass decay, Journal of Analytical Atomic Spectrometry 28 (7) (2013) 1118–1124. doi:10.1039/c3ja30374h.

[253] D. Lützenkirchen-Hecht, M. Wagemaker, P. Keil, A. Van Well, R. Frahm, Ex situ reflection mode EXAFS at the Ti K-edge of lithium intercalated TiO_2 rutile, Surface science 538 (1-2) (2003) 10–22. doi:10.1016/s0039-6028(03)00722-2.

[254] C. Natoli, M. Benfatto, C. Brouder, M. R. Lopez, D. Foulis, Multichannel multiple-scattering theory with general potentials, Physical Review B 42 (4) (1990) 1944. doi:10.1103/physrevb.42.1944.

[255] E. Merzbacher, Quantum Mechanics, Wiley, 1970. doi:10.1063/1.882667.

[256] L. I. Schiff, Quantum mechanics, 3rd, New York: M cGraw-Hill, 1968. doi:10.1119/1.1987309.

[257] J. G. Norman Jr, Non-empirical versus empirical choices for overlapping-sphere radii ratios in SCF-Xα-SW calculations on ClO_4 and SO_2, Molecular Physics 31 (4) (1976) 1191–1198. doi:10.1080/00268977600100921.

[258] W. L. Schaich, Comment on the theory of extended X-ray-absorption fine structure, Physical Review B 8 (8) (1973) 4028. doi:10.1103/physrevb.8.4028.

[259] P. Lee, J. Pendry, Theory of the extended x-ray absorption fine structure, Physical Review B 11 (8) (1975) 2795. doi:10.1103/physrevb.11.2795.

[260] C. Natoli, M. Benfatto, A unifying scheme of interpretation of X-ray absorption spectra based on the multiple scattering theory, Le Journal de Physique Colloques 47 (C8) (1986) C8–11. doi:10.1051/jphyscol:1986802.

List of Figures

List of Tables